

IMPERIAL COLLEGE OF SCIENCE, TECHNOLOGY,
AND MEDICINE.
UNIVERSITY OF LONDON.

DEPARTMENT OF MINERAL RESOURCES ENGINEERING.
ROYAL SCHOOL OF MINES, LONDON SW7 2BP.

CHARACTERISATION AND MODELLING OF
LAYERED DISCONTINUOUS RESERVOIRS
FOR WATERFLOOD PREDICTIONS.

BY

Omar Badawi ABU-ELBASHAR
B.Sc. (Pet. Eng.)

A thesis submitted for the degree of Doctor of Philosophy of the
University of London and for the Diploma of Imperial College.

London, April, 1990.

(In the name of God, Most Gracious, Most merciful.)

ABSTRACT

Analytical statistical methods have been developed for the calculation of effective horizontal and vertical permeabilities in fluvial sands. These sands are characterised by discontinuous shales, converging shales, and sand compartmentalisation. The methods developed have been verified by experimental and numerical modelling of these phenomena.

The additional problem of discontinuity of stochastic faults has also been addressed by a computational modelling scheme, based on outcrop data and field observations. An analytical method for the representation of this effect on permeability is developed.

The stochastic reservoir modelling techniques developed involve a sequential conditioning process to simplify the sand description while retaining the essential characteristics. An automatic parameter pseudoization scheme then generates a two dimensional model representing adequately the three dimensional character of the reservoir. An equivalent homogeneous model is created by this hybrid averaging technique.

The application of analytical waterflood prediction methods to this equivalent homogeneous reservoir have been studied, and comparisons of the standard methods have been evaluated. The limitations of these analytical methods are emphasised and appropriate modifications are introduced to obtain satisfactory waterflood predictions.

ACKNOWLEDGEMENTS

I am grateful to my supervisor, Professor C. G. Wall for his technical guidance which has made this thesis possible.

My sincere gratitude to Dr. T. S. Daltaban for his assistance and technical advice; and also to Dr. A. N. Folefac and Professor J. S. Archer, Dean of the Royal School of Mines, for advice and moral support.

My thanks to my colleague J. Wang for his help in preparation of this thesis. My thanks also to my colleagues A. Al-Gheithy, D. Wong, K. Padua, M. Al-Rumhy, X. Jing, P. Enwere, and M. Santiago for their assistance and encouragement. I will always remember their question: when is your examination?

I would like to express my appreciation to my wife for patiently standing by me all these years.

The financial support of the General Petroleum Corporation of Sudan is deeply acknowledged.

Praise be to God, the Cherisher and Sustainer of the Worlds for enabling me to complete this work.

Omar Badawi ABU-ELBASHAR

London, April, 1990.

TABLE OF CONTENTS

i	TITLE.....	1
ii	ABSTRACT.....	3
iii	ACKNOWLEDGEMENTS.....	4
iv	TABLE OF CONTENTS.....	5
v	LIST OF FIGURES.....	10
vi	LIST OF TABLES.....	13

CHAPTER 1

GENERAL TYPES OF HETEROGENEITY IN FLUVIAL RESERVOIRS AND THEIR IMPACT ON OIL RECOVERY

1.1	INTRODUCTION.....	14
1.2	FLUVIAL SAND GEOMETRY AND CONTINUITY.....	15
1.3	PERMEABILITY DISTRIBUTION IN FLUVIAL SANDS.....	19
1.3.1	POINT-BAR AND OXBOW DEPOSITS.....	20
1.3.2	CHANNEL-FILL AND BRAIDED STREAM DEPOSITS.....	20
1.3.3	FLOOD-SHEET DEPOSITS.....	23
1.4	DISTRIBUTION OF SHALE FACIES AND THEIR EFFECT ON RESERVOIR PERMEABILITIES.....	23
1.4.1	SHALE FACIES IN FLUVIAL DEPOSITS.....	24
1.4.2	SHALE GEOMETRY, DIMENSIONS, AND DISTRIBUTION IN FLUVIAL DEPOSITS.....	26
1.5	STOCHASTIC FAULTS AND THEIR EFFECT ON RESERVOIR PERMEABILITIES.....	28
1.6	EFFECT OF THE VARIOUS TYPES OF HETEROGENEITY ON OIL RECOVERY.....	30
1.6.1	EFFECT OF HETEROGENEITY WITHIN THE SAND FACIES.....	30
1.6.2	THE IMPACT OF DISCONTINUOUS BARRIERS ON OIL RECOVERY.....	31
1.6.3	EFFECT OF SAND DISCONTINUITY ON OIL RECOVERY.....	32
1.6.4	EFFECT OF FAULTING ON OIL RECOVERY.....	34

CHAPTER 2

REVIEW OF THE ANALYTICAL WATERFLOOD PREDICTION METHODS FOR HETEROGENEOUS RESERVOIRS

2.1	INTRODUCTION.....	35
2.2	REVIEW OF THE PREDICTION METHODS.....	35
2.3	DRAWBACKS AND OVERSIMPLIFICATIONS.....	39
2.4	EFFECT OF GRAVITY SEGREGATION ON WATERFLOODING.....	40
2.5	THE ROLE OF CAPILLARY PRESSURE IN WATERFLOODING.....	43
2.6	THE EFFECT OF MOBILITY RATIO ON WATERFLOODING.....	46
2.7	COMPARATIVE STUDY ON A SIMPLE 5-BED VERTICAL STRATIFICATION PROBLEM.....	47
2.7.1	A SIMPLE 5-BED VERTICAL STRATIFICATION PROBLEM.....	48
2.7.2	RESULTS.....	50
2.7.3	DISCUSSIONS.....	51
2.7.4	REMARKS.....	53

CHAPTER 3
 NUMERICAL AND ANALYTICAL MODELLING OF THE EFFECT OF
 HORIZONTAL AND OBLIQUE SHALES ON RESERVOIR PERMEABILITIES

3.1	INTRODUCTION.....	55
3.1.1	SHALE FACIES AND THEIR DISTRIBUTION IN FLUVIAL DEPOSITS.....	56
3.1.1.1	DRAPE.....	56
3.1.1.2	SLOUGH AND EDDY FACIES.....	56
3.1.1.3	OXBOW AND ABANDONED CHANNEL SHALES.....	56
3.1.1.4	BAY SHALES.....	58
3.1.1.5	GLACIODELTAIC AND OTHER FACIES.....	58
3.2	FLUVIAL SHALE DIMENSIONS AND GEOMETRY.....	58
3.2.1	VARIATION OF SHALE DIMENSIONS WITH ENVIRONMENT OF DEPOSITION.....	59
3.2.2	SHALE CONVERGENCE AND SAND COMPARTMENTALISATION.....	60
3.3	MODELS FOR CALCULATION OF EFFECTIVE PERMEABILITIES IN PRESENCE OF SHALES.....	63
3.3.1	MODELS FOR VERTICAL PERMEABILITY.....	63
3.3.1.1	DELHOMME'S MODEL.....	63
3.3.1.2	PRAT'S MODEL.....	63
3.3.1.3	WEBER'S MODEL.....	64
3.3.1.4	RICHARDSON'S MODEL.....	64
3.3.1.5	HALDORSEN'S MODEL.....	66
3.3.1.6	BEGG AND KING MODEL.....	66
3.3.1.7	BEGG AND CARTER MODEL.....	70
3.3.1.8	OTHER MODELS.....	70
3.3.2	MODELS FOR HORIZONTAL PERMEABILITY.....	70
3.4	ANALYTICAL CALCULATION OF PERMEABILITY IN PRESENCE OF DISCONTINUOUS SHALES.....	73
3.4.1	CALCULATION OF THE EFFECTIVE VERTICAL PERMEABILITY..	73
3.4.1.1	ASSUMPTIONS.....	73
3.4.1.2	BRIEF DESCRIPTION OF THE STEPS OF CALCULATION.....	75
3.4.1.3	A SIMPLIFIED FORMULA FOR CALCULATION OF THE STREAMTUBE'S LENGTH.....	80
3.4.1.4	CALCULATION OF THE STREAMTUBE'S LENGTH FOR THE CASE OF HORIZONTAL PERMEABILITY ANISOTROPY.....	81
3.4.1.5	VERTICAL PERMEABILITY FOR STRATIFIED RESERVOIRS....	83
3.4.2	CALCULATION OF THE EFFECTIVE HORIZONTAL PERMEABILITY.....	84
3.4.2.1	CALCULATION OF THE LENGTH OF THE STREAMTUBE.....	84
3.4.3	RESULTS AND DISCUSSIONS.....	88
3.4.4	VERIFICATION.....	91
3.5	NUMERICAL CALCULATION OF EFFECTIVE PERMEABILITIES IN PRESENCE OF OBLIQUE SHALES.....	92
3.5.1	CONSTRUCTION OF THE MODEL.....	92
3.5.2	CALCULATION PROCEDURE.....	95
3.5.3	VERTICAL PERMEABILITY CALCULATION.....	95
3.5.4	HORIZONTAL PERMEABILITY CALCULATION.....	97
3.6	SUMMARY.....	98

CHAPTER 4
EXPERIMENTS ON THE EFFECT OF STOCHASTIC SHALES
ON AVERAGED ABSOLUTE RESERVOIR PERMEABILITIES

4.1	INTRODUCTION.....	100
4.2	EQUIPMENT AND PROCEDURE.....	101
4.3	DESCRIPTION OF THE EXPERIMENT.....	103
4.3.1	CALCULATION OF THE NUMBER OF SHALES AND DCSUs.....	103
4.3.2	ARRANGEMENT OF THE EQUIPMENT AND MEASUREMENT PROCEDURE.....	104
4.3.3	CALIBRATION.....	106
4.3.3.1	CALCULATION OF THE MODEL RESISTIVITIES.....	106
4.3.3.2	EFFECT OF THE CLEARANCE ON THE RESULTS.....	107
4.4	RESISTIVITY CALCULATION (WITH BARRIERS).....	108
4.4.1	CALCULATION OF THE VERTICAL RESISTIVITY.....	108
4.4.2	CALCULATION OF THE HORIZONTAL RESISTIVITY.....	110
4.4.3	ACCOUNTING FOR THE DISTRIBUTION EFFECT.....	110
4.5	RESULTS AND DISCUSSIONS.....	110
4.6	VERIFICATION OF THE STREAMTUBE METHOD.....	117
4.7	DISCUSSION OF THE RESULTS OF THE STREAMTUBE METHOD.....	119
4.8	COMPARISON OF THE EXPERIMENTAL RESULTS WITH AND WITHOUT DCSUs.....	121
4.8.1	COMPARISON AT LOW SHALE FREQUENCIES.....	121
4.8.2	COMPARISON AT HIGH SHALE FREQUENCIES.....	121
4.9	SUMMARY.....	121

CHAPTER 5
EFFECT OF THE STOCHASTIC FAULTS ON
RESERVOIR PERMEABILITIES

5.1	INTRODUCTION.....	123
5.2	FAULTS SHAPE AND GEOMETRY.....	124
5.3	STOCHASTIC FAULT LENGTH AND THROW DISTRIBUTION.....	130
5.4	EFFECT OF STOCHASTIC FAULTS ON RESERVOIR PERMEABILITIES.....	133
5.5	RESULTS.....	138

CHAPTER 6
MODELLING AND SIMULATION OF FLUVIAL
RESERVOIRS COMPOSED OF STOCHASTIC SANDS

6.1	INTRODUCTION.....	140
6.2	DIMENSIONS AND ORIENTATIONS OF STOCHASTIC SANDS.....	141
6.2.1	SHAPES AND SPATIAL DISPOSITION OF STOCHASTIC SANDS.....	141
6.2.2	DEVELOPMENT OF THE STATISTICAL DATA BASE.....	145
6.2.2.1	THE SPECIFIC DATA BASE.....	145
6.2.2.2	THE GENERAL DATA BASE.....	146

6.3	STOCHASTIC MODELLING OF FLUVIAL RESERVOIRS.....	146
6.3.1	SPECIFICATION OF THE SIMULATION GRID DIMENSIONS....	147
6.3.2	GENERATION OF THE STOCHASTIC SANDS.....	148
6.3.3	STEPS OF THE SAND GENERATION SCHEME.....	149
6.3.4	THE AUTOMATIC SAND CONDITIONING PROCESS.....	150
6.3.5	GENERATION OF 3-D REALISATIONS OF THE SAND BODIES..	153
6.3.6	CONTROL OF THE GENERATED SAND FRACTION.....	157
6.4	CHARACTERISATION OF THE STOCHASTIC SANDS FOR SIMULATION.....	161
6.4.1	ASSIGNMENT OF THE NTG RATIOS.....	161
6.4.2	ASSIGNMENT OF THE HORIZONTAL PERMEABILITIES.....	161
6.4.3	ASSIGNMENT OF THE VERTICAL PERMEABILITIES.....	164
6.4.4	ASSIGNMENT OF THE POROSITIES.....	164
6.5	USE OF PSEUDO PARAMETERS FOR 2-D RESERVOIR DESCRIPTION.....	166
6.5.1	PSEUDO HORIZONTAL PERMEABILITY AND NTG.....	166
6.5.2	BACK PSEUDOIZATION OF HORIZONTAL PERMEABILITY.....	168
6.5.3	PSEUDO VERTICAL PERMEABILITY.....	169
6.5.4	BACK PSEUDOIZATION OF VERTICAL PERMEABILITY.....	171
6.5.5	ASSIGNMENT OF PSEUDO POROSITIES.....	171
6.6	COMPARATIVE SIMULATION STUDIES.....	171
6.6.1	GENERATION OF THE RELATIVE PERMEABILITY CURVES....	173
6.6.2	COMPUTATION OF THE CAPILLARY PRESSURE.....	175
6.6.3	THE 3-D SIMULATION STUDY.....	176
6.6.4	THE 2-D SIMULATION STUDIES.....	176
6.6.5	SIMULATION RESULTS AND DISCUSSIONS.....	177
6.6.5.1	RESULTS OF THE 3-D STUDY.....	177
6.6.5.2	RESULTS OF THE 2-D STUDY WITH PSEUDO PARAMETERS....	177
6.6.5.3	RESULTS OF THE 2-D STUDY WITHOUT PSEUDO PARAMETERS.	180
6.6.5.4	DISCUSSION OF THE SIMULATION RESULTS.....	180
6.6.5.5	SUMMARY.....	184

CHAPTER 7
NUMERICAL AND ANALYTICAL PREDICTION OF THE
WATERFLOOD PERFORMANCE OF FLUVIAL RESERVOIRS

7.1	INTRODUCTION.....	187
7.2	AVERAGING THE RESERVOIR PROPERTIES.....	187
7.2.1	AVERAGING THE HORIZONTAL AND VERTICAL PERMEABILITIES.....	188
7.2.1.1	AVERAGING THE HORIZONTAL PERMEABILITY.....	188
7.2.1.2	AVERAGING THE VERTICAL PERMEABILITY.....	192
7.2.2	AVERAGING THE POROSITY.....	193
7.2.3	GENERATION OF THE AVERAGED RELATIVE PERMEABILITIES.	193
7.3	SIMULATION OF BUILD-UP AND DRAW-DOWN TEST TO VERIFY THE AVERAGED HORIZONTAL PERMEABILITY.....	193
7.3.1	CONSTRUCTION OF THE RADIAL MODEL.....	195
7.3.2	THE TEST PROCEDURE.....	195
7.3.3	ANALYSIS OF THE TEST RESULTS.....	196

7.3.3.1	ANALYSIS OF THE DRAW-DOWN TEST.....	196
7.3.3.2	RESERVOIR LIMIT TESTING.....	200
7.3.3.3	ANALYSIS OF THE BUILD-UP TEST.....	202
7.4	SIMULATION OF THE RESERVOIR PERFORMANCE USING AN ANISOTROPIC (HOMOGENEOUS) MODEL.....	206
7.4.1	COMPARISON OF THE SIMULATION RESULTS OF THE HOMOGENEOUS MODEL WITH THE 2-D & 3-D MODELS.....	207
7.4.2	OBSERVATIONS ON THE WATER-FRONT PROFILES FOR DIFFERENT RATES.....	211
7.4.3	CALCULATION OF THE ACTUAL BREAKTHROUGH TIME.....	212
7.4.4	CALCULATION OF THE WATER-CUT BEFORE THE SHOCK-FRONT VALUE.....	217
7.5	PREDICTION OF THE RESERVOIR PERFORMANCE BY BUCKLEY-LEVERETT.....	221
7.5.1	COMPARISON BETWEEN BUCKLEY-LEVERETT AND THE SIMULATION RESULTS OF THE HOMOGENEOUS MODEL.....	224
7.6	SIMULATION OF THE FLUVIAL RESERVOIR PERFORMANCE USING A 3-LAYER MODEL.....	226
7.7	WATERFLOOD PREDICTION OF THE LAYERED RESERVOIR BY ANALYTICAL METHODS.....	228
7.7.1	CALCULATION OF THE SYSTEM POROSITY.....	228
7.7.2	CALCULATION OF THE SYSTEM MOBILITY RATIO.....	229
7.7.3	CALCULATION OF THE PERMEABILITY VARIATION.....	229
7.7.4	PREDICTION OF THE RESERVOIR PERFORMANCE BY DYKSTRA-PARSONS METHOD.....	230
7.7.5	PREDICTION OF THE RESERVOIR PERFORMANCE BY REZNIK METHOD.....	235
7.7.6	COMPARISON OF THE SIMULATION AND ANALYTICAL RESULTS.....	239

CHAPTER 8
CONCLUSIONS AND RECOMMENDATIONS

8.1	CONCLUSIONS.....	242
8.2	RECOMMENDATIONS.....	244
9.0	REFERENCES.....	245

APPENDICES

3.A	PROGRAM VERSIM.....	254
3.B	PROGRAM OMASOL.....	254
4.A	PROGRAM FAULT.....	254
4.B	PROGRAM THROW.....	254
6.A	PROGRAM SAND.....	254
6.B	PROGRAM SANDPL.....	255
7.A	PROGRAM OKING.....	255

LIST OF FIGURES

FIGURE	TITLE	PAGE NO.
1.1	Different Facies of Fluvial sands.	17
1.2	Point Bar Channel Deposits.	21
1.3	Festoon cross-bedding.	21
1.4	Interpreted Depositional Environments and Associated Genetic Shale facies.	25
1.5	Relationship between shale break frequency and magnitude of discontinuities in channel and deltaic outcrops.	27
1.6	Continuity of shale intercalations as a function of depositional environment.	29
1.7	Gas Cusping and Water Tanguing aided by Shales.	33
1.8	A Fault with Clay Gouge.	33
2.1	Calculation of the permeability variation.	49
2.2	Water-cut vs. Fractional Recovery of different methods.	52
3.1	Interpreted Depositional Environments and Associated Genetic Shale facies.	57
3.2	Shale Lengths observed in outcrops may not be the lenfth or width.	61
3.3	Cross-section representing sands with Discontinuous Shales in Hassi-Messaoud field.	62
3.5	Computer restitution of Shale Breaks.	65
3.6	An Element Model in an Idealised distribution of impervious layers.	65
3.7	Schematic drawing of Computer model.	67
3.8	Synthetic cross-section with Shales.	67
3.9	Shale distribution in fine Simulation grids.	68
3.10	Anisotropy Determination by means of Conducting Paper.	68
3.11	Numerical Experiment to obtain effective Horizontal Permeability.	72
3.12	Cross-section showing Converging Shales and DCSUs.	74
3.13	Shale thickness Frequency Curve.	76
3.14	A Horizontal Flow Path around Converging Shales.	87
3.14a	Increase of travel distance caused by converging shales.	87
3.15	A Simulation model Considering Shale Convergence.	93
3.16	Flow Chart of Program Versim.	99
3.17	Plot of the results from the Analytical, Experimental, and Simulation methods.	94
4.1	Diagram of the Experiment.	102
4.2	Brine Resistivity as a function of Temperature.	105
4.3	Shale frequency vs anisotropy (Brine Conc. 10gm/lit).	111
4.4	Shale frequency vs anisotropy (Brine Conc. 5 gm/lit).	112
4.5	Average Permeability Anisotropy vs Shale Frequency.	114
4.6	Permeability results vs shale frequency, 10 gm/lit.	115
4.7	Permeability results vs shale frequency, 5 gm/lit.	116

4.8	Experimental results of permeability ratio vs shale frequency.	120
5.1	Stochastic Faults resulting from basement rock faulting.	126
5.2	Displacement Variations along fault Traces in different Formations.	127
5.3a	Deformation of the Formations in the Hanging Block.	129
5.3b	Deformation of the Formations in the Foot Block.	129
5.4	Histogram of Fault Throw Frequency.	131
5.5	Distribution Function for Fault Throws.	131
5.6a	Smeared areas at Faulting Stage.	136
5.6b	Smeared areas after Back Stripping.	136
6.1	Cross-section of a Fluvial Reservoir.	142
6.2	Stochastic sands Represented by Rectangles.	143
6.3	Stochastic sands represented by half ellipsoids.	143
6.4	Sampling Random Angles for the 3-D modelling.	144
6.5	Effect of Decreasing the grid thickness.	144
6.6	Generation and Conditioning of sand bodies.	151
6.7a	Calculation of the sand X coordinates in the rear Grid section.	154
6.7b	Extension of the Sand Bodies in the Direction of flow.	156
6.8	Theoretical vs Net (observed) sand fraction.	159
6.9	Cross-section of a Fluvial Reservoir.	160
6.10	Horizontal Permeability vs Dimensionless Distance.	163
6.11	Plan view Demonstrating the complex communication between the grid blocks.	165
6.12	Side View of the 3-D Model.	170
6.13	Cross-section of the 3-D model.	165
6.14	Empirical Relative Permeability Correlation Chart.	174
6.15	Water-cut and Dimensionless oil Production vs time.	178
6.16	Pore Vol. of oil Produced vs P.V. of water Inj. 3-D.	178
6.17	Water-cut and Dimensionless Oil Production vs Time (2-D with Pseudos).	179
6.18	Pore Volumes of Oil Produced vs P.V. of Water Inj. (2-D with Pseudos).	179
6.19	Water-cut and Dimensionless Oil Production vs Time (2-D No Pseudos).	181
6.20	Pore Volumes of Oil Produced vs P.V. of Water Inj. (2-D No Pseudos).	181
6.21	Dimensionless Oil Production vs Time (All Models).	182
6.22	Water-cut vs Time for all Models.	183
6.23	Pore Volumes of Oil Produced vs P.V. of water Inj. (All Models).	185
7.1	Averaging a Model with 4 Permeabilities.	190
7.2	Averaging the Horizontal Permeability.	190
7.3	Cross-section of the Radial Cylindrical Model.	194
7.4	Log-Log Plot (Drawdown Test).	198
7.5	Semi-log Drawdown Curve.	198
7.5a	Cartesian Plot of the Drawdown data.	201

7.6	Log-Log Plot (Build-Up Test).	204
7.7	Horner Plot (Build-Up Test).	204
7.8	Dimensionless Oil Production vs Time (Homogeneous, 2-D Pseudos, and 3-D Model).	208
7.9	Pore Volumes of Oil Produced vs P.V. of water Inj. (Homogeneous, 2-D Pseudos, and 3-D model).	209
7.10	Water-cut vs Time (Homo., 2-D Pseu., 3-D model).	210
7.11a	Water Saturation Profiles (Inj.=Prod.=9900 RB/Day).	214
7.11b	Water Saturation Profiles (Inj.=Prod.=20000 RB/Day).	214
7.12	Water-cut vs Water Saturation (Homogeneous Model).	216
7.13	Water-cut vs Time (Homo. Model, Rate=9900 RB/D).	216
7.14	Water-cut vs Time (Homo. Model, Rate=20000 RB/D).	219
7.15a	Water-cut vs Time (Rate=5000 RB/D Rock Type B).	219
7.15b	Water-cut vs Time (Rate=9900 RB/D Rock Type B).	220
7.15c	Water-cut vs Time (Rate=20000 RB/D Rock Type B).	220
7.16	Dimensionless Oil Production vs Time (BL).	225
7.17	Pore Volumes of Water Injected vs P.V. of Oil Produced, (BL).	225
7.18	Water-cut and Dimensionless Oil Production vs Time (2-D 3-Layer model).	227
7.19	Pore Volumes of Water Injected vs P.V. of Oil Produced, (2-D 3-Layer Model).	227
7.20	Calculation of the Permeability Variation.	231
7.21a	Permeability Variation vs Mobility Ratio, Water Oil Ratio of 1.	232
7.21b	Permeability Variation vs Mobility Ratio, Water Oil Ratio of 5.	232
7.21c	Permeability Variation vs Mobility Ratio, Water Oil Ratio of 25.	233
7.21d	Permeability Variation vs Mobility Ratio, Water Oil Ratio of 100.	233
7.22	Water-cut vs Dimensionless Oil Production for simulation and Analytical Methods	241

LIST OF TABLES

TABLE NO.	TITLE	PAGE NO.
1.1	Association of shale continuity and environment of deposition.	16
3.1	Calculated effective vertical permeabilities considering shale convergence.	89
3.2	Different results for different random number seeds.	90
3.3	Calculated effective horizontal permeabilities considering shale convergence.	90
3.4	Kve Values calculated by the simulation method.	97
4.1	The Model Dimensions.	101
4.2	Scaling of the Perspex Sheets.	102
4.3	Description of the Run Parameters.	103
4.4	Measured Resistivities for different Barrier Frequencies (Conc. 10 gm/lit).	113
4.5	Measured Resistivities for different Barrier Frequencies (Conc. 5 gm/lit).	113
4.6	Calculation of the Average Permeability Anisotropy.	113
4.7	Description of the Parameters for runs neglecting Shale Convergence.	118
4.8	Calculation of the Anisotropy Factor.	119
5.1	Statistical Data on Fault Throws.	132
5.2	Permeability Results at Frequency of 2 Shales/100 ft.	138
5.3	Permeability Results at Frequency of 6 Shales/100 ft.	139
5.4	Permeability Results at Frequency of 12 Shales/100 ft.	139
6.1	Statistical Data Base for Fluvial Sands.	146
6.2	Characteristics of an Example Fluvial Reservoir.	149
6.3	Theoretical (effective) vs Observed (net) NTG.	158
6.4	Permeability Distribution accross a Channel Sand.	164
6.5	Characteristics of the Model used for the Study.	172
7.1	Analysis of the Drawdown Test.	199
7.2	Analysis of the Build-up Test.	205
7.3	Calculation of the Water-cut.	215
7.4	Breakthrough Times for different Rates rock type B.	215
7.5	Water-cut Calculation for Inj. rate of 9900 RB/D.	218
7.6	Water-cut Calculation for Inj. rate of 20000 RB/D.	218
7.7	Calculation of the Saturation at the Producer at BT.	223
7.8	Oil Recovery Calculation.	223
7.9	Characteristics of the 3-Layer Model.	228
7.10	Recovery Calculation by the Graphical Representation of Dykstra-Parsons.	230
7.11	Calculation of the Bed Ordering Parameter.	235
7.12	The Fractional Front Positions at Successive BTT of the Layers.	236
7.13	The results of Reznik method.	238

CHAPTER 1

GENERAL TYPES OF HETEROGENEITY IN FLUVIAL RESERVOIRS AND THEIR IMPACT ON OIL RECOVERY

1.1 INTRODUCTION

Good understanding of the distribution, internal characteristics, and continuity of sandstones is a key factor to effective maximum exploitation of the hydrocarbons in them. Nearly all petroleum reservoirs are heterogeneous. The degree of heterogeneity depends mainly on the depositional environment. Thorough understanding of the nature of these environments leads to better geological modelling of the reservoir and hence, to more successful recovery projects. Criteria for recognising the various types of depositional environment are well established (87,88).

Examination of sand bodies deposited in similar environments showed how remarkably similar they are with respect to their sedimentary structures and related grain size variation (102). This is the background to the art of using log shapes for identifying the environment of deposition. The primary differences between sands deposited in similar environments is caused by the supply rate and source of materials (63, 99, 102).

When good statistical data have been established for a group of associated fields, only limited additional data may be needed for making predictions of the internal build-up of another, similar, reservoir.

General knowledge of the formation of various crossbedding types allows the design of reliable sedimentary structural models (102).

Pressure transient tests (interference and pulse tests) can aid in evaluating the inter-well reservoir characteristics (52, 55). Since the overall heterogeneity may be dominated by faults, diageneses, and contrasting lithologies (74) it becomes very important to check for these heterogeneities before designing the structural model.

Fluvial sands are one of the most heterogeneous deposits due to their variable geometries and complex networks. Unlike marine or transitional deposits, fluvial sands are characterised by their elongate shapes with a relatively small width-length ratio. Recent studies on their geometry and continuity have greatly extended the present state of knowledge on these sands (20, 25, 38, 61, 63, 76, 77, 87, 88, 104).

The main types of fluvial deposits described in the literature are the alluvial fans, braided streams, meandering streams, and flood-sheets. Each of these types include subunits that are characterised by special features that distinguish them.

Sand bodies deposited in fluvial environments create extremely complex networks. Reservoir description studies using well observations in thoroughly drilled fluvial reservoirs – for example – Pryor (77), Campbell (15), and Sneider (93, 94), showed the common features of random sand facies distribution, lateral stacking, vertical or multistorey stacking, and isolated accumulations. Moreover, discontinuous shales may exist within the different sand facies severely affecting their flow patterns and reducing their permeability. Diagenesis is another factor that may affect the geometry of the flow paths of the fluvial discontinuous (stochastic) sands.

The sand heterogeneity may be dominated by stochastic faults that – in the presence of sand-shale sequences – severely reforms the architecture of the reservoir flow system.

In this chapter, the different types of heterogeneity in fluvial reservoirs are investigated and their effect on water flood performance are discussed.

1.2 FLUVIAL SAND GEOMETRY AND CONTINUITY

Detailed knowledge of a reservoir's continuity and interconnectedness is a prerequisite for establishing the optimum method for oil recovery. Many factors are involved, that together develop the specific features of a reservoir zone such as, depositional mechanism, amount of material supplied to the depositional site, supply rate and tectonic stability of the source and receiving basins (45, 63, 87, 88).

Outcrop studies (77, 110) and subsurface data reinforce the notion that many fluvial reservoir consist of a great number of isolated and/or interconnected discontinuous (stochastic) sand bodies.

In fluvial systems, the sands are generally elongated with their long axis more or less parallel to the general direction of flow. The spatial disposition and the interconnectedness of the reservoir's building blocks (sand bodies) influence the accessibility and floodability of the fluids they contain (42).

Two major groups of sand may be recognised according to internal continuity (77, 51, 87), sheets and elongate bodies, *Figure 1.1*.

TABLE 1-1 ASSOCIATION OF SHALE CONTINUITY AND ENVIRONMENT OF DEPOSITION

Principal Depositional Environment*	General Shale Continuity in Subenvironment		Some Considerations in Shale Barrier Description
	Continuous	Discontinuous	
Dunes (Aeolian)		Interdune playas and wadi (stream) deposits	Shales rare
Alluvial fan	Lower fan "sheets"	Upper fan channels	Channel spacing and gradients; debris flow deposits
Braided stream		Channel braids and lateral secondary channels	Channel depth (based on fundamental bed thicknesses), valley width
Meandering stream	Flood basin (remnant in meandering belt complexes)	Top part of point bars and abandoned channels	Channel depth (based on fundamental bed thicknesses), valley width
Upper deltaic plain	Flood basin (remnants; as above)	Upper point bar, abandoned channels, channel braids	Channel depth, coastal plain vs valley confinement
Lower deltaic plain	Interdistributary areas	Distributary channels	Channel depth, spacing of distributaries
Delta fringe	Areas marginal to river mouth bars	River mouth bars	Size of feeder river, wave, tidal, and strength of currents along the shore
Beaches-barrier island	Lagoons, shoreface	Tidal inlet channel, shoreface	Shales uncommon in lower, rare in upper parts
Tidal flat	High flat	Low flat and channels	Tide range
Submarine fan	Lower fan "sheet"	Upper fan	Feeder canyon size, particle-size range

(After Ref. 82)

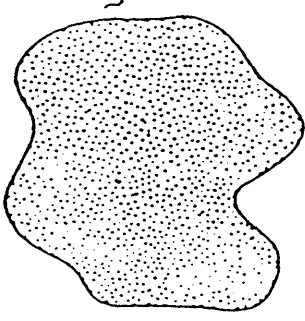
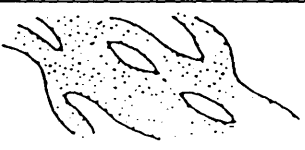


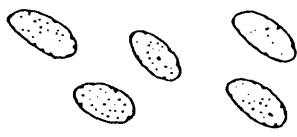
Name		Length-width ratio	
Sheet		$\approx 1-1$	
Elongate	Belt	Sheet with holes	
	Dendroid	$> 3-1$ bifurcating	
	Ribbon, or shoestring	$> 3-1$	
	Pod	$< 3-1$	

Fig. 1.1 Different facies of fluvial sands
(After ref. 87)

Sheets are more or less continuous with length-width ratio of 1:1. Sheets can be divided into continuous and discontinuous subunits. Continuous sheets are characterised by lateral stacking of their constituent elements, while discontinuous sheets are characterised by non-deposition in some parts, or some parts being subjected to later erosion. Discontinuous sheets are also characterised by isolated stacking, therefore, they grade into belt sands with increase of the degree of isolation of sand-bodies.

Elongate reservoir sands may be belts (channels) shoe-string sands, dendroids (braided streams), or pods. Belt sands are prismatic features with internal structures characterised by vertical stacking of the constituent elements.

Shoe-string and dendroid sands have length-width ratios greater than 3:1 and they are normally relatively thin, while pods have length-width ratios less than 3:1.

The different sand facies may superficially appear sheet-like and homogeneous while in reality their probability of (connecting-up), and their spatial disposition is far from this simple case.

Considered vertically, later deposited sand-bodies may cut into older ones creating good physical contact and increasing the reservoir accessibility. There are different types of physical contact between the sand bodies. Some near shore deposits may stack by plastering onto older elements reducing the hydraulic communication between them (38, 45, 87). Such kinds of accretionary contacts were found in many fields. The contact line between the sand bodies may be completely or partially isolating them from each other.

Pryor and Fulton (77) introduced the concept of continuity indices to reflect the reservoir continuity in quantitative form instead of the conventional terms such as (good), (fair), and (poor).

The vertical continuity index (VCI) is the ratio of the thickness of the maximum continuous sand penetrated by the well to the measured maximum (net) sand thickness. The Lateral continuity index (LCI) is the ratio of the lateral length of the sand to the length of the cross-section. If numerous sands of a specific environment were present in a cross-section, maximum, minimum, and average LCI's could be computed. Such indices can be used to quantify the connectivity of meandering or braided streams within the meander belt or the river valley, but their reliability depends on availability of ample data for the specific reservoir zone.

Fluvial reservoir characteristics such as variation of sizes of the sand bodies, random distribution of the different sand facies, variation in types of stacking, and complex vertical and horizontal connectivities requires an enormous amount of data to perform an explicit reservoir description study. Therefore, stochastic techniques were adopted by many investigators (3, 42, 50, 58, 66) to generate possible realisations of fluvial reservoir structures. These techniques are discussed in detail in Chapter 6 of this thesis.

Heterogeneity on a lower scale (within the sand bodies) is – by far – the most important characteristic as this is the vicinity where flow takes place.

Extensive shales which can be correlated over wide areas (deterministic) may divide the reservoir into many zones (layers) having poor or no communications between them. Sand and fluid characteristics may differ between these layers and the reservoir becomes a set of different reservoirs on top of each other.

Analytical techniques for handling the performance prediction of layered reservoirs (composed of homogeneous sets of layers) are established in the literature (20, 31, 43, 49, 51, 81, 96). The performance of fluvial reservoirs – which are composed of stochastic sand bodies with their complex connectivities – cannot be predicted by simple analytical techniques as above. Reservoir layering caused by deterministic or relatively extensive discontinuous shales adds an extra degree of heterogeneity to fluvial reservoirs.

In the next section the internal heterogeneity of fluvial sand bodies is discussed. The discussion is based on published informations reported by many investigators in the area.

1.3 PERMEABILITY DISTRIBUTION IN FLUVIAL SANDS

Sandstone reservoirs are the results of long and frequently complex histories of geologic evolution. The combined process of deposition, burial, compaction, diagenesis and structural deformation yield final reservoir bodies of widely varying characteristics that are difficult to predict (77). In fluvial sands, the internal structure of layered sand bodies, such as those resulting from deposition of sand in channels, could for instance, cause an overall permeability anisotropy. The details of internal geometries of the sand bodies, the continuity of the individual sand packets making up the bodies, their internal bedding forms and arrangements; and the relationship between grain textures and permeability porosity variations

are very important to understand and predict the production performance of the reservoir.

The main sand facies in fluvial reservoirs are point bar deposits, channel-fills, and floodsheets. The permeability distribution in each sand facies is briefly discussed below.

1.3.1 Point-bar and oxbow deposits :

Meandering high sinuosity channels are usually found on flat alluvial planes where the slope is very low (85). During the different stages of river discharge, three facies of sand are deposited. These are point-bar deposits left by channel migration, oxbow-lake deposits left in loops of the river course abandoned when the stream cuts a new course during the flooding period, and flood-sheets deposited when the river spills over the banks at extremely high floods. In this section we will concentrate on permeability distribution in point-bars and oxbow deposits.

In the flood periods the meandering streams cut into the outer boundaries of their semi-circular loops. Fine deposits are deposited on the lee side of the streams (at the interior part of the loop) and they grade into coarser and coarser towards the deepest parts of the streams. Therefore, the permeability decreases from top to bottom along the inclined laminae. Caving of the river banks after the flood periods at low-river stages drapes fine silts and clays over the depositional surfaces. These clay drapes are small isolated barriers that reduce but do not prevent lateral and vertical continuity within the sands. Adjacent loops may have poor lateral continuity because they grow in opposite directions and may leave clays and silts in the region in between. *Figure 1.2* shows the sequence of point bar deposition. Permeability of sands and gravels at the base may be more than 3,000 md while at the top it may be around 10 millidarcy (md), (63, 85).

If the course of the river becomes too sinuous as the loops grow, the river may cut a new course during the flood period and the abandoned loops will form oxbow lakes. These may be filled by clay, silts, and sands during later floods. Therefore, oxbow lakes form effective barriers to lateral flow.

1.3.2 Channel-fill and braided stream deposits :

When the slope of the alluvial plane is greater than 2 degree, the streams form a complex braided pattern of low-sinuosity channels (83). During the flood period

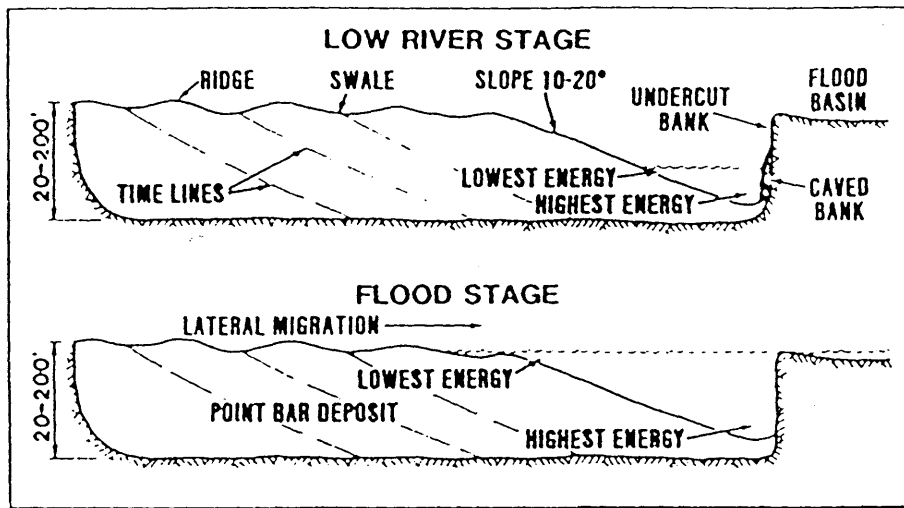


Fig. 1.2 Point-bar channel deposits (after ref. 85)

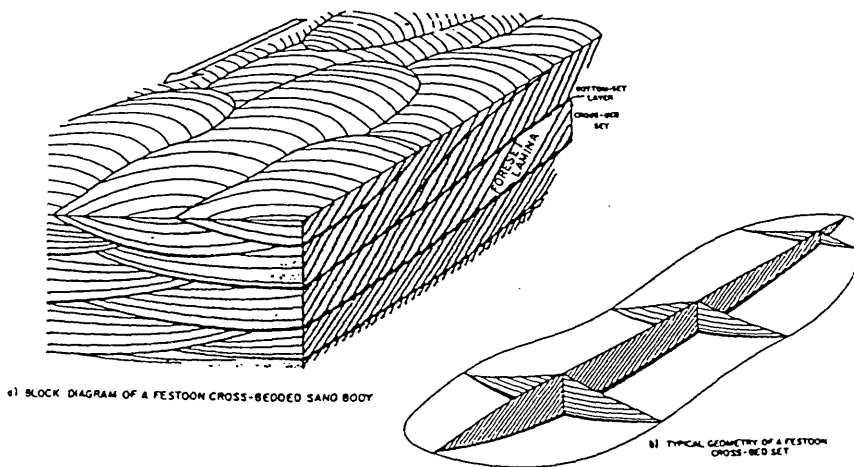


Fig. 1.3 Festoon cross-bedding (After ref. 104)

this network of streams may be overloaded with sediments leading to cutting of new paths which are quickly filled with coarse deposits. The streams may move their locations back and forth cutting and eroding older deposits within the valley.

Due to the network shape of the streams, the connectivity within braided sands is usually very good. Vertical stacking is quite frequent in meandering stream valleys and the permeability varies rapidly in the vertical direction according to the depositional cycles. Permeabilities are higher at the base of the constituent channel deposits where coarse materials exist, and decrease towards the top of the sand bodies due to presence of finer materials. Very thin laminae of discontinuous shales are frequently observed (in cores) on top of the channel sands. Due to their stochastic nature, these shales have a limited effect in reducing the permeability and connectivity of the reservoir. Correlation of braided stream deposits is not possible from well to well in the same stratigraphic depth because they may represent different positions in a bed, but zonal correlation is applicable as the zones represent many depositional cycles of the streams. From the above, we infer that the channel sand bodies are the constituent elements of braided stream reservoir. Weber et al (104) have presented valuable work on permeability distribution in channel-fills. Pryor (76) investigated the inhomogeneities of recent sand bodies. These two studies have provided good insight information on the variation of permeability in channel-fill and braided stream deposits.

Due to the high energy at the middle of the channels, coarse materials are deposited in their middle (at the bottom) while finer materials are deposited towards the flanks (25, 102, 104). At low-river stages silts, clays, and fine materials may drape at the bottom of the river with increasing rate as the energy of the river decreases. The process is repeated every flood period resulting in general coarsening of deposits from flank to centre and from top to bottom of the channel. Consequently, the permeability of the channel sands increases from flank to centre and from top to bottom.

Looking into a smaller scale, channel-fill sand bodies are predominately composed of a rather regular pattern of festoon cross-bed sets. The festoons have spoon-shaped troughs and are elongate in the direction of flow (76,104). The bottoms of these festoons are composed of fine silty materials that form the bottom-set beds which bound them. Between the bottom-set beds the fine fore-sets laminae dip to the direction of flow with an average angle of 30 degrees, see *Figure 1.3*.

The permeability of the bottom-set beds is very low due to their silt content,

and the contrast of permeability between them and the cross-bed sets is usually more than 4 (depending on the amount of clay or silt present in both)(104). The fore-set laminae increase in permeability from top to bottom. The permeability of the individual cross-bed sets is greater in the direction normal to the flow direction, but the overall permeability of the festoon cross-bedded sand body depends on the number of bottom set beds per unit length in each direction. Knowing that the cross-bed sets are elongate in the direction of flow, the overall permeability of the channel sands is greater in the direction of flow as it is the direction of lower bottom-set frequency. Understanding of the internal structure of these constituent elements of the channels sands is of great importance for obtaining directional permeabilities and anisotropy ratios. Formulae were derived for such calculation by Weber (102, 104).

1.3.3 Flood-sheet deposits:

Fluvial sheet sandstones provide an ideal reservoir for hydrocarbons, such sandstone bodies are large enough to contain giant hydrocarbon reservoirs as well as an aquifer. Flood-sheets are massive sandstone deposits that can laterally extend to tens of miles and can be as much as 200 ft. thick (63).

Flood-sheets are deposited during flood periods when the river over-rides its banks and covers extensive areas of its valley. The sands deposited during this process usually have homogeneous permeability in the horizontal direction. The connectivity within flood-sheets is excellent in both horizontal and vertical directions and they form the most continuous facies of fluvial sands.

Presence of discontinuous shales within or alternating with the reservoir sands drastically affects their flow characteristics and reduces substantially their averaged absolute permeabilities. Shales are deposited in different environments and each shale facies can be identified by its lithologic characteristics. The different shale facies and their effect on reservoir permeabilities are briefly discussed in the next section.

1.4 DISTRIBUTION OF SHALE FACIES AND THEIR EFFECT ON RESERVOIR PERMEABILITIES

A complex problem when predicting reservoir performance is the assessment of permeability of a formation with nonpay intervals (shales). Even if the nonpay intervals are discontinuous and randomly distributed, still their effect can be very

profound (82). Particularly, vertical permeability is highly influenced by presence of shale intercalations.

Shale breaks are often detected by logs. Their thickness varies between few centimetres to a few meters, but their continuity and petrophysical properties are usually unknown.

Outcrop studies have shown that geometry, frequency, and lithology of shale and silt intercalations are determined largely by their environment of deposition (38, 42, 61, 71, 82, 97, 98, 102, 104, 110). Therefore, detailed studies of outcrops in different environments are very important to provide a statistical data base for shale dimensions and geometry for each environment of deposition. Considerable similarities were noticed in rocks deposited in fluvial, transitional, and marine environments. Well logs, rock cuttings, and cores provide the basic data for recognising the depositional environments and the type and frequency of shale facies in them. In fluvial environments many shale facies are frequently encountered by wells or observed in outcrops. These facies are briefly discussed below.

1.4.1 Shale facies in fluvial deposits :

Geehan (39) described the different shale facies in a giant fluvial reservoir (Prudhoe Bay) and discussed their continuity and distribution.

Pro-delta and fringe-bar facies are restricted to the deltaic sequence and they are extremely continuous. Bar-fringe shales inter-finger with sandstones of the distributary mouth-bars and usually have a thin-bedded character (less than 2 feet in thickness).

March-bay facies are usually found interbedded with distributary channel deposits. Continuity of these facies is variable but generally high.

Abandoned channel shales usually conform with the shapes of channels and oxbow lakes within the distributary channel complex, braided stream, and meandering stream belts. Therefore, abandoned channel shales are usually elongate more or less in the direction of flow.

Floodplain shale facies are usually extensive due to the wide areas on which they are deposited (during the flood period). In many fields they can be correlated for several miles, but they may be subjected to subsequent channel erosion resulting in dissecting them into smaller units.

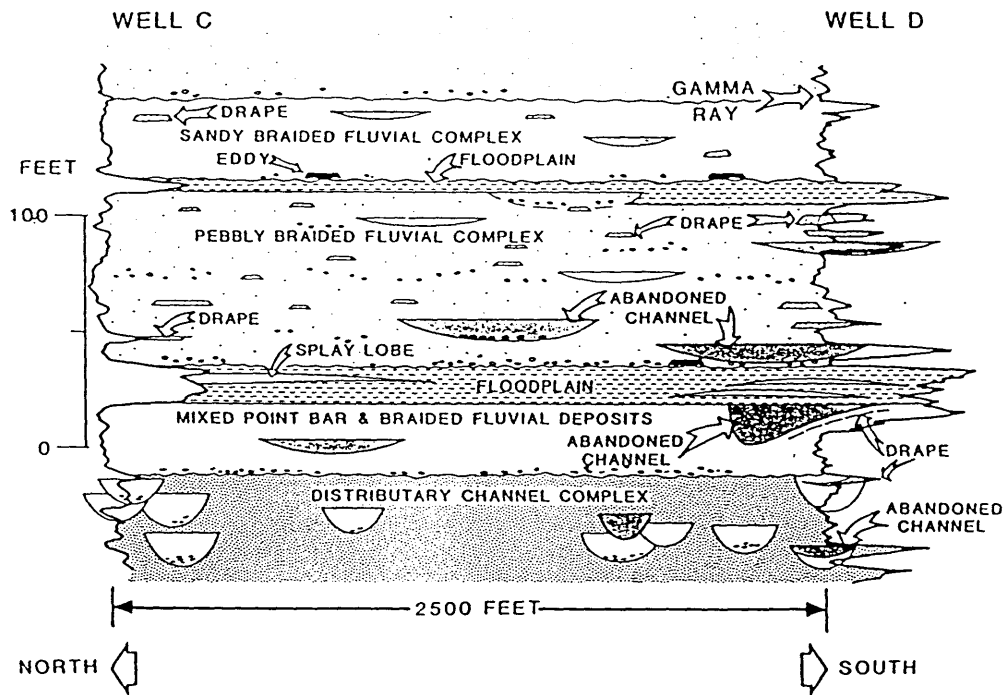


Figure 14. Interpreted depositional environments and associated genetic shale facies for Zone 2 in two wells in the Eastern Operating Area, Prudhoe Bay field. Well C is a cored well for which core was described. Genetic shale facies in Well D are based on the predictive model described here; sandstone depositional environments are based on correlation and log character.

(After Ref. 43)

Eddy, drape, and slough shales are the smallest discontinuous shale types. Eddy facies are usually found at the bottom of the channels while drape and slough facies are randomly distributed within the sand bodies. *Figure 1.4* demonstrates the shape and location of different shale facies in a cross-section of a fluvial reservoir (39).

1.4.2 shale geometry, dimensions, and distribution in fluvial deposits:

Discontinuous shales are usually observed in outcrops of fluvial reservoirs or detected by well logs and cores (25, 42, 61, 77, 97, 104, 110). They are usually scattered throughout the sand facies in the reservoirs and their distribution is completely random (38, 71, 93, 98, 104). An important feature of the discontinuous shales is the tendency of adjacent shale breaks to converge upon each other over small distances. This phenomenon is highly significant (62 to 70 percent of the shale breaks converge in less than 250 feet (110)). From the sections presented by Verrien et al (97) the average degree of inclination of the shale breaks (with a horizontal line) is found to be 7 degrees and two adjacent shale breaks will continue as one unit. The portion of sand bounded by the two shale breaks tends to become discontinuous with regard to flow. Even if the sands are not completely sealed by shales (i.e. if the shales form a Y shaped barrier) the impact of such barriers on reservoir permeabilities may still be very severe.

To evaluate the resulting magnitude of discontinuity for various shale frequencies, Zeito(110) presented *Figure 1.5* which demonstrates the association found between the frequency of shale breaks and the frequency of discontinuities within the sand bodies in channel and deltaic outcrops. This phenomenon will be investigated in detail in Chapter 3 of this thesis.

The most popular shape of shales used in effective permeability estimation schemes is the rectangular shape as the shales are considered elongate in the general direction of flow. Circular shapes were also used (61) but this shape is not associated with the geological observations on shale breaks.

As mentioned earlier, shale geometry and continuity in a field depend on where the sediments were deposited. The depositional environment – as shown by outcrop studies – is found to be the main factor that governs shale geometry and continuity (102), therefore, stratigraphically equivalent shales may not be continuous if continuity prediction is not linked to the depositional environment interpretations.

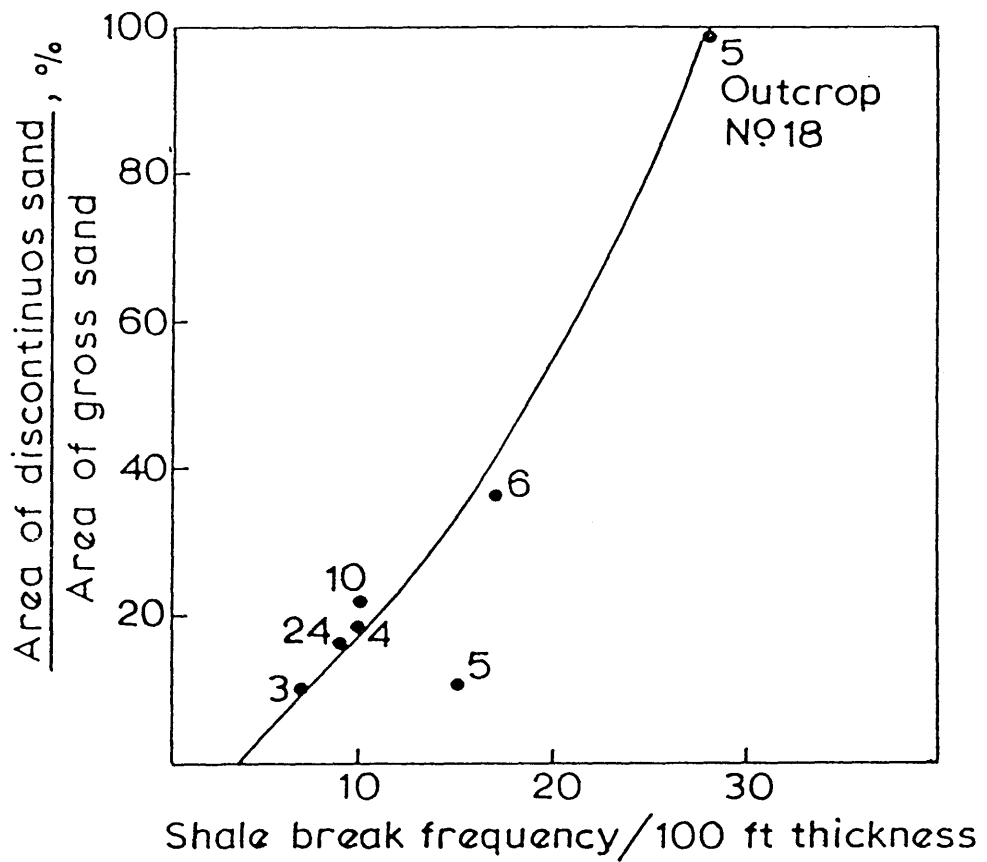


Fig. 1.5 Relationship between shale break frequency and magnitude of discontinuities in channel and deltaic outcrops (After ref. 110)

Weber has made an attempt to combine statistical data on shale continuity in a single graph relating the probability of a shale break extending over a certain length to the depositional environment. *Figure 1.6* reveals that marine and deltaic shales are extensive while distributary channel and point bar shales are relatively short. Therefore, continuity of the latter group is highly unexpected and they are usually discontinuous.

Richardson et al (82) presented a table which associates shale continuity and the environment of deposition as shown by table 1.1.

Sampling of shale dimensions from *Figure 1.6* is frequently applied by stochastic techniques for calculation of averaged absolute (effective) permeabilities of fluvial reservoirs (39, 42, 44, 68). Shales are frequently considered impermeable in the above techniques. In cores, fluvial reservoirs often appear to have no overall vertical permeability, but burrows in many cases provide the main vertical communication across the thin clay intercalations (102). Statistical estimation of the number of burrows per unit area, the average diameter of burrows, and the permeability of burrows are a prerequisite for making a rough estimate of vertical permeability over an interval of thinly interbedded sands and clays.

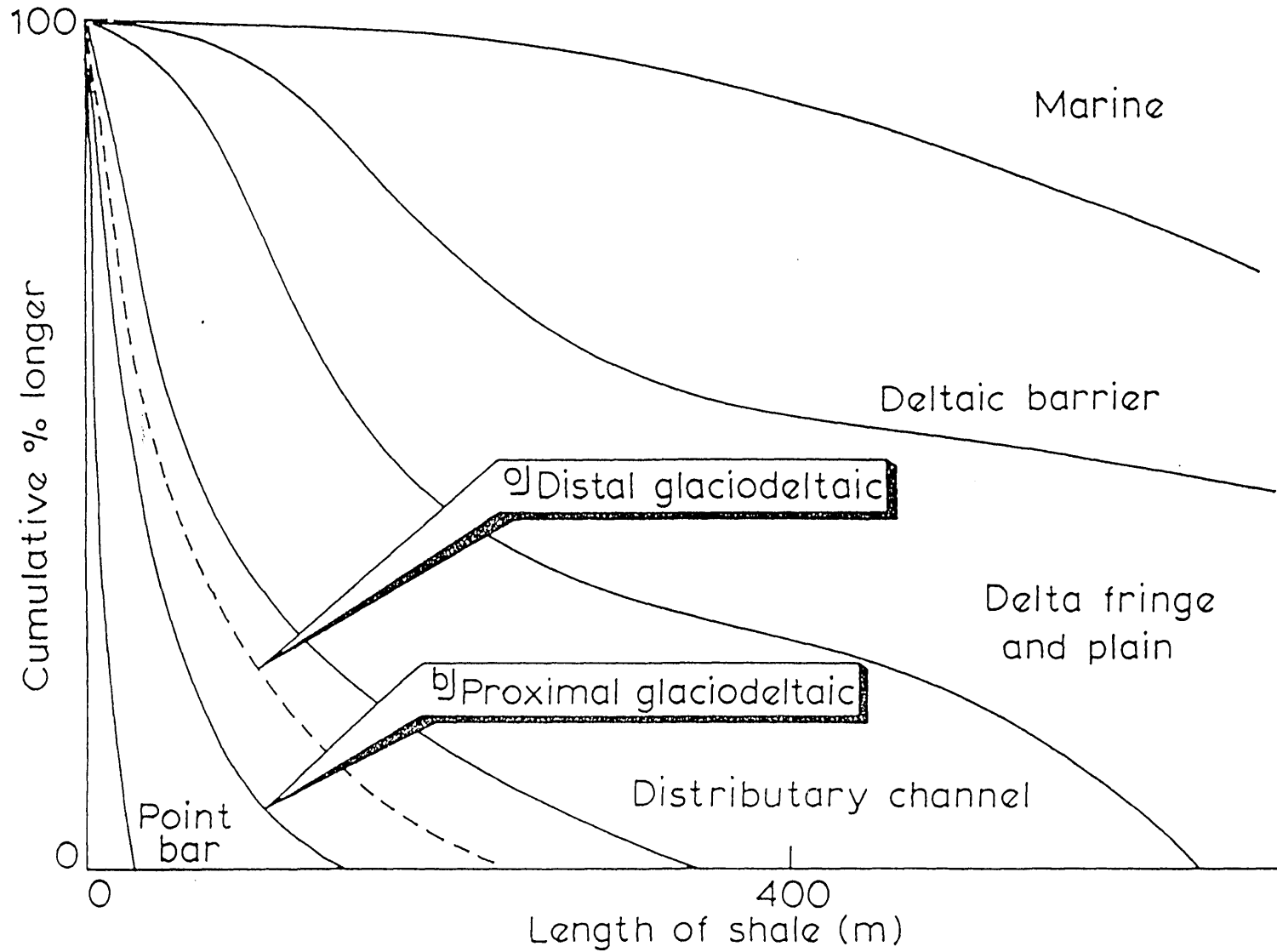
In practice, the bedding is often disturbed by bioturbation causing intermixing of clay and sands. This mixing creates a certain degree of improvement for the vertical permeability although it is detrimental to horizontal permeability.

Presence of shales in a reservoir might create another problem if the depositional site is subjected to tectonic movements or any other factor leading to creation of faults. Shales may smear on fault planes reducing the transmissibility (specially in case of small throws and thick shales). Further discussion on the effect of these faults on reservoir permeabilities is presented in the next section.

1.5 STOCHASTIC FAULTS AND THEIR EFFECT ON RESERVOIR PERMEABILITIES

Faults with very small throws or with lengths shorter than the distances between the seismic lines are often not detected. This is due to the resolution limitations of seismic techniques (11). Regarding the thicknesses of fluvial sands, faults with small throws (less than 50 foot) can still have a tremendous effect on reservoir averaged absolute (effective) permeabilities and overall connectivity. Tectonic movements as well as faulting accompanying advancing deltas could lead

Fig. 1.6 Continuity of shale (silt) intercalations as a function of depositional environment (After ref. 67, 102)



to creation of stochastic faults (105).

In the presence of discontinuous shales, the effect of stochastic faults on effective reservoir permeabilities may become extremely severe. The shales smear on fault planes leading to isolation of parts of the reservoir sands. The impact of stochastic faults on horizontal permeability is greater because the smeared fault planes act as barriers to horizontal flow. The invisibility of the smeared stochastic fault planes to seismic techniques and well tests may lead to erroneous reservoir parameter definition, and hence, inaccurate performance predictions.

Modelling of stochastic faults and calculation of effective permeabilities in the presence of stochastic faults and stochastic shales is discussed in more detail in Chapter (5) of this thesis.

1.6 EFFECT OF THE VARIOUS TYPES OF HETEROGENEITY ON OIL RECOVERY

1.6.1 Effect of heterogeneity within the sand bodies :

Heterogeneity in general is detrimental to waterflood performance of oil reservoirs, but the impact of heterogeneity on the water flood processes depends on its type and scale within the reservoir (99). Small scale heterogeneities such as sedimentary structures, interlamination of different rock types, and mineralogical characteristics may lead to non-uniform residual oil saturation distribution in swept zones (103). This non-uniformity may result from significant contrasts in capillary pressure within the porous media which leads to oil entrapment in small cul-de-sacs (103).

Berruin (10) performed a reservoir simulation study on various heterogeneous systems and concluded that randomly heterogeneous systems can be represented by homogeneous ones having a permeability equal to the geometrical mean of the individual permeabilities of the heterogeneous reservoir. Warren and Price (101) reported the same conclusion as Berruin.

In an intermediate scale (within the sand bodies), types of heterogeneity such as permeability increase upwards in bar sands, and permeability decrease upward in channel sands may have variable effects on waterflood performance. In channel sands the permeability distribution is not favourable. Both gravity and the higher permeability at the bottom pull the water downwards, whereas in bar sands the

higher permeability (at the top) pulls the water upwards, while gravity is pulling it downwards, resulting in higher vertical sweep efficiency. Simulation studies confirmed the above behaviour as reported by Berruin (9). Berruin stated that waterflood performances of layered models with the layers ordered in decreasing permeability (from top to bottom), increasing permeability, and random permeability patterns are completely different. The first two patterns simulate bar sands and channel sands respectively, while the random pattern simulates the a randomly heterogeneous system studied by Warren and Price (101); and Berruin (10). Discontinuous (stochastic) shales are frequently deposited within or interbedded with fluvial sands. These shales create a larger scale of heterogeneity and their impact on reservoir performance is extremely severe as discussed below.

1.6.2 The impact of discontinuous barriers on oil recovery:

Randomly distributed, discontinuous barriers can cause significant reduction in vertical transmissivity because of the tortuous paths the fluid must follow. Small shale facies such as eddy, drape, and slough are usually distributed within fluvial sands. Therefore, these create a degree of heterogeneity within the sand bodies. Other facies of shale such as prodelta, floodplain, abandoned channels, and oxbow lake deposits create a higher degree of heterogeneity by interbedding with the reservoir sands in the sedimentary basin.

The shale convergence phenomenon reported by Zeito (110) which leads to sand compartmentalisation, may isolate a considerable part of the reservoir sand. Reduction of the recoverable fraction of oil caused by this compartmentalisation can be very high in cases of high shale frequencies (110). Resulting from the same phenomenon (shale convergence) reduction in horizontal permeability can occur due to the additional tortuosity caused by the Y shaped shale barriers.

In a gas-invaded region, oil tends to flow vertically downward by gravity until it reaches an impervious rock (shale), where it accumulates in a layer of high oil saturation. The oil layer above the barrier will spill off its edges driven by the gravity head (82). For large barriers the time needed for the oil layer to drain is considerable. If we take into consideration the number of pore volumes to be injected during that time it becomes clear that oil layers on shale barriers should be considered non-recoverable due to their high production costs (not economically feasible).

Capillary effects can cause a transition zone of oil saturation above the oil

layers on the barriers, which may reduce recovery by a certain percentage (2.7% for the models used by Richardson et al (82)).

Underrunning of shales by gas (Cusping) is quite frequent. When the production rate exceeds the critical rate, the viscous forces override the gravity forces and the gas-oil contact will tilt until it is parallel to the formation dip (61). Similarly, shales aid in initiating water tonguing from the aquifer below. *Figure 1.7* demonstrates cusping and water tonguing aided by shales (61).

Depending on the frequency and dimensions of shales, cross-flow may be minimised or eliminated. Water coning can be minimised by presence of shales below the perforations while gas coning can be minimised by presence of shales above the perforations (42). Shale distribution affects the uniqueness of the history match. If the shale distribution is accurate and representative of the domain, this will increase confidence in the history match (42, 61).

1.6.3 Effect of sand discontinuity on oil recovery:

The various types of fluvial sand geometry are discussed in Section 1.1. It is shown that sand bodies may be isolated and surrounded by shales. Due to this discontinuity, flow of oil from isolated or partially isolated sand accumulations may not be possible. Therefore, a considerable percentage of oil may not be producible due to this entrapment (45, 66, 94). In-fill wells in developed fields composed of stochastic sands may penetrate sand accumulations with virgin pressure (62). The accessibility of reservoir sands by wells is very low in this type of formation (58). If the direction of paleocurrent is not well identified, fluids may move in a direction different from that in which it is pushed. This is because the effective horizontal sand permeabilities are higher in the general direction of paleocurrent. Anisotropy of permeability may enhance or retard this phenomenon according to orientation of injectors and producers (60).

Development planning of this type of reservoirs requires reliable conditional modelling techniques that incorporate seismic and well data to produce representative synthetic models of the reservoir. Decisions on the distribution of injectors and producers rely on mainly on these synthetic models. Many investigators (1, 17, 28, 35, 53, 69, 79) presented different techniques for conditional simulation of fluvial reservoirs relying on well or well and seismic data. The accuracy of these techniques depends on the availability and quality of the relevant data; and on the reality of the modelling technique. Relevant data in newly discovered fields are

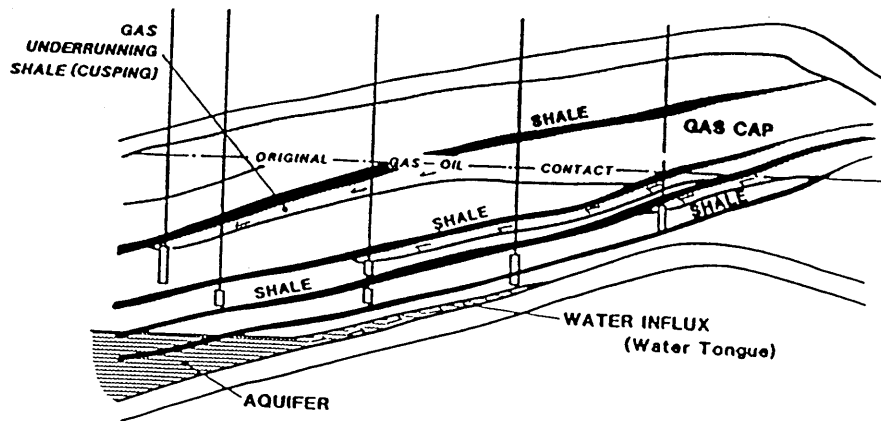


Fig. 1.7 Gas cuspings and water tanguing aided by shales (After ref. 61)

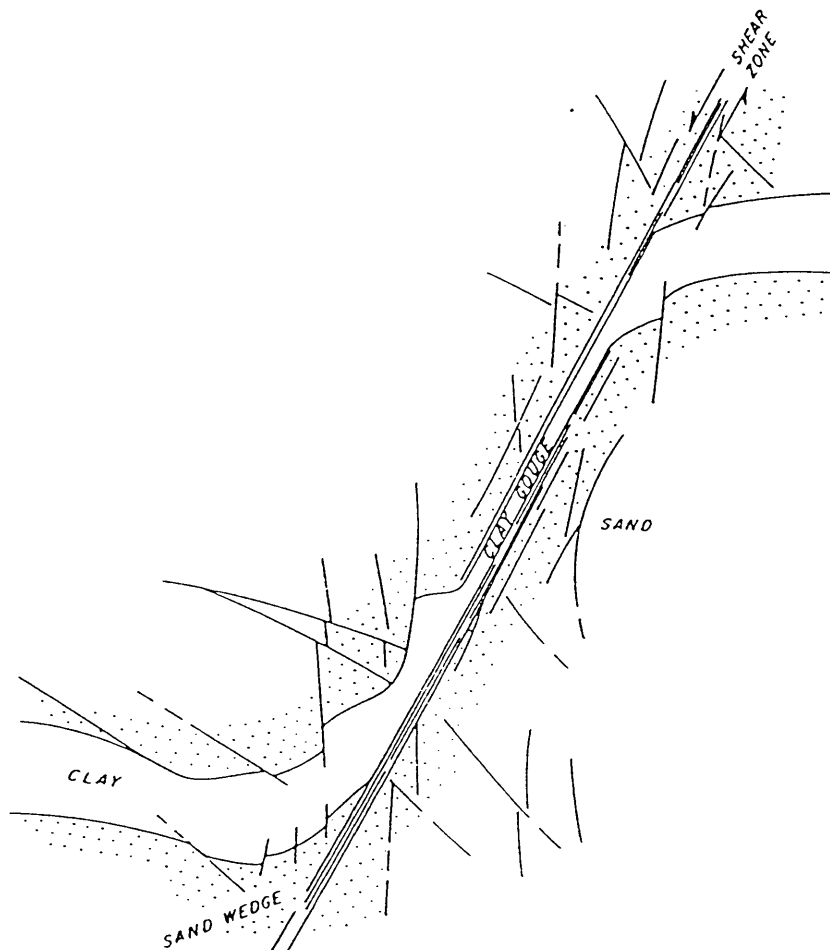


Fig. 1.8 A fault with clay gouge (After ref.103)

usually scarce. Due to the above modelling difficulties, development of reservoirs composed of stochastic sands is extremely difficult.

1.6.4 Effect of faulting on oil recovery :

Major faults - which can be detected by seismic techniques - distort the continuity of fluvial reservoirs. These faults may be sealing or non-sealing (103) depending on the materials in the fault plane. In sand-shale sequences the clay gouge smeared in the fault plains (see fig 1.8) can form an effective seal if the throw is not big, while it may wedge leaving the central part of the fault plane non-sealing or partially sealing (91, 92, 105). As a result, juxtaposed sand layers across smeared fault planes may not be connected.

Due to the additional degree of sand compartmentalisation caused by shale smearing on fault planes, recoverable oil percentage is further reduced and water-floods may end up with variable residual oil saturations.

The impact on reservoir permeabilities may lead to by-passing of complete regions of the reservoir due to the newly added barriers (smeared fault planes). Juxtaposed sands across smeared fault planes may not be connected.

CHAPTER 2

REVIEW OF THE ANALYTICAL WATERFLOOD PREDICTION METHODS FOR HETEROGENEOUS RESERVOIRS

2.1 INTRODUCTION

The prediction of waterflood performance in stratified reservoirs was attempted by many investigators. Since most of the reservoirs are heterogeneous, and the type and degree of heterogeneity differ according to the environment of deposition, it became difficult to account for the various types of heterogeneity in simple analytical methods for waterflood performance prediction. Assumptions were introduced to the various techniques to simplify the calculations while other factors were ignored due to the difficulty of accounting for them. Assumptions such as piston-like displacements, no communication between the layers (in stratified systems), and constant porosity were quite popular, while many factors such as capillary pressure, gravity segregation and variation of mobility ratio are often ignored.

In this chapter, the popular analytical waterflood prediction methods are briefly reviewed. Drawbacks and oversimplifications are pointed out. Factors such as capillary pressure, gravity segregation, and variation of mobility ratio (which are usually ignored) are assessed to investigate their effect on waterflood performance. A comparative study based on a simple 5-layer problem is used to investigate the accuracy of these analytical methods. Then, the results are discussed and remarks are stated.

2.2 REVIEW OF THE PREDICTION METHODS

Stiles (96) presented a method for prediction of waterflood performance of depleted or nearly depleted reservoirs. His method is based on the assumption that the presentation of the waterfront follows the individual permeability variations as if such variation were continuous from input to producing well. The derivation of the calculation procedure is based on a plot of dimensionless permeabilities (individual permeability values divided by the average permeability) and the cumulative fractional thickness. Although the performance curve of the example he presented fitted well with the actual performance of the field, the limitations of the method are very serious.

Assumptions of piston-like displacement, incompressible fluids, and no cross-flow between adjacent layers were introduced. The method does not take into account many factors that influence the production history such as, presence of gas or water zones, distance from fluid contacts, rate of production, and shape of the field. Due to the numerous limitations of the method, the reliability of its predictions is questionable.

Johnson (51) used combinations of porosity-permeability data from several wells to prepare plots relating the permeability and porosity capacities for stratified reservoirs. He presented schemes to predict both cumulative water injected and cumulative oil produced in terms of percent water-cut.

The advantages of this method are consideration of change of mobility ratio and absence of assumptions of uniform porosity and water saturation within the layers.

Neglect of gravity segregation, capillary pressure, and production behind the front (piston-like displacements) are the main disadvantages of the method which he (51) recommended for thick stratified reservoirs.

Dykstra and Parsons method(31) attracted the attention of many investigators and became one of the best-known methods for predicting waterflood performance in stratified reservoirs. This semi-empirical method for recovery calculation is based on a series of tests on cores to determine the effect of initial fluid saturations, mobility ratio, and permeability variations on oil recovery by waterflooding.

Dykstra and Parson (31) introduced the term (coefficient of permeability variation) by statistical manipulations of core permeabilities, and plotting the outcome (Percent of permeability values greater than indicated values) against indicated permeability values covering the range observed in the reservoir. The values are plotted on log-probability paper and the permeability variation is calculated using an introduced formula.

The observed recovery from core-flood experiments is correlated with the permeability variation and mobility ratio in charts used for recovery prediction. The relative water permeabilities behind the oil-water interface are assumed to be constant for all the layers and the relative oil permeabilities ahead of the interface were also assumed to be constant. The porosities and change in oil saturation are assumed to be equal for all the layers. The methods also does not account for variation in mobility ratio and assumes piston-like displacement, incompressible

fluids, and no communication between the layers.

Johnson (49) simplified the calculations by Dykstra-Parsons method by graphical representations of the calculation procedure. The correlations are restricted to water-oil ratios (WOR) of 1 to 25 provided that initial oil saturation is above 0.45 (fraction).

Recently, Reznik (81) introduced an extension to Dykstra-Parsons method to enable analysis of the cumulative and instantaneous waterflooding parameters between successive bed breakthrough points. Due to this continuous and generalised extension the waterfront positions, fractional recovery, water-oil ratio, and volumetric coverage could be calculated at any time during the waterflooding process. Breakthrough times of the various layers can also be calculated although only the breakthrough time of the first (most permeable) layer can be calculated using Dykstra-Parsons.

Reznik et al (81) also introduced an expanded bed ordering parameter to specify the sequence in which the beds are watered-out taking into consideration the mobility ratio, the porosity and the fractional recoverable oil in each layer. Layers with low permeabilities may breakthrough before layers with higher permeabilities depending on the bed ordering parameter (the bed with smallest bed ordering parameter breaks through first).

Later, Enick et al (34) introduced a new version of their original paper (Reznik et al (81)). In this new version, statistical and graphical representation of the vertical stratification provided a rapid means of predicting or matching waterflood performance for both constant production rate and constant injection rate cases. The term (reference time) was introduced instead of the concept of real or process time. The reference time corresponds to the breakthrough time of the layer with the highest bed ordering parameter (last one to be watered-out) of a system composed of (N) layers. The use of this method minimised the decrease of water-cut after breakthrough (i.e. no dual values of water-cut).

Hornbrook (47) used a computer programme to solve a set of empirical equations for calculation of the volumetric coverage, the conductance ratio, and the fractional flow of water. All these functions were plotted against the distance travelled by the front in the least permeable layer.

The popular assumptions such as, no vertical communication between the layers, piston-like displacement, and homogeneous permeability within the layers

are included in the calculations. Moreover, permeability is considered log-normally distributed and the relative permeability effects are assumed independent of a given bed.

Dake (23) presented a method for waterflood performance prediction in stratified reservoirs for both cases of non-communicating layers (with no cross-flow) and communicating layers (with cross-flow). The reservoir properties were reduced to one dimension by means of thickness-averaged relative permeabilities, thickness averaged water saturation and pseudo-capillary pressure. The method can be applied equally well when the end-point saturations vary from layer to another. As Buckley-Leverett (13) is applied after reduction of the properties to one dimension, all its assumptions apply to Dake's (23) method of calculation. Dake's approach was originally presented by Hearn (46) in 1971. Hearn also pointed out the importance of the spatial disposition of the layers with different permeabilities (the displacement is most favourable when the graduation of permeability is from high to low from top to bottom).

El-khatib(33) developed a mathematical model for waterflood performance prediction in stratified systems with or without cross-flow. The method accounts for the variation of porosity, permeability, and saturation in the different layers. Prediction of fractional oil recovery, water-cut, total volume injected, and the change in pressure can be done at successive breakthrough times.

The study investigated the effect of variable mobility ratio, porosity, and fluid saturation on waterflood performance. It was demonstrated that cross-flow enhances oil recovery for systems with favourable mobility ratios, and it causes the effect of mobility ratio to be more pronounced.

Warren and Cosgrove (100) developed a model approximating the effect of cross-flow due to viscous forces. Recovery (coverage) charts similar to Dykstra-Parsons charts were produced. Compared with Dykstra-Parsons results, Warren and Cosgrove calculations gave lower recoveries in case of unfavourable mobility ratios and higher recoveries in case of favourable mobility ratios.

Piston-like displacement, homogeneous non-communicating layers, negligible capillary and gravitational effects are the main assumptions applied to this method.

Berruín (9, 10) performed a numerical simulation study of the accuracy of some engineering methods for predicting waterflood performance of stratified reservoirs using a two-phase (water-oil) model. The model included the effect of capillary

pressure and gravity segregation. The sensitivity of waterflooding to injection rate and permeability ordering were also investigated. It was found that the performance of stratified systems is not significantly affected by flooding rates and it approaches the performance of a uniform systems with a flow capacity equal to that of the stratified system. The waterflood performance of a randomly heterogeneous system was found to be nearly rate insensitive and its performance can be approximated by a uniform system with an absolute permeability equal to the geometric mean of the individual permeabilities. Hence, one dimensional waterflood prediction techniques can be used to predict the performance of the model. Other studies for investigation of waterflood performance of stratified systems are numerous to detail here. The methods demonstrated above are frequently referred to or used for waterflood predictions.

Oversimplifications of the heterogeneous (or stratified) reservoir models is obvious in many of the methods demonstrated above. More details of the draw-backs and oversimplifications are discussed below.

2.3 DRAWBACKS AND OVERSIMPLIFICATIONS

Most of the techniques presented above neglect the effects of capillary pressure, gravity segregation, and variation of mobility ratio (for different layers) on waterflood performance.

Assumption of piston-like displacement and negligible gravity segregation may not be applicable for thick reservoirs, specially in case of unfavourable mobility ratios.

At low injection rate, enough time is allowed for capillary effects to take place. At infinitesimally small injection rates no water will be produced until all the recoverable oil is produced (106). Therefore, the effect of variation of the injection rate on recovery must be taken into account, which is not the case for many methods.

Assumptions of homogeneous layers with no cross-flow are ideal and rarely found in real nature. Moreover, utilisation of one mobility ratio for the system (31) increases the doubts about reliability of such models.

Recent studies (9, 10, 20, 70) evaluated Dykstra-Parsons (31) method and showed that its recovery estimates are very pessimistic due to neglect of the above factors, in addition to the following reasons :

- (i) recovery calculations are based on averages,
- (ii) the curves used for recovery calculations were based on widely scattered data, and
- (iii) accurate calculation of the permeability variation factor requires a lot of data values.

The performance of fluvial reservoirs composed of discontinuous (stochastic) sands cannot be studied using the above techniques due to the inherent over-simplification of the reservoir architecture, and degree of interconnectedness. Moreover, the intermediate and major scales of heterogeneity in fluvial (stochastic shales and faults) sands are not catered for in these techniques. Bearing in mind the various factors that affect recovery, which are usually ignored, it becomes clear that straight forward application of the above methods for prediction of waterflood performance of fluvial reservoirs is not possible. To visualise the effect of the main factors ignored by the above methods, a brief overview on the effect of gravity segregation, capillary pressure, and variation of mobility ratio on waterflood performance is given in the following sections.

2.4 EFFECT OF GRAVITY SEGREGATION ON WATERFLOODING

Gravity segregation – underrun or override – is detrimental to oil recovery. Gravity effects were thoroughly investigated and the factors influencing their severity were carefully studied (21, 36, 48, 106). Simulation studies were used in such investigations and conclusions stated the importance of ascertaining the severity of gravity effects before deciding whether to ignore them or not.

Due to gravity effects the water-fronts can be tilted extending over a large portion of the reservoir (106). Water and oil undergo gravity segregation with water flowing towards the bottom of the reservoir (higher density) and oil flowing towards its top. These types of displacements are characterised by early breakthrough of water as well as the displacement of the recoverable oil with high water-oil ratios.

Craig et al (21) reported the results of a detailed study of the phenomenon. These experiments showed that the degree of gravity segregation, measured in terms of volumetric sweep efficiency at breakthrough, depends on the ratio of viscous to gravity forces. As the injection rate increases, horizontal viscous forces become more dominant over vertical gravity force. However, within the range

of field operations, gravity effects can lead to recoveries far below the expected values. Craig et al (21) also studied different stratified systems and compared their performances with homogeneous systems with and without gravity. The effect of the spatial distribution of the layers with different permeabilities on recovery was noticed and studied.

Fayers and Sheldon (36) studied the effect of gravity segregation by displacing with and against gravity for both oil-water and gas-oil systems. The computed profiles for a system in which water was initially above oil revealed the twin opposite moving fronts associated with gravity segregation. Similar profiles were shown for the problem in which oil is initially above gas. The difference in specific gravity of the two fluids is greater in this case than in water-oil systems, therefore, the segregation rates are faster. Conclusions were drawn stating that gravity segregation rates can be appreciable and their effect on waterflood can be pronounced.

Hovanessian and Fayers (48) noticed the effect of gravity segregation on pressure distribution curves for a certain range of flow rates. The greater the angle of dip, the greater the pressure drop (sweeping upwards). Also with increase of the dip angle the front water saturation at breakthrough increased. At higher angles of dip, the waterfronts moved more slowly and the breakthrough recoveries were approaching the maximum.

Coats et al (18) introduced the concept of vertical equilibrium by analogy to heat conduction. The whole concept is based on fluid segregation in the reservoir due to gravity.

Whillhite (106) demonstrated the effect of gravity segregation and cross-flow on stratified reservoirs. He approximated the vertical flow in a horizontal displacement model using thickness averaged properties. Such properties were thickness averaged relative permeabilities, thickness averaged permeabilities, and thickness averaged water saturation. Three models to approximate vertical flow were presented. One method used vertical equilibrium of capillary and gravity forces to determine the vertical saturation distribution. Vertical equilibrium dominated by gravity segregation was the basis for the second method. The third method assumed that pressures are equal in each vertical cross-section.

Dake (23) reduced the description of the segregated displacement to one dimension. The reduced properties such as pseudo- relative permeabilities and thickness averaged water saturation are used in Buckley-Leverett method for performance

prediction. This approach was originally investigated by Dietz(26).

Allan Spivak (2) studied gravity segregation in two-phase secondary recovery processes. Reservoir simulation was used to investigate the factors that influence gravity segregation and the magnitude of gravity effects for both waterfloods and gas floods.

The degree of gravity segregation was qualitatively described by a dimensionless group. A correlation between the degree of gravity segregation and the dimensionless group was also established. This correlation group can aid in determining the degree of significance of gravity segregation, and to check the validity of the vertical equilibrium assumption.

The degree of gravity segregation was determined by comparing the results of calculations with and without gravity effects. The effect of anisotropy on gravity segregation was also studied. In general, anisotropy increases gravity effects, but increase of vertical permeability has a more pronounced effect.

Spivak (2) concluded that gravity segregation effects increase with (1) increase of permeability (either horizontal or vertical), (2) increase of mobility ratio, (3) increase of fluid density difference, (4) decrease of production rate, (5) decrease of level of viscosity for a fixed viscosity ratio.

Berruin (9) showed the effect of gravity and cross-flow on the performance of stratified reservoirs. The spatial distribution of the layers with different permeabilities has a pronounced effect on waterflood performance.

SUMMARY

- 1 - Gravity segregation is detrimental to secondary recovery processes (waterflooding), and its severity must be ascertained before deciding whether to ignore it or not.
- 2 - Gravity effects increase with increase of :
 - Horizontal and vertical permeabilities
 - Fluid density difference
 - Mobility ratio
 - Decrease of production rate
 - Decrease of the level of viscosity for a fixed viscosity ratio

- 3 - The spatial distribution of the layers with different permeabilities has a pronounced effect on waterflood performance. The favourable arrangement is the decreasing permeability from top to bottom.
- 4 - The displacements become unstable if the injection rate exceeds a certain critical value.
- 5 - Many techniques considering gravity segregation are based on the assumption of vertical equilibrium. Therefore, the validity of this assumption must be checked before applying such techniques.

2.5 THE ROLE OF CAPILLARY PRESSURE IN WATERFLOODING

The saturation profiles of the waterflood performance studies determine the ultimate economic oil recovery. The more accurate the profiles, the more confident the prediction results are. Capillary pressure effects – which were neglected by analytical waterflood prediction methods – were thought to have an effect on the accuracy of the waterflood prediction methods. The triple-valued behaviour of Buckley-Leverett (13) saturation profile – which he tackled by the shock-front conversion – was suspected to be due capillary pressure effects.

In the late fifties many investigators studied the effect of capillary pressure on both laboratory (core-floods) and field waterfloods. Various approaches were followed such as experimental (59, 73), numerical (9, 27), and analytical approaches (64, 109).

Most of the studies assumed the reservoirs to be homogeneous, horizontal, and linear. The experimental and numerical techniques were the first approaches to address the problem, later, an analytical solution was developed to describe the model waterfloods at low injection rates (high capillary effects) (109). It was shown that the analytical results approach the associated Buckley-Leverett solution at large values of injection rates for both favourable and unfavourable mobility ratios.

The significance of capillary effects in the description of the performance of a linear waterflood was assessed for a wide range of injection rates. It was deduced that Buckley-Leverett solution is inadequate to describe accurately saturation profiles for rates below a certain value.

Based on Leverett's work (64) (neglecting gravitational effects), Perkins(73) plotted the saturation profile against distance for many core-flood experiments. The triple-valued behaviour was eliminated, but the end effects were manifested by increase of water saturation near the end of the cores.

At low injection rates, capillary forces dominated and the water saturation at the end of the cores (end effects) was almost the maximum (oil saturation approaches the irreducible value). At high injection rates the capillary forces were reduced and viscous forces dominated giving lower water saturations at breakthrough.

Other experiments showed that end-effects can be minimised by using longer cores and high injection rates (73, 106).

End-effects were also investigated by Kyte and Rapoport (59). They found that as flood progresses, water tends to enter the cores at localised areas. If the injection rate is very low, capillary dispersion may counteract the distortion from linear behaviour caused by this partial penetration. If the injection rate is so high or the core is very short, the phenomenon of water-fingering dominates a great part of the core or its entire length.

Highly viscous oils enhance the end-effects because the resistance to flow of the water invaded areas is less than the rest of the core. Water tends to flow in the same paths leading to more distortion from the linear waterflood behaviour (59). When the liquids come to the end of the core, they enter a common header where their pressures are equal. Therefore, in order to bring the capillary pressure to zero, the saturation of the wetting phase increases to a degree that brings the pressure difference between the two phases (capillary pressure) to zero. This creates a zone of high wetting phase saturation near the end of the cores. Water cannot flow so long as its pressure is less than the oil phase pressure. Since oil is flowing at a constant rate (during the flooding process), its pressure must increase too, leading to enhancement of end-effects. As soon as the capillary pressure drops to zero, water starts to flow and breakthrough occurs. Build-up of high saturation zones leads to misinterpretation of breakthrough times for core-floods. Also end-effects affect the pressure drop and the fractional flow data used in the computation of relative permeabilities from experimental data.

High displacing rates can minimise the end-effects because the water phase

pressure becomes high enough to flow at the end of the cores.

Fayers and Sheldon (36) derived two equations to account for the effect of gravity and capillary pressure on waterflood performance. A finite difference scheme was used for the computations. The performance curves were single-valued and the solution approached Buckley-Leverett (13) at high injection rates.

Hovanessian (48) derived a dimensionless equation which described the one dimensional flow behaviour from Darcy's law and material balance (accounting for capillary pressure). The equation was then solved by a finite difference scheme. He achieved the same results as Perkins (73).

Douglas (27) developed a numerical method for determining the behaviour of a linear waterflood with the inclusion of capillary pressure. High speed computers were used to run the lengthy calculations. As a results, a series of curves were plotted. Each group represents the the saturation distribution at a certain time for a certain dimensionless displacing rate. At extremely low injection rates, the saturation was uniformly distributed along the cores (capillary forces dominate) and water was not produced until all the producible oil was produced.

As the rate increased, the capillary effects such as (spreading of the front) and (end effects) began to take place resulting in a slight decrease of breakthrough recovery.

Finally, with high rates, capillary forces diminished and the saturation distribution curve approached the Buckley-Leverett solution which assumes no capillary effects. Applying rates higher than a certain maximum added no improvement to waterflood efficiency.

Yortsos and Focas (109) used a numerical technique for calculation of the saturation profile – accounting for capillary pressure – for various oil-water viscosity ratios. The same result reported by Douglas was obtained (i.e. consideration of the capillary pressure eliminates the triple-valued behaviour of the saturation profiles). For viscosity ratios greater than one, the solution had the features of Buckley-Leverett (13) (shock-front), while it gave smooth saturation distributions for viscosity ratios smaller than one. At extremely low injection rates, capillary forces dominated and the saturation was the same all over the reservoir.

SUMMARY

- 1 - At low injection rates the assumption of piston-like displacement is not valid due to capillary effects.
- 2 - Erroneous relative permeability curves could result from core-floods if capillary effects (end-effects and spreading of the front) were ignored. Such processes are characterised by long periods of production after breakthrough (trailing zone).
- 3 - The injection rate has a very pronounced effect on the significance of capillary pressure effects.
- 4 - Consideration of the capillary pressure effects leads to more accurate performance profiles and eliminates the triple-valued behaviour of Buckley-Leverett saturation curve.

2.6 THE EFFECT OF MOBILITY RATIO ON WATERFLOODING

Mobility ratio is one of the important factors that influence the waterflood performance of hydrocarbon reservoirs. In stratified reservoirs with different fluid characteristics, mobility ratio is one of the main factors that indicate which layer will breakthrough first (20, 34). In general, small mobility ratios are favourable for waterflooding as they yield higher sweep efficiency and greater breakthrough recovery (20, 23, 26). In segregated flow conditions the displacements are unconditionally stable if the mobility ratio is smaller than one.

Berruin (9) studied the effect of mobility ratio on the performance of randomly stratified reservoirs with or without crossflow; and uniform reservoirs. He used Dykstra-Parsons and Buckley-Leverett methods to predict the waterflood performance for various values of mobility ratio. All of the models gave better performance at lower mobility ratios (higher breakthrough recovery). This is simply because, low mobility ratios reflect lower oil viscosity and higher oil relative permeability that lead to increase of oil floodability and minimising of water-fingering and water-tonguing.

Allan (2) concluded that gravity segregation increases with increase of mobility

ratio. Fluid resistance to flow enables gravity forces to pull-down the heavier fluids towards the bottom of the reservoir.

El-khatib (33) stated that cross-flow enhances oil recovery for systems with favourable mobility ratios, and tends to make the influence of mobility ratio on flooding performance more pronounced. He also found that the injectivity ratio changes as the displacement progresses according to variation of mobility ratio.

SUMMARY

- 1 - Displacement is improved for smaller values of mobility ratio.
- 2 - For stratified systems, mobility ratio is the main factor which indicates which layer is watered-oil first.
- 3 - Effects of cross-flow on recovery are influenced by the value of mobility ratio. Cross-flow enhances recovery for systems with favourable mobility ratio.

2.7 COMPARATIVE STUDY ON A SIMPLE 5-BED VERTICAL STRATIFICATION PROBLEM

A 5-bed model is used to investigate the accuracy of 5 popular methods for waterflood prediction in stratified reservoirs. The results are presented in tables and the performance curves are compared to demonstrate the variations in prediction results due to variation of the considered or ignored parameters in the different methods.

Detailed calculations using the methods that gave the smallest recovery (31, 49) and biggest recovery (81) are presented in Chapter 7, and compared with the simulation results of a fluvial reservoir.

2.7.1 A SIMPLE 5 – BED STRATIFICATION PROBLEM

(Constant Injection Rate)

To be solved by:

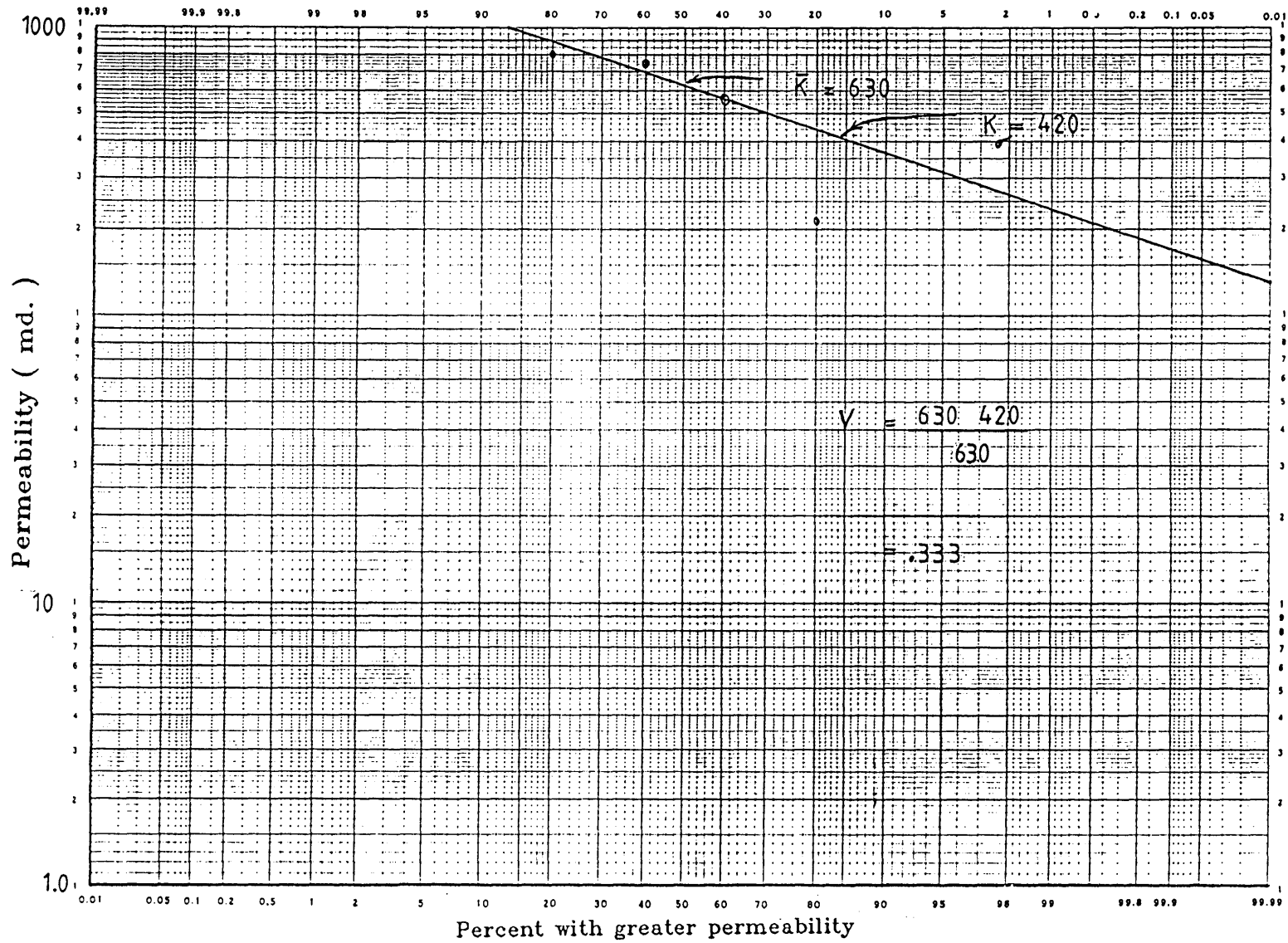
1. Dykstra and Parsons method(31).
2. Graphical representation of Dykstra and Parsons (49).
3. Continuous solution of Dykstra and Parsons (81).
4. Statistical and dimensionless time analog (34).
5. The new method presented by Hornbrook (47).

Data:

Bed	K_i md	H_i ft.	ϕ_i	M	$S_{w_{irr}}$	S_{or}	μ	NPR_j	K_{rw}	K_{roil}
1	800	2	0.20	1	0.22	0.15	1	19549.64	0.75	0.75
2	880	3	0.23	2.069	0.24	0.17	1	31582.00	0.60	0.87
3	217	2	0.20	0.173	0.24	0.17	1	18308.40	0.78	0.90
4	754	3	0.21	2.494	0.31	0.15	0.9	26392.01	0.55	0.49
5	545	1	0.20	0.984	0.10	0.05	1.1	13188.25	0.64	0.65

- * $Q_t = 100$ RB/D
- * NPRT = Total producible oil = 109020 RB
- * Number of beds $N = 5$
- * Distance between Wells $L = 660$ ft.
- * Flood front width $W = 660$ ft.
- * System mobility ratio $M = 1.55$
- * Areal coverage $C = 0.75$
- * Average porosity = 0.211
- * Average oil viscosity = 1.682

Fig. 2.1 Calculation of the permeability variation, V.



2.7.2 RESULTS

The following tables and plots (*Figure 2.1, 2.2*) summarise the results:

1. Prediction results using Dykstra-Parsons (31):

WOR	Water-cut (fraction)	Fractional recovery
1	0.50	0.30
25	0.962	0.459
999	1.00	–

2. Prediction results using the graphical representation of Dykstra-Parsons (49):

WOR	Water-cut (fraction)	Fractional recovery
1	0.50	0.303
5	0.833	0.403
25	0.962	0.475
100	0.99	0.515

3. Prediction results using the analytical extension of Dykstra-Parsons (81):

WOR	Water-cut (fraction)	Fractional recovery
0.480	0.324	0.562
1.531	0.605	0.933
2.012	0.668	0.953
14.17	0.934	0.976
99999	1.000	1.000

4. Prediction results using the generalised Dykstra-Parsons (34):

WOR	Water-cut (fraction)	Fractional recovery
0.333	0.25	0.570
2.450	0.71	0.840
2.704	0.73	0.910
4.000	0.80	0.925
99999	1.00	1.000

5. Prediction results using Hornbrook and Kelkar (47).

WOR	Water-cut (Fraction)	Fractional recovery
1	0.5	0.5
2.33	0.7	0.77
5.57	0.85	0.97

2.7.3 DISCUSSIONS

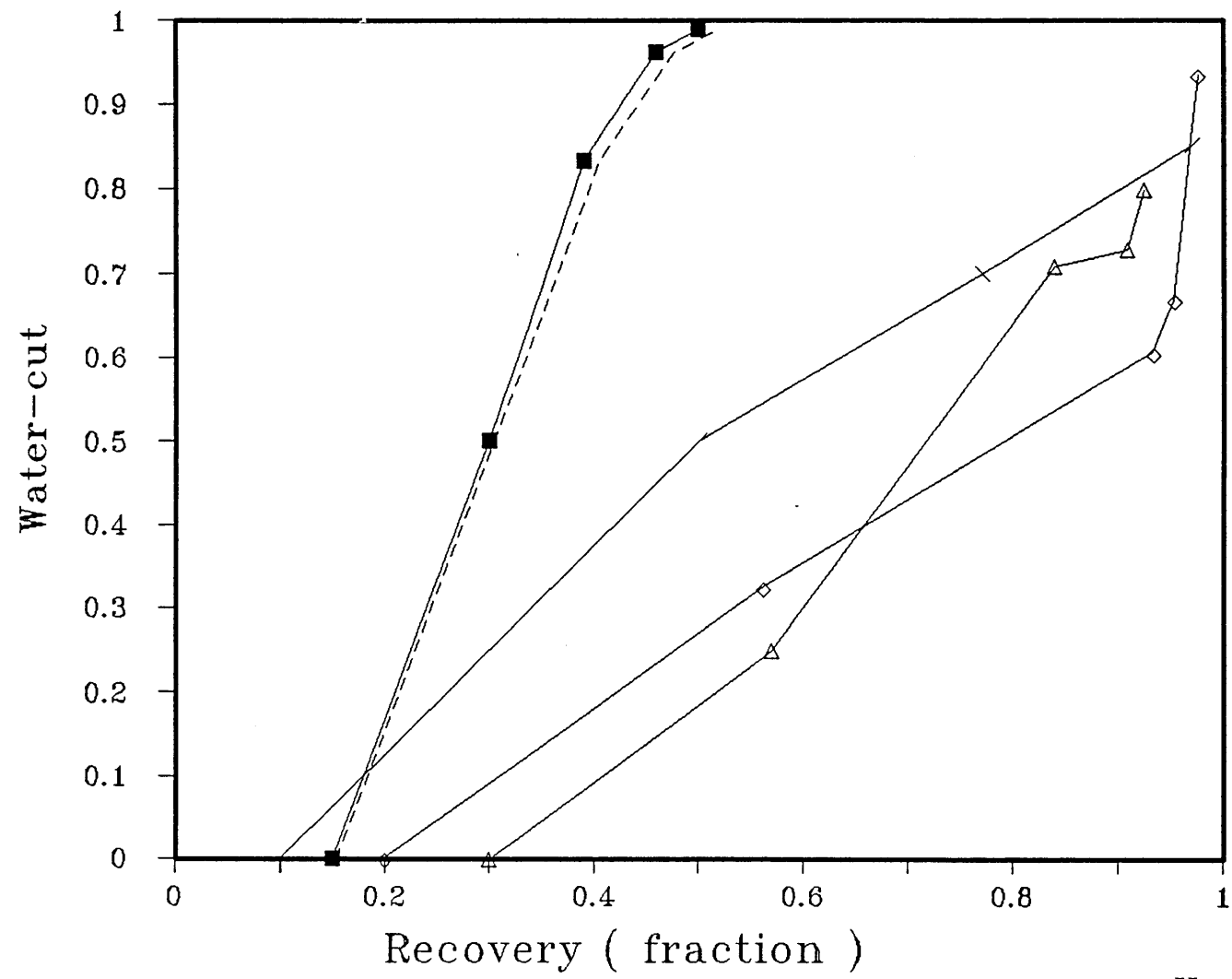
From the plot (*Figure 2.2*) we can notice the great degree of similarity between the results of Dykstra-Parsons (31) and it's graphical representation (49). The predicted recoveries are very low (very pessimistic as reported by Mobarek (70)).

The trend of (The Analytical Extension of Dykstra-Parsons(81)) and it's modified version (34) is approximately the same but the degree of similarity is not as close as the above methods (31, 49).

The recoveries calculated by these methods are almost double the recoveries calculated by Dykstra-Parsons.

The new method of Hornbrook (47) produced intermediate values.

Fig. 2.2 Water-cut versus fractional recovery for different methods



■ D&P Method △ Generalised D&P ---- Graphical D&P ◇ Anal. Ex. D&P × Hornbrook

2.7.4 REMARKS

The variation of performance profiles of the methods is very wide. This is due to the inherent assumptions and oversimplifications which vary between the methods. Neglect of the important factors such as gravity segregation (cross-flow), capillary effects, and variation of mobility ratio may have enhanced the diversity of the prediction results. Some remarks with regard to the accuracy of the various methods are stated below.

* The prediction results of Dykstra-Parsons and its graphical representation are very conservative because of the following reasons:

- i. It does not account for the variation of mobility ratio between the layers. Layer 2 broke through before layer 1 because of the assumption of one system mobility ratio.
- ii. Calculations are based on averages.
- iii. Accurate calculation of the coefficient of permeability variation needs many data values.
- iv. The curves he introduced were based on widely scattered data points.

* The analytical extension of Dykstra-Parsons seems to be the best of these methods although it does not account for cross-flow between the layers (in addition to the inherent assumptions). The advantages of this method are the following :

- i. It accounts for variations in mobility ratio.
- ii. The use of the concept of a bed ordering parameter – which is a function of mobility ratio, water mobility, porosity, and displaceable oil saturation – is more accurate in predicting which layer will breakthrough first.
- iii. Breakthrough times can be calculated for all beds.
- iv. Recovery parameters can be calculated at any time.

* The statistical and dimensionless time analog of the generalised Dykstra-Parsons (34) uses a system mobility ratio which affects the degree of accuracy. The concept of dimensionless time and the use of graphs simplified the calculations.

* Hornbrook (47) did not account for the variations of mobility ratio between the

beds. Furthermore he used the coefficient of permeability variation which affects the accuracy of the calculations, this is in addition to the popular assumptions such as piston-like displacement, no cross-flow, etc...

CHAPTER 3

NUMERICAL AND ANALYTICAL MODELLING OF THE EFFECT OF HORIZONTAL AND OBLIQUE SHALES ON RESERVOIR PERMEABILITIES

3.1 INTRODUCTION

Heterogeneity in fluvial sands may be dominated by stochastic and deterministic shales. The effect of these shales on effective permeabilities of oil reservoirs has been investigated by many engineers (7, 8, 25, 41, 102). The numerical approach has been considered to be the most appropriate solution to the problem, analytical and statistical methods being introduced as alternatives having reasonable degrees of accuracy as compared with the numerical results (7, 107).

Different models have been used for calculation of effective permeabilities (61, 75, 82, 97, 107). Some models assumed the shales to be circular lenses (75), others considering them rectangular (82, 97, 107). All shared the general assumptions that shales are horizontal, impermeable, and without burrows.

Identification of the depositional environment was considered as the key for shale modelling as it led to the use of an appropriate continuity distribution function (CDF) for shales length and width. These continuity distribution functions have been estimated by statistical analyses of field data gathered from outcrops of various depositional environment (61, 97, 110).

Different shale facies in the same site of deposition may have different CDFs. Recently, attempts (39) have been made to improve shale modelling techniques by introduction of facies discrimination in preparation of the CDFs.

In this chapter the different shale facies, their geometry, permeability dimensions, and orientations are discussed. The various models for shale representation are reviewed and a new method for calculation of effective permeabilities of formations containing stochastic sands is presented. This new method allows for shale convergence and sand compartmentalisation. Verification of this new method is done both numerically and experimentally.

3.1.1 SHALE FACIES AND THEIR DISTRIBUTION IN FLUVIAL DEPOSITS

Various facies of shale occur in fluvial deposits (channel and deltaic deposits). Some of these facies are deterministic and correlatable for long distances while others are stochastic and extend over relatively short distances. Regardless of the presence of burrows that may exist in many facies, shales are very effective barriers to fluid flow. The nature of the depositional site governs the types of shale facies that are likely to exist. The topography of the area affects the speed of water in the channels, this speed plays a very important role in the creation and distribution of the different shale facies.

The shale facies frequently found in fluvial deposits are:

3.1.1.1 DRAPE

Drapes are often deposited on the bottom of channels as the speed of water decreases at the end of the flood period. Drapes are also deposited on the slopes of the point bars as the river flow diminishes (39, 85). The dimensions of these drapes are small and they vary according to the speed and topography of the bottom of the river (see *Figure 3.1*).

3.1.1.2 SLOUGH AND EDDY FACIES

Both facies are deposited at the bottom of channels. Slough is predominantly interbedded with point bars while Eddy shales occur at the bottom where eddy currents exist. Subsequent flood periods may cover these facies with gravels and sands. At the end of these flood periods sloughs and eddies may also be deposited, therefore, sloughs and eddies are found all over the fluvial sands.

Sloughs and eddy shales always extend over a very short distance and they are not correlatable between wells.

3.1.1.3 OXBOW AND ABANDONED CHANNEL SHALES

Meandering and braided streams are common fluvial reservoirs (77, 83, 85). Streams may change their direction and flow path within the meander belt leaving

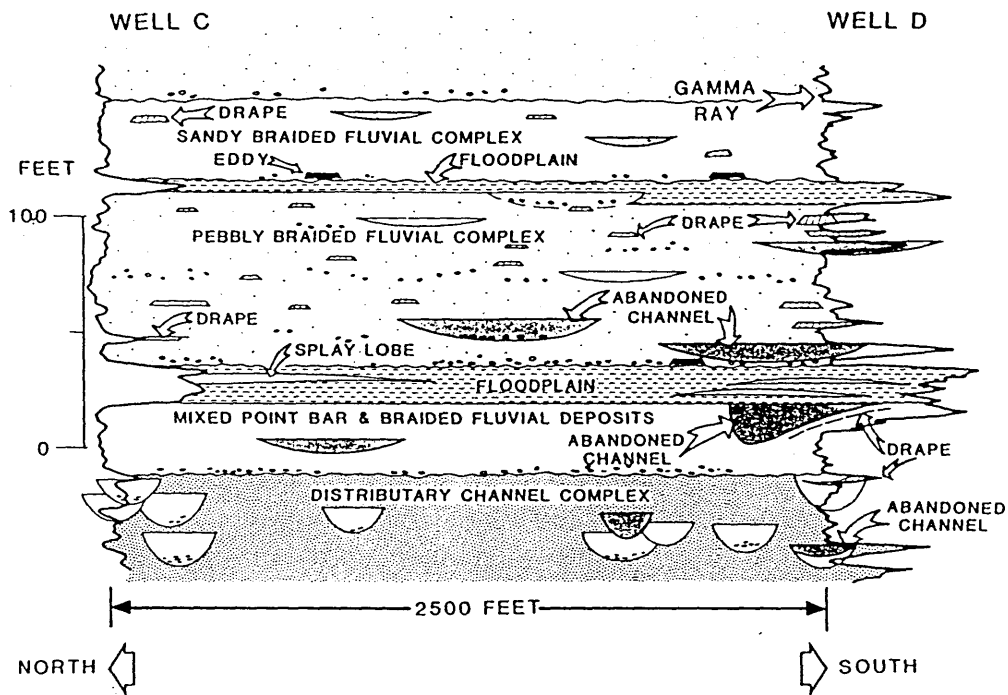


Figure 3.1 Interpreted depositional environments and associated genetic shale facies for Zone 2 in two wells in the Eastern Operating Area, Prudhoe Bay field. Well C is a cored well for which core was described. Genetic shale facies in Well D are based on the predictive model described here; sandstone depositional environments are based on correlation and log character.

(After Ref. 43)

oxbow lakes and abandoned channels to be filled with silt and clay. The shales belonging to this type are expected to conform to the dimensions of the original channels, therefore they may be elongate with width approximated by the width of the channel. The oxbow lake shales are expected to have oxbow shapes and may also be shorter than the entire length of the oxbow if these were broken into smaller lakes (1).

3.1.1.4 BAY SHALES

Depending on the depositional site a Bay shale may be deterministic or stochastic (39). It is likely to be extensive as inferred from the geology of some existing fields (39).

3.1.1.5 GLACIODELTAIC AND OTHER FACIES

Glaciodeltaic facies are also stochastic but some of them may be permeable to the wetting phase and impermeable to the non-wetting phase (oil or gas) due to their high threshold capillary pressure (67). Other shale facies (marine, prodelta, and bar-fringe) are not discussed here as they are usually extensive and correlatable over wide areas. Examples of these extensive shales are floodplain, bar-fringe, and prodelta facies.

3.2 FLUVIAL SHALE DIMENSIONS AND GEOMETRY

Outcrop observations are the main source of information about shale geometry and continuity. Outcrop studies (25, 76, 97, 110) of various depositional environments have been carried by many geologists. The general rule inferred from these studies was the remarkable similarity of sand bodies with respect to sedimentary structure and related grain size variation, shale frequency, and shale geometry, if their depositional environments match closely (102).

Observations from various environments were statistically analysed and combined into plots as continuity distribution functions (110) of shale length. These plots were subsequently used in characterising reservoirs (ie. calculation of effective permeabilities, *Figure 3.1*)

Doubts have been raised about the accuracy of these plots as the exposed

outcrops containing shales may not be normal to the axes of the channels, the distributions being biased towards longer values, (see *Figure 3.2*). Wu et al. (108) stated that errors introduced due to erroneous (CDF) data are negligible if the shales were assumed to be circular, but this assumption cannot be valid for all shale facies.

3.2.1 VARIATION OF SHALE DIMENSIONS WITH ENVIRONMENTS OF DEPOSITION

As indicated by *Figure 3.1* the marine shales are the most extensive facies followed by the deltaic shale facies. The shales in these environments are usually correlatable over wide areas and are mostly deterministic.

Distributary channel, point bar, and glacio-deltaic (67) shale facies are the shortest of all. They are not correlatable between wells, and constitute the stochastic shales dealt with in modelling schemes.

In preparation of the above graphs shale bodies were assumed to have rectangular shapes. The sides of the rectangles may or may not be equal depending on the facies. Eddy and slough shales are likely to be square or circular. The eddy shales are created by eddy currents that move circularly while sloughs are likely to conform with the point bars having their specific shapes.

Attempts to relate the shale thickness with length were made by Wu et al. (108) but no universal validation of the relation they produced was claimed. The relation was given as follows:

$$\text{Log}(L) = 1.5604 + 0.7684\text{Log}(H)$$

It might be much safer to find the percentage of each shale facies in the wells observations and then use different CDF for their lengths and widths.

Facies reference models may be the best tool for shale characterization as they provide more accurate CDFs for permeability calculations. Recent studies (39) used shale facies discrimination techniques to specify the percentage of each facies. Hence, the specific length CDFs for each facies were used. The reliability of these facies CDFs depends on the quantity and quality of data used for their

preparation.

3.2.2 SHALE CONVERGENCE AND SAND COMPARTMENTALISATION

As mentioned in section 1.4.2, Zeito (110) examined many outcrops of various origin and pointed out the important fact that shales may converge upon each other within a short distance. This phenomenon is common in all environments but is very pronounced in fluvial environments. He found that, in channel outcrops, 62 to 70 percent of the shale converge upon each other within a distance of 250 foot.

Verrien et al. (97) also observed this phenomenon as can be inferred from the cross-section they produced for an outcrop, (see *Figure 3.3*).

Delhomme (25) stated that the theoretical studies on shale characterization dealt mainly with regular arrangements whereas the actual reservoir arrangements are scarcely regular.

Due to the phenomenon of shale convergence, sand entrapments or sand compartmentalization may lead to partial or complete isolation of some parts of the reservoir, hence decreasing the floodable sand volume and increasing the tortuosity of the flow paths.

Pryor (76) investigated the inhomogeneities in recent sand bodies in the United States. Although he was much concerned with the sand permeability distribution, the shale convergence phenomenon emerged from the various figures he generated.

Martin and Cooper (67) also showed complexity of permeability barriers (shales) in a clastic reservoir of glaciodeltaic origin. Again the shale convergence phenomenon was obvious in the figures presented although they followed the simplified approach for modelling the barriers.

The overall effect of the above phenomena is to reduce the effective vertical and horizontal permeabilities of the reservoir sand, as well as the recovery factor.

These phenomena are not accounted for by the published methods for the estimation of averaged absolute (effective) permeabilities of the reservoir sands. Neglect of such important phenomena may severely affect the accuracy of the

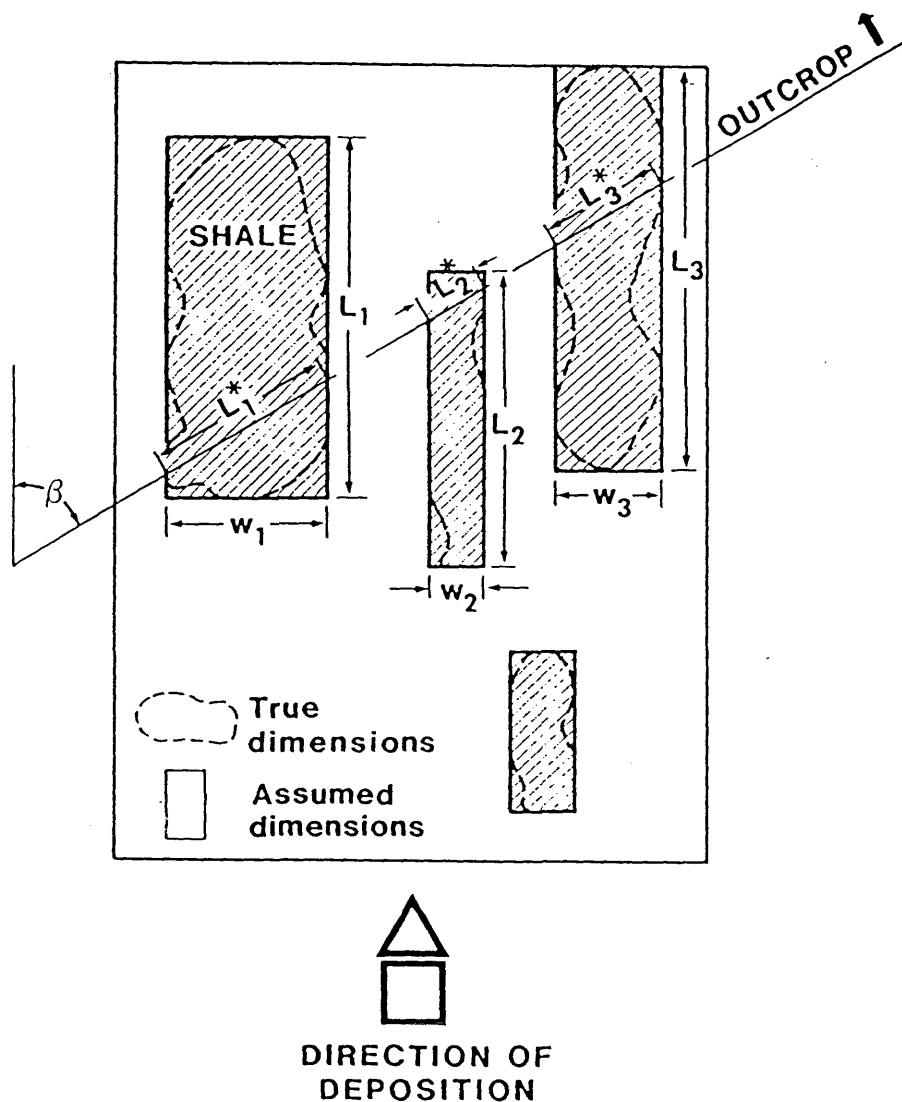


FIGURE 32: SHALE LENGTHS OBSERVED IN OUTCROPS MAY NOT BE L OR W.

(After Ref. 61)

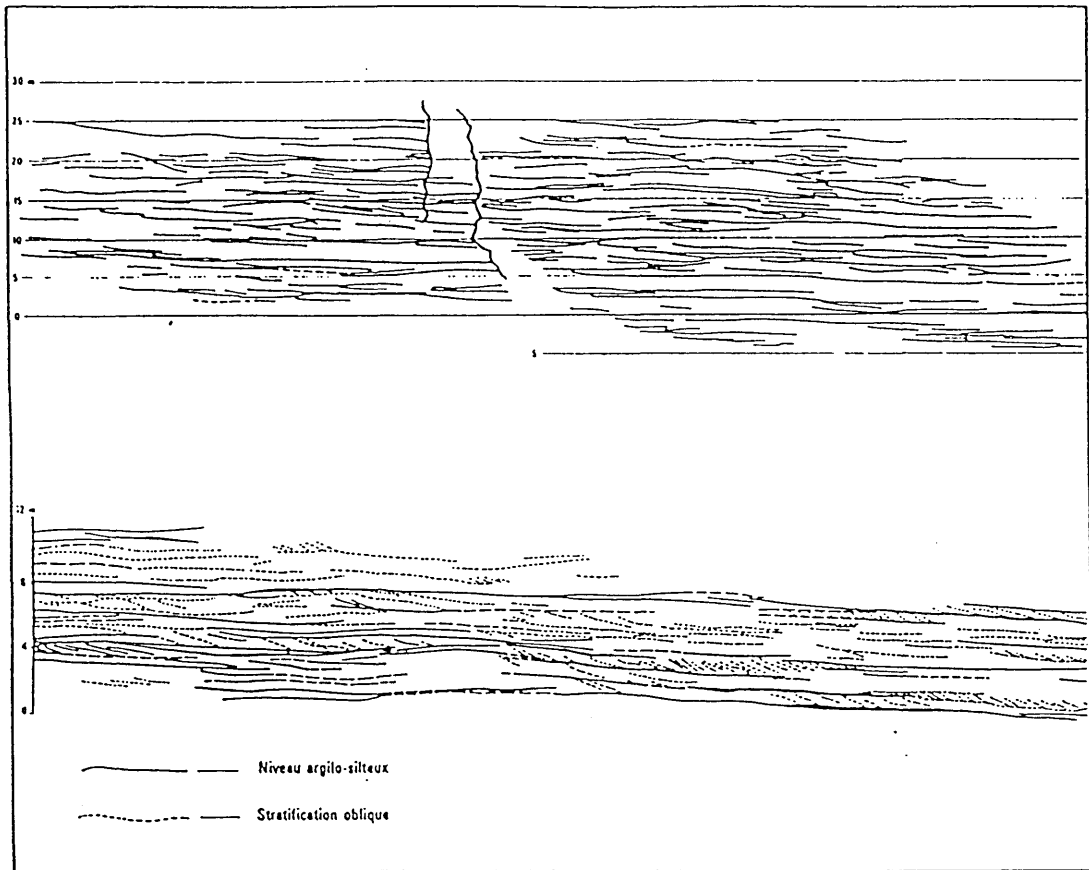


Fig. 3.3 A cross-section representing sands with discontinuous shales in Hassi-Messaud field (After Ref. 24)

results and the consequent performance predictions.

Zeito (110) has also produced a curve relating the isolated areas of the cross-section to the vertical frequency of shale breaks in fluvial environments, *Figure 1.5*. Although no universal validity was claimed for that curve, no other data has been published on the particular problem. Similar studies are extremely important to assist in improvement of reservoir characterization.

3.3 MODELS FOR CALCULATION OF EFFECTIVE PERMEABILITIES IN PRESENCE OF SHALES

3.3.1 MODELS FOR VERTICAL PERMEABILITY

3.3.1.1 Delhomme's Model (25):

For the description of Hassi-Messaoud field in Algeria, Delhomme and his colleagues designed a restitution model which builds vertical cross-sections displaying randomly distributed shales. These shales were generated from reference length distributions and observed vertical frequency of shales.

The anisotropy factors reflecting the ratio of effective vertical permeability to horizontal permeability were calculated by a mathematical model which takes as an input the observed shale frequency in the wells. The most important factors influencing the results were said to be the shale frequency and the ratio of the shale break length to the length of the model.

Delhomme generated horizontal shales with constant lengths and thicknesses. Overlapping was allowed for but shale convergence was not considered. *Figure 3.5* is a realization of shales in a cross-section.

3.3.1.2 Prat's model (75):

A simple model was presented by Prat for calculation of the ratio of effective vertical to horizontal permeabilities. He considered the shales as impermeable layers with infinitesimal thickness. The distribution of those layers was assumed to have a repetitive pattern, and all of them were to have the same dimensions, deduced from their depositional environments. Because of the geometrical symmetry of the distribution, an element model could be taken for calculation of effective

vertical permeability by means of single incompressible fluid flow.

The results of the calculations showed the importance of the distance between the shale streaks, the length of the streaks, and the dimensions of the element model, *Figure 3.6*.

It is obvious that the model did not reflect the real arrangements of shale barriers in nature nor the inclusion of factors not easily estimated for a real situation.

3.3.1.3 Weber's model (102):

Weber used the same element model of Prat (75) (Distribution with repetitive patterns) but he considered the shale intercalations to be semipermeable. An anisotropy factor relating the flow rate with barriers to the flow through a homogeneous system without barriers was calculated.

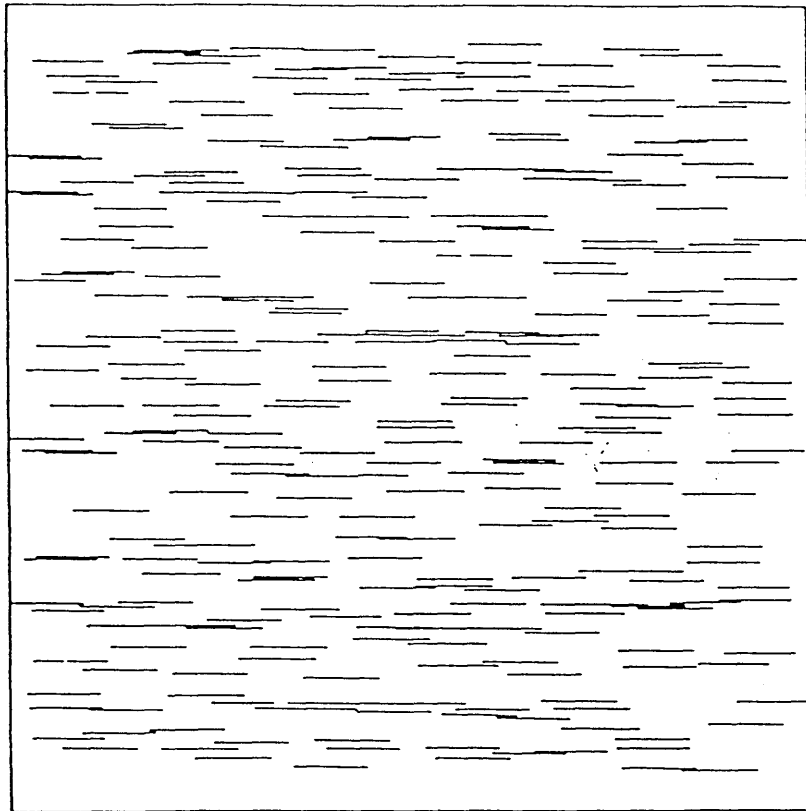
Factors influencing the results were the same as those mentioned by Prat (75), plus the effect of shale permeability.

There were no reference data for the ratio of shale length to the element model length adopted to develop the curves given in his paper (102). This may lead to reliance on assumptions which affects, the reliability on the method.

Again, shale convergence and sand compartmentalization phenomena were not accounted for in the calculations.

3.3.1.4 Richardson's model (82):

Richardson used a computer model to simulate fluid flow in the presence of shale barriers. Those barriers were simple horizontal sheets with a known length as shown in *Figure 3.7*. The results were compared with runs using homogeneous models with reduced permeabilities. The good agreement in results between the model with barriers and some homogeneous models suggested the use of reduced vertical permeabilities to simulate the effect of vertical barriers. Lengths of barriers were to be chosen according to the depositional environment but no method for their distribution was mentioned.



X-Z Section 100 m x 100 m

Fig.35 - Computer restitution of shale breaks.
(After Ref. 25)

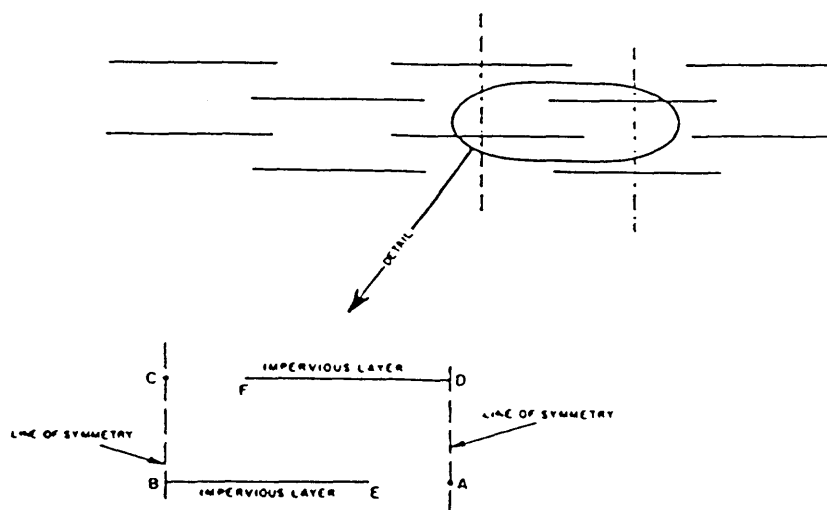


Fig. 3.6 An element model in an idealised Distribution
of impervious layers (After Ref. 75)

3.3.1.5 Haldorsen's model (41, 42, 43, 44):

Halderson used the same technique for shale generation as Delhomme (25), but he varied the shale dimensions which he generated from CDF's using random numbers, (see *Figure 3.8*). The major difference between Halderson's model and Delhomme's was the mathematical model. The effective length of the stream tube was taken equal to the height of the model plus fractional lengths of all the barriers met by the streamtube as if travelled upwards. This length was then used in the mathematical model to calculate the effective vertical permeability.

The shales he generated were horizontal, and their dimensions were independent of each other. Therefore, thick long narrow shales (Bar-shaped) could be generated. Such shales were not supported by geological observations.

The restrictions of the method were the aspect ratio of the grid block's dimensions; and the restriction on the horizontal dimensions as compared to shale length. The aspect ratio (ratio of vertical to horizontal dimensions) should not be greater than 0.1 and the horizontal dimensions should be greater than those of the longest shale in the CDF.

3.3.1.6 Begg and King's models (7, 8) :

Begg and King (7, 107) presented three methods. The statistical method which is a modification of Halderson's method (42, 44), the analytical method, and the simulation method.

1 – The analytical method: this method determines the effective permeability by calculating the flow around a single shale barrier given a uniform flow across the surface of an averaging volume. For many shales it was assumed that the external uniform flow is that due to the sum of the individual flows and that perturbations in the flow were confined within the averaging volume of the individual shales.

The flow was described by Darcy's law for incompressible fluids taken along with the boundary conditions of no flow through the shale and the assumption of uniform background permeability. Elliptical co-ordinates were used in the calculations.

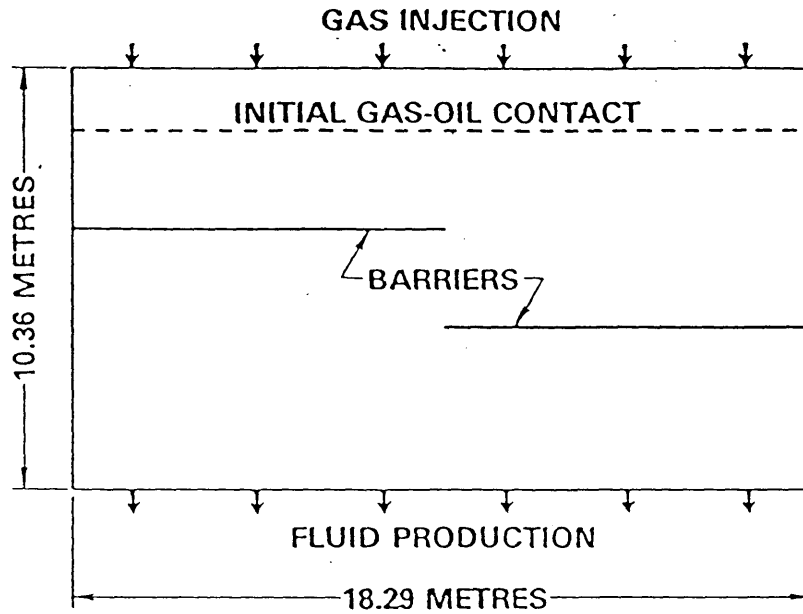


Fig. 3.7 Schematic drawing of computer model.

(After Ref. 82)

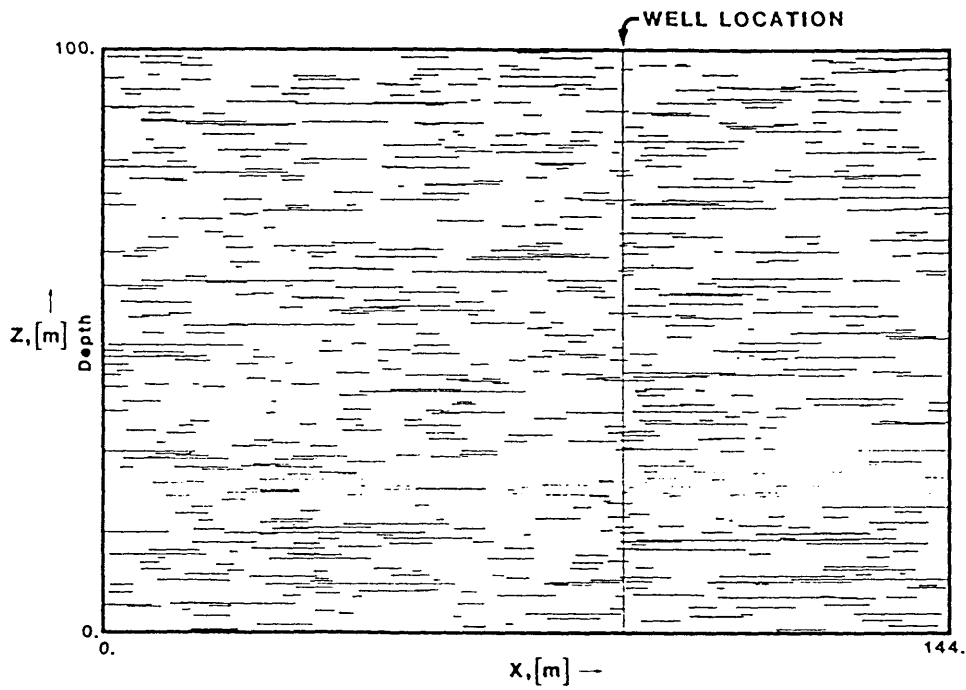


Fig. 3.8 Synthetic cross-section with shales
(After Ref. 43)

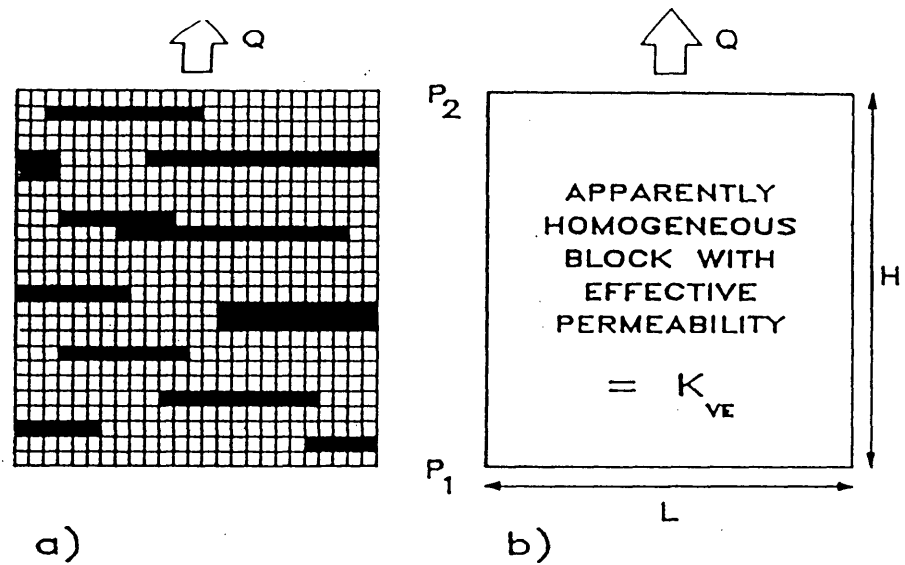
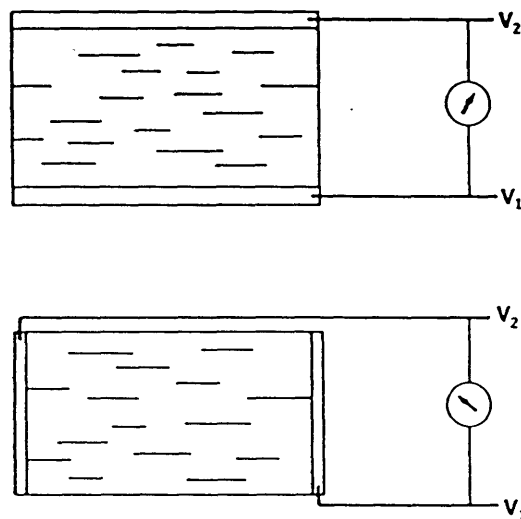


Fig. 3.9 Shale distribution in fine simulation grids
(After Ref. 8)



- VERTICAL RESISTANCE: 9,870 Ω :
- HORIZONTAL RESISTANCE: 4,150 Ω :
- HEIGHT: 50 cm:
- WIDTH: 72 cm:
- VERTICAL RESISTIVITY: $9,870 \times 72/50 = 14,200 \Omega$
- HORIZONTAL RESISTIVITY: $4,150 \times 50/72 = 2,880 \Omega$
- ▶ ANISOTROPY FACTOR: 0.203.

Fig. 3.10 Anisotropy determination by means of conducting paper.

(After Ref. 8)

The drawbacks of this method were the assumptions of constant length and infinitesimal thickness of shales. Again it considers the shales to be horizontal (no convergence).

2 – The simulation method: It solves Darcy's law by finite differences with conservation of mass for the pressure in each fine scale grid block of the simulation grid block in *Figure 3.9A*. Shale identification is done by assigning shale permeability to the fine-grids occupied mostly by shales. The boundary conditions were no-flow through the sides of the model and constant pressure at its top and bottom.

The total flow was then compared with flow through a homogeneous model having the same dimensions and flow characteristics *Figure 3.9B*. The effective permeability was then deduced.

The main disadvantages of this method are the need for large computer capacity to accommodate the fine-scale grids which are needed for accurate shale description; and the need for long computing times.

3 – The stream-tube method (7, 8): This method is a modification of Halder-son's method (41, 42) to remove the restrictions on length and aspect ratio of the simulation grid-blocks. The orientation of the shales was considered horizontal without convergence. A simplified formula for calculation of the effective vertical permeability was also presented. This formula uses the average length of the shale breaks and assumes half that length to be travelled horizontally by streamtubes at any intersection with shales.

Calculations were done in two and three dimensions and validation was done using the simulation method (8) as well as the experimental approach presented by Dupuy and Le Febure (29), *Figure 3.10*.

All methods including the streamtube method share the general assumption of horizontal shales. Although the shales are allowed to overlap, no convergence is allowed.

3.3.1.7 Begg and Carter model (6):

This model caters for the anisotropy of sand permeability in horizontal directions. Therefore a modification was done on Begg and King's streamtube method (7, 8) to account for anisotropy. No change in the geometry and orientation of shale was considered. They tackled the anisotropy problem by homogenising the grid block using scaling factors. Consequently, the shale dimensions were re-scaled to match the resulting homogeneous model. No bases were presented for the derivation of the multipliers. Close inspection of these multipliers reveals that they result in shortening the shale dimensions in the direction of the lower permeabilities, although in reality, the corresponding dimensions in a homogeneous model should be larger. this will be demonstrated later in this chapter.

3.3.1.8 Other models :

Other models are generally inferior to the recent techniques by Halderson (41, 42, 43), Begg and King (7, 8); and Willis (107). This is because such methods either use repetitive patterns, constant shale thickness, or constant length. Such early models were presented by Dupuy et al. (29), Brydges (12), and Wadman (98).

Private communications indicated the interest of many investigators in the effect of vertical permeability barriers on fluid flow. Many are engaged in this kind of study and hopefully relevant publications in future may enrich the petroleum engineering literature.

3.3.2 MODELS FOR HORIZONTAL PERMEABILITY

Although the effect of shales on vertical permeability has been thoroughly investigated, the effect on horizontal permeability is rarely assessed. This may be due to the popular assumption of horizontal shales with either infinitesimal or constant thickness. The problem was considered simple due to the above assumptions, and mathematical models were derived to calculate the effective values of horizontal permeability in the presence of discontinuous shales.

Halderson (41) presented a method for calculation of effective horizontal permeability based on the model shown in *Figure 3.11*. This two dimensional model

considers the block as homogeneous with a varying cross-sectional area in the direction of flow. The variation is caused by the presence of shales, therefore the area of shales is chopped from the section. An analytical formula for horizontal permeability was presented and the model verified by numerical simulation.

Considering the shale convergence phenomenon, the increase in streamline length can become considerable. These may travel along the junction of two converging shales creating a (Y) shaped structure. These transverse movements will increase with increase of shale frequency resulting in a considerable reduction of horizontal permeability.

SUMMARY

All the methods discussed above share the general assumption that shales are horizontal isolated barriers within the reservoir sands. This oversimplification may result in high calculated values of horizontal permeability due to neglect of the transverse movements of the reservoir fluids caused by converging shales.

Low vertical permeabilities are expected to result from such methods as they use the observed shale frequency (well data) in the calculation whereas the actual number is smaller (each two converging shales become one barrier).

Sand compartmentalisation which results from the shale convergence phenomenon, may have an impact on the calculated effective permeabilities as it reduces the volume of the reservoir sand available for fluid flow.

To take the above phenomena into account in the calculation of the effective reservoir permeabilities, an analytical technique is presented in the next chapter.

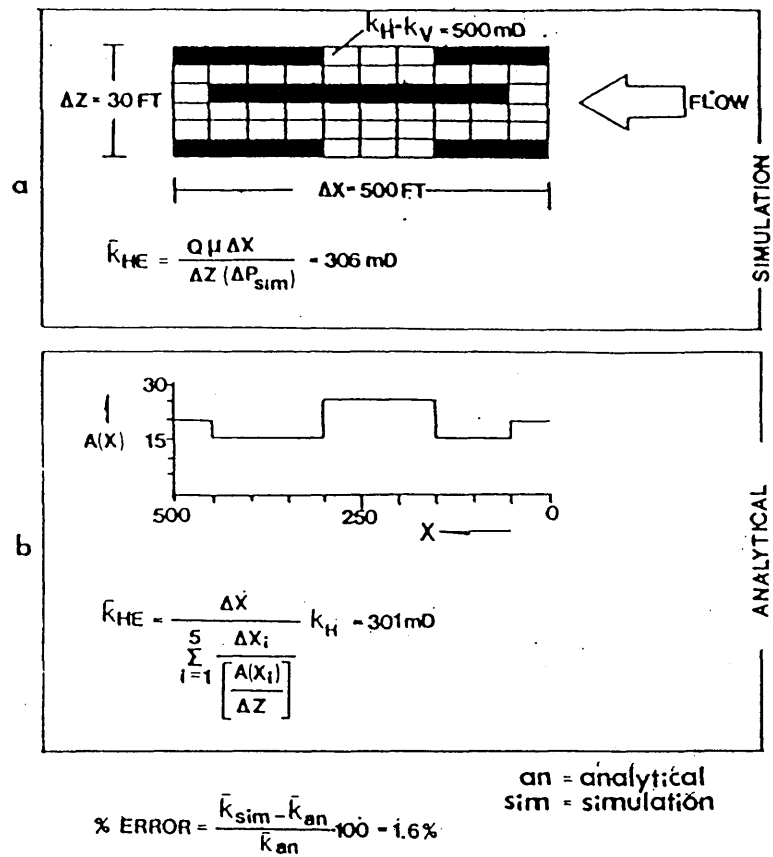


Fig. 3.11 (a) Numerical experiment to obtain effective horizontal permeability; (b) analytical calculation of effective horizontal permeability for the arrangement in (a).

(After ref. 44)

3.4 ANALYTICAL CALCULATION OF PERMEABILITIES IN PRESENCE OF DISCONTINUOUS SHALES

Begg and King (7, 8); and Haldorsen (41, 42) presented analytical methods for the calculation of the effective vertical permeability of homogeneous sands containing discontinuous (non-converging) shales. In the following pages a streamtube method for calculation of effective horizontal and vertical permeabilities is presented. This method allows for shale convergence and sand compartmentalisation as well as permeability anisotropy.

Due to shale convergence, some shales may intersect at one side forming a Y-shaped barrier or may intersect on both sides forming a discontinuous sand unit DCSU. Considering the third dimension, some sands may be completely isolated in the form of DCSU's and other sands may be partially isolated.

According to Zeito's study (110), 62-70 % of shales converge upon each other within a distance less than 250 ft. He also related the fraction of the cross-section (of the reservoir) occupied by DCSU's to the vertical shale frequency observed in wells. In the following calculations 66 % of the shales are considered converging and the rest to be isolated. Out of the 66 % some shales are used to envelop the desired number of DCSU's. The ratio of the total area of this number of DCSU's to the area of the cross-section is equal to the value read from *Figure 3.4* (fraction of the cross-section occupied by DCSUs) using the observed vertical shale frequency.

The length and width continuity distribution function for the DCSU's is the same as for the shales and their thicknesses vary between 3.6 ft and 10 ft (110). Two thicknesses are used in the calculations, 5 ft and 7.5 ft. *Figure 3.12* shows a two dimensional realisation of shale distribution considering shale convergence.

3.4.1 CALCULATION OF EFFECTIVE VERTICAL PERMEABILITY

3.4.1.1 Assumptions:

The following assumptions apply to the method of calculation:

- * Shale data from wells and outcrops are statistically representative of the part of the reservoir under consideration.

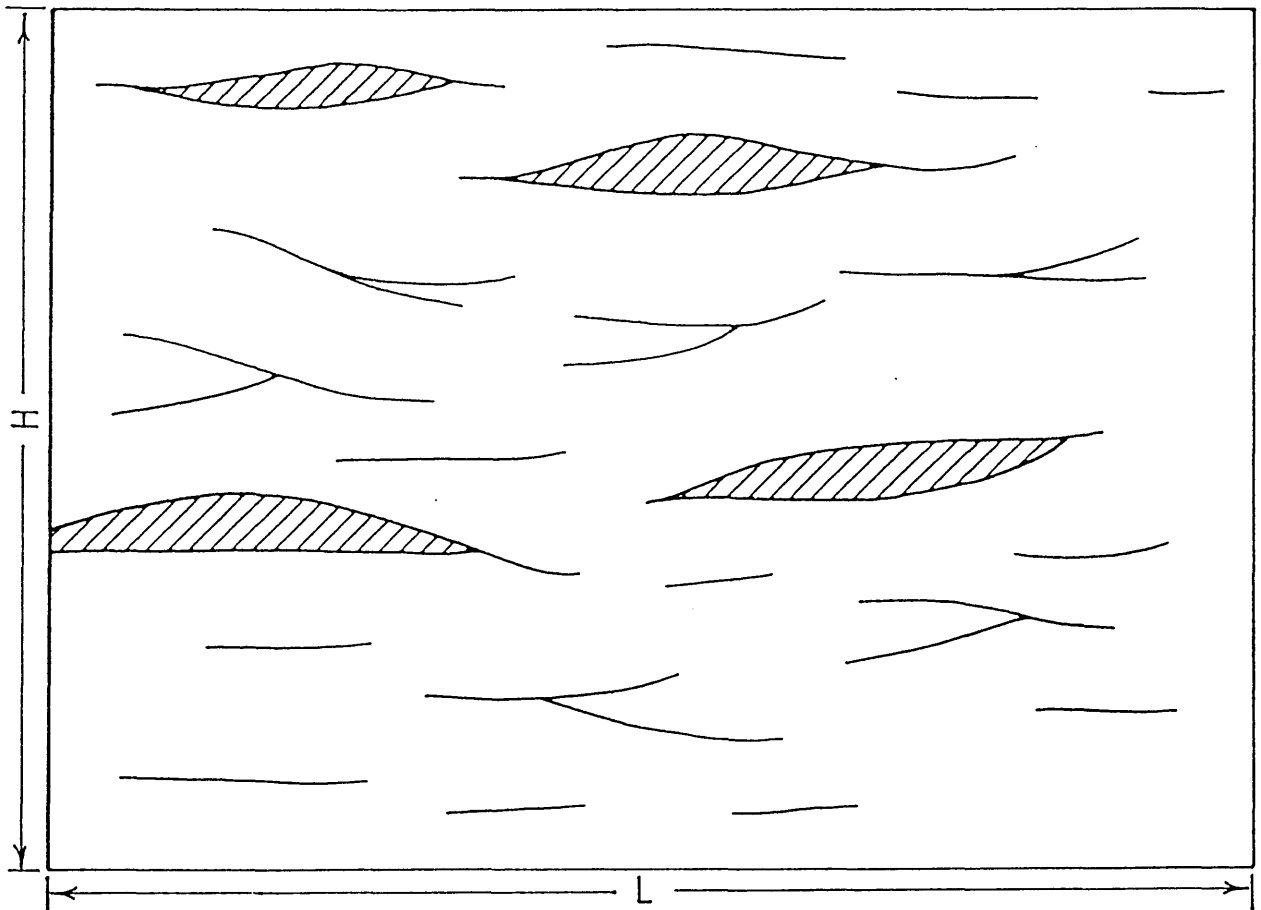


Fig. 3.12 Cross-section showing converging shales and DCSUs.

- * The discontinuous sand units resulting from shale convergence are randomly distributed (as they are bounded with shales which are randomly distributed).
- * The areal fraction of the DCSU's in cross-section or their volume fraction of the reservoir is equal to their thickness fraction in the wells.
- * The shales are randomly distributed in space.
- * Shale permeability is zero.
- * Steady state incompressible single phase flow.
- * No flow through the walls of the model parallel to the flow direction.
- * Only one phase is flowing and the effects of gravity and capillary pressure are negligible.

3.4.1.2 Brief description of the various steps of calculation

Following earlier published work (7, 8), the block under consideration, *Figure 3.12*, is divided into an arbitrary number (N_s) of equally spaced streamtubes.

On its way upwards, the streamtube travels horizontally a random fraction of half the length or width (whichever is the smaller) of the barrier it meets. This is different from published works (7, 8) which assume the streamtube to travel a random fraction of the whole length or width. The following algorithm demonstrates the method and calculation procedure:-

Step 1 Record the shale's frequency from the wells and outcrops of the same formations (No. of shales /100 ft).

Step 2 Record the shale thicknesses to draw the shale thickness frequency curve, *Figure 3.13*.

Step 3 Construct a similar curve as in step 2 for sand thickness frequency.

Step 4 Using the shale frequency recorded in step 1 enter *Figure 3.4* to find the percentage of the cross-sectional area occupied by the discontinuous sand units DCSU, F_{dc} .

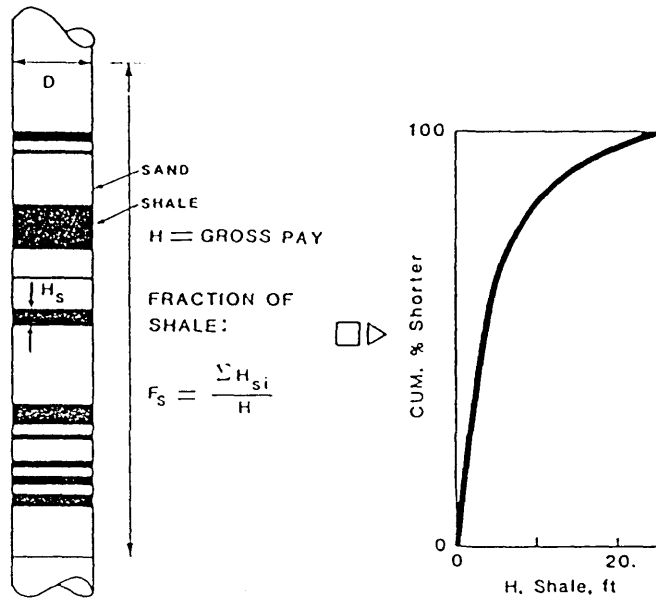


Fig. 3.13 Shale thickness frequency curve
(After Ref. 61)

Step 5 Calculate the cumulative shale thickness as a fraction of the total sand thickness, F_s .

Step 6 Regarding the cross-section on *Figure 3.12*:

(i) The total cross-sectional area allowed for fluid flow:

$$Area = (1 - F_s - F_{dc}) * H * L$$

where,

H = the height of the block.

L = the block's length.

(ii) The area occupied by a streamtube in the cross-section, $W_i * S_i$, is:

$$W_i * S_i = \frac{(1 - F_s - F_{dc}) * H * L}{N_s} \quad (3.1)$$

where,

S_i = The average length of the streamtube.

W_i = The width of the streamtube.

Step 7 Consider the streamtubes to have equal areas and lengths, and let W_{ei} equal the harmonic mean of the streamtube's width. Let K_{ei} equals the effective permeability of the streamtube in the direction of flow.

Therefore, the vertical flow rate is given by,

$$Q_t = \sum_{i=1}^{N_s} \frac{K_{ei} W_{ei} \Delta P}{\mu S_i} \quad (3.2)$$

Step 8 Regarding the blocks as homogeneous with an effective vertical permeability K_{ve} ,

$$Q_t = \frac{K_{ve} L \Delta P}{\mu H} \quad (3.3)$$

Equations (3.2) and (3.3) give,

$$K_{ve} = \frac{H}{L} \sum_{i=1}^{N_s} \frac{K_{ei}W_{ei}}{S_i} \quad (3.4)$$

Substituting for W_I from 3.1 in 3.4,

$$K_{ve} = (1 - F_s - F_{dc})H^2 \sum_{i=1}^{N_s} \frac{K_{ei}}{S_i^2} \quad (3.5)$$

Considering the streamtubes having equal lengths, S_e , and effective permeabilities,

$$K_{ve} = \frac{(1 - F_s - F_{DC})H^2 k_{ei}}{S_e^2} \quad (3.6)$$

Step 9 Calculation of the average stream-tube length:

$$S_e = H + (\text{sum. of horizontal distances})$$

To find the horizontal distances we have to calculate the number of shales and discontinuous sand units encountered.

Step 9.1 First, No. of DCSU, N_{DCSU} :

The thickness fraction of the DCSU hit by the well = F_{dc} .

The cumulative thickness of the DCSU :

$$S_{cum} = F_{dc} * H \quad ft. \quad (3.7)$$

Calculation procedure:

- (i) Generate a random number between zero and one.
- (ii) Using this random number enter the CDF of the DCSU to find a value for the thickness of a discontinuous sand unit.

- (iii) Repeat step (i) and (ii) till the summation of all the thicknesses equals the cumulative thickness calculated by equation (3.7).
- (iv) Find the number of the discontinuous sand units generated by steps (i)—(iii).

Step 9.2 Second, calculation of the number of barriers encountered:

- * Since each DCSU is bounded between two adjacent shale breaks, the number of shales used for bounding, N_{sh-b} , equals $2N_{DCSU}$.
- * The total number of barriers encountered by a streamtube:

$$\begin{aligned}
 N_B &= N_{DCSU} + \text{No.of}(Y)\text{shapedbarriers} + \text{No.ofisolatedshales} \\
 &= N_{DCSU} + (f * H * 0.66 - 2N_{DCSU})/2 + f * H * 0.34 + 1 \\
 &= 0.67f * H + 1
 \end{aligned}$$

Where,

f = Shale frequency per foot. 0.66= The fraction of shale that converge.

NB: (One is added to force the stream-tube to come to the same horizontal position at the end of the block).

Considering two dimensions,

$$S_e = H + \sum_{i=1}^{N_B} \min(R_{1i}W_{shi}, R_{2i}L_{shi})/2 \quad (3.9)$$

Where,

W_{shi} =width of shale or DCSUs chosen at random from the continuity distribution function (CDF).

L_{shi} = length of shale chosen at random (using the same random number used for generating the width) from a CDF or calculated from a length-width ratio if it is available.

R_{1i}, R_{2i} = random numbers between 0 — 1.

To account for the sand's anisotropy, i.e. difference between horizontal and vertical permeability (7, 8), K_{ei} is averaged harmonically as follows:

$$\frac{S_e}{K_{ei}} = \frac{S_v}{K_v} + \frac{S_h}{K_h} \quad (3.10)$$

Where,

S_h = summation of the horizontal distances.

S_v = summation of the vertical distances.

K_v = Sand vertical permeability.

K_h = Sand horizontal permeability.

Calling $\frac{S_e}{K_{ei}}$ the effective length S_{ei} , from (9) and (10) we find,

$$S_{ei} = \frac{H}{K_v} + \frac{1}{K_h} \sum_{i=1}^{N_B} \min(R_{1i}W_{shi}, R_{2i}L_{shi})/2 \quad (3.11)$$

Substituting for $S_{ei} = S_e/K_{ei}$ in equation 3.6,

$$K_{ve} = (1 - F_s - F_{DC})H^2 \sum_{i=1}^{N_B} \frac{1}{S_e S_{ei}} \quad (3.12)$$

Or based on assumption (4),

$$K_{ve} = \frac{(1 - F_s - F_{DC}) * H^2}{S_e S_{ei}} \quad (3.13)$$

3.4.1.3 A simplified formula for calculation of the stream-tube's length (7):

Let ℓ = the mean horizontal extension of the DCSU and shale in the layer. We can assume the distance travelled along each barrier equals quarter it's lateral extension.

Therefore the distance travelled horizontally = $\frac{\ell}{4}N_B$.

Equation (3.9) can be simplified to be,

$$S_e = H + \frac{\ell}{4}N_B \quad (3.14)$$

and equation (3.11) will become,

$$S_{ei} = \frac{H}{K_v} + \frac{1}{K_h} \frac{\ell}{4} N_B \quad (3.15)$$

3.4.1.4 Calculation of the streamtube length for the case of horizontal permeability anisotropy

Due to the complete anisotropy, a homogenisation process is needed before applying the methods above for calculation of the effective vertical permeability. This implies using a special coordinate transformation to reduce the flow equation into Laplace form. The process is effected as shown below.

Consider the following flow equation for anisotropic porous media:

$$K_x \frac{\delta^2 P}{\delta X^2} + K_y \frac{\delta^2 P}{\delta Y^2} + K_z \frac{\delta^2 P}{\delta Z^2} = 0 \quad (3.16)$$

In order to reduce this equation to the solvable Laplace form, let

$$\bar{X} = X \sqrt{\frac{K_x}{K_y}} \quad (3.17)$$

$$\bar{Y} = Y \sqrt{\frac{K_x}{K_y}} \quad (3.18)$$

$$\bar{X} = Z \sqrt{\frac{K_x}{K_z}} \quad (3.19)$$

Therefore,

$$\frac{\delta \bar{Y}}{\delta Y} = \sqrt{\frac{K_x}{K_y}} \quad (3.20)$$

Similar expressions can be obtained for X & Z directions.

The differential part of the second term of equation (3.16) can be expressed as follows:

$$\begin{aligned}
\frac{\delta^2 P}{\delta Y^2} &= \frac{\delta}{\delta Y} \left(\frac{\delta P}{\delta \bar{Y}} \frac{\delta \bar{Y}}{\delta Y} \right) \\
&= \sqrt{\frac{K_x}{K_y}} \frac{\delta}{\delta \bar{Y}} \left(\frac{\delta P}{\delta \bar{Y}} \right) \\
&= \sqrt{\frac{K_x}{K_y}} \frac{\delta}{\delta \bar{Y}} \frac{\delta \bar{Y}}{\delta Y} \left(\frac{\delta P}{\delta \bar{Y}} \right) \\
&= \frac{K_x}{K_y} \frac{\delta}{\delta \bar{Y}} \left(\frac{\delta P}{\delta \bar{Y}} \right) \\
&= \frac{K_x}{K_y} \frac{\delta^2 P}{\delta \bar{Y}^2}
\end{aligned} \tag{3.21}$$

Similarly,

$$\frac{\delta^2 P}{\delta Z^2} = \frac{K_x}{K_z} \frac{\delta^2 P}{\delta \bar{Z}^2} \tag{3.22}$$

Substituting equations 3.21 & 3.22 in equation 3.16 gives,

$$K_x \frac{\delta^2 P}{\delta \bar{X}^2} + K_y \frac{K_x \delta^2 P}{K_y \delta \bar{Y}^2} + K_z \frac{K_x \delta^2 P}{K_z \delta \bar{Z}^2} = 0 \tag{3.23}$$

Thus,

$$\frac{\delta^2 P}{\delta \bar{X}^2} + \frac{\delta^2 P}{\delta \bar{Y}^2} + \frac{\delta^2 P}{\delta \bar{Z}^2} = 0 \tag{3.24}$$

Equation 3.21 – which is in Laplace form – can be solved to find the pressure distribution in the domain under consideration. Thus, the effect of anisotropy in permeability can be replaced by equivalent shrinking or expansion of the model in different directions.

If the new homogeneous model is to have a permeability equal to that in X direction, then the the new dimensions $\bar{X}, \bar{Y}, \bar{Z}$ will be given by multiplying the old dimensions X, Y, and Z by the following multipliers:

1 for X direction.

$\sqrt{\frac{K_x}{K_y}}$ for Y direction (equals $\frac{\bar{Y}}{Y}$).

$\sqrt{\frac{K_x}{K_z}}$ for Z direction (equals $\frac{\bar{Z}}{Z}$).

In the presence of shale intercalations, the same multipliers are used to find the corresponding distance travelled by the streamtube in the isotropic medium. Thus the corresponding form of equation (3.9) is given as follows:

$$S_e = \bar{H} + \sum_{i=1}^{N_B} \frac{1}{2} \min(R_{1i} \bar{W}_{shi}, R_{2i} L_{shi}) \quad (3.25)$$

Where,

$$\bar{W}_{shi} = W_{shi} * \sqrt{\frac{K_x}{K_y}} = W_{shi} * \frac{Y}{Y}$$

$$\bar{H} = H \sqrt{\frac{K_x}{K_z}} = H * \frac{Z}{Z}$$

3.4.1.5 Vertical permeability for stratified reservoirs:

For a reservoir composed of N_L layers, consider equation (3.16),

1- Use S_s instead of S_e

Where,

$$S_s = \sum_{i=1}^{N_L} S_e$$

N_L =the number of the layers.

2- Use K_{eis} instead of K_{ei} .

Where,

$$K_{eis} = \frac{S_s}{\sum_{i=1}^{N_L} \frac{S_{iv}}{K_{iv}} + \frac{S_{ihx}}{K_{ihx}} + \frac{S_{ihy}}{K_{ihy}}} \quad (3.26)$$

3- The effective length equals:

$$S_{eis} = \frac{1}{\sum_{i=1}^{N_L} \frac{S_{iv}}{K_{iv}} + \frac{S_{ihx}}{K_{ihx}} + \frac{S_{ihy}}{K_{ihy}}} \quad (3.27)$$

Therefore, the effective vertical permeability (K_{VES}) for the stratified reservoir becomes,

$$K_{VES} = \frac{(1 - F_{ss} - F_{dcs})H_s^2}{(S_s S_{eis})} \quad (3.28)$$

Where,

F_{dcs} = The areal fraction of all the reservoir cross-section occupied by DCSUs.

F_{SS} = The shale fraction of the total stratified reservoir's thickness.

H_s = The total thickness of the stratified reservoir.

i = Denotes the layers.

3.4.2 CALCULATION OF THE EFFECTIVE HORIZONTAL PERMEABILITY

Due to shale convergence, the effect of shale geometry on the length of the streamtubes is more pronounced. For example, a horizontal streamtube may travel a transverse distance normal to the direction of flow to by-pass (Y) shaped barriers. The travel distance may also be increased due to by-passing of the DCSUs. Therefore, to estimate the effective horizontal permeability, stochastic shales can be generated in the block under consideration using the well known stochastic shale generation technique (7, 8, 59). Shales will be generated in the block on (2-D) basis till the areal fraction of the shales equals the thickness fraction of the shales hit by the well (F_s).

Considering the average angle of inclination of the shales to be 7 degrees (97), (different angles can be used for other fields according to outcrop observations), the problem is reduced to finding the length of the stream-tube.

3.4.2.1 Calculation of the length of the stream-tube:

S_i = Length of the model L

+ increase in travel distance caused by movement along the DCSU and the (Y) shaped junctions having the (Y) tail against the direction of flow.

+ a random fraction of half the shale length for each (Y) shaped junctions having the tail to the direction of flow.

Therefore,

$$S_i = L + (\text{distance caused by } N'_{yc}) + (\text{distance caused by } N'_{yo})$$

Where,

N'_{yc} =the number of the (Y) shaped barriers - having the tail against the direction of flow), plus the number of DCSUs met by the streamtube.

N'_{yo} = the number of the (Y) shaped barriers - having the (Y) tail to the direction of flow - met by the stream-tube.

Calculation of the number of barriers from each type:

* Let the number of shales generated in the block = N_{sh} .

* The percentage of converging shales = 66% (Mid. of the range in ref. (110)).

*34% of the shale will be horizontal.

* The number of converging shales = $N_{shc} = N_{sh} * 0.66$

* $N_{sh-b} = N_{DCSU} * 2$

*Total number of (Y) shaped barriers, N_y :

$$N_y = \frac{N_{shc} - N_{DCSU} * 2}{2} \quad (3.29)$$

(We divided by 2 because every two converging shale breaks make one (Y) shaped barrier)

At this stage it is reasonable to assume that half N_y may have the tail in the direction of flow and the rest have the tail against that direction. This then implies the calculation of the arithmetic mean thickness of DCSUs, that is, S_{th} , followed by division of the cross-section into horizontal streaks according to this mean thickness. The number of barriers encountered by a horizontal streamtube is regarded as the number of barriers contained in one horizontal streak.

Therefore,

$$N'_{yo} = N_y * \frac{S_{th}}{H} \quad (3.30)$$

$$N'_{yc} = N'_{yo} + \frac{N_{DCSU} * S_{th}}{2H} \quad (3.31)$$

The streamtube travels a random distance of the length (C) as shown in *Figure 3.14 & 3.14a* for all N'_{yo} and N'_{yc} , (i.e. N_{yt}).

The increase in travel distance caused by a (Y) shaped barrier is calculated as follows:

$$* \text{ Length } X = Y/\tan \theta = S_{th}/2\tan\theta$$

$$* \text{ Length } C = Y/\sin \theta = S_{th}/2\sin\theta$$

The increase in travel distance due to travel along (C) is given by,

$$C - X = \frac{S_{thi}(1 - \cos\theta)}{2\sin\theta} \quad (3.32)$$

Taking θ as 7 degrees, then,

$$C - X = \frac{S_{thi}(1 - \cos 7)}{2\sin 7}$$

Since the streamtube travels a random distance along (C), then the increase in travel distance caused by each barrier is a random fraction of (C - X), which is given by,

$$\text{Increase} = R_i \left(\frac{S_{thi}}{2\sin\theta} - \frac{S_{thi}}{2\tan\theta} \right) \quad (3.33)$$

Where,

R_i = Random number between 0 - 1.

Therefore, the length of the streamtube is calculated by,

$$S_e = L + \sum_{i=1}^{N'_{yo}} 0.5R_i \ell_{shi} + \sum_{i=1}^{N_{yt}} R_i \frac{S_{thi}}{2\sin 7} - \frac{S_{thi}}{2\tan 7} \quad (3.34)$$

Where,

ℓ_{shi} = Random generated shale width.

S_{thi} = Random generated thickness of the DCSUs.

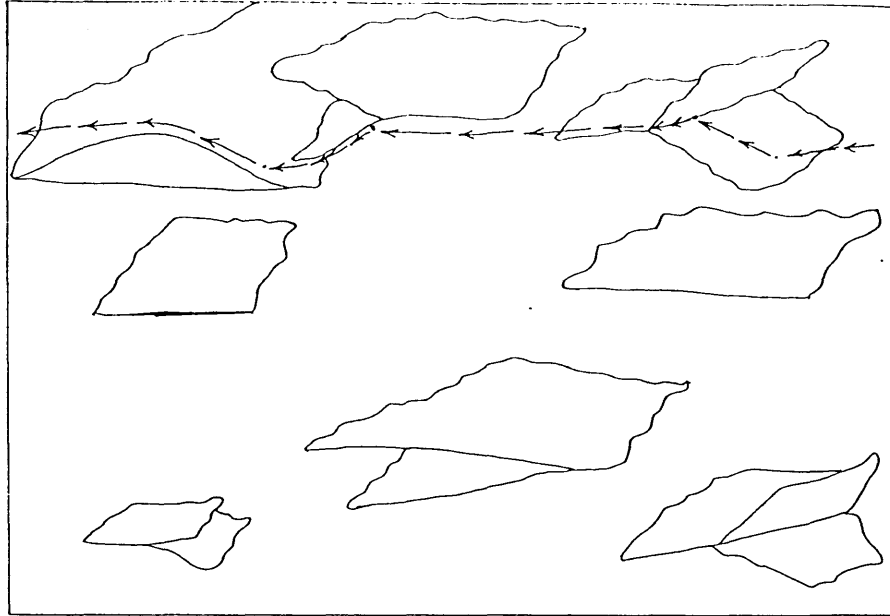


Fig. 3.14 A horizontal flow path around converging shales

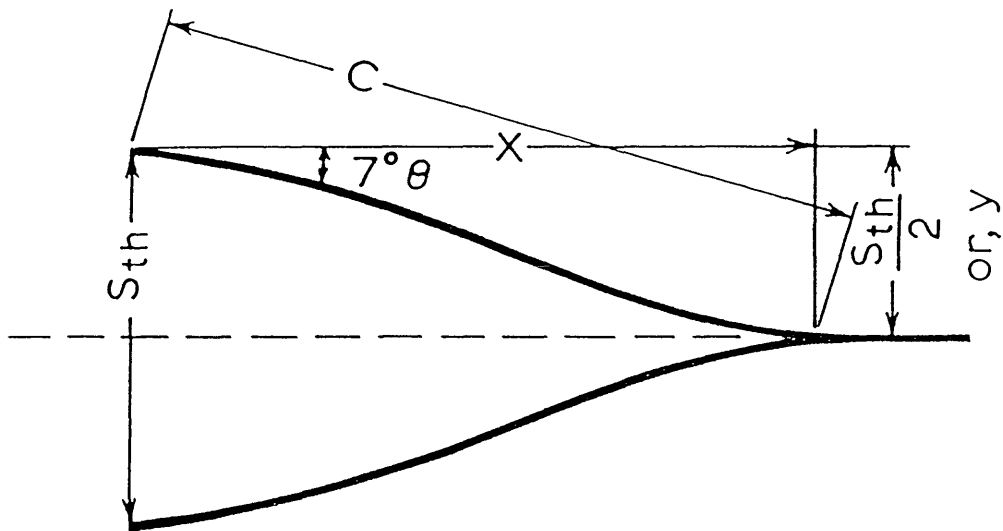


Fig. 3.14a Increase of travel distance caused by converging shales.

Usually the third term of equation 3.34 is relatively small, therefore, we can use an average value for S_{thi} , (i.e. multiply by $\frac{1}{2}$ instead of a random number). This will yield the following simplified expression:

$$S_e = L \sum_{i=1}^{N'_{yo}} \frac{1}{2} R_i \ell_{shi} + \frac{1}{4} N_{yt} S_{th} \left(\frac{1}{\sin\theta} - \frac{1}{\tan\theta} \right) \quad (3.35)$$

Therefore, the effective horizontal permeability K_{VE} is calculated as follows:

$$K_{EH} = \frac{(1 - F_s - F_{DC}) * L^2 * K_e}{S_i^2} \quad (3.36)$$

Where,

K_e = the effective permeability of the streamtube in the horizontal direction.

Similar to equation (19),

$$\frac{S_i}{K_e} = \frac{L}{K_x} + \frac{(S_i - L)}{K_y} \quad (3.37)$$

(Equation (25) is applicable if the cross-section is normal to the Y axes of the channel, Fig 13)

Or,

$$\frac{S_i}{K_e} = \frac{L}{K_y} + \frac{(S_i - L)}{K_x} \quad (3.38)$$

3.4.3 RESULTS AND DISCUSSIONS

[A] Effective vertical permeability prediction:

Table 3.1 shows the estimated vertical permeabilities for different shale frequencies using equation 3.13. Also shown in the same table are the predictions of the statistical streamtube method (7, 8). Both results are plotted in *Figure 3.17*. Based on these results the following observations are made:

* For the first two frequency levels used in equation 3.13, the DCSU's gradually manifest themselves in an appreciable amount of reservoir sand compartmentalization. For a shale frequency of 12 shales/100 foot, for example, the sand fraction occupied by the DCSU's is 0.23.

* There is a clear discrepancy between the predictions of the analytical method presented in this chapter and the statistical streamtube method (7, 8). As can be seen in table 3.1 and *Figure 3.17*, although both methods show a decreasing permeability trend with increasing shale frequency, the latter gives very low results. For a shale frequency of 12/100 foot the analytical method yields a vertical permeability of 21.8 md whereas the statistical streamtube method gives 5.93 md. There are many reasons for this discrepancy:

- (i) The statistical streamtube method ignores the phenomenon of shale convergence which reduces the number of barriers met by a vertical streamtube.
- (ii) It assumes the vertical streamtube travels horizontally a random fraction of the barrier's length or width, although in reality it travels a random fraction of half the length or width.

Shale Frequency	Frac. DCSU	Shale Frac.	$\frac{K_{ve}}{K_H}$	K_{ve} md
2	0.0	0.01	0.270	81.00
4	0.0	0.02	0.157	47.15
6	0.075	0.03	0.13	39.00
8	0.115	0.04	0.101	30.24
10	0.18	0.05	0.088	26.25
12	0.23	0.06	0.077	23.228

Table 3.1 Calculated effective vertical permeabilities considering shale convergence (horizontal Perm. = 300 md)

Random no. Seed	Vertical Perm.
1234	52.84
2234	29.46
3234	53.09
4234	44.02
5234	56.53
6234	27.30
7234	67.16

Table 3.2 Different results for different random No. seeds

[B] Effective horizontal permeability prediction:

Presented in table 3.3 and *Figure 3.17* are the results of equation 3.36 for effective horizontal permeability using different shale frequencies. As in the vertical permeability case, at low shale frequencies (2 – 3 shales/100 ft) the DCSU's do not appear, and the rate of effective horizontal permeability decrease is very low because the only reduction factor is the transverse movements of the streamtubes due to the Y-shaped barriers. At higher shale frequencies, the DCSU's begin to appear resulting in further reduction of horizontal permeability by an additional factor, namely, the sand compartmentalisation which hinders fluid flow within the sand bodies sealed by shales, thus reducing the ability of the reservoir to transmit the fluids.

Shale Frequency	Frac. DCSU	Shale Frac.	$\frac{K_{he}}{K_H}$	K_{he} md
2	0.0	0.01	0.99	297.00
4	0.0	0.02	0.98	294.00
6	0.075	0.03	0.894	268.31
8	0.115	0.04	0.844	253.28
10	0.18	0.05	0.769	230.60
12	0.23	0.06	0.709	212.61

Table 3.3 Calculated effective horizontal permeabilities considering shale convergence

[C] Effect of random number seeds:

The random numbers generated by computers depend on the seeds used to generate them. It is of interest, therefore, to investigate the seed sensitivity of the permeability predictions. Table 3.2 shows the effect of various random number seeds on the effective vertical permeability predictions. It is clear from the presented permeability values that there is an appreciable seed dependency of the predictions (minimum being 27.3 and maximum being 67.17 with an average value of 47.15). To overcome this apparent non-uniqueness of the permeability values, an arbitrary large number of seeds are used in the computer code developed for the calculation methods presented in this chapter, to generate large numbers of streamtube lengths and then their arithmetic average is taken as the length of the streamtube to be used in permeability calculations. By this way, the variation of the results have become infinitesimal. For example, the streamtube lengths used to prepare table 3.1 and 3.3 are averages of 150 lengths. Increasing the number of the generated lengths beyond 50 resulted in no variation in the predicted permeabilities.

3.4.4 VERIFICATION

Two methods of verification were used for the above methods, a simulation method and an experimental method. The simulation method is presented in the next section (sec 3.5) and the experimental method is presented in chapter 4 of this thesis.

Detailed discussions and comparison with the statistical streamtube method are presented at the end of chapter 4. For the sake of completeness *Figure 3.17* is a plot of results from three methods (analytical, simulation, and experimental) for similar shale frequencies.

3.5 NUMERICAL CALCULATION OF THE EFFECTIVE PERMEABILITIES IN PRESENCE OF CONVERGING SHALES

3.5.1 CONSTRUCTION OF THE MODEL

A three dimensional model is constructed as shown in *Figure 3.15*. It consists of 20 layers of fine grids in the vertical direction, 20 vertical layers in x-direction, and 16 vertical layers in y- direction. Each fine-grid block is 2.5 foot thick, 50 ft long in X-direction, and 50 ft wide in y-direction.

Shales are generated explicitly in the light of the CDF of fluvial shales presented by Zeito (110) *Figure 3.1*. The length and width dimensions used are varying around the moderate values in the CDF although they are multiples of the grids length. Shale thickness is confined to the thickness of the fine-grids (i.e., 2.5 ft). Constant shale thickness is preferred to using variable thickness, to avoid discretization errors resulting from using constant grid thickness for the variable shale thicknesses. This will also conserve the volume fraction of shale in the model which is equal to the observed shale fraction in the wells.

The model is then translated into a data file in the form of layers of (zeros) and (ones). The grid block is assigned zero if it contained shale, otherwise it is assigned one. Later, when this file is processed, the grids with (zeros) are assigned shale permeability while grids with (ones) are assigned sand permeability.

The Y-shaped barriers are discretized as U-shapes and the discontinuous sand units are presented as parallelograms.

The generated number of DCSU's have an areal fraction of the cross-section equals to the value read from *Figure 1.5* using the shale frequency.

The volumetric and cross-sectional fraction of shale; and the volume fraction of DCSU's is conserved while building the 3-D model.

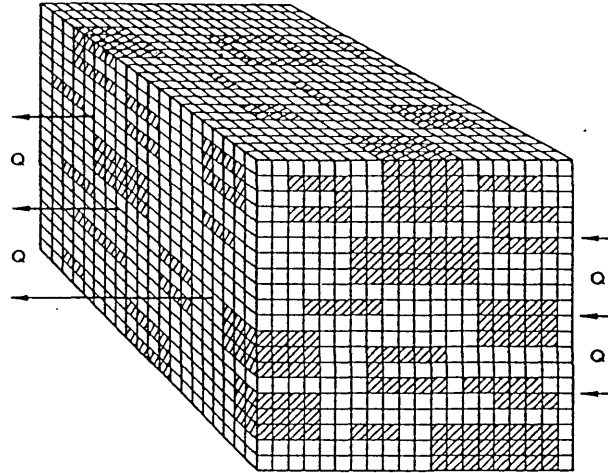


Fig. 3.15 A simulation model considering shale convergence

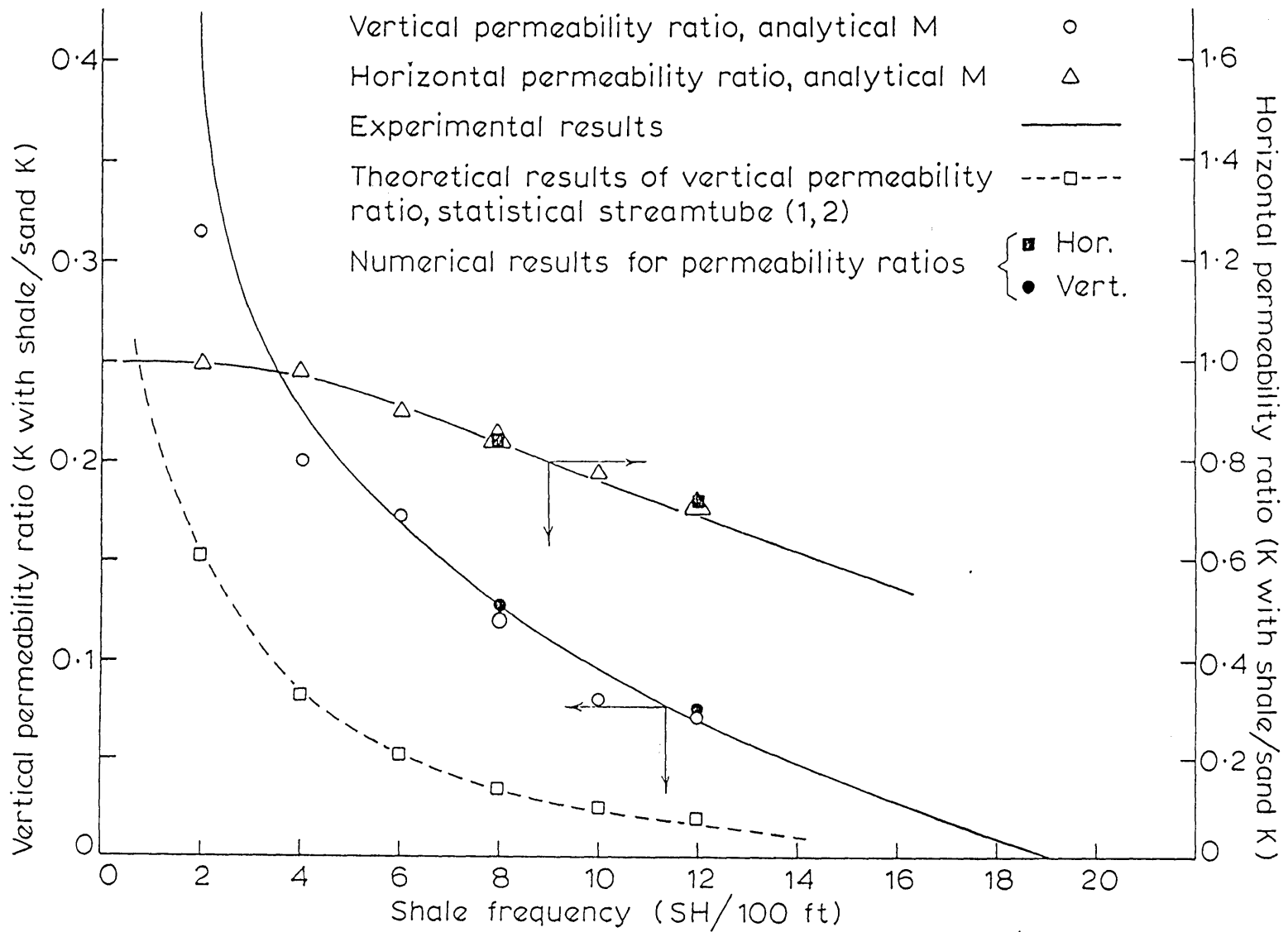


Fig. 3.17 A plot of results from the analytical experimental, and simulation methods

3.5.2 CALCULATION PROCEDURE

The simulation technique used for calculation of the effective vertical permeability follows closely the simulation method presented by Begg and King (8). But here a three dimensional model is used instead of a two dimensional one. In addition, shale convergence and sand compartmentalisation phenomena are accounted for.

The assumptions inherent in the calculations are the same as those in Section (3.4). As for boundary conditions, constant pressure boundaries are imposed at the inlet and outlet faces of the model (bottom and top) and no flow boundaries are imposed for the other faces of the domain. Constant upstream and downstream pressure ($P_1, P_2 = 0$) are maintained by adding top and bottom layers with these pressures assigned to their grid block centres. This implies forced unidirectional flow simulation.

Using the finite difference approach, a program is coded to solve Darcy's law, with conservation of mass, for pressure in each fine-scale grid block. This program - the solver (Appendix 3.B) - uses the incomplete Cholesky-Conjugate gradient method for solution of the pressure matrix. The coefficients of this matrix were prepared by another program, Versim (Appendix 3.A). This program, Versim, reads the translated version of the model (Zeros and ones) as well as sand and shale permeabilities from a data file. Apart from the preparation of the matrix coefficients, Versim does other calculations that will be discussed later. A flow chart, *Figure 3.16*, shows the functions of the program and the calculation procedure.

Because the program (Versim) needs a very big computer memory, a super-computer is used to perform the calculations.

3.5.3 VERTICAL PERMEABILITY CALCULATION

The total flow rate through the model is the summation of the flow rates through each grid block of the model, which is given by,

$$Q_T = \sum_{i=1}^{NX} \sum_{j=1}^{NY} q_{i,j,NZ} \quad (3.39)$$

Where, $q_{i,j,NZ}$ is the volumetric flow rate through block i,j,NZ which is given by,

The solution obtained from the solver is in the form of a map for pressure distribution in the grid blocks. Since we use the constant down-stream pressure ($P_2 = 0$) at the centres of the extra grid layer (107), we can use the pressure at the top layer of the model to calculate the flow rate from each grid of that layer using Darcy's law as shown below,

$$q_{i,j,NZ} = \frac{-K_{i,j,NZ} * \Delta X \Delta Y (P_2 - P_{i,j,NZ})}{\mu \Delta Z} \quad (3.40)$$

Where,

$K_{i,j,NZ}$ = Grid block permeability.

μ = Liquid viscosity.

NX, NY, NZ = Number of grids in X, Y, and Z directions.

$\Delta X, \Delta Y, \Delta Z$ = Grid length, width, and thickness.

$P_{i,j,NZ}$ = Grid block pressure of the top layer.

If the model is replaced by a homogeneous one having the same dimensions and flow conditions with an effective permeability, K_{ve} , the flow through this block can be calculated using Darcy's law as shown below,

$$Q_T = \frac{-K_{ve} L W (P_2 - P_1)}{\mu (H + \Delta Z)} \quad (3.41)$$

Where,

L = The length of the model.

W = The width of the model.

H = The height of the model.

ΔZ is added due to the increase of the model thickness by half the grid-layer thickness at the top and bottom to the centres of the imaginary layers at top and bottom.

Equating (3.39) and (3.41), and substituting for $q_{i,j,NZ}$ gives,

$$K_{VE} = \frac{(H + \Delta Z)}{LW(P_2 - P_1)} \sum_{i=1}^{NX} \sum_{j=1}^{NY} K_{i,j,NZ} \Delta X \Delta Y (P_2 - P_{i,j,NZ}) \quad (3.42)$$

Three models for different shale frequencies were used. The results from all the models are shown in table 3.4 and plotted in *Figure 3.17*.

A remarkable similarity is obtained between the results of the analytical method presented in this chapter and the numerical method. This verifies the analytical technique and suggests the validity of it's use for a wide range of shale frequencies.

Model no.	Shales/ ft	Fraction of DCSU	K_{ve}
1	0.04	0.000	70.5
2	0.08	0.115	38.16
3	0.12	0.230	22.27

Table 3.4 K_{ve} values calculated by the simulation method

3.5.4 HORIZONTAL PERMEABILITY CALCULATION

The calculation of effective horizontal permeability was performed in the same way as the vertical permeability, except for the flow direction, and position of no-flow boundaries. The flow direction is horizontal from one side of the model to the opposite side, and the no flow boundaries are the four other faces. We can simply turn the model in *Figure 3.15* ninety degrees vertically and apply all the conditions for the vertical model.

The results using three models with different shale frequencies are presented in table 3.5. *Figure 3.17* shows good similarity between the results obtained by this method and the analytical method presented in section 3.4.2. This similarity suggests the use of the analytical method for calculation of effective horizontal permeabilities of formations with stochastic shales.

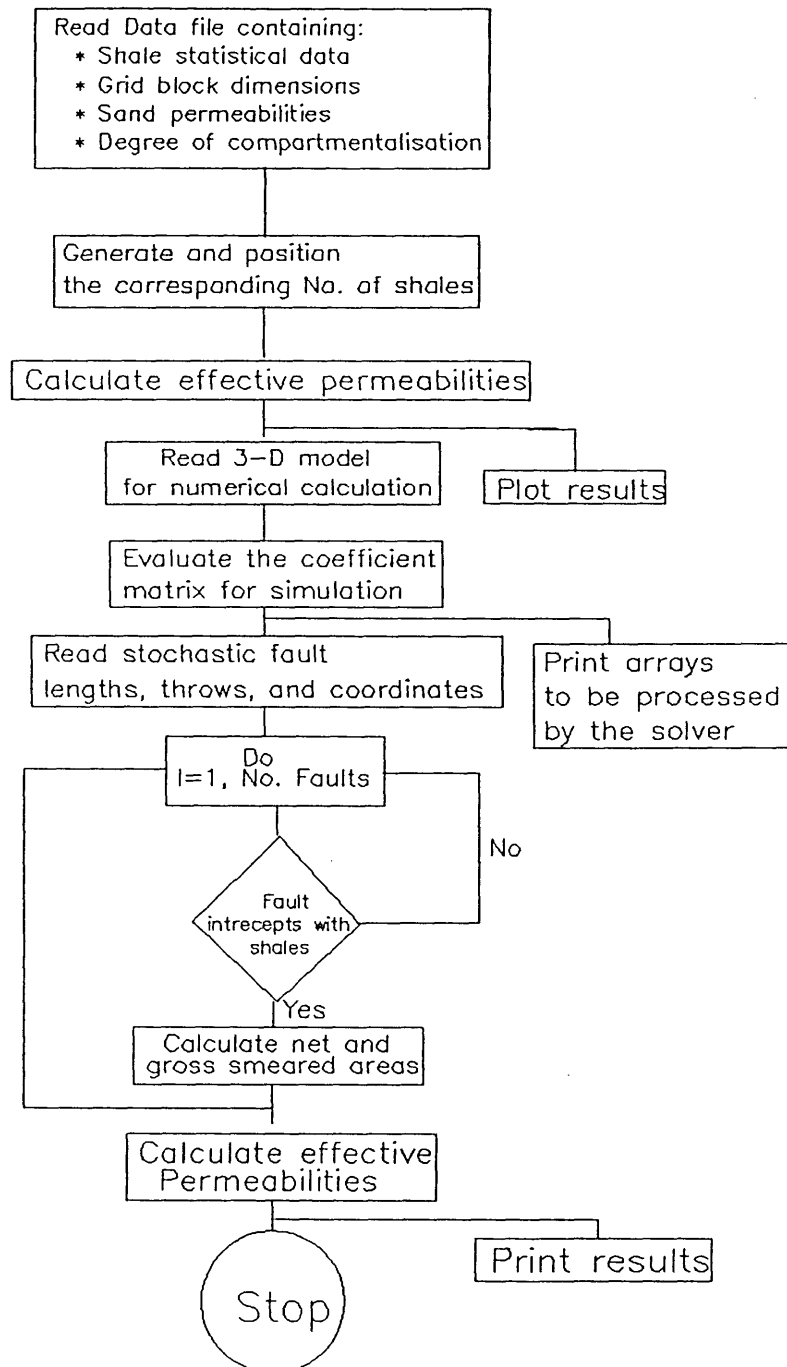
Model No.	Shales/ ft	Fraction of DCSU	K_{he}
1	0.04	0.000	299.5
2	0.08	0.115	251.4
3	0.12	0.230	218.03

Table 3.5 K_{he} values calculated by the simulation method

3.6 SUMMARY

- Two analytical methods for calculation of the averaged absolute (effective) horizontal and vertical permeabilities of formations containing discontinuous shales are presented. These methods account for the phenomena of shale convergence and sand compartmentalisation.
- The methods are verified by both numerical and experimental techniques (as will be demonstrated in the next chapter).
- The statistical streamtube method (7, 8) gives pessimistic results due to neglect of shale convergence phenomenon and inaccuracy in its calculation procedure (consideration of the streamtube to travel a random fraction of the whole barrier length or width instead of half the length or width).
- The shale convergence phenomenon has a pronounced effect on the effective horizontal permeability, especially at high shale frequencies.

Fig. 3.16 Flow chart of program versim



CHAPTER 4

EXPERIMENTS ON THE EFFECT OF STOCHASTIC SHALES ON AVERAGED ABSOLUTE RESERVOIR PERMEABILITIES

4.1 INTRODUCTION

Studies of the effect of stochastic shales on vertical and horizontal permeabilities have been made by many investigators (7, 8, 29, 41, 42, 97). Both numerical approaches (107) and analytical studies have been planned to investigate the problem. Comparisons were made between simulation and analytical results using a variety of models (77, 104). Little experimental work has been done in this area. The experiment done by Dupuy and Le Febvre (29), on conductive paper (Two dimensional) seems to be the only one published on this particular problem.

The phenomenon of shale convergence and sand compartmentalisation (sand trapping between shales) has not been accounted for by any of the previous methods. To account for these phenomena, three dimensional calculations are necessary.

The experimental work presented here is meant to account for the above phenomena carrying out the studies on three dimensional systems. The effect of stochastic shales on both horizontal and vertical permeabilities is calculated.

The porous permeable sand is simulated by brine with a fixed conductivity and impermeable shale is simulated by sheets of perspex having different sizes analogous to the continuity distribution function (CDF) of shales in fluvial deposits, *Figure 3.1*. Converging shales and discontinuous sand units were simulated by (U) shaped sheets and thick sheets respectively.

The perspex sheets are suspended in brine by means of a carrier model. An alternating current (AC) is generated in the circuit and vertical and horizontal conductivities are measured by a digital voltmeter via horizontal and vertical electrodes.

Comparison is then made with readings without the perspex sheet to find the reduction in conductivity caused by the sheets. The results were scaled to

determine the analogous reduction in sand permeability due to stochastic shales.

4.2 EQUIPMENT AND PROCEDURE

The experimental work was carried out in a glass tank, 38.5 cm long, 27 cm high, and 26.5 cm wide.

The carrier model is fitted inside the glass tank. The purpose of the model is to carry the electrodes and suspend the perspex sheets simulating shales. The model is, composed of two screened side sheets of perspex along the length of the tank, some fittings to hold the vertical electrodes along the width of the tank, and a cover to hold the top electrode. A thin plastic wire is netted between the side sheets to form a series of horizontal wires covering the whole space between the sheets. Three types of perspex sheets are randomly suspended on the plastic wires to simulate the discontinuous sand units, the converging shales, and the isolated shales. Their dimensions and corresponding volumes in field units are shown in tables 4.1 and 4.2.

Horizontal scale: 1 cm = 12.5 ft

Vertical scale: 1 cm = 3.125 ft

Dimension	Real dimension	equivalent dimension
Height	17 cm	53.13 ft
Width	26 cm	325.00 ft
Length	38.5	481.25 ft
Tank volume		8309864 ft^3

Table 4.1 The model dimensions

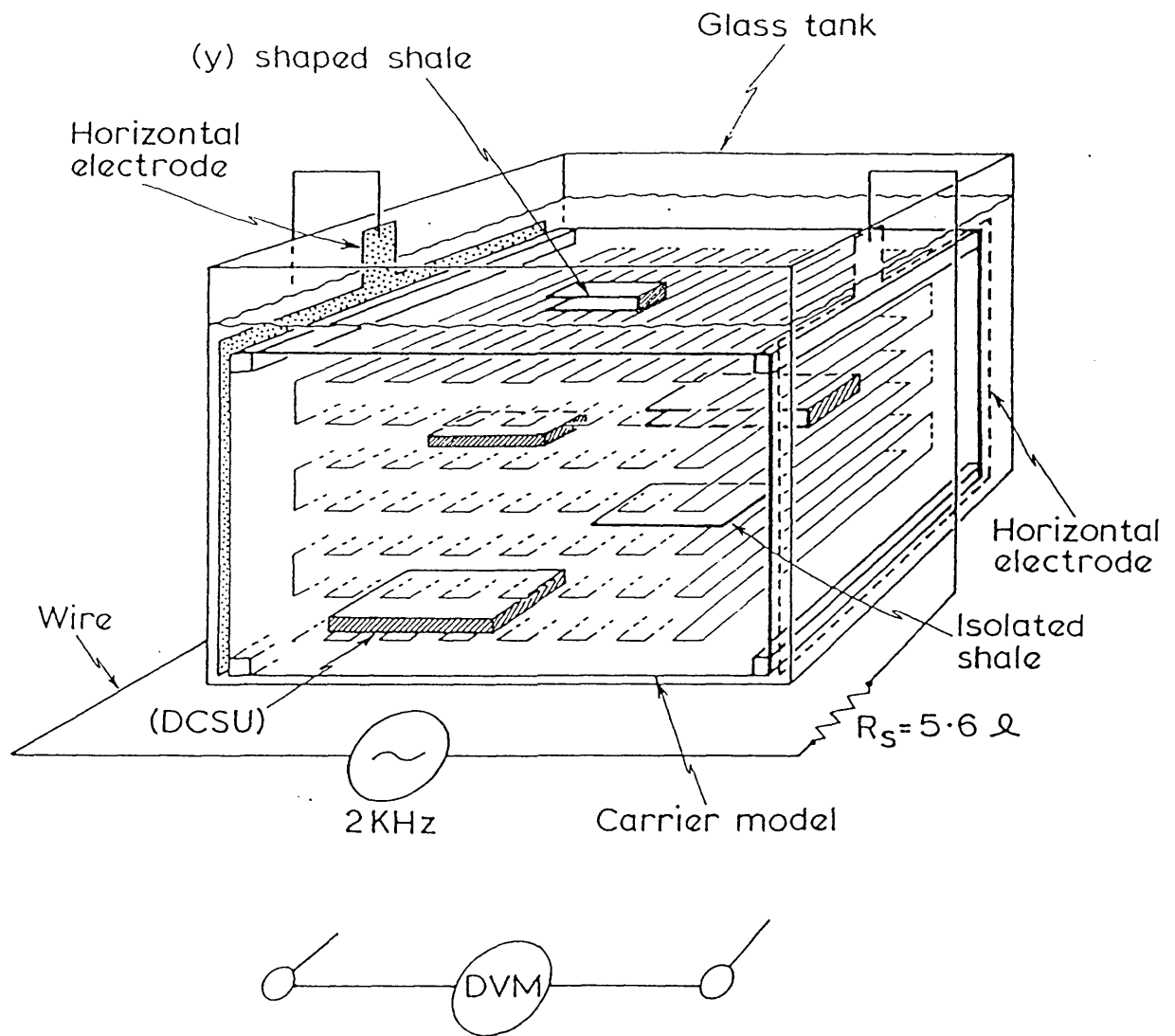


Fig. 4.1 Diagram of the experiment (set-up for measuring the horizontal permeability)

1/16 inch thick Perspex sheets				
No.	Dimensions, cm	Dim. ft	Volume cu.ft.	Vol. of U shapes
1	12*8	150*100	7500	15977
2	16*10	200*125	12500	26221
3	20*12	250*150	18750	38965
4	8*5.5	100*70	3500	7672
5	5*3	65*40	1300	
NO.	3/4 inch thick perspex sheets			
1	20*12	250*150	223242	—
2	16*10	200*125	148828	—
3	12*10	150*100	89297	—
4	24*16	300*200	357187	—

Table 4.2 Scaling of the perspex sheets

Thin stainless steel electrodes are used for measurements of the system's resistivity. These are thin sheets of 24 gauge thickness. The electrodes used for horizontal measurements are 26 cm long 17 cm wide while those used for vertical measurements are 26 cm wide and 38 cm long. A small clearance is left to facilitate fitting the electrodes inside the tank.

A resistance (5.6Ω) is connected in series with the system to help in calculation of the electric current and hence the resistance of the system in the glass tank.

An oscillator (frequency generator) was used to induce alternating electric current through the circuit with a frequency of 2 KHz. The voltage across the whole circuit is kept between zero and one volt.

A digital voltmeter (DVM) with an accuracy of 0.01 MV is used for reading the voltage drop across the system in the tank (between the electrodes) and that across the 5.6Ω resistance. See *Figure 4.1*.

4.3 DESCRIPTION OF THE EXPERIMENT

Two sets of experiments were performed. The first one using brine with a concentration of 10 grams/litre and the second one with a concentration of 5 grams/litre. The repetition with different concentrations is meant to investigate their effect on the results.

The shale frequency (Perspex frequency), shale fraction, and volume fraction occupied by the discontinuous sand units are shown on table 4.3. Six runs for each set were done increasing the shale frequency from 2 sh/100 ft to 12 sh/100 ft. Shale frequencies higher than that are very unlikely to be handled by the carrying model (Heavy weight of perspex).

Run No.	Shale frequency Sh/100 ft	Fractional shale Thickness	Vol. of DCSUs (Fraction)
1	12	0.06	0.23
2	10	0.05	0.18
3	8	0.04	0.115
4	6	0.03	0.075
5	4	0.02	0.00
6	2	0.01	0.00

Table 4.3 Description of the run parameters

4.3.1 CALCULATION OF THE NUMBER OF SHALES AND DCSU's

The fraction of sand occupied by the DCSUs is read from *Figure 3.4* which is presented by Zeito (110). The dimensions of the DCSUs are chosen randomly from table (4.1) and their volume is summed up to meet approximately the volume fraction corresponding to the shale frequency.

After calculation of the number of DCSUs, the volume of shales used for their coating is calculated. Knowing the total volume fraction of shale, (hence the shale's volume), the volume of shales yet to be calculated could be found. The number of the isolated shales; the Y-shaped shales and the lenticular shaped (DCSU) shales

is calculated assuming that 66% of shales converge upon each other (110). The dimensions of the shales used from each type were chosen randomly from table 4.2. The volume fraction of shales should meet the thickness fraction of the shales encountered by the well.

4.3.2 ARRANGEMENT OF THE EQUIPMENTS AND MEASUREMENT PROCEDURE

The two sets of electrodes (horizontal and vertical) are connected in series with the resistance in the electric circuit, *Figure 4.2*. The voltage across the tank (which is containing the carrier model) is measured by the (DVM) and denoted by (V1). The voltage across the resistance is denoted by (V2). Then the resistivity of the system inside the tank is calculated by means of Ohms Law:

$$V = I.R \quad (4.1)$$

where,

V = Voltage difference (milli-volt, mV)

I = Electric current (milli-ampere, mA)

R = Resistance, $m\Omega$.

$$RI = \frac{RA}{L} \quad (4.2)$$

where,

RI = Resistivity, Ωcm

A = Cross-sectional area, cm^2 .

L = Length of conductor, cm.

Knowing the value of the used resistance (5.6Ω) and the voltage drop across it, the current could be calculated using Eq.(4.1). Hence, the resistance of the system is calculated.

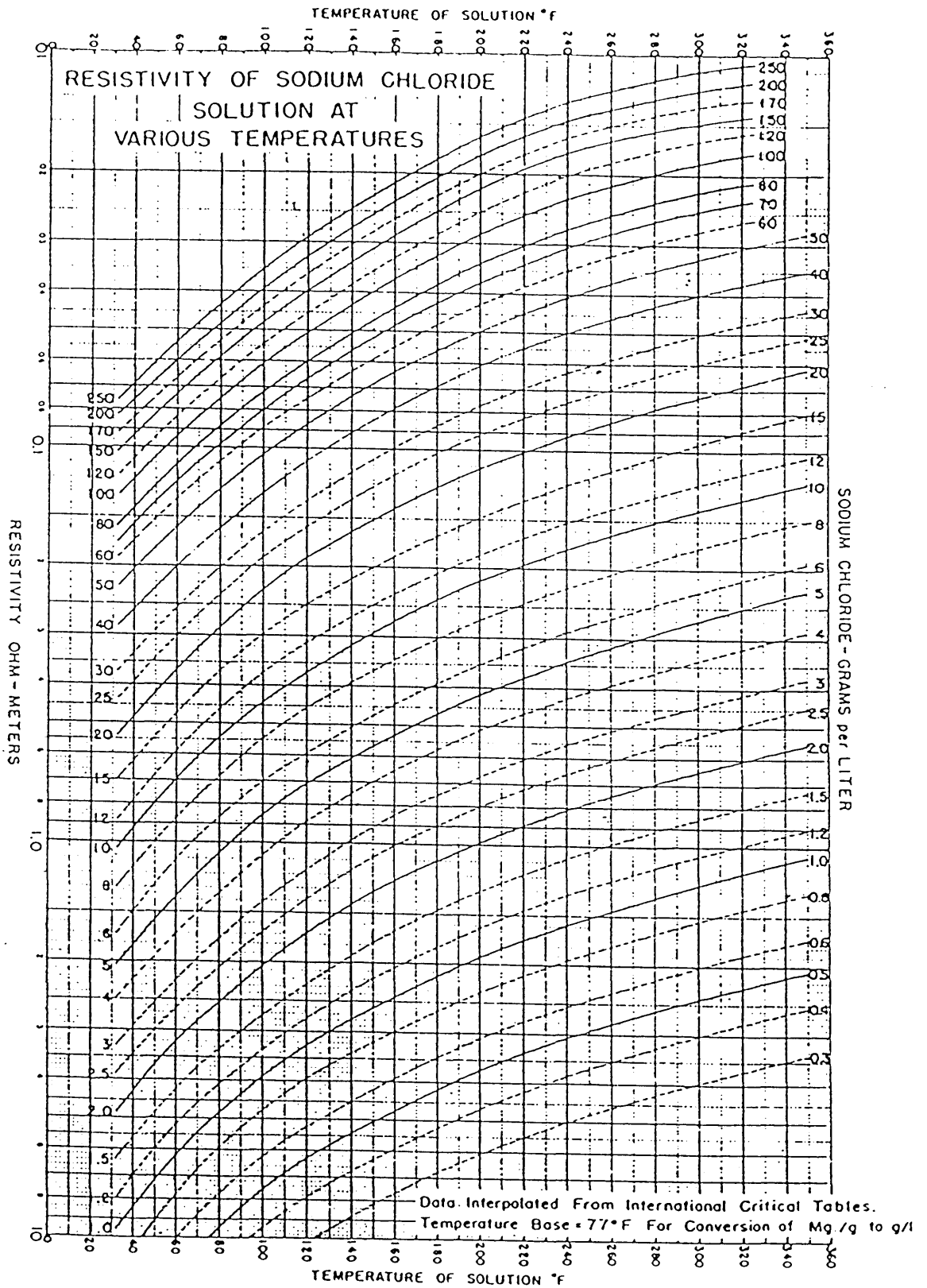
For calculation of the cross-sectional area, the inner dimensions of the tank (Dimensions of the system) are used.

Length = 38.5 cm

Breadth = 26 cm (accounting for the screened sheets)

Height = 16 cm (height of the system)

Figure 42 Brine resistivity as a function of temperature.



4.3.3 CALIBRATION

The resistivities of brines at room temperature for both concentrations is found from *Figure 4.2* as follows:-

Room temperature = 60 Degree Fahrenheit

Brine Resistivity (10 gms/litre) = 70 Ω cm

Brine Resistivity (5 gms/litre) = 137.85 Ω cm

Since the carrier model will be used for all measurements, brine resistivity with the carrier is to be used in the calculation instead of pure brine resistivities.

4.3.3.1 Calculation of the Model Resistivities

First, calculation for brine concentration of 5 gm/litre :-

[A] - Vertical Resistivity :

V1 = 64.2 mV (Voltage across the tank)

V2 = 155.9 mV (Voltage across the standard resistance RS)

Therefore,

I = 27.84 (V2/5.6 Ω) mA (electric current)

R = 2.348 Ω (The resistance in the tank)

RIV = 2.348 x 26 x 38.5 / 16 Ω .cm

RIV = 146.9 Ω cm (vertical resistivity)

[B] - Horizontal resistivity :

V1 = 287.4 mV.

V2 = 135.7 mV.

Therefore,

I = 24.232 mA.

R = 11.86 Ω

RIH = 128.15 Ω cm (Horizontal resistivity)

Second, calculation of 10 gms/litre :-

[i] - Vertical resistivity:

V1 = 33.33 mV.

V2 = 137.38 mV.

I = 24.532 mA.

R = 1.3586 Ω cm

[ii] - Horizontal resistivity:

$$V1 = 155.47 \text{ mV.}$$

$$V2 = 126.00 \text{ mV.}$$

$$I = 22.5 \text{ mA.}$$

$$R = 6.91 \Omega$$

$$RIH = 74.66 \Omega\text{cm}$$

4.3.3.2 EFFECT OF THE CLEARANCE ON THE RESULTS

(Clearance Between the Tank and Model)

Two sheets of perspex 0.5 cm thick cut to the cross-sectional areas of the model (horizontal and vertical cross-sectional areas) were used to block the model and simulate zero permeabilities. The resultant resistance was considered as the resistance of the system without barriers plus the resistance of the clearance. Since the resistance without barriers is known from above, the resistance of the clearance (0.5 cm long) can be calculated and extrapolated to find the resistance of a clearance having the length or height of the model. This simulates the resistivities of the system with a block of perspex (26x16x38.5 cm) which matches the experimental zero conductivity.

EFFECT OF THE CLEARANCE ON VERTICAL RESISTIVITY MEASUREMENTS.

$$V1 = 276.96 \text{ mV.}$$

$$V2 = 137.00 \text{ mV.}$$

$$I = 24.464 \text{ mA.}$$

$$\text{Therefore, } R1 = 10.953 \Omega$$

$$\text{Clearance Resistance} = \text{Total res.} - \text{Brine Res. (with the model)}$$

$$\text{Clearance Resistance} = 10.953 - 2.306 \Omega$$

$$\text{Res. of 0.5 cm clearance} = 8.647 \Omega$$

$$\text{Total Resistance} = 8.647 \times 16 / 0.5 \Omega$$

$$\text{Total Resistance} = 276.7 \Omega$$

$$\text{Clearance resistivity} = 276.7 \times 26 \times 38.5 / 16.5 \Omega$$

$$\text{Clea. Resistivity} = 16786.71 \Omega$$

Therefore,

Brine clearance resistivity ratio(BCRR) = $146.9 / 16786.71 \Omega\text{cm}$

BCRR = $0.0087 \Omega\text{cm}$

Therefore, the zero for the vertical permeability ratios will be 0.0086 which obviously have no effect on the calculation results.

EFFECT OF THE CLEARANCE ON HORIZONTAL RESISTIVITY MEASUREMENTS

$V_1 = 648.2 \text{ mV}$.

$V_2 = 101.3 \text{ mV}$.

$I = 18.09 \text{ mA}$.

$R_1 = 35.833 \Omega$

Clearance R = $35.833 - 11.86 \Omega$

Clearance R = 23.973Ω

Total resistance = $23.973 \times 38.5 / 0.5 = 1845.921 \Omega$

Total resistance = 1845Ω

Clearance resistivity = $1845.921 \times 26 \times 16 / 38.5 \Omega\text{cm}$

Clea. resistivity = $19945.54 \Omega\text{cm}$

Therefore,

brine/clearance resistivity = 0.0064

Therefore the zero for the horizontal permeability ratios will be 0.0064.

4.4 RESISTIVITY CALCULATION (WITH BARRIERS)

4.4.1 CALCULATION OF THE VERTICAL RESISTIVITIES

The calculated number and type of perspex sheets are distributed randomly in the carrier model. The bottom sheet electrode is then submerged to rest on the bottom of the tank with its plastic coated extensions sticking out of brine along the tanks walls. The carrier model - with its sheets - is then submerged to land on the bottom electrode followed by the top sheet electrode.

The voltages across the tank and the standard resistance are measured, and the vertical resistivity is calculated using eq.(4.2). The true vertical resistivity is calculated by the following procedure:-

For (5 gm NaCl/litre):

At 60 degrees fahrenheit the brine resistivity is 137.85 Ωcm (from standard charts). Therefore the corresponding vertical resistance of brine in the tank is calculated using equation (4.2) as shown below.

$$\begin{aligned} \text{Resistance} &= 137.85 * 16 / (38.5 * 26.5) \\ &= 2.162\Omega \end{aligned}$$

Since brine vertical resistance (with the model) is 2.348 Ω , then, for a system resistance (with perspex sheets) of 5.8 Ω , the increase of resistance caused by the perspex sheets is (5.8 - 2.348) Ω .

Since the (vertical/horizontal) scale of the model is 4:1, then, the real increase in resistance cause by the sheets is given by, RIN,

$$RIN = 4(5.8 - 2.348) \tag{4.3}$$

The total resistance of the system equals RIN plus resistance of brine in the tank.

Therefore,

$$\begin{aligned} \text{Totalresistance} &= 4(5.8 - 2.348) + 2.162\Omega \\ &= 15.97\Omega \end{aligned}$$

The vertical resistivity is then calculated using equation (4.2) to give,

$$\begin{aligned} \text{Resistivity} &= 15.97 * 26 * 38.5 / 16\Omega\text{cm} \\ &= 999.12\Omega\text{cm} \end{aligned}$$

4.4.2 CALCULATION OF THE HORIZONTAL RESISTIVITIES

After calculating the vertical resistivity the carrier model is taken out to remove the bottom electrode and then re-submerged. The level of brine is kept just covering the model (16 cm) for horizontal resistivity calculations. The horizontal electrodes are slid along the inner walls of the tank and kept apart at a distance of 38.5 cm. The horizontal electrodes are connected to the circuit by the same way as shown in *Figure 4.1*, and the voltage measurements are taken for the resistance and the tank. The horizontal resistivity is then calculated in the same way as the vertical permeabilities.

4.4.3 ACCOUNTING FOR THE DISTRIBUTION EFFECT

To account for the effect of changing the distribution of the perspex sheets on the results the above measurements are repeated three times rearranging the perspex sheets each time. The average value of the three results is retained as the most correct value for that run. The differences between the runs with changed sheet locations were very small. This fulfils the assumption of random shale distribution.

Having done the first run, a new set of perspex sheets corresponding to another shale frequency is distributed in the model. The experiments are carried on to cover the whole sets indicated in table (4.3).

4.5 RESULTS AND DISCUSSIONS

Tables 4.4, 4.5 and 4.6 summarise the results from the two sets of experiments (5 gm NaCl/lit. and 10 gm /lit.). Figures (4.3),(4.4) and (4.5) represent the anisotropy (vertical conductivity to horizontal conductivity) versus shale frequency for set 1, set 2, and the average of set 1 and 2 respectively.

Fig. 4.3 Shale Frequency vs Anisotropy

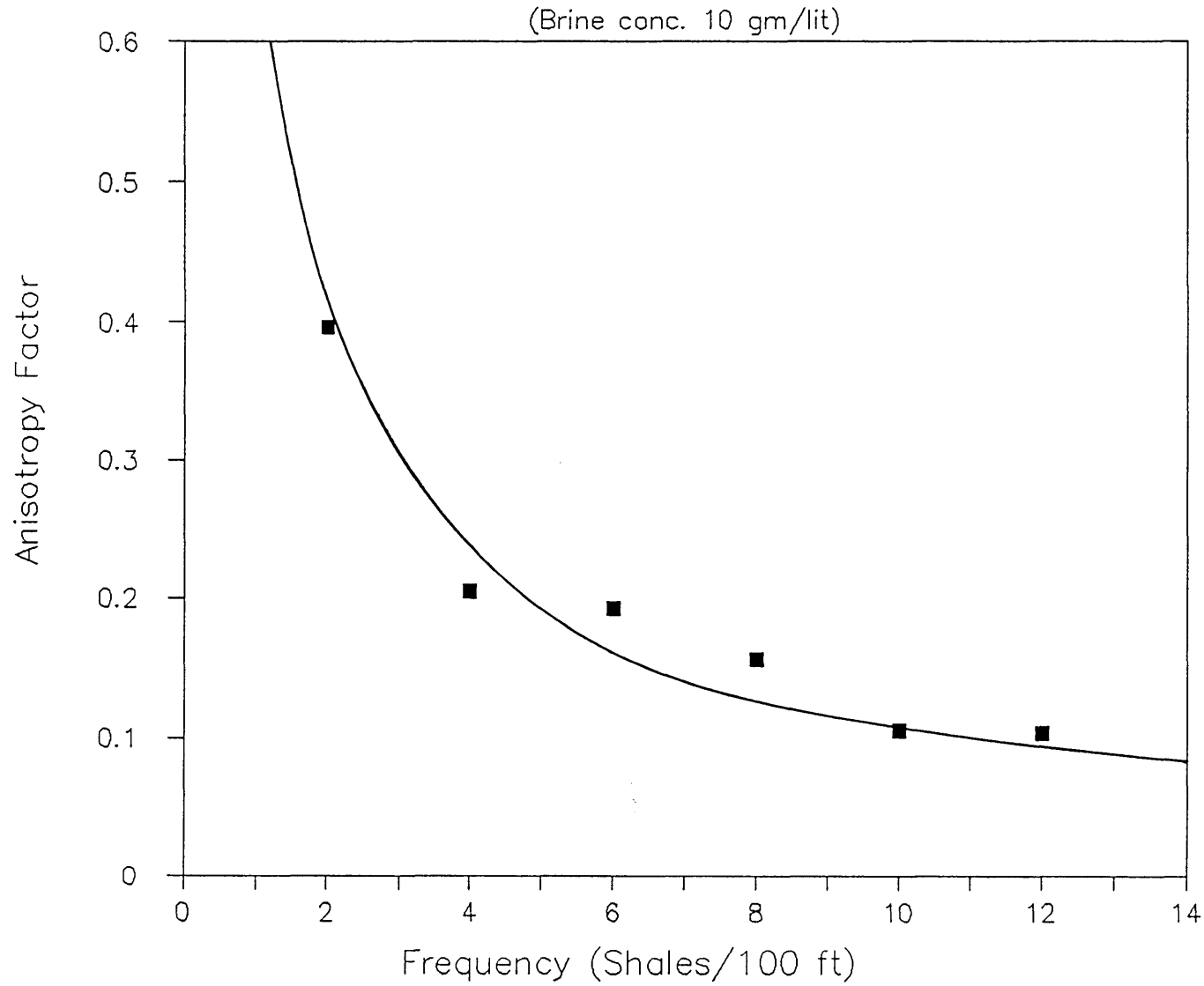
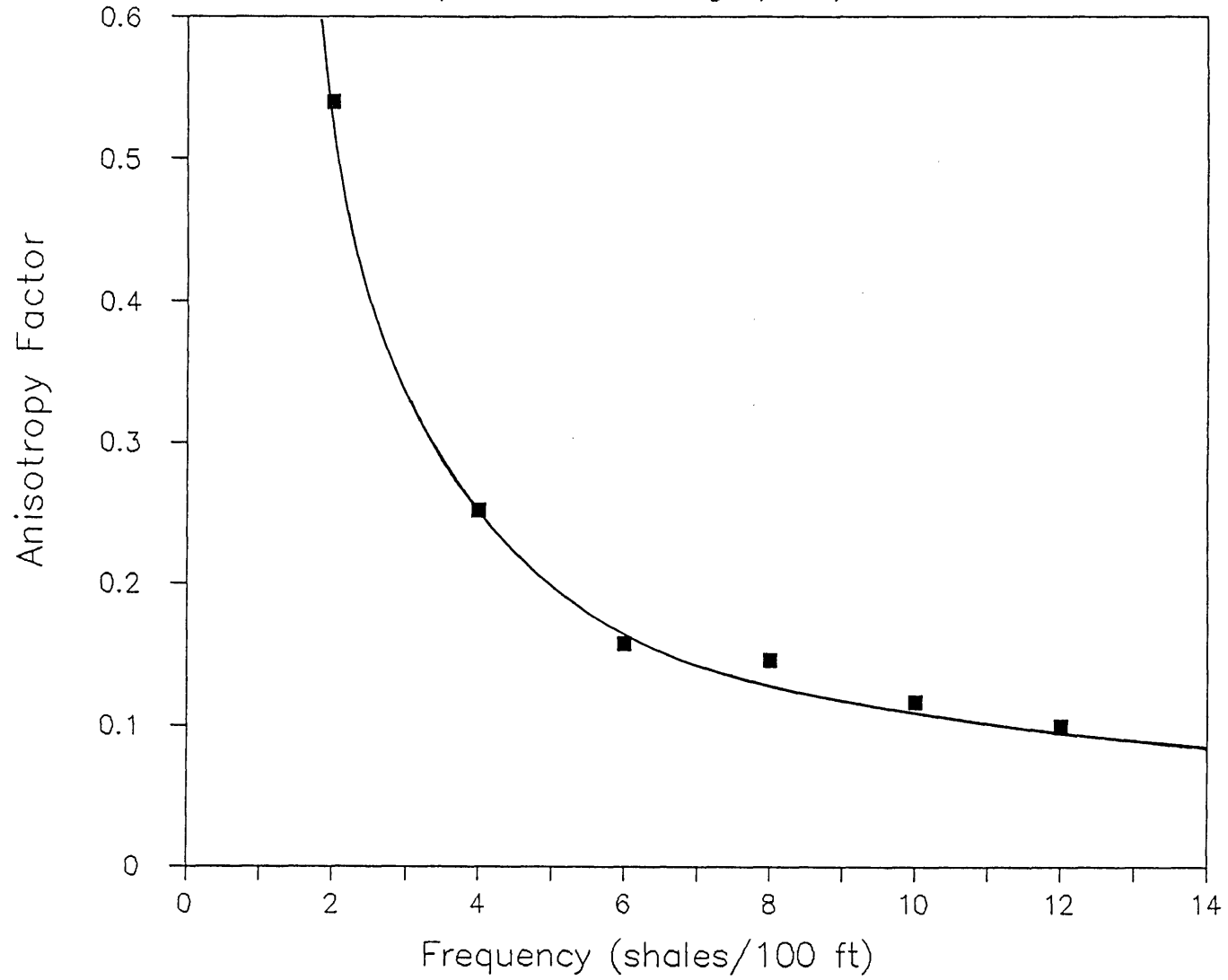


Fig. 4.4 Shale Frequency vs. Anisotropy
(Brine conc. 5 gm/lit)



Sh/100 ft	Vertical Resistivity	$\frac{Brine-Res.}{Ver.Res.}$	Horizontal Resistivity	$\frac{Brine-Res.}{Hor.Res.}$	Anisotropy column(3)/(5)
12	898.33	0.0757	105.44	0.711	0.1042
10	792.67	0.083	95.45	0.785	0.1057
8	509.04	0.1297	90.68	0.827	0.1568
6	380.74	0.1733	83.33	0.900	0.1926
4	369.84	0.203	75.95	0.9898	0.2051
2	146.47	0.396	74.95	1.000	0.396

Table 4.4 Measured resistivities for different barrier frequencies (10 gm/lit.)

Sh/100 ft	Vertical Resistivity	$\frac{Brine-Res.}{Ver.Res.}$	Horizontal Resistivity	$\frac{Brine-Res.}{Hor.Res.}$	Anisotropy column(3)/(5)
12	1794.5	0.067	190.05	0.669	0.1001
10	1398.13	0.0858	173.34	0.734	0.1169
8	994.61	0.1206	155.17	0.819	0.1472
6	824.16	0.146	145.48	0.874	0.1587
4	494.2	0.243	131.78	0.965	0.2518
2	227.39	0.528	130.01	0.978	0.540

Table 4.5 Measured resistivities for different barrier frequencies (5 gm/lit.)

Shales/100 ft	$\frac{Av.K_{vc}}{K_{sand}}$	$\frac{Av.K_{hc}}{K_{sand}}$	Av. anisotropy
12	0.00714	0.69	0.1022
10	0.884	0.76	0.1113
8	0.1252	0.823	0.152
6	0.1595	0.887	0.176
4	0.223	0.977	0.226
2	0.462	0.989	0.468

Table 4.6 Calculation of the average permeability anisotropy

Fig. 4.5 Average permeability versus shale frequency

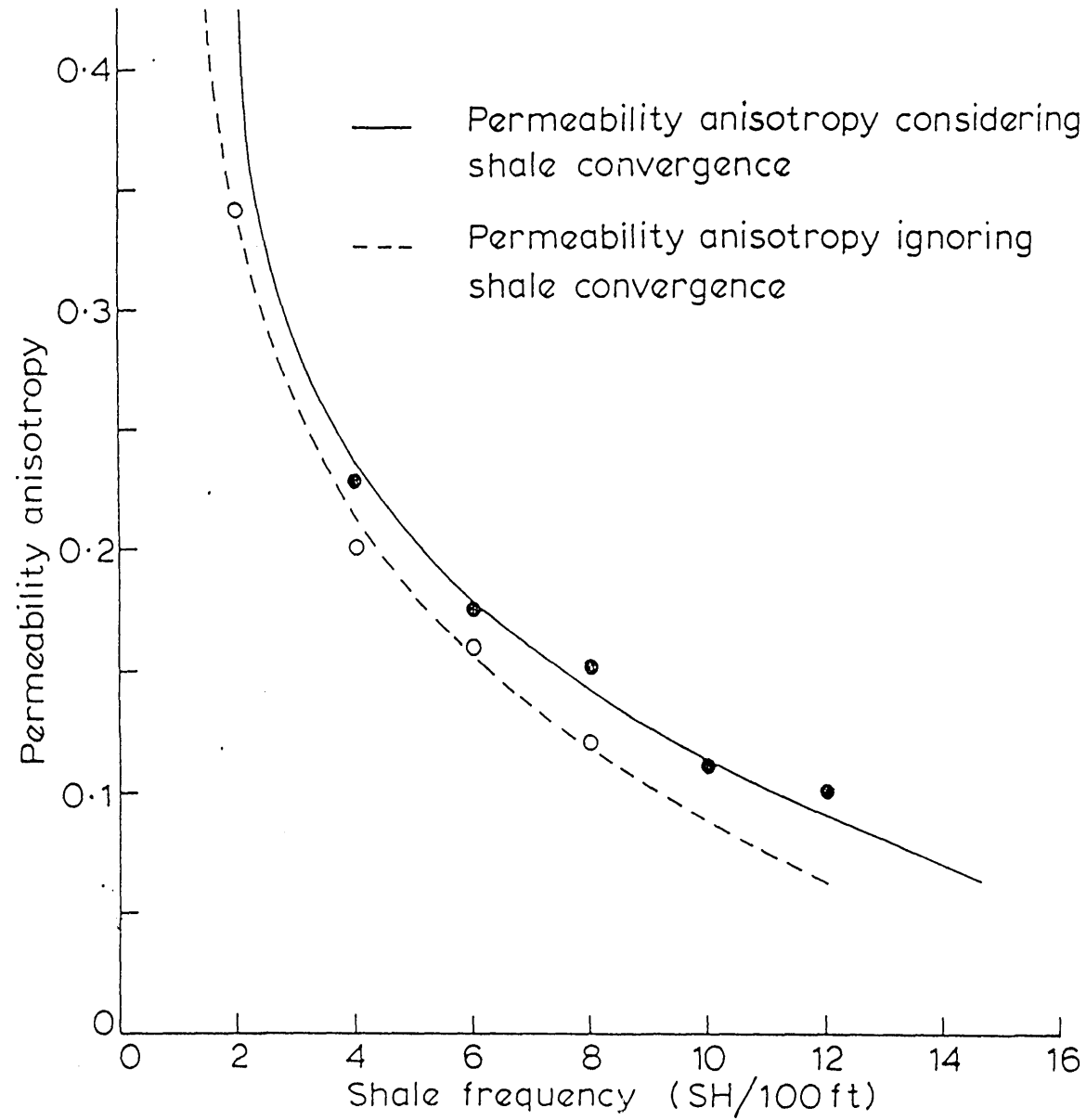


Fig. 4.6 Permeability results vs shale

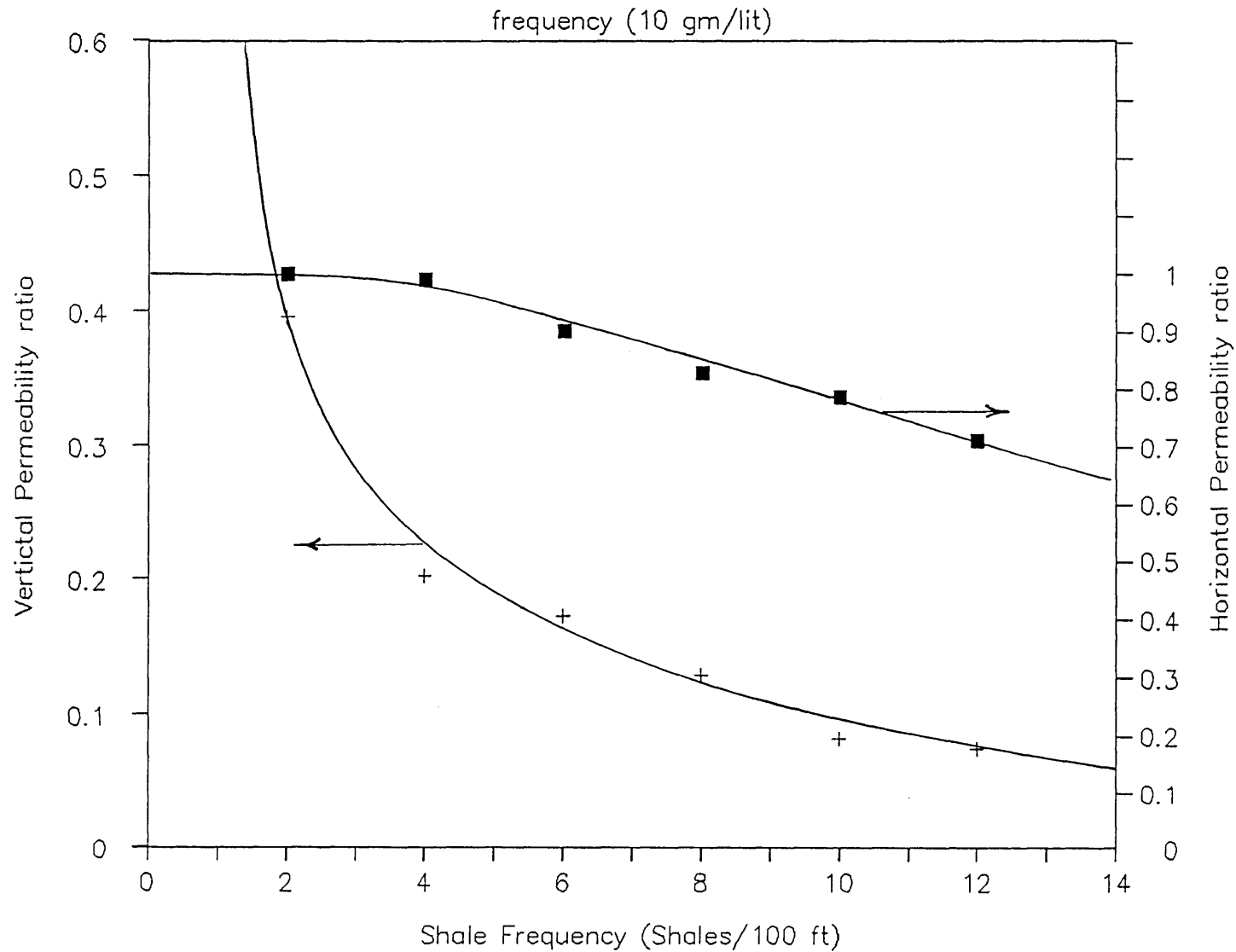
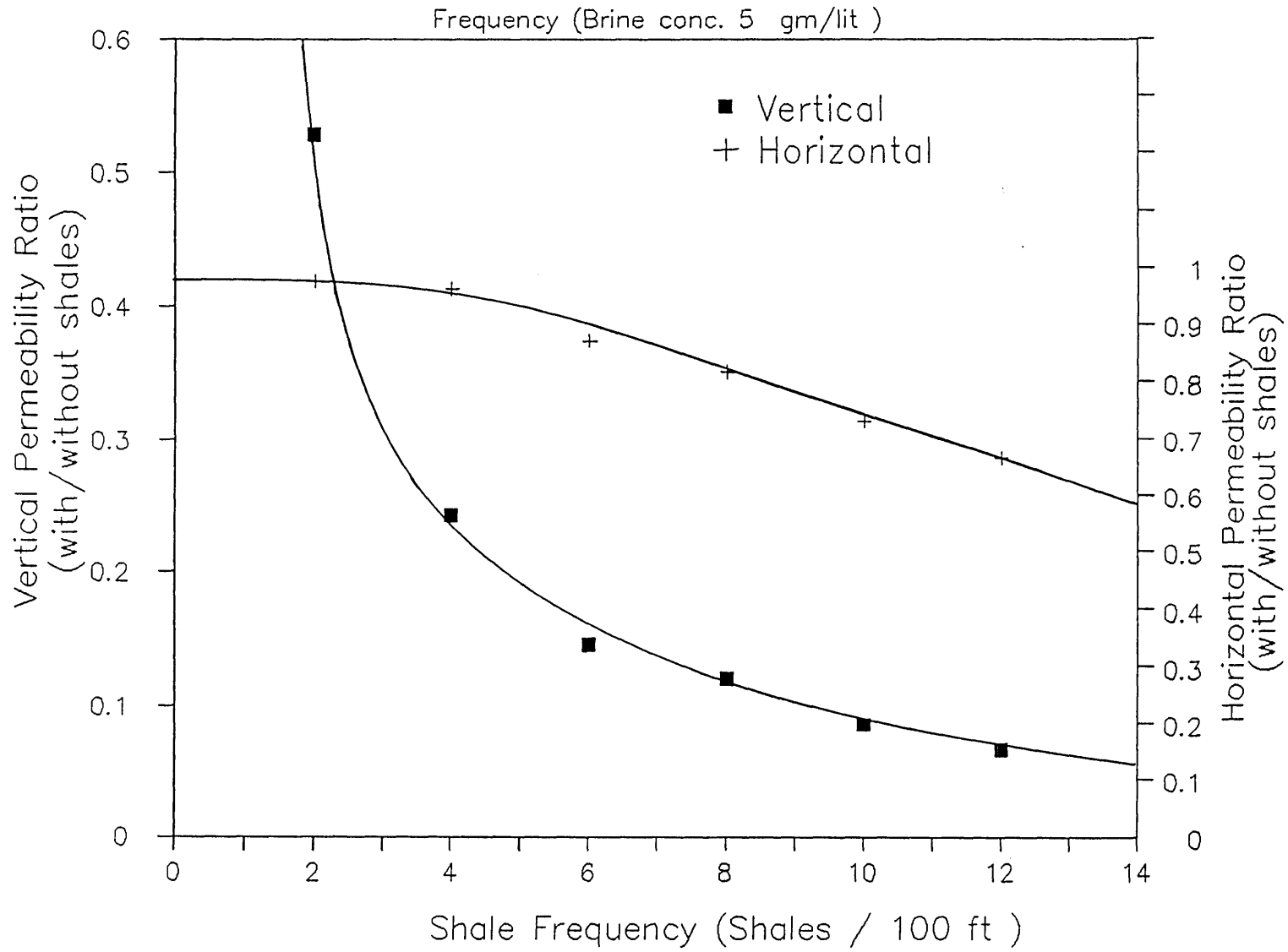


Fig. 4.7 Permeability results vs Shale



The dotted line on *Figure 4.5* represents the results for the statistical streamtube method (7, 8). Figures 4.6 and 4.7 are plots of the ratios of vertical and horizontal effective permeabilities to pure sand permeability versus shale frequency using two concentrations. *Figure 4.8* represents the arithmetic average of the values plotted in figures 4.6 and 4.7.

From *Figure 4.5* and *Figure 4.8* (the averages) we can notice that, at first a small frequency of shale will produce a considerable amount of vertical permeability reduction although it does not seriously affect the horizontal permeability. This is manifested by abrupt reduction of the anisotropy factor between 0.0 and 6.0 sh/100ft in *Figure 4.5*.

When the shale frequency further increases, the shales begin to converge with an intensity high enough to create DCSUs. The resulting sand compartmentalization is offset by a decrease in the tortuosity of the paths followed by the streamtubes (the number of barriers encountered by the streamtube becomes smaller). The overall outcome of these phenomena is reduction of the rate of decrease of the anisotropy factor (vertical k). This is manifested by the low inclination of the portion of the curve in *Figure 4.5* between 6 and 12 sh/100 ft.

Negligible reductions are observed on the horizontal permeability between 0.0 and 6 shales/100 ft, beyond that range a steady decrease of permeability is observed. The rate of decrease (above 6 shale/100 ft) is almost linear, and both curves (horizontal and vertical ratios) become almost linear and parallel. At low shale frequency no DCSU's exist, therefore the reduction of permeability is minute and is mainly due to loss of brine volume displaced by perspex (the cross-sectional area of the perspex sheets is negligible compared with that of the model (16 cm x 26 cm)).

Further increase of shale frequency creates DCSU's that have bigger cross-sectional areas as well as volume. Therefore an appreciable amount of permeability reduction is observed.

4.6 VERIFICATION OF THE STREAMTUBE METHOD (17,62)

Comparison between results from the streamtube method and results from the experiment on conductive paper done by Dupuy and LeFebure (29) showed reasonable agreement. The comparison was done for only one model with spe-

cific characteristics on two dimensional basis. But outcrop studies (61, 76, 87, 97, 104, 110) showed the shales to be elongated with the long axis more or less parallel to the direction of flow (channels). To examine the effect of variation of shale dimensions – in different directions – on effective permeability results, three dimensional calculations are necessary. Also, since the path of the streamtube around the shales follows the shortest way, consideration of the third dimension may provide a shorter option (path) for the streamtube. Therefore, 3-D calculation of effective vertical permeability are expected to produce higher values than the 2-D calculations.

For the sake of comparison of the experimental results using the statistical streamtube model (7, 8, 41) and the model considering shale convergence using a wider range of shale frequencies, four experiments were done using frequencies of 2, 4, 6, and 8 shales per 100 ft, table 4.7.

The shale length distribution, shale thickness, and shale frequencies were the same as the last four runs of table (4.3).

The perspex sheets used were all plain sheets (no U-shapes or DCSUs). The measurements of the resistivities were done by the same way as for the runs of table (4.3) and the results are summarised in table (4.8). The results are also plotted on figs.(4.5) and (4.8) (Broken lines).

Run No.	Shales/100 ft	Shale thickness fraction
1	2	0.01
2	4	0.02
3	6	0.03
4	8	0.04

Table 4.7 Description of the parameters for runs ignoring shale convergence

Shales/100 foot	Vertical Resistivity	Brine Res./ Ver. Res.	Horizontal Resistivity	Brine Res./ Hori. Res.	Anisotropy Column (3)/(5)
8	1192.3	0.1156	134.03	0.956	0.121
6	876.7	0.1576	132.05	0.970	0.162
4	690.58	0.1996	128.83	0.995	0.201
2	404.15	0.341	128.25	0.997	0.342

Table 4.8 Calculation of the anisotropy factor (ignoring shale convergence)

4.7 DISCUSSION OF THE RESULTS OF THE STREAMTUBE METHOD

Examination of *Figure 4.5* and *Figure 4.8* immediately reveals that the vertical permeability is not a linear function of shale frequency. The curve flattens out to give permeability values higher than one should expect from linear trends at high shale frequencies. The great discrepancy observed between the experimental vertical permeability results (shown in *Figure 4.8*) and the linear trend is due to the following reasons:

- * At high shale frequencies, the streamtubes can by-pass several flow-barriers at one step - as it travels horizontally - due to the existence of a long barrier which may shadow several smaller ones.
- * The statistical streamtube method was validated only for two dimensional cases (78) which may lead to erroneous results, because in reality, the flow barriers dimensions can show variation in three dimensions. Under these circumstances it is possible for the third dimension to provide the shortest path, resulting in high permeabilities.
- * The statistical streamtube method assumes that the horizontal distance travelled along the barriers to be a random fraction of the whole length or width, whereas the most sensible value is a random fraction of half the length or width (as the streamtube follows the direction of the least resistance).

The outcome of the combined effect of the above reasons is divergence of the experimental results (simulating the statistical streamtube method) to give higher vertical permeability values at high shale frequencies.

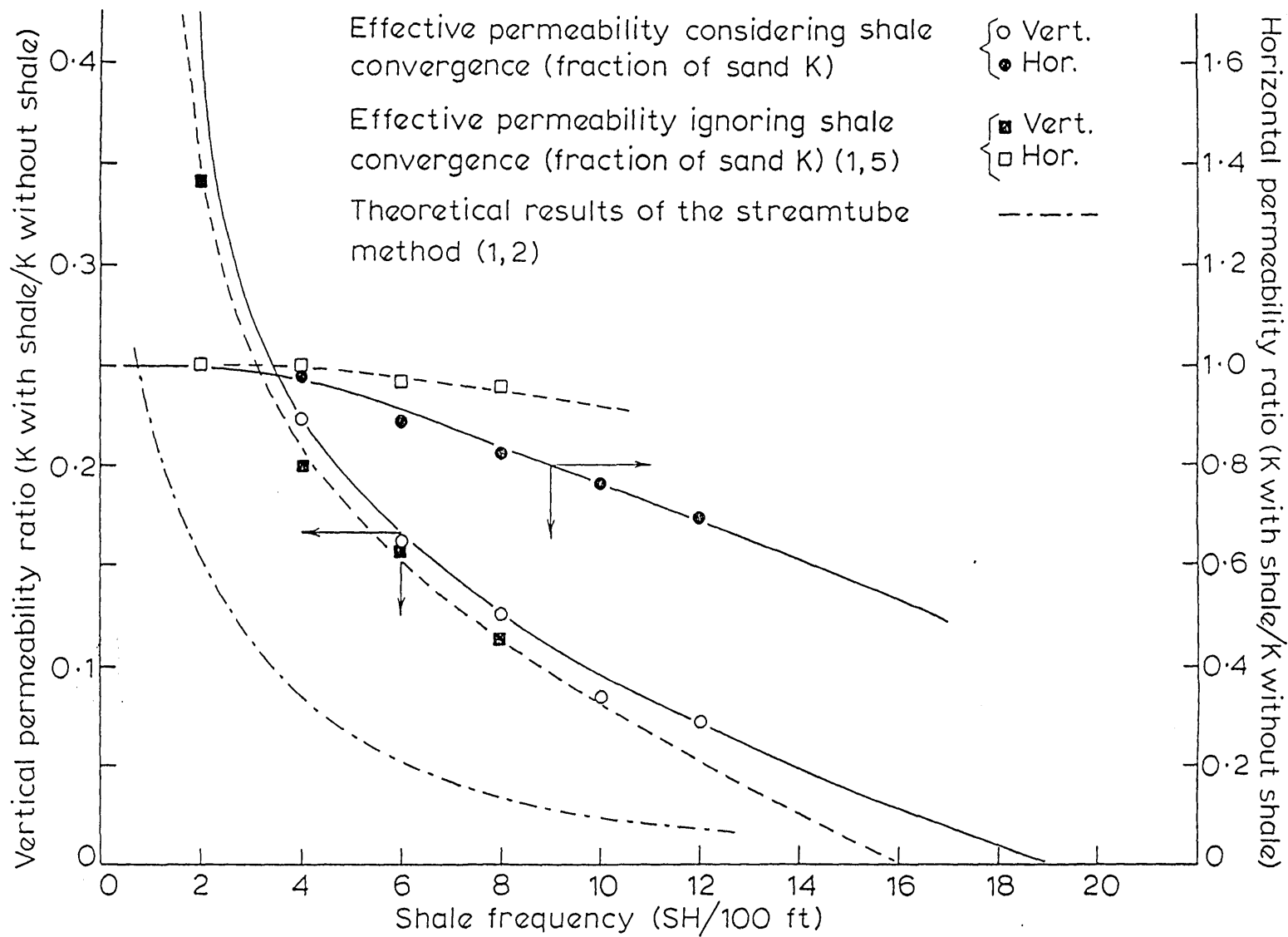


Fig. 4.8 Experimental results of permeability ratio vs shale frequency

4.8 COMPARISON OF THE EXPERIMENTAL RESULTS (WITH AND WITHOUT DCSUs)

4.8.1 At low shale frequencies (≤ 6 shales/100 ft):

Since the statistical streamtube method ignores the shale convergence phenomenon, it takes into consideration all the observed shale frequency, whereas the actual effective frequency is much lower. Due to the shale convergence phenomenon, the actual number of barriers met by the streamtube is 66% of the observed number (110). Therefore, the vertical permeabilities predicted by this method are lower than the actual.

As for horizontal permeabilities, the prediction technique presented by Halvorsen (41) yields similar results to the experiment considering shale convergence. This is due to the negligibly small increase of streamtube length caused by the transverse movements along the converging shales at these low frequencies.

4.8.2 At high shale frequencies (> 6 shales/100 ft)

In this case there is an increasing discrepancy between the statistical streamtube method and the case with DCSU's. In addition to the reasons stated above, the cumulative effect of shale convergence is also responsible for this discrepancy as it slows down the rate of decrease of the vertical permeabilities resulting in further divergence between the curves of the two methods as shown in *Figure 4.8*.

For horizontal permeabilities, the increase of shale frequency and the appearance of the DCSU's result in an increase of the length of the streamtube due to the transverse movements, and decrease of sand areas available for fluid flow. Therefore, the two curves (solid and broken lines) diverge and the model ignoring shale convergence gives very optimistic results.

4.9 SUMMARY

- 1 - A small amount of shale will considerably reduce the effective vertical permeability of the formations.
- 2 - At low shale frequencies (> 6 sh/100 ft) the effect of shale on the horizontal permeability is negligible.

- 3 - Shale convergence and sand compartmentalisation phenomena must be considered in the calculations of effective horizontal and vertical permeabilities. Due to these phenomena the rate of vertical permeability decrease is reduced as compared with the statistical streamtube method (41, 44, 61). The reduction is small at frequencies ≤ 6 sh/100 ft but may be considerable at greater frequencies.
- 4 - The permeability decrease with increase of shale frequency is linear only at shale frequencies higher than 6 sh/100 ft when the DCSUs begin to appear.
- 5 - The statistical streamtube method is very conservative and can estimate erroneously low permeabilities.
- 6 - Figure 4.5 is suitable for the calculation of anisotropy factor for different sand permeabilities in a fluvial environment.
- 7 - Haldorsen's method (41) for calculation of effective horizontal permeability (in presence of stochastic shales) is very optimistic and can estimate erroneously high values due to neglect of shale convergence phenomenon.
- 8 - Further efforts are needed to investigate the relation between shale frequency and the resulting sand compartmentalisation. For the time being the main source of data is ref. (110).

CHAPTER 5

EFFECT OF THE STOCHASTIC FAULTS ON RESERVOIR PERMEABILITIES

5.1 INTRODUCTION

Due to the resolution limitations of seismic techniques, faults with lengths smaller than the distance between seismic lines, or with very small throws are often not detected. Since the transmissibility across the formations is highly affected by the presence of faults, the distribution, geometry, and effect of these undetected faults on reservoir permeability must be evaluated before characterising and simulating the reservoir's performance. These short faults (stochastic faults) were modelled by Brand (11) in one of the very first studies in this area.

According to the number of faults met by 30 wells in a specific area, he used Monte Carlo techniques to find the expected number of stochastic faults for that area (to produce the same number of intersections by 30 vertical lines or wells).

Brand (11) investigated the effect of stochastic faults on transmissibility assuming the fault planes to create no restriction to flow if sands are juxtaposed across the fault.

However, in the presence of sand/shale sequence the observations on fault planes showed how different the situation is.

Model experiments (65) and outcrop studies (5) have indicated that the shear zones of normal faults in sand/shales sequences usually consist of smeared in laminae of shale and wedges of sands. Shi (89) designed a special ring-shear apparatus to study the development of shear zones under continuous shearing. A series of tests were done with sand/shale sequences under various simulated overburden pressures along a median slip plane.

The clay bands sheared-off in this fashion formed one continuous multi-layered clay gouge along the median slip plane of the shear zone. The clay gouge was somewhat contaminated with sand grains derived from boundary zones, but proved to be an effective seal to water flow when tested (65, 89).

Sandy materials between two different clay bands were found in the fault planes when two or more clay beds were sheared (65). If the fault throw is considerably big, the sand wedges out and two clay gouges on both sides amalgamate to form one continuous gouge.

Studies on the Niger delta faults in Nigeria (105) showed the fault zones to vary from less than one foot to about two feet. The continuity of the clay gouge was observed over about 400 metre of exposure. Clay gouge was always present whether shale beds were sheared-off by a minor shear or a major fault.

If the fault throw is large, and the shales are relatively thin, the clay gouge becomes very thin and may disappear at the central part of the fault plane.

The sealing capacity of the fault depends on the displacement pressure of the formation present in the fault zone (91, 92). If clay gouge is present, very high displacement pressures are needed to force oil into its very minute pores. Therefore, the trapping capacity of the faults is related directly to the amount of smeared shale in the shear zone.

For the case of stochastic faults, the pressure may balance around the faults because of their small throws and short lengths. Stochastic faults may result from tectonic movements as well as various other factors.

Differential loading is often caused by advancing deltas (advancing seaward) covering the fine grains in the deeper waters (80). This differential loading may lead to creation of growth faults in the deeper formation ahead. Uneven loading may also produce normal faults with the down thrown block to the sea direction.

Deformation of soft rocks may also occur as a result of faulting of the underlying formations (80). In this case, the resulting faults never show clean knife edge breaks. There is always a considerable amount of drag at the deformation plane.

5.2 FAULTS SHAPE AND GEOMETRY

According to the definition of the stochastic faults (short lengths and small throws), they can be considered as shallow detachments within the sedimentary pile (19). Depending on the way the faults were created, they may or may not have any linkage with the basement fault architecture. Compaction or overthrusting at

the toe of the fault must occur, otherwise basement extension is involved.

Studies on growth faults (22, 40, 78) indicated similar features to those described above without any linkage with the basement fault architecture. In response to differential sedimentation on a gravitationally unstable slope, growth faults usually occur both in continental and delta fringe deposits. Sedimentary growth across these faults may cause decompaction and back-stripping which may lead to reconstruction or balancing the section (89).

Ameen (15) studied - via an experimental rig - the faulting patterns in a layered cover of soft formations due to basement normal or reverse faulting. The layered cover was represented by wax layers and the basement was represented by pieces of wood. Faulting was simulated by movements of the wooden pieces and observations were noted from the deformation of the wax layers.

Different scales of faults were observed and basement extension of the faults was possible. Stochastic faults were also created and their orientations depend on the type of faulting underneath. They appeared as short traces in the vertical cross-section and the top surface of the model as shown in *Figure 5.1* (faults 3,4,5, and 6).

Detailed studies on the geometry and displacement variation of fault planes were conducted by Muraoka and Kamata (66), and Beach (5).

Muraoka and Kamata conducted their studies on minor faults in Japan. They demonstrated that the displacement variation along the fault traces depends on the type of formations faulted. In soft formations the displacement increases gradually from zero at the upper end of the trace towards its middle where it starts decreasing towards the bottom end of the trace. *Figure 5.2 a&b* demonstrates the throw variation along the fault trace from top to bottom in soft formations. In a sequence of soft and competent rocks, the displacement remains constant along the sections of competent rocks while it increases or decreases in the soft rock sections according to their position with respect to the midpoint of the fault trace.

The maximum displacement of a particular fault trace (at its midpoint) is greater when the trace is nearer to the central point of the fault plane (66). Therefore, fault planes can be approximated by elliptical shapes with zero displacement at both ends in the horizontal direction. *Figure 5.3(a)* shows a fault plane having

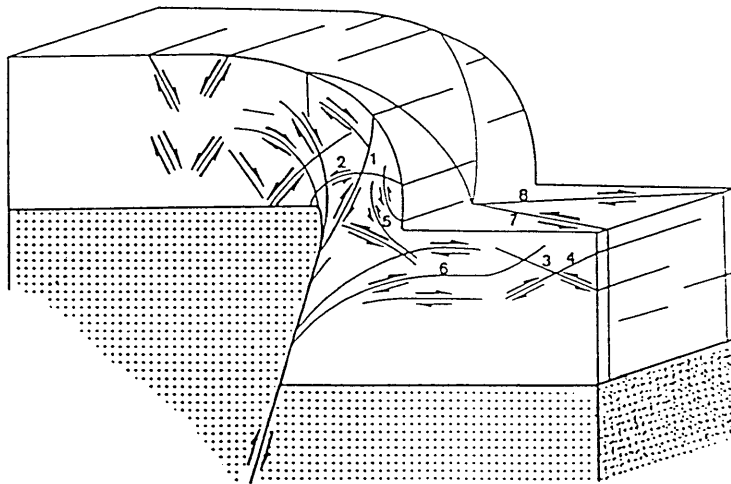
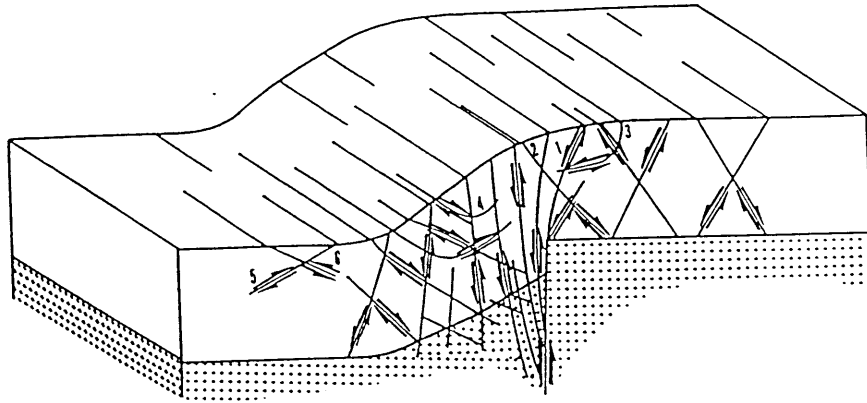
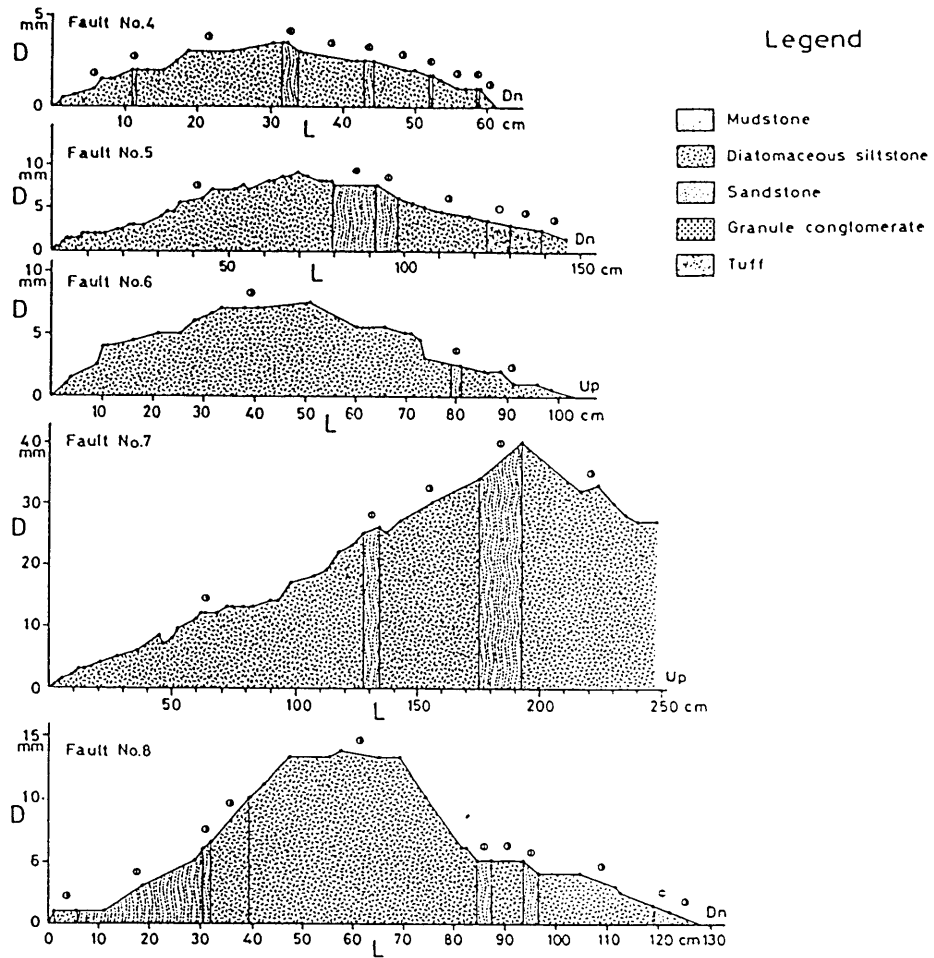


Fig. 5.1 Stochastic faults resulting from basement rock faulting (After ref. 4)



L = Distance from one end along a fault trace
 D = Displacement in the direction of dip separation

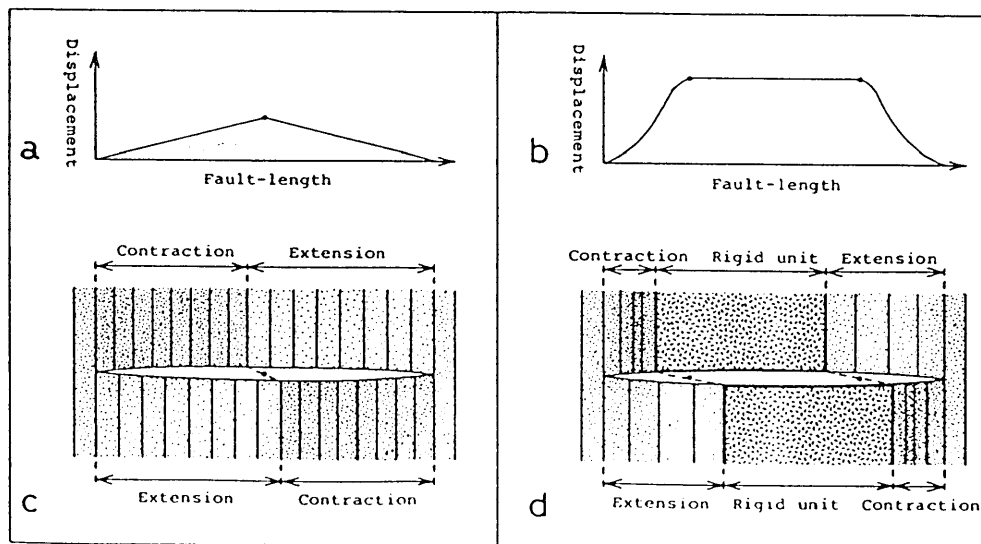


Fig. 5.2 Displacement variation along fault traces in different formations (After ref. 66)

an elliptical shape as discussed above. The cross-section in this figure coincides with the fault plane, therefore the distorted formations on one side of the fault plane (the hanging block) are shown. As demonstrated in *Figure 5.3(a)*, the soft formations on the upper part of the up-thrown side are compressed to have thinner thicknesses while those at the bottom of the plane are stretched to have bigger thicknesses. The reverse happens with the foot block where the lowest soft formations are compressed and the top layers are stretched to have a greater thickness as demonstrated in *Figure 5.3(b)*.

On both sides the competent layer is not affected by the compaction or stretching actions although slight deformation of the layer's profile may occur.

Fault planes can be approximated by ellipsoidal shapes (19) with zero displacements at both ends in the horizontal direction. Therefore, a relatively large decrease of vertical displacement happens near the ends of the plane and a gradual variation of displacement takes place at the central section.

Comparison between the minor fault's behaviour and major faults (San Andreas Fault) showed remarkable geometrical similarity (72). Therefore, stochastic faults (an intermediate scale) are expected to exhibit the same phenomena.

Kakimi (54) made a statistical study on minor faults in many areas subjected to tectonic activities. The observed number frequency of fault traces for each range of fault throws was presented in plots for many areas. The throws range from one centimetre to several metres. An equation relating the number of faults with a particular throw to the amount of throw was derived.

The number of faults with a throw between the values T , and $T + \Delta T$, is given by, N_T , where

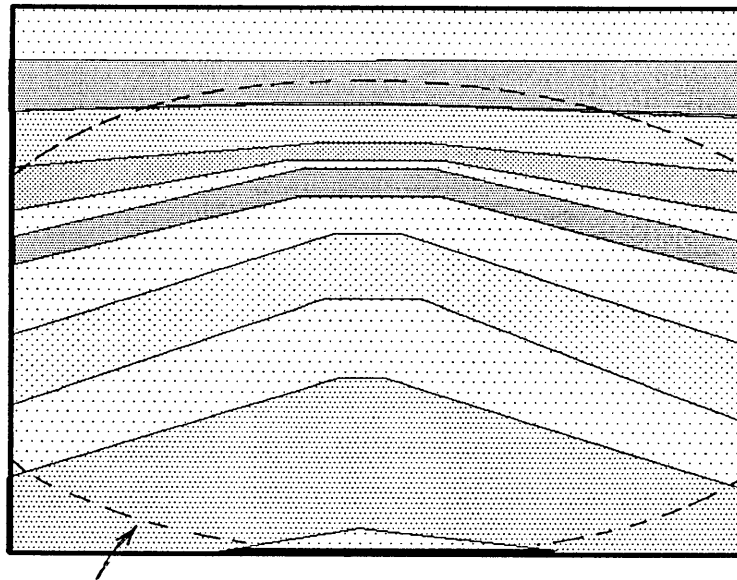
$$N_T = KT^{-m}\Delta T \quad (5.1)$$

m = constant, ranges between 1.54 – 1.95

K = constant, ranges between 3.5 – 5.33, depending on the area and faulting intensity, with an average value of 4.56.

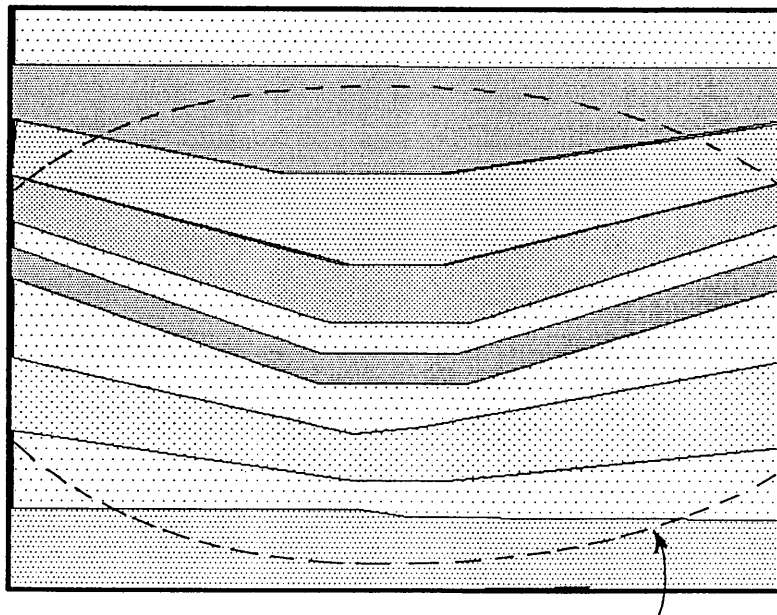
A relation between lengths and throws of fault traces was also presented (54,

Fig. 5.3(a) Deformation of the formations in the hanging block



Boundaries of the fault plane

Fig. 5. 3(b) Deformations of the formations in the foot bolck



Boundaries of the fault plane

72). The plot shown for those data showed different trends for soft and hard rock deformation. The throws were smaller in soft rocks because of their compactability, whereas the throws of the hard rocks were almost double those of the soft ones (for similar fault trace lengths).

The rate of displacement varies along the fault plane horizontally from end to end. It is rather smaller for long faults, therefore they reach their maximum gradually whereas the short ones almost jump to the maximum (54).

5.3 STOCHASTIC FAULT LENGTH AND THROW DISTRIBUTION

The maximum length of the stochastic faults existing in a certain area is governed by the spacing between the seismic lines (11). The closer the seismic lines, the shorter will be the lengths of these faults not detected by seismic techniques. Therefore, different triangular distribution parameters (maximum, minimum, most likely) are to be used depending on the density of the seismic lines or distances between them. (normally less than 500 ft).

Since fault planes tend to take an ellipsoidal shape with the shorter axis in the vertical direction, in extreme cases, short fault planes can be approximated by a circle. Therefore, the fault throw is always less than its length.

The data presented by Kakimi (54) on fault trace lengths are further treated, for the purpose of this project, to calculate the percentage of faults with traces shorter than specific values as shown in table 5.1. The results in table 5.1 are plotted in *Figure 5.4* and 5.5. In *Figure 5.4* the number of the faults in each throw category are plotted. From this figure we can find the median (most-likely) value of throw for the range of data in table 5.1. The minimum and maximum throws in this case are zero and 400 centimetre respectively. *Figure 5.5* is the continuity distribution function of the fault throws (CDF).

Considering these figures to reflect the general shape of throw distribution, similar curves can be generated for bigger maximum throws (bigger than 400 centimetre) by scaling up of the two figures. Consequently, the triangular distribution parameters can be deduced for a wider range of throws. For the purpose of this study, the maximum throw for stochastic faults in a field is calculated as follows:

Fig. 5.4 Histogram of fault throw frequency.

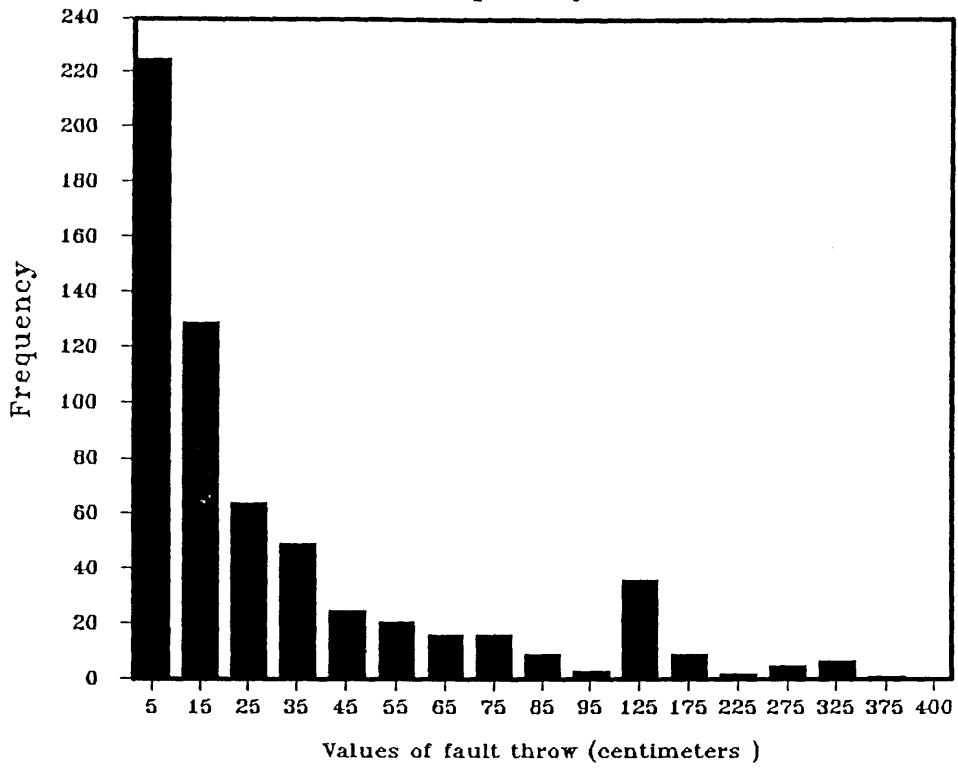
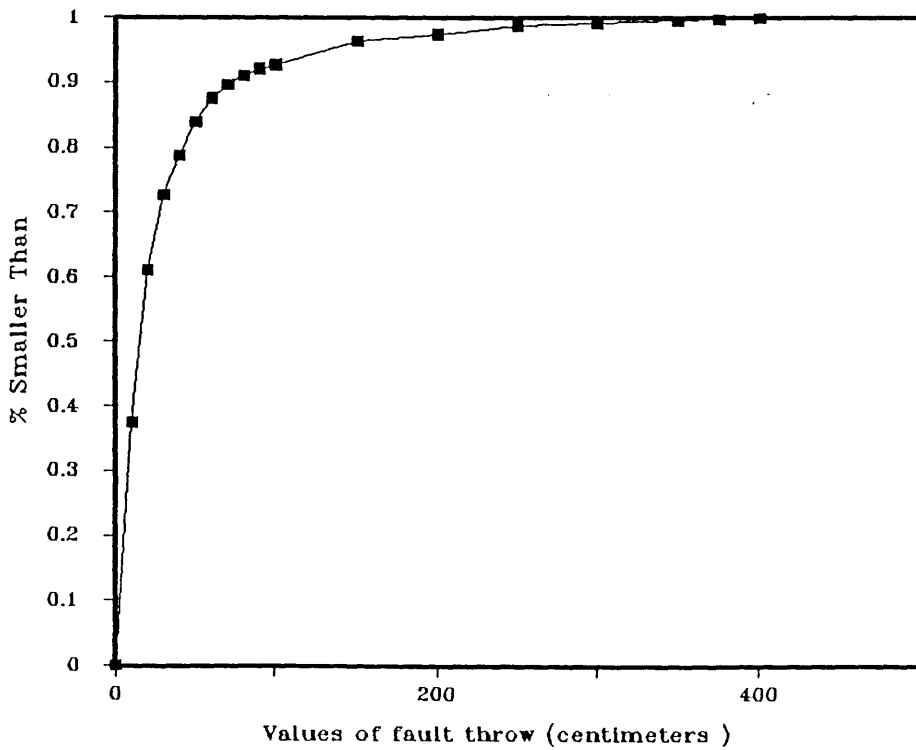


Fig. 5.5 Distribution function for Fault throws.



Let T_s equal the throw of the shortest fault detected by seismic techniques. Let L_s be the length of this fault.

If the distance between the seismic lines is denoted by D , then, the maximum throw for stochastic faults in the field, T_{max} , is given by

$$T_{max} = D * \frac{T_s}{L_s} \quad (5.2)$$

For the stochastic fault lengths, the maximum length is taken to be the distance between the seismic lines in the area. The minimum length is zero and the median length can either be an intermediate value between the maximum and minimum, or a median value derived from scaling-up of the *Figure 5.4* using the maximum and minimum fault lengths.

Throw range cm.	No. of faults	% of throws smaller Than
0 – 10	255	0.374
10 – 20	129	0.611
20 – 30	64	0.727
30 – 40	49	0.788
40 – 50	25	0.839
50 – 60	21	0.875
60 – 70	16	0.896
70 – 80	16	0.910
80 – 90	9	0.920
90 – 100	3	0.926
100 – 150	36	0.963
150 – 200	9	0.973
200 – 250	20	0.986
250 – 300	5	0.990
300 – 350	7	0.994
350 – 400	1	0.996
400 – 450	4	0.998

Table 5.1 Statistical data on fault throws

5.4 THE EFFECT OF STOCHASTIC FAULTS ON RESERVOIR PERMEABILITIES

From the previous sections we can infer that stochastic faults are shallow detachments within the sedimentary pile (19) that may be subjected to back stripping or balancing (in case of advancing deltas or continental deposits). Shales may smear on the fault planes transforming them into effective barriers which may increase the tortuosity of the liquid flow paths. In fluvial reservoirs, stochastic shales are randomly distributed in the reservoir sands. If these shales are encountered by a stochastic fault plane, the distribution and size of the resulting smeared areas within the fault plane depends on:

- 1 – The position of the shale with respect to the fault plane (horizontally): Due to the ellipsoidal shape of the fault planes, the displacement is high at the central part and zero at the edges.
- 2 – The value of the fault throw: Big throws create wider smeared areas. Two or more shales overlying each other may join their smeared areas or create a multi-layered gouge (65). Such a phenomenon may result in creating wider smeared areas with very high displacement pressure.
- 3 – The thickness of the shale breaks: Thick shales tend to smear wider areas than thin shales.
- 4 – The frequency of shales breaks: High shale frequency increases the probability of encountering shales by stochastic faults.

Evaluation of the effect of stochastic faults on reservoir permeabilities (in presence of stochastic shales) is extremely difficult. This is due to the complexity of the resulting horizontal permeability barriers (smeared planes) and the random distribution of stochastic faults.

Numerical evaluation of such effects may require thousands of fine grid blocks to simulate the individual variation of throw for each fault and the resulting smeared areas. Due to the big number of grids required, this method becomes impractical for such calculations.

An analytical method is presented below in an attempt to evaluate the effect of stochastic fault on averaged absolute (effective) horizontal permeability. In this method, the effect of stochastic shales on the reservoir permeabilities is treated separately – assuming the absence of stochastic faults – using the techniques presented in chapter 3. After calculating the effective permeabilities, the vertical barriers (fault planes) are introduced to the system and the effective permeabilities in the presence of stochastic faults are calculated. The calculations are performed in 3 stages as follows:

STAGE 1

For a specific area of the field the appropriate number of stochastic faults are generated and positioned. At this stage, the calculations closely follow the technique presented by Brand (11) using fault plane CDF as presented in section 5.3. The computations at this stage are done by the program (FAULT) listed in appendix 5.A at the end of this thesis.

At the end of this stage the areal co-ordinates of the faults and the values of their throws are listed in a result file.

STAGE 2

In the light of fault orientations, divide the area under consideration into coarse grid blocks (aligning their boundaries with major fault directions).

Divide the coarse blocks into fine grids similar to those in chapter 3 (see *Figure 3.19*).

Generate stochastic shales, calculate the effective permeabilities (using the techniques in chapter 3), and retain the co-ordinates of the shales in each block.

Using the co-ordinates of the stochastic faults calculated in stage 1 specify the faults encountering the coarse block.

Position the faults in the grid block adjusting the fault plane with the vertical layers of the fine grid blocks.

At this stage, the stochastic faults are specified and positioned in each coarse grid block.

STAGE 3

In this stage the calculations are performed within each coarse grid block as follows:

- * For each fault plane specify the shales encountered. Then approximate the co-ordinates of each shale (in the direction parallel to the fault plane) in units of fine grid blocks (for example, say the length is 5 grids, width 3 grids).
- * Divide the fault plane into vertical slides, each slide one grid block wide (either in X or Y directions, depending on fault orientations). Calculate the smeared areas caused by the shales overlapping with each slide. If two shales overlap, their corresponding smeared areas may overlap causing multi-layered gouge. The cumulative smeared area of the smeared areas caused by each individual shale is calculated and stored. The net smeared area is also calculated (which reflects the reduction of the cross-sectional area caused by the fault plane), see *Figure 5.6 a & b*.
- * For each fault, find the summation of the smeared areas caused by the shale breaks accounting for fault throw variation along the fault plane.
- * Use the CDF for fault throws as the CDF for barrier height (fault plane). Use the CDF for shale breadth or length as the CDF for barrier width (depending on the fault plane orientation, in x- or y-directions). Generate and distribute a number of barriers – in the same location of the fault plane – using the above CDFs till the summation of the areas of the generated barriers equals the cumulative smeared areas caused by that fault. Store the co-ordinates of the generated barriers for further calculations.
- * Repeat the previous step for all the faults with the same orientation in the block. Consider the barriers as having infinitesimal thickness.
- * A horizontal streamtube in the direction perpendicular to the fault planes may encounter a number of vertical barriers not exceeding the number of fault planes. Using the techniques presented in chapter 3 for calculation of effective vertical permeability, the average number of barriers encountered by a horizontal streamtube can be calculated. As it travels around the barriers, the streamtube moves horizontally due to the higher horizontal permeability

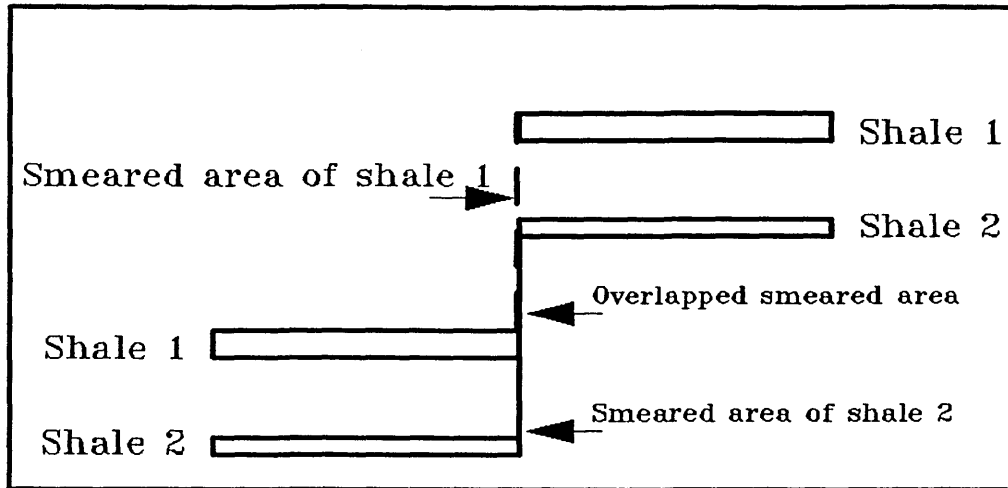


Fig. 5.6 (a) Smeared areas at faulting stage.

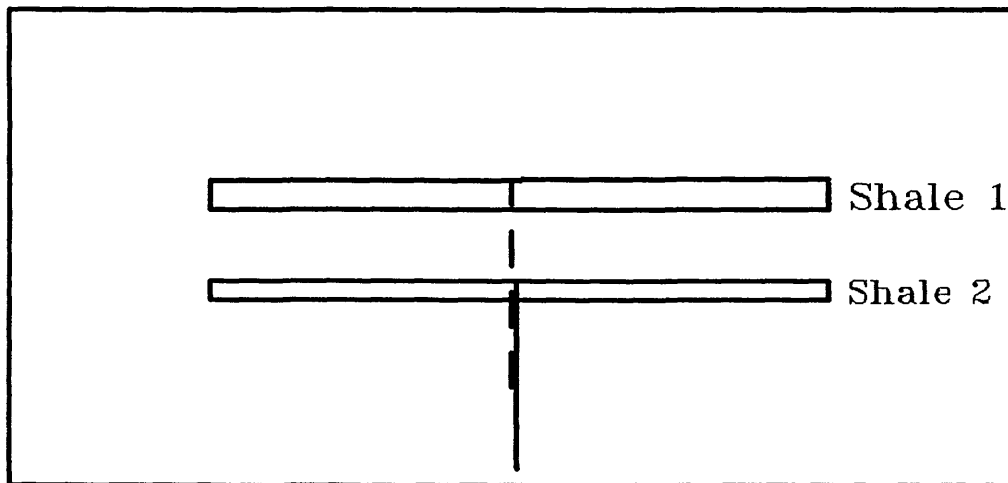


Fig. 5.6 (b) Smeared areas after back stripping.

of the sands as compared with their vertical permeability; and due to the effect of the shale breaks.

* The length of the streamtube, S_e , is given by,

$$S_e = L + L_B \quad (5.3)$$

where,

L = length of the coarse grid

L_B = Distance travelled around the barriers. This is the arithmetic average of the transverse movements of an arbitrary large number of streamtubes (5151) uniformly distributed in a cross-section normal to the direction of flow.

The effective horizontal permeability is calculated by a modified form of equation 3.6 ignoring the fraction of shale and DCSUs as given below,

$$K_{hf} = \frac{L^2 K_e}{S_e^2} \quad (5.4)$$

where,

K_{hf} = Effective horizontal permeability.

K_e = Effective permeability of the streamtube.

K_e is given by,

$$\frac{S_e}{K_e} = \frac{L}{K_x} + \frac{L_B}{K_y} \quad (5.5)$$

If the faults are parallel to (X) direction, swap the position of K_x and K_y in equation 5.5.

5.5 RESULTS

For various shale frequencies, the effective horizontal permeabilities are calculated for an increasing number of faults, from 1 to 6. The results are listed in tables 5.2, 5.3, and 5.4.

For high shale frequencies, for example 12 shales/100 ft, the effective horizontal permeability is reduced by 4% when one fault is introduced to the system. The reduction increased to 11.6% when six faults – with varying dimensions – are introduced to the system. From above it can be inferred that higher permeability reduction may result from increasing fault density.

At low shale frequencies, (2 shales /100 ft), the permeability reduction caused by one fault is 0.081% while six faults result in 2.5% reduction of permeability.

Comparison of the two sets of results reveals that the impact of stochastic faults on reservoir permeability is more pronounced at high shale frequencies. Intermediate degrees of permeability reduction can be obtained for intermediate shale frequencies as shown in table 5.3 (1.8 % to 6.23 % for 6 shales/100 ft).

The above results suggest assessing the severity of the effect of undetected faults (stochastic faults) on reservoir permeabilities before predicting the reservoir's performance.

No. of Faults	K_{hf}
6	289.6
5	290.5
4	291.3
3	292.4
2	294.0
1	294.6

Sand permeability = 300 md, Effective permeability with shales =297 md.

Table 5.2 Permeability results at frequency of 2 shales/100 ft.

No. of Faults	K_{hf}
6	251.6
5	251.2
4	254.9
3	257.0
2	260.6
1	263.6

Sand permeability =300 md, Effective permeability with shales = 268.3 md.

Table 5.3 Permeability results at frequency of 6 shales/100 ft.

No. of Faults	K_{hf}
6	188.0
5	190.7
4	192.7
3	194.6
2	201.5
1	204.4

Sand permeability =300 md, Effective permeability with shales = 212.6 md.

Table 5.4 Permeability results at frequency of 12 shales/100 ft.

CHAPTER 6

MODELLING AND SIMULATION OF FLUVIAL RESERVOIRS COMPOSED OF STOCHASTIC SANDS

6.1 INTRODUCTION

Accurate modelling of the networks of stochastic sands is a challenge to the reservoir engineers due to their complex structures and variable characteristics. These characteristics such as:

- i- variation in size;
- ii- random sand distribution;
- iii- and complex vertical and horizontal connectivities;

may need tens of thousands of grid blocks for detailed description prior to simulation.

The literature is rich in studies describing reservoirs of various sizes (45, 66, 77, 78, 83, 85, 87, 93, 94). Campbell(15), Pryor(77), and Sneider(93, 94) described thoroughly drilled reservoirs using well observations. In their studies, the various features of the stochastic sands were also observed. It was revealed that the horizontal and vertical connectivities of the reservoirs depend on the frequency of the vertical or lateral stacking patterns. Parts of the reservoir may be continuous while other parts may isolated and surrounded by shales.

Due to the enormous amount of well data required to perform an explicit reservoir description study, stochastic techniques were adopted by many investigators (3, 42, 50, 58, 66). These aim to generate possible realisations of fluvial reservoir structures. Fewer data are required by the latter techniques as they use analogue statistical data for sand thickness and thickness/width ratios; and a set of rules derived from observations in outcrops and thoroughly drilled fields (confining the sands to the river belt, consideration of the paleocurrent direction, etc...).

Discretization of these complex conceptual models for simulation becomes a real problem regarding the random distribution of the sand bodies and their variable sizes. Available techniques (3, 42, 50, 58, 66) are inadequate to tackle the complex connectivities between the sand bodies. Therefore, to generate reliable models that can give accurate simulation results without the need for enormous

computer memory and time, a stochastic technique for description of stratified fluvial reservoirs composed of stochastic sands is presented in this chapter. The distribution of the generated sand bodies is conditioned to simplify their discretization, and pseudo parameters are used to enhance Two-dimensional models to represent the three-dimensional reservoir characteristics.

Establishing a reliable statistical data base is a pre-requisite of successful probabilistic modelling of fluvial reservoirs. In the following section the required statistical data are discussed, and a data-base is established for the subsequent modelling and characterisation techniques.

6.2 DIMENSIONS AND ORIENTATIONS OF STOCHASTIC SANDS

In chapter (1) fluvial sands were divided into sheets and elongate bodies. Sheets vary in size and have a length-width ratio of 1:1 while pods, belts, dendroids, and shoestring sands have length-width ratios more than one. All the above sand facies are frequently found in fluvial reservoirs. The shapes and geometry of fluvial sand facies are discussed below.

6.2.1 SHAPES AND SPATIAL DISPOSITION OF STOCHASTIC SANDS

In a cross-section of a fluvial reservoir, the stochastic sands appear as shown by the shaded areas of *Figure 6.1*. In this figure are shown the various characteristics of the stochastic sands, such as, lateral and multistory stacking, size variation, complex connectivities, etc... Some investigators represented the sands by rectangles (25, 42) while others used half circles or half ellipsoidal shapes as shown in *Figure 6.2* and *Figure 6.3*. Due to shape variation as the channels change direction along the flow paths, the rectangular shape is considered a good approximation for the sand bodies. In particular, the rectangular shape simplifies handling of the complex connectivities, as will be shown later in this chapter.

Random angles (between 45 and 135 degrees) are used in this study to specify the direction in which the sand bodies may extend in the regional paleocurrent direction of flow,(see *Figure 6.4*). Improved knowledge of the reservoir may lead to updating the models using appropriate ranges of angles. The occurrence of the stochastic sand bodies is always confined within the river valley or a meander belt (15, 45, 83).

FIGURE - 6.1 : CROSS-SECTION OF
A FLUVIAL RESERVOIR

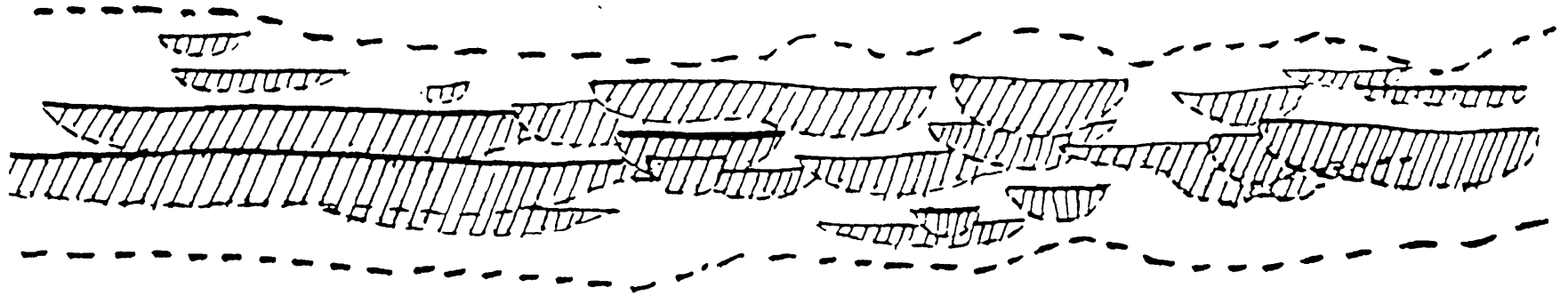


Fig. 6.2 Stochastic sands represented by rectangles

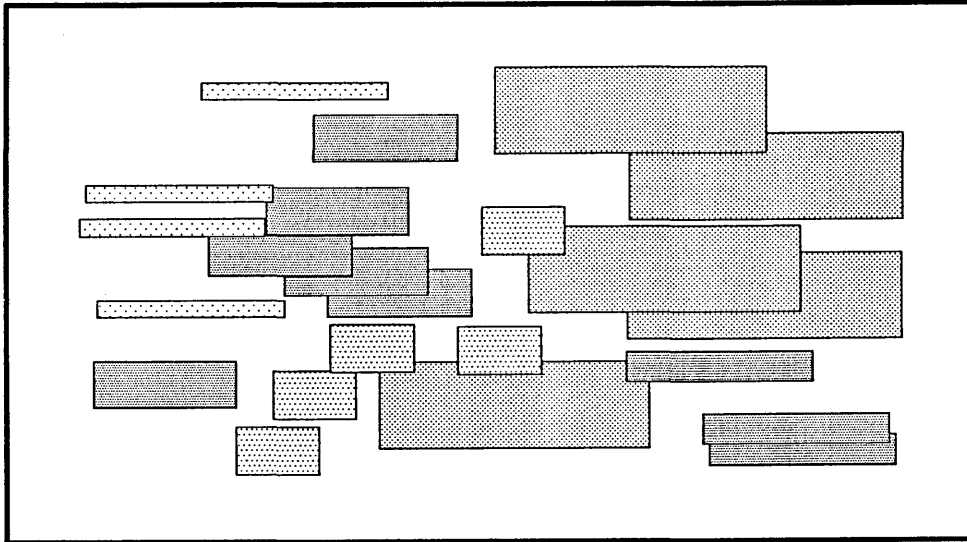
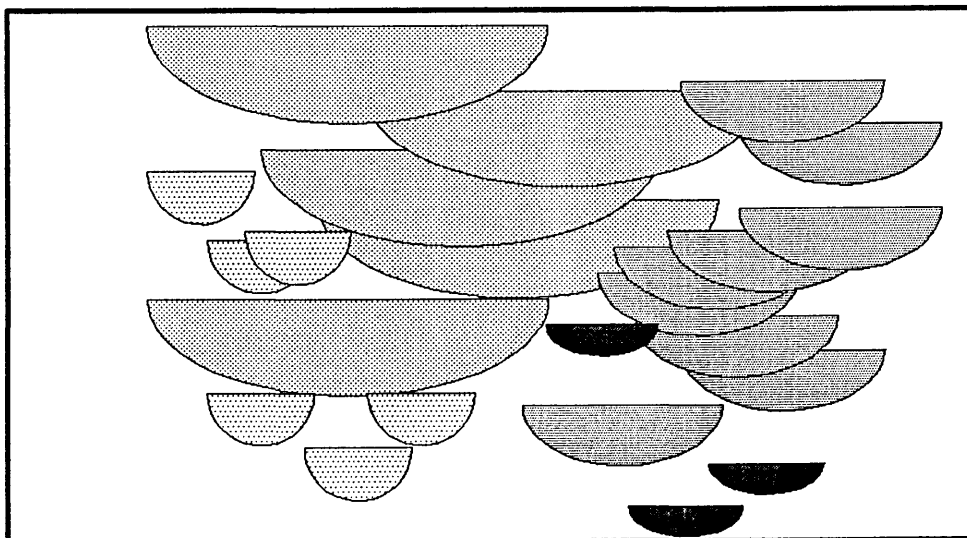


Fig. 6.3 Stochastic sands represented by half ellipsoids



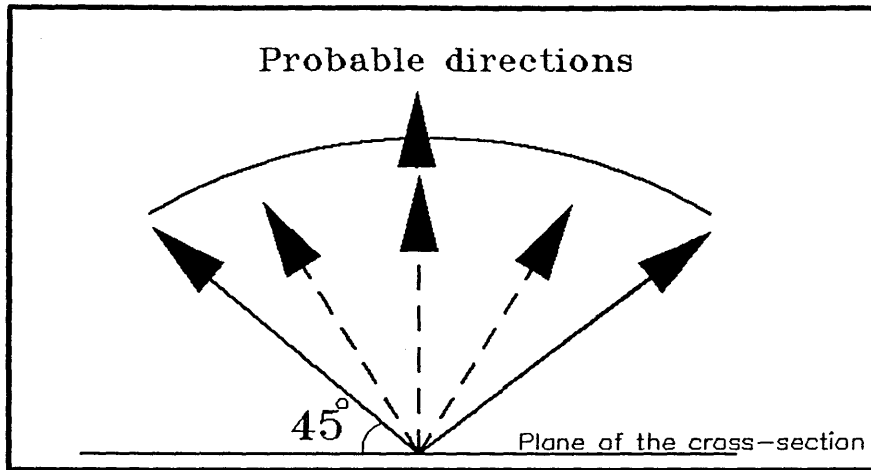


Fig. 6.4 Sampling random angles for the 3-D modelling

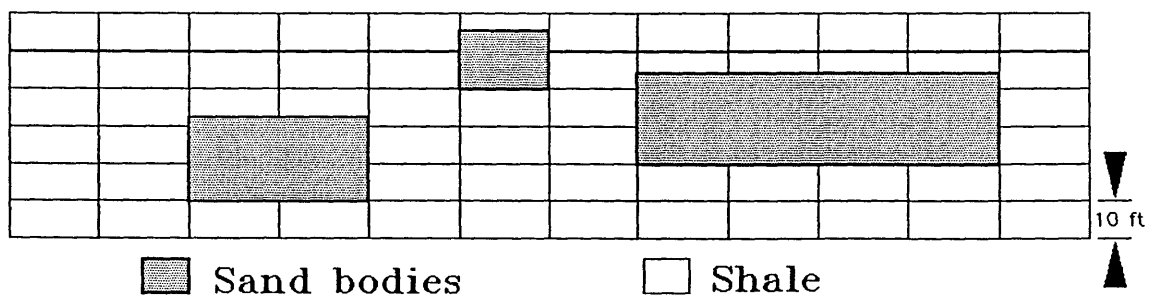


Fig. 6.5 Effect of decreasing the grid thickness

For the modelling scheme presented in this chapter, a data-base for sand dimensions is prepared for each layer of the reservoir zone. The preparation of a data-base for the new modelling scheme is reviewed in the following section.

6.2.2 DEVELOPMENT OF A STATISTICAL DATA BASE FOR SAND MODELLING

Statistical data for fluvial sand dimensions are scarcely found in the literature. Martin *et al* (66) presented a curve reflecting the frequency of occurrence of different channel thicknesses for Stratfjord formations in Stratfjord field (Norway). Knuston (58) has done a valuable statistical study on data from many fluvial outcrops. The thickness, width, and width/thickness ratios were calculated for each sand body. He divided the sand bodies into categories according to their thickness; and for each thickness range he calculated the median of the length/thickness ratios. Knuston's study together with well observations provides the basis for establishing the data-base for each zone. Therefore, the statistical data-base is composed of two parts, the specific data-base and the general data base.

6.2.2.1 THE SPECIFIC DATA BASE

This part of the data-base is obtained from from well observations, and it includes:

- i - maximum sand thickness;
- ii- minimum sand thickness;
- iii- and most frequent (most-likely) sand thickness.

The specific data-base can be prepared for specific areas in the same reservoir zone according to the intensity of drilling activities. Well logs provide the tools for specification of the above parameters that are needed for sampling sand thickness based on the triangular distribution, (see top part of table 6.1).

Maximum sand thickness = 30 ft

Minimum sand thickness = 2 ft

Most-likely sand thickness = 20 ft

Thickness	Length/thickness ratio			
	range	Minimum	Maximum	Most-likley
	2 – 5	5	160	26
	5 – 10	8	160	18
	10 – 20	9	160	21
	20 – 30	9	160	45
	30 – 50	9	160	18

Table 6.1 Statistical data base for fluvial sands

6.2.2.2 THE GENERAL DATA BASE

The general data-base (bottom part of table 6.1) is applicable for all zones of the fluvial reservoir, as it is obtained from statistical studies involving many outcrops of the same fluvial environment. The basis for this part of the data-base are provided by Knuston's study (58).

For the purpose of the modelling scheme presented here, Knuston's data were further processed to indicate the minimum, maximum, and most-likely ratios for each thickness interval (length/thickness) as shown in table 6.1. These calculated statistical parameters are needed for sampling the sand length in the modelling scheme below.

6.3 STOCHASTIC MODELLING OF FLUVIAL RESERVOIRS

The task of building a reliable realisation of a reservoir requires knowledge of the types and frequency of the sand facies it contains. Considering the fluvial reservoirs, the sand facies such as channel sands, point bars, and flood-sheets frequently exist and their distribution is always random. The dimensions of these facies are represented by our data-base in table 6.1.

In the stochastic sand modelling scheme presented here, the sand bodies are first generated in a vertical cross-section which is divided into fine grids. Then they are conditioned with the grid layers and extended to create a 3-D realization of the reservoir. Grid parameter specification is automatically performed during the sand generation stage. The various steps of sand characterisation are discussed

in detail in subsequent sections.

Specification of the optimum dimensions of the grid-blocks is of prime importance for generating reliable models, in reducing the number of grids (computational costs), and handling the complex connectivities of such reservoir domains. This will be demonstrated in the next section.

6.3.1 SPECIFICATION OF THE SIMULATION GRID DIMENSIONS

Several trials of representing the stochastic sands in grid blocks suggested the use of the most-likely sand thickness – observed in wells – as the simulation grid height (20 foot in our case). Using smaller grid thicknesses may lead to unnecessary increase of the number of grid blocks. In this case many grid blocks – in vertical succession – may represent the same body (if we use a thickness of 10 foot, a sand body of 25 foot thickness may need 3 grid layers to represent it.), *Figure 6.4* demonstrates the effect of decreasing the grid thickness. On the other hand, if we use a greater thickness, (more than 20 foot, say 50) the conditioning process introduced in this scheme will severely affect the randomness of the sand distribution. In this case it will be rather a reform of the reservoir (as it implies vertical movement of the sand bodies up to quarter the grid block thickness) which affects the reality of our model (as will be seen later). Moreover, increasing the grid thickness affects the accuracy of handling the complex connectivities of the reservoir.

Considering the grid length, it is found that the optimum length is calculated using the optimum grid thickness and the most-likely length/thickness ratio for the range where the optimum thickness falls, see table 6.1.

Having smaller lengths will increase the accuracy of sand description, but on the other hand this will unnecessarily increase the number of grid blocks and the computational time (no pronounced improvement in accuracy). Using the most-likely length/thickness ratio of 21 ft - which corresponds to the optimum grid thickness, 20 ft - the calculated length of the grid block is 420 ft, or 400 (for simplicity).

This length can be reduced to the minimum, 200 foot (using the minimum length/thickness ratio, 9) at the stage of averaging the reservoir properties (this averaging is described in the next chapter).

Due to the elongate geometry of the stochastic sands – apart from flood-sheets – the breadth of the grid blocks in the major (paleocurrent) direction of flow is longer than the length which is normal to the flow direction. Therefore, the value of 800 foot is considered for the grid's width (using grid width/length ratio of 2). For the simulation studies presented in the subsequent sections a width value of 400 foot is used seeking the maximum degree of accuracy for the comparative study.

6.3.2 GENERATION OF THE STOCHASTIC SANDS

For the sand generation scheme, a set of assumptions and rules were adopted as they comply with observations from outcrop studies (12, 39, 88, 91, 94).

ASSUMPTIONS

- * The different sand facies are randomly distributed.
- * The sand bodies may not extend beyond the river valley or meander belt.
- * The sand bodies in the top or bottom layers may not extend above or below the reservoir region.
- * The sand bodies may overlap freely.
- * The net sand fraction observed in wells is considered statistically representative of the reservoir layer or region.
- * The sand bodies may extend up to quarter of their thickness into the overlying or underlying layers (if any).

The last assumption is applied to create a reasonable degree of communication between the layers. Different criteria (greater or smaller than quarter) can be used depending on the state of knowledge of the internal reservoir structure.

A stratified fluvial reservoir with 3 layers is taken as an example to demonstrate the various model generation steps. The characteristics of this reservoir are shown in table 6.2.

Total reservoir length = 20000 ft

Total reservoir thickness = 700 ft

Total reservoir width = 8000 ft

Number of zones = 3 zones

ZONE	PROPERTY	VALUE
	Gross thickness	140 ft
	Average sand fraction (NTG)	0.45
1	Permeability range	100 – 1000 md
	Effective NTG	0.56
	Gross thickness	260 ft
	Average sand fraction (NTG)	0.744
1	Permeability range	100 – 1000 md
	Effective NTG	1.4
	Gross thickness	300 ft
	Average sand fraction (NTG)	0.566
1	Permeability range	100 – 1000 md
	Effective NTG	0.8

Table 6.2 Characteristics of an example fluvial reservoir

6.3.3 STEPS OF THE SAND GENERATION SCHEME

To generate a three dimensional realization of a channelised reservoir composed of three zones (layers), sand generation is performed section by section (sections within the layers), layer by layer from the top to the bottom as follows:

- (a) In a vertical cross-section (with length L and height H) generate X and K coordinates for the sand centre.

$$X = (\text{randomnumber}, R_1) * L$$

$$K = (\text{randomnumber}, R_2) * H$$

- (b) Using the specific data-base, sample a random thickness for the sand body,

SDT.

- (c) Use the sampled thickness to identify the thickness zone (in table 6.1) and hence, find the triangular parameters for length/thickness (L/H) ratio for that sand body.
- (d) Sample a random (L/H) ratio, RA, for the sand body using the triangular distribution parameters and calculate the sand length, SL (using SDT and L/H).

$$SL = RA * SDT$$

- (e) Using, SDT, SL, and the coordinates of the sand centre, identify the coordinates of the corners of the sand body. The generated sand bodies are placed in the cross-section as denoted by the dotted lines in *Figure 6.6*.

Now the sand body is generated and positioned. If we consider the areas occupied by sand in grids a, b, and c, in *Figure 6.6*, the net-to-gross (NTG) may be a high non-zero value, but the effective horizontal and vertical permeabilities of the grids are zeros due to the shale occupying the rest of the blocks. A problem arises here, how can we represent the sand in these grid blocks for simulation ? If we reduce the sizes of the grid blocks to very small dimensions we will have tens of thousands of grid blocks, and if we ignore the sand corners and edges we will have less NTG and false models. In an attempt to overcome this difficulty without affecting the reality of the models, an automatic sand conditioning process is introduced to the modelling scheme.

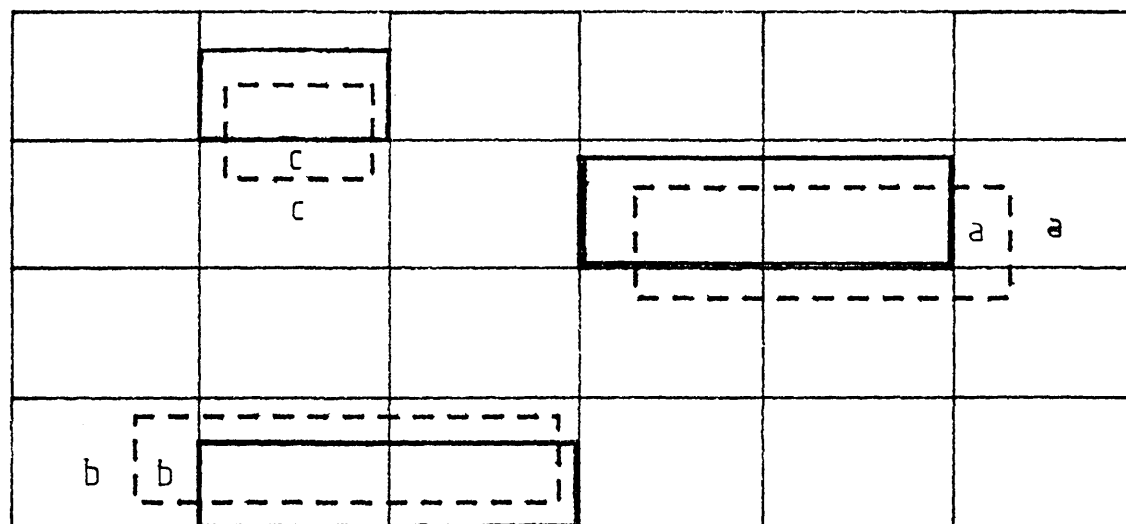
6.3.4 THE AUTOMATIC SAND CONDITIONING PROCESS

To facilitate the stochastic sand discretization while conserving a random distribution characteristic, the sand conditioning is applied to each generated sand body. The process involves two stages:

- (i) The spatial conditioning:

At this stage the generated sand bodies are moved up or down to confine their bases to the nearest grid layer boundary. This eliminates a part of the difficulty in sand discretization. This spatial conditioning involves an average vertical sand

FIGURE -6.6 : GENERATION AND
CONDITIONING OF SAND BODIES



— Conditioned
- - - - - Generated

movement of ± 5 foot, which is very small compared with the reservoir thickness. For the simulation grid thickness of 20 foot, if the K coordinate for the bottom of a sand body is 54 foot, it will be rounded to 60 foot, while a value of 43 or 45 will be rounded to 40 foot. At the end of this stage the K coordinates of the sand bodies are readjusted while the sand thickness is always conserved.

(ii) The dimensional conditioning:

To avoid having sands occupying grid corners as shown in *Figure 6.6* (grid A) a further stage of conditioning is required. If we force the lengths of the generated sands to be multiples of the simulation grid lengths, the above phenomenon can be avoided. The process is effected by rounding the X coordinates of the sand bodies to the nearest integer multiple of grid length. The resulting conditioned X coordinates should not be equal (i.e. the smallest sand body length is one grid length). Considering 400 foot as the grid length, a sand body having X coordinate of 780 and 1550 foot will be assigned the conditioned coordinates 800 and 1600 foot. The new length will be 800 foot instead of 770 foot. This falls within the boundaries of our general data-base. The dimensional conditioning might involve only a slight increase or decrease of the sand length, but the effect of this conditioning – in terms of simplifying sand description problems – is substantial.

The conditioned sand bodies are represented by the bold frames in *Figure 6.6*. Discretization of the conditioned sand bodies is very simple after eliminating the odd features, and their characterisation is simple and straightforward. Grid parameters such as porosity, NTG, and horizontal permeability can be assigned accurately without any further treatments.

Since the bases of the sand bodies are confined to the boundaries of the grid layers, the tops of the grid blocks will be no-flow boundaries if their NTG ratios are less than one (if sand thickness less than 20 foot). This is due to the thin non-conductive shale streaks occupying the tops of the grids. Flow across the bases of the grids, or flow into or from the grids (horizontally) is possible, therefore, zero vertical permeabilities cannot be assigned to these grid blocks. The transmissibility modifiers that are available in most of the simulation packages (Pores, Simbest, Eclipse, etc...) can handle this situation. To represent the above phenomenon, the grid block is assigned the corresponding vertical sand permeability and the transmissibility between the block and the one overlying it is multiplied by zero.

If the NTG in a grid block is 1, a vertical permeability is assigned to the block, with no transmissibility modification.

At this stage, the sand has been generated and conditioned in a 2-D cross-section. Now the task is to generate a 3-D realisation of the sand body.

6.3.5 GENERATION OF 3-D REALISATION OF THE SAND BODIES

As mentioned in section 6.21, random angles are used to specify the direction of the channels between grid sections (see *Figure 6.4*). After conditioning the sand body, a random angle is generated and used to calculate the X coordinates of the stochastic sand in the rear parallel grid section as follows (see *Figure 6.4*):

- * Let θ be the random angle.
- * Let X_1, X_2 be the X coordinates of the sand body in the first grid section.
- * Let X_{12}, X_{22} be the X coordinates of the sand body in the rear grid section.

The smaller X coordinate, X_{12} in the rear grid section is displaced by a distance C from it's corresponding location in the first grid section (see *Figure 6.7 a*). This distance is given by:

$$C = -Tan(90 - \theta) * B \quad (6.1)$$

where,

θ = Random angle.

B = breadth of the grid block.

The displacement C is then rounded to the nearest integer multiple of the grid length as below:

$$C_{new} = \text{nearest integer to } (C / \text{grid length})$$

Therefore,

$$X_{12} = X_1 + C_{new} \quad (6.2)$$

and

$$X_{22} = X_{12} + (X_2 - X_1) \quad (6.3)$$

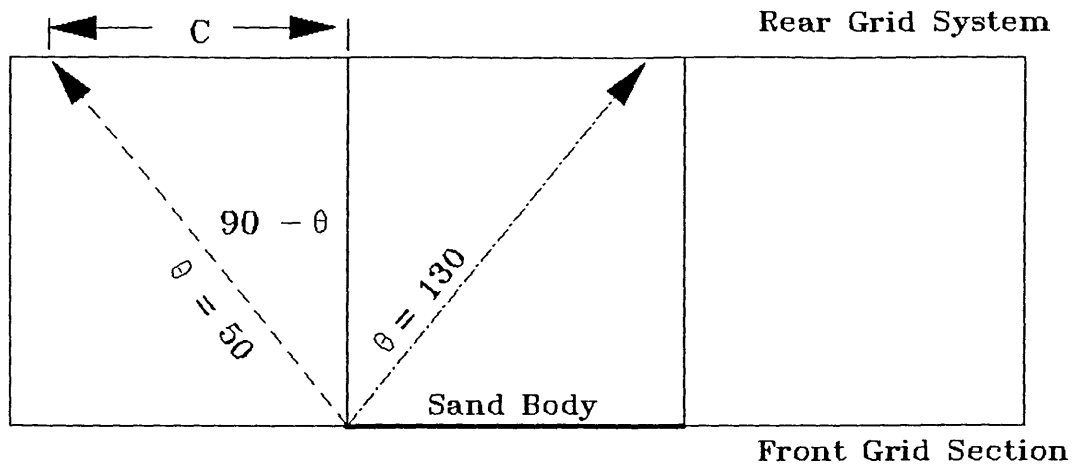


Fig. 6.7(a) Calculation of the Sand's X-Coordinates in the Rear Grid Section

The same process can be repeated for the next grid section, and so on till we reach the end of the reservoir. *Figure 6.7 b* demonstrates the extension of the sand bodies to the third dimension. The assumptions mentioned earlier apply to all the sections.

The following examples serve to demonstrate the method of calculation presented in this section.

Example 6.1

Find the X coordinates of the sand body in the rear grid section using the following data:

$$X_1 = 800, X_2 = 1600, \theta = 50 \text{ degrees, grid - breadth} = 400 \text{ ft}$$

Solution:

$$C = -\tan(90 - 50) * 400$$

$$C = -336$$

$$C_{new} = 400$$

Therefore,

$$X_{12} = 800 - 400 = 400$$

$$X_{22} = 400 + (1600 - 800) = 1200$$

Example 6.2

Repeat example 6.1 using $\theta = 130$ degrees.

Solution:

$$C = -\tan(90 - 130) * 400$$

$$C = +335$$

$$C_{new} = +400$$

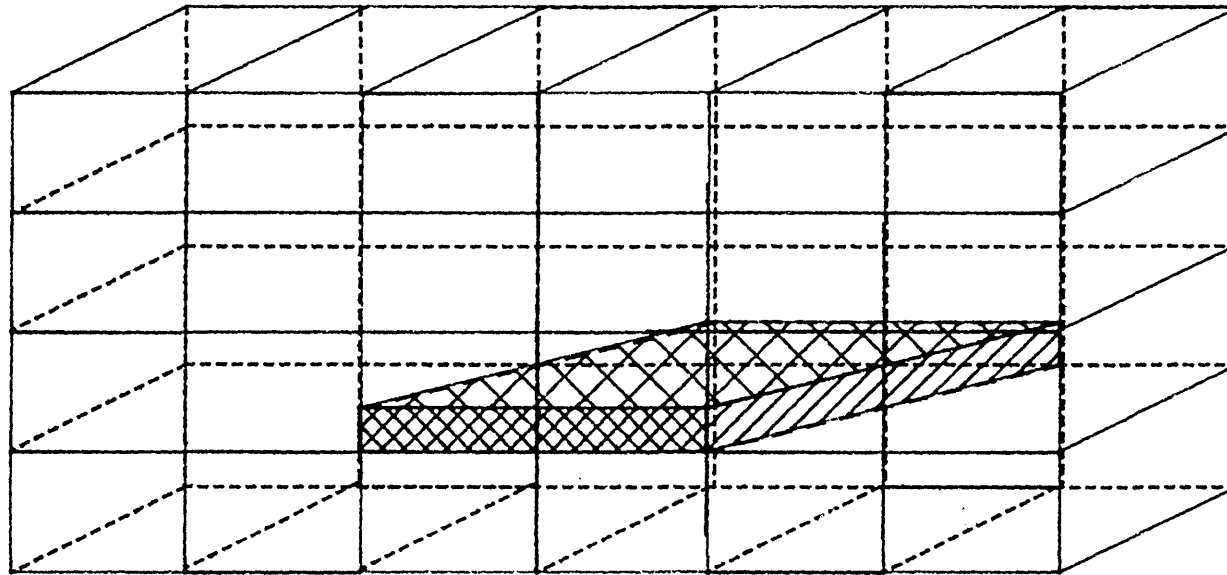
Therefore,

$$X_{12} = 800 + 400 = 1200 \text{ foot}$$

$$X_{22} = 1200 + (1600 - 800) = 2000 \text{ foot}$$

Sand generation continues till the ratio of the cumulative gross areas of the generated sand bodies to the cross-sectional area of the layer equals the effective NTG, NTG_{eff} . At this stage the net sand fraction in the cross-section of the layer equals the NTG observed in the wells, NTG_{obs} . The NTG_{eff} is specified by a computer software specially coded for this purpose. The calculation procedure for this software are demonstrated in the next section.

FIGURE -6.7B : EXTENSION OF SAND BODIES IN THE DIRECTION OF FLOW



6.3.6 CONTROL OF THE GENERATED SAND FRACTION

The net fractional area of the cross-section (of the layer or zone) occupied by sand bodies, NTG_{obs} , is always smaller than the NTG_{eff} due to the free overlapping of the sand bodies. To specify the value of NTG_{eff} which gives the desired NTG_{obs} , a software is coded and linked to the sand generation programme. This software divides the cross-sectional area of the layer into very fine grids (down to 1 * 1 foot if required) and then uses the coordinates of the generated (and conditioned) sand bodies to check each fine grid block to determine whether or not it is occupied by sand. The software finds the number, N, of the fine grids occupied by sand. The net NTG ratio of the sand in the cross-section equals N divided by the total number of fine grids in that layer or zone. For high observed sand fractions, the degree of overlapping becomes very severe and the NTG_{eff} increases to values higher than one. The software is used either by direct insertion into the sand generation scheme or through a pre-prepared graph as described below:

(i) Direct insertion in the generation scheme:

In this case, the software is entered as a loop in the scheme. The fine grid checking and the NTG calculation is performed after conditioning of each of each generated sand body. Sand generation is automatically stopped when the NTG_{obs} is exceeded. Due to the lengthy calculations involved, the graph form is preferred.

(ii) Pre-prepared graphs:

In this case a pre-determined value of NTG_{eff} is used for each zone or layer in the sand generation scheme. This value will give the desired sand fraction on the cross-section of the layer when used by the sand generation scheme. Sand generation automatically stops when the NTG_{eff} is exceeded. The values of NTG_{eff} are determined using a graph relating the NTG_{eff} and NTG_{obs} , see *Figure 6.8*. This graph is prepared by running the sand modelling scheme several times, changing the input NTG_{eff} each time and calculating the net sand fraction in the cross-section of the layer at the end of each run. The process is repeated for three different cross-sectional areas using the same input NTG_{eff} value to investigate the effect of variation of cross-sectional area on the resulting net sand fraction. Negligible differences were observed which supports the validity of the produced graph for a wide range of cross-sectional areas. The arithmetic average

of the corresponding values in the three runs is shown in table 6.3, and plotted in *Figure 6.8*. Appendix 6.A is a listing of the sand generation programme including the software for NTG control.

When the desired sand fraction of the cross-section is reached, the sand modelling scheme produces two files before stopping. The first file, SANDR, contains the geometrical data of the model (i.e. sand coordinates, reservoir dimensions, etc...). This data file will be used by another programme, SANDPL, (appendix 6.B) to generate 2-D plots demonstrating a cross-section of the reservoir as shown by *Figure 6.9*. The second file contains the grid's parameters such as permeabilities, NTG ratios, porosity, and transmissibility modifiers. This file will be used to prepare the data file for simulation studies. It can also be used for averaging the reservoir properties to generate one dimensional models that can be solved by analytical waterflood prediction methods.

Theoretical (effective) NTG	Observed NTG
0.1	0.108
0.2	0.201
0.3	0.284
0.6	0.4546
0.7	0.5302
0.756	0.554
0.8	0.572
0.96	0.621
1.0	0.655
1.2	0.694
1.4	0.742
1.7	0.805
2.0	0.850

Table 6.3 Theoretical (effective) versus Observed NTG

FIGURE - 6.8 : THEORETICAL [EFFECTIVE]
VS NET [OBSERVED] SAND FRACTION

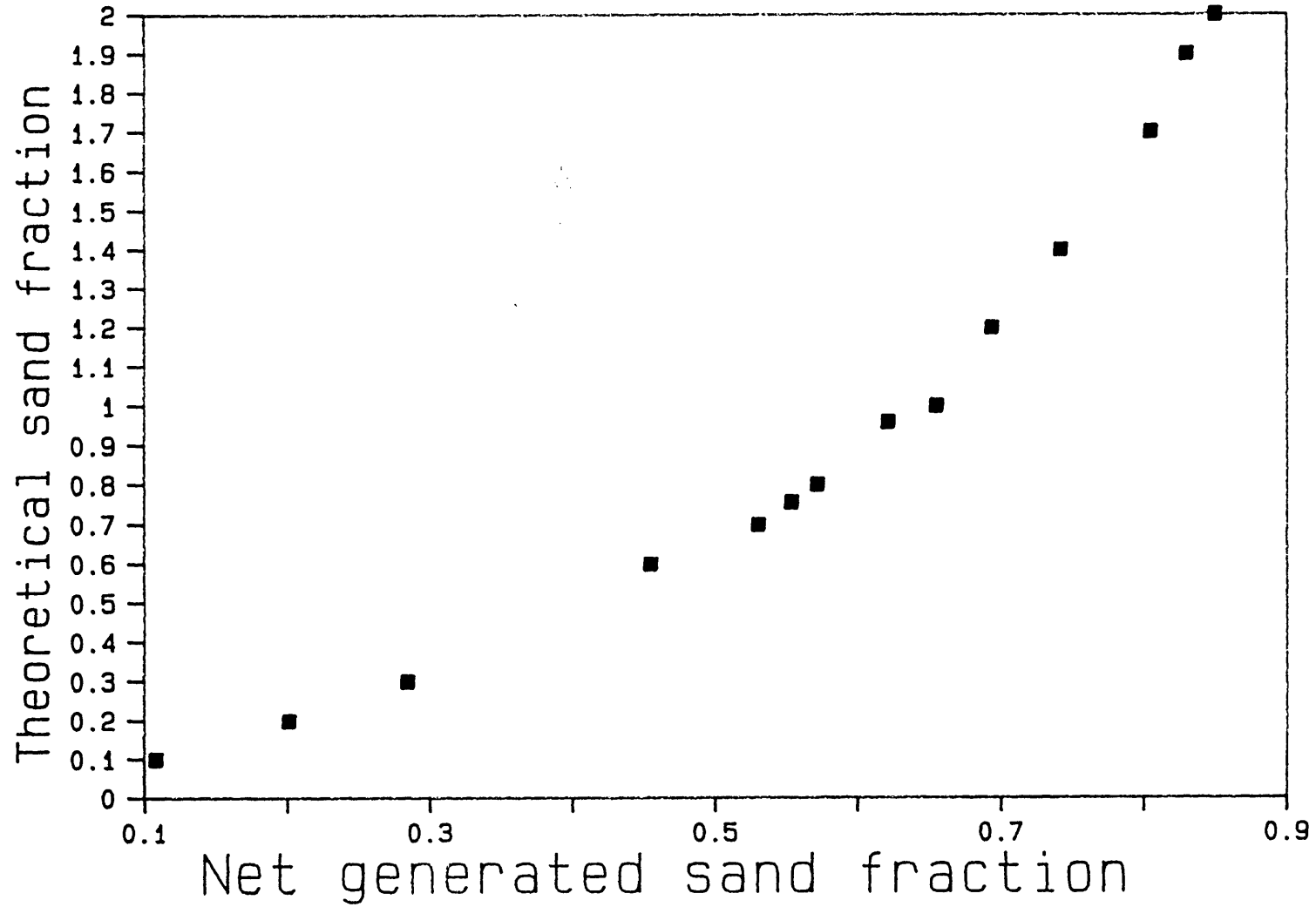
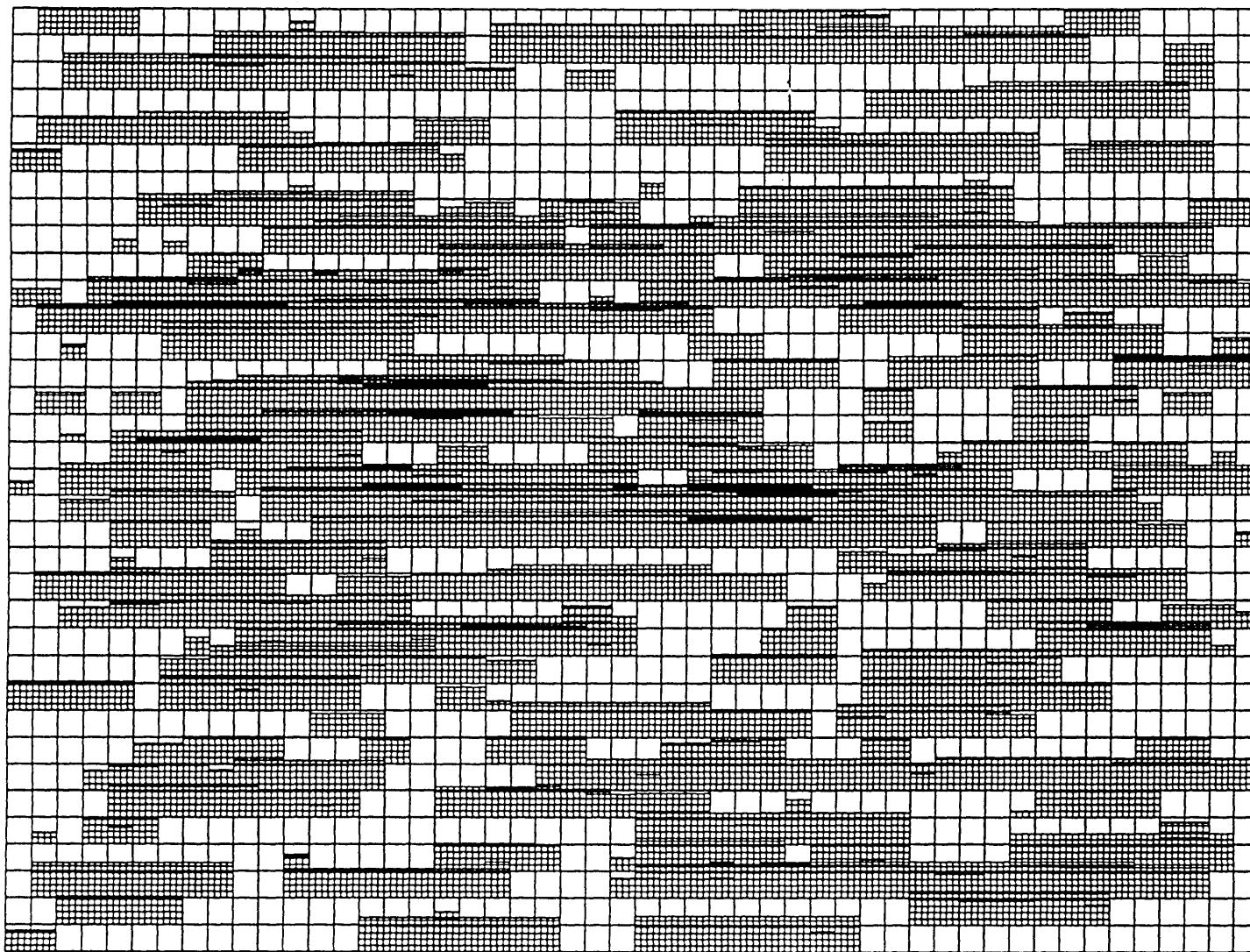


FIG. 6.9 CROSS-SECTION OF A FLUVIAL RESERVOIR



■ Sand

□ Shale

6.4 CHARACTERISATION OF THE STOCHASTIC SANDS FOR SIMULATION

Calculation of the grid block parameters is done automatically during the sand generation stage. Due to the conditioning process introduced, the parameter calculation and assignment is simple and straightforward as shown below.

6.4.1 ASSIGNMENT OF THE NTG RATIOS

If a grid block contains stochastic sands, the NTG ratio of that grid block will be the thickness of the sand body (if less than 20 foot) divided by the thickness of the grid block, 20 foot. As a result of the free overlapping, many sand bodies may occupy the same grid block. In this case the NTG ratio of the grid block is the thickness of the thickest sand body (if less than 20 foot) divided by the thickness of the grid block.

Earlier in section (6.3.1) it was stated that the grid thickness equals the most-likely thickness of the sand bodies. Therefore, some sand bodies may extend vertically in more than one grid block. In this case the lower occupied grid block is assigned a NTG ratio of 1 while the top one is assigned a lower value according to the percentage of sand it contains.

6.4.2 ASSIGNMENT OF THE HORIZONTAL PERMEABILITIES

Weber (4) presented a series of core horizontal permeabilities across a channel sand with increasing distance from the channel flank to centre. The permeabilities corresponding to the lee side of the channel are presented in table 6.4. Regarding these values as representative of the permeability across channel sands (from flank to centre), and assuming symmetry of both sides from the channel centre, then, permeability distribution across channels of various sizes could be generated.

The dimensionless permeabilities (permeability/maximum permeability) are plotted versus the dimensionless distances (distance from flank/half the channel's width) as shown in *Figure 6.10*. From this figure a straight line relation could be observed, and the following formula for calculation of the dimensionless permeabilities at given dimensionless distances is deduced:

$$R_k = 0.57 + 0.9R_d \quad (6.4)$$

Where,

0.57 = Intercept with (Y) axis.

0.9 = Slope of the line.

R_k = Dimensionless permeability.

R_d = Dimensionless distance.

Or generally,

$$R_K = a + bR_d$$

where,

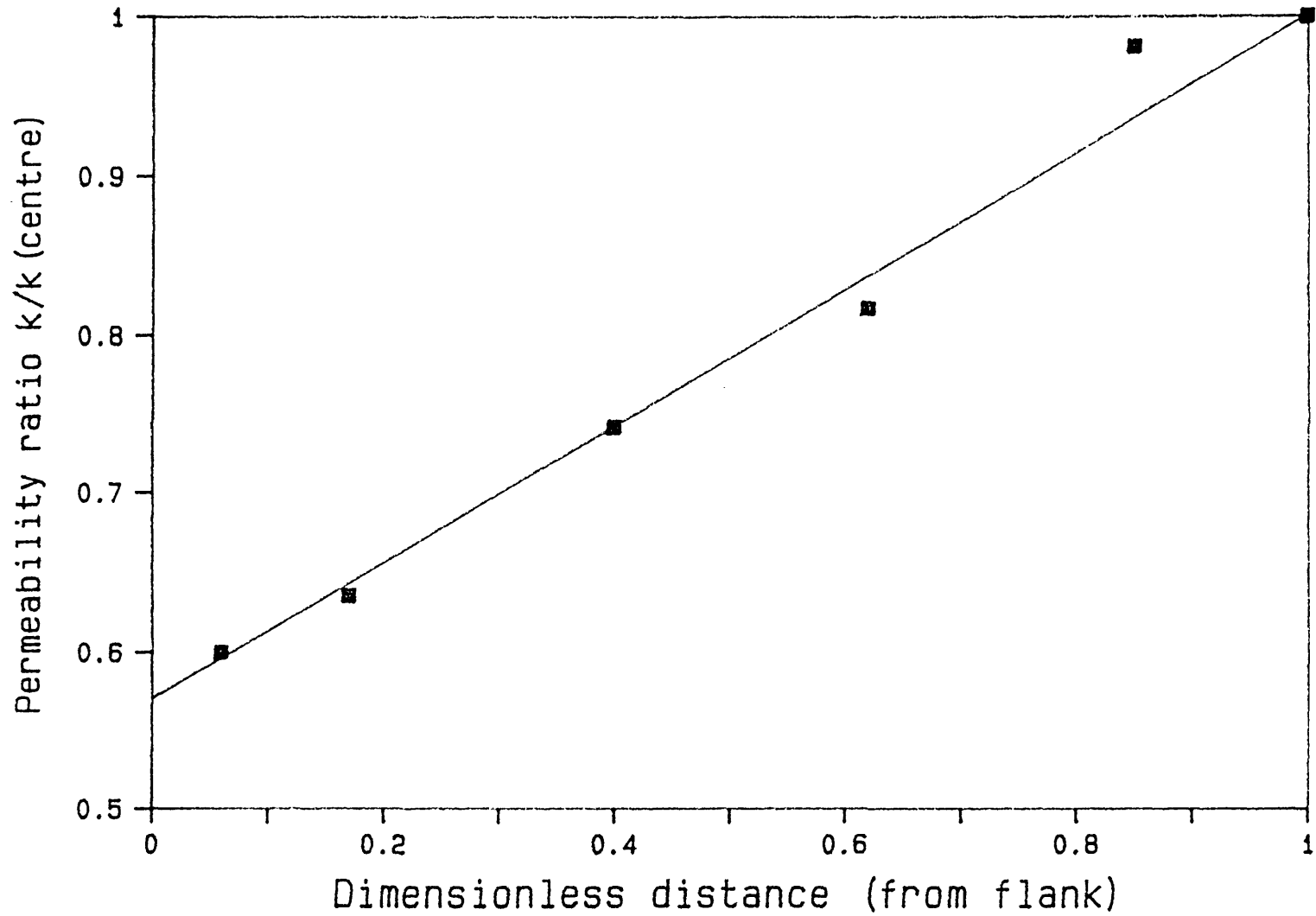
a = constant

b = slope

The average value of the maximum permeability observed in each sand body of the region under consideration is used as the maximum permeability at the centres of the generated sands in the region. A subroutine uses this value in equation 6.4 to generate ten permeabilities distributed from the channel centre to the flank. The same subroutine then calculates the harmonic mean of the generated values to obtain one permeability value for that sand body. This value will be assigned to all the grids occupied by the sand body. Alternatively, different permeabilities can be assigned to the grids without harmonic averaging.

If a later generated channel overlaps with an older one in a certain grid block, the permeability of the thicker channel will be assigned to that grid block.

FIGURE - 6.10 : HORIZONTAL PERM.
VERSUS DIMENSIONLESS DISTANCE



Sand Thickness	Core K Darcies	K/K_{max}	Dimensionless distance %
50	45	0.6	6
100	47.5	0.636	17
250	55.4	0.742	40
375	61	0.817	62
375	73.3	0.981	85
372	74.7	1	100

Table 6.4 Permeability distribution across a channel sand

6.4.3 ASSIGNMENT OF THE VERTICAL PERMEABILITIES

The effective vertical permeability is calculated for each zone allowing for shale convergence as demonstrated in chapter 3. A single anisotropy factor (vertical/horizontal permeability) is retained for each zone. This factor is multiplied by the horizontal permeabilities of the grid blocks to find their vertical permeabilities.

6.4.4 ASSIGNMENT OF POROSITIES

From porosity-permeability plots of core data, a relation between porosity and permeability could be obtained. Different relations are possible for different fields. The relation derived for the range of data in this study is given by:

$$\phi = \left[\left(\frac{k - 700}{200} \right) / 100 \right] + 0.20 \quad (6.5)$$

where,

ϕ = Porosity (fraction).

K = Horizontal permeability, md.

Therefore, the grid porosities can be calculated by substituting the precalculated values of horizontal permeabilities in equation 6.5. At K=700 md. the calculated value of ϕ is .20, while at K=0.0 $\phi = 0.165$.

Fig. 6.11 Plan view (X-Y) demonstrating the complex communication between the grid-blocks. (Arrows show the flow-paths)

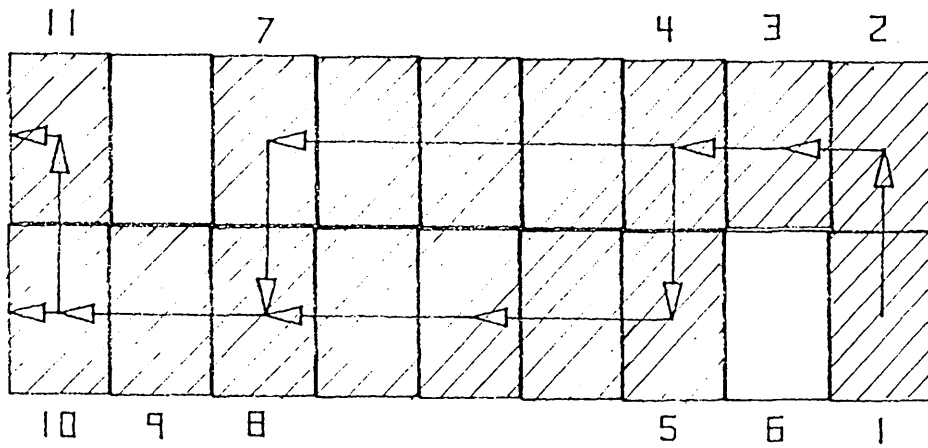
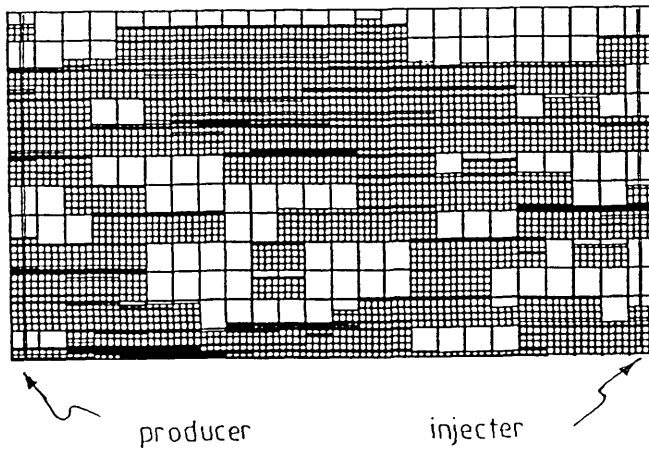


FIG. 6.13 CROSS-SECTION OF THE 3-D MODEL



Reaching this stage, the 3-D model of the reservoir is generated and characterised. Although the number of grid blocks is reduced substantially by the automatic conditioning process, the ambition is to generate 2-D models that can give the same performance of the 3-D model for this complex domain.

Straightforward utilization of a 2-D cross-sectional model taken from the 3-D model will not represent the complex vertical and horizontal connectivities of the network. Grids apparently isolated in a 2-D cross-section may be in vertical or horizontal communication through a parallel grid section. In *Figure 6.11* there is a rear path between grids 1 and 5 through grids 2, 3, and 4. This path cannot be represented by a conventional 2-D cross-sectional model from grid 1 to 10. To generate 2-D models representative of the 3-D characteristics of the reservoir, use of pseudo parameters is necessary. In the following section the various pseudoization techniques applied to generate representative 2-D models are discussed.

6.5 USE OF PSEUDO PARAMETERS FOR 2-D RESERVOIR DESCRIPTION

Careful study of *Figure 6.11* reveals the severe reduction of transmissibility in conventional 2-D cross-sectional models of fluvial reservoirs. As demonstrated above, rear communication may exist between apparently isolated grid blocks. To represent the rear path in a 2-D cross-sectional model – and hence maintain the 3-D connectivity of the reservoir – an automatic parameter pseudoization procedure is applied. The isolated grid blocks in the rear section which are sharing the flow paths of the front grid section are also taken into account. The pseudoization process is effected in the vertical and horizontal directions at the end of the sand generation scheme. During this process, the following parameters are pseudoized:

6.5.1 PSEUDO HORIZONTAL PERMEABILITY AND NTG

In *Figure 6.11*:

- (i) Assign a pseudo NTG value of 1 to grid 6.
- (ii) Calculate the pressure drop for oil flow through blocks 1-2-3-4-5.

$$\Delta P_T = \Delta P_{(1-2)} + \Delta P_{(2-3)} + \Delta P_{(3-4)} + \Delta P_{(4-5)} \quad (6.6)$$

Where,

ΔP_T = Total pressure drop from grid 1 to 5.

ΔP = Pressure drop between the specified grids (subscripts).

From darcy's law,

$$\Delta P = Q \frac{L\mu}{KA} \quad (6.7)$$

Substituting Eq. 6.7 in Eq. 6.6 gives,

$$\begin{aligned} \Delta P_T &= \frac{Q\mu L_p}{(KA)_p} \\ \Delta P_T &= \frac{q\mu\Delta y}{2(AK)_1} + \frac{2q\mu(\Delta x + \Delta y)/2}{(AK)_2} + \frac{2q\mu\Delta x}{(AK)_3} + \frac{2q\mu(\Delta x + \Delta y)/2}{(AK)_4} + \frac{q\mu\Delta y}{2(AK)_5} \quad (6.8) \end{aligned}$$

Where,

q = Flow rate.

μ = Viscosity.

K = Grid's horizontal permeability.

A = Grid's cross-sectional area (in X or Y directions).

Δx = Grid's length.

Δy = Grid's width.

p = Subscript for pseudo parameters.

1,2,3,4,5 = Subscripts for grid specification.

As grids 2, 3, and 4 will be shared by oil from the front section, only half the NTG ratio is considered in the calculation of pseudo permeability (see equation 6.8). This is why the cross-sectional areas in the intermediate terms are divided by 2.

Equation 6.8 can be further reduced to give,

$$\Delta P_T = \frac{\Delta y}{2(AK)_1} + \frac{\Delta x + \Delta y}{(AK)_2} + \frac{2\Delta x}{(AK)_3} + \frac{\Delta x + \Delta y}{(AK)_4} + \frac{\Delta y}{2(AK)_5} \quad (6.9)$$

(ii) If the flow path is represented by a direct line from grid 1 to 5 maintaining the same pressure drop, then the pressure drop between 1 & 5 is given by,

$$\Delta P_T = \frac{\Delta x}{2(AK)_1} + \frac{\Delta x}{(A_p K_p)_6} + \frac{\Delta x}{2(AK)_5} \quad (6.10)$$

Equating 6.9 & 6.10, substituting for A_p by 1 (as mentioned in step (i)), and solving for K_p ,

$$K_p = \frac{\Delta x}{\left[\frac{\Delta y}{2(AK)_1} + \frac{\Delta x + \Delta y}{(AK)_2} + \frac{2\Delta x}{(AK)_3} + \frac{\Delta x + \Delta y}{(AK)_4} + \frac{\Delta y}{2(AK)_5} - \frac{\Delta x}{2(AK)_1} - \frac{\Delta x}{2(AK)_5} \right]} \quad (6.11)$$

(iv) Similar calculations can be done if the grids between 1 & 5 are more than one. In this case all the grids (between 1 & 5) will be assigned the same pseudo permeability, NTG, and zero vertical permeabilities (unless pseudo vertical permeabilities are assigned).

6.5.2 BACK PSEUDOIZATION OF HORIZONTAL PERMEABILITY

In real nature, liquids of the front cross-section may share the paths of the rear cross-section, and vice versa. Therefore, the transmissibilities of some grids of the front section – for the fluids of the front cross-section in 2-D case – may be affected by this cross-flow.

To accomodate this phenomenon in the 2-D model, the back pseudoization technique is introduced. The process is effected as follows:

(i) Check the gaps between the grids of the rear section layer by layer from $X = 1$ to $X = X_{(max)}$. If there are inactive blocks (occupied by shale) between any two successive active blocks (occupied by sand), check the continuity of active blocks between the corresponding two blocks in the front cross-section.

(ii) If there are inactive blocks between the corresponding two blocks in the front section, no back pseudoization is needed, otherwise the path in the front cross-section is to be shared.

(iii) Sharing is performed by dividing the permeability of the corresponding grids in the front section and all the grids between them by 2. Therefore, the horizontal permeability of grids 8, 9, and 10 in *Figure 6.11* is to be divided by 2.

6.5.3 PSEUDO VERTICAL PERMEABILITY:

The same rear-path phenomenon mentioned above may happen in the vertical direction. In this case, due to the confinement event of the bases of the generated sands to the grid layer boundaries, the phenomenon may happen even between two adjacent grid blocks (the bottom one having less than 1 NTG), see *Figure 6.12* (Grids 15, 16). The grids maintaining the rear path (in the rear grid section) must all have 1 NTG value (except the top one). In *Figure 6.12*, communication between grids 1 and 3 is maintained by grids 12, 13, and 14. Also communication between grids 9 and 10 is maintained by grids 20 and 21.

Derivation of the equation for calculation of the pseudo horizontal permeability follows the same principles as for the pseudo vertical permeability. Therefore, the corresponding form of the equation 6.9 for pseudo-vertical permeability between grids 1 and 3 is given by,

$$\Delta P_T = \frac{\Delta Y}{2(AK)_1} + \frac{\Delta Y + \Delta Z}{(AK)_{12}} + \frac{2\Delta Z}{(AK)_{13}} + \frac{\Delta Y + \Delta Z}{(AK)_{14}} + \frac{\Delta Y}{2(AK)_3} \quad (6.12)$$

To represent the rear path by a front one from 1 to 3 through grid 2, then,

$$\Delta P_T = \frac{\Delta Z}{2(AK)_1} + \frac{\Delta Z}{2(A_p K_p)_2} + \frac{\Delta Z}{2(AK)_3} \quad (6.13)$$

Equating 6.12 and 6.13, substituting for A_p by 1, and solving for K_p gives,

$$K_p = \frac{\Delta Z}{\left[\frac{\Delta Y}{2(AK)_1} + \frac{\Delta Y + \Delta Z}{(AK)_{12}} + \frac{2\Delta Z}{(AK)_{13}} + \frac{\Delta Y + \Delta Z}{(AK)_{14}} - \frac{\Delta Z}{2(AK)_1} - \frac{\Delta Z}{2(AK)_3} \right]} \quad (6.14)$$

Similar calculations can be done if the grids between 1 and 3 are more than one. In this case all grids between 1 and 3 will be assigned the same pseudo-permeabilities and NTG. If these grids were not assigned pseudo-horizontal permeability during the horizontal pseudoization stage, they will be assigned zero horizontal permeabilities.

Front grid section

Rear grid section

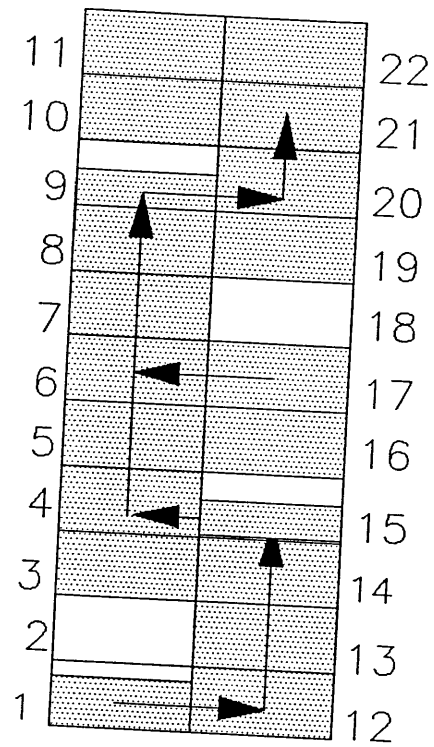


Fig. 6.12 Side view of the 3-D model

6.5.4 BACK PSEUDOIZATION OF VERTICAL PERMEABILITY :

The same principles as for horizontal back pseudoization are applied for vertical back pseudoization. In *Figure 6.12* grids 4 and 5 of the front grid section are shared by the rear grid section to transmit fluids between grids 15 and 16, therefore, the vertical permeabilities of grids 4 and 5 are divided by 2. The same sharing is applied to grids 6, 7, and 8.

6.5.5 ASSIGNING PSEUDO PROPERTIES :

Many reservoir simulators consider the grids to be inactive if they have zero porosities. Therefore the grids assigned pseudo- properties to represent the rear paths must be assigned non-zero (pseudo) porosities to declare them active. At the same time the assigned pseudo-porosities must be negligibly small so as not to increase the initial fluids in place. An arbitrary value of pseudo-porosity is chosen to be 0.0001 (fraction).

6.6 COMPARATIVE SIMULATION STUDIES:

To validate the pseudoization technique presented above, the simulation approach is adopted. The comparative simulation is meant to emphasise the importance of the pseudoization technique to create 2-D cross-sectional models representing the reservoir (3-D) behaviour. Therefore, three reservoir models were used in this study as follows:

(i) a 3-D model of a layered reservoir composed of stochastic sands;

(ii) a 2-D cross-sectional model of the above reservoir;

(iii) and a 2-D cross-sectional model with pseudo-parameter to represent the same reservoir.

Figure 6.13 is a cross-section of the 3-D model which represents model (ii). This model is then enhanced by pseudo-parameters to create model (iii) which represents model (i).

The characteristics of the models are given in table 6.5. The fluid characteristics were kept the same for all models and the following scheduling ratios were

kept constant:

(A) Daily water injection/daily liquid production = 1.0

(B) Daily injection rate/initial oil in place.

The maximum allowable water-cut is 0.90 and the producers will be shut-in if the water-cut exceeds this value.

The generation of relative permeabilities for this heterogeneous porous media was tackled by an empirical relative permeability correlation chart (24) after a series of permeability averaging steps.

A detailed discussion of the relative permeability generation procedure is given below.

Property	Value
Length	9600 ft
Width	800 ft (400 ft for 2-D)
Thickness	240 ft
Zone (1)	Top zone
Thickness	140 ft
Observed NTG	0.744
Effective NTG	1.4
Sub zones in X dir.	3
Zone (2)	Bottom zone
Thickness	100 ft
Observed NTG	0.566
Effective NTG	0.8
Sub zones in X dir.	3

Table 6.5 Characteristics of the model used for the study

6.6.1 GENERATION OF THE RELATIVE PERMEABILITY CURVES

Due to the variation of permeabilities in fluvial reservoirs the corresponding relative permeabilities also vary from one location to another. Since it is impossible to obtain cores from all the locations in the reservoir having different permeabilities, (and hence measure their relative permeabilities) the generalised relative permeability correlation charts become the only source of such informations (24). For various permeability values, an equivalent number of relative permeability tables will result which is impractical for simulation purposes. Therefore, reservoir zonation according to permeability ranges and averaging of permeabilities within each zone, to obtain a single representative value, will considerably reduce the number of relative permeability tables for the domain.

In these studies, the reservoir is divided into two zones vertically and three zones horizontally (in x-direction), therefore, the reservoir consists of 6 zones. For the purpose of relative permeability generation, the reservoir is divided into only 3 zones in the horizontal (x) direction due to similarity in permeability ranges for zones in vertical succession.

The arithmetic and geometrical averaging techniques were used to obtain a single representative value for each zone (considering the active blocks only). These averaged values are then used with the correlation chart, *Figure 6.14*, to generate a relative permeability curve for each zone. The generation process is effected as follows:

- * Using the averaged permeability, enter the bottom part of the chart (*Figure 6.14*) to identify the end-point relative permeabilities, K_{ro} at initial water saturation and K_{rw} at residual oil saturation.
- * From the top parts identify the residual oil saturation, S_{or} , and initial (connate) water saturation, S_{wi} .
- * The relative permeabilities are computed using the following empirical equations.

Water relative permeability, K_{rw} ,

$$K_{rw} = (\bar{S}_w)^2 * K'_{rw} \quad (6.15)$$

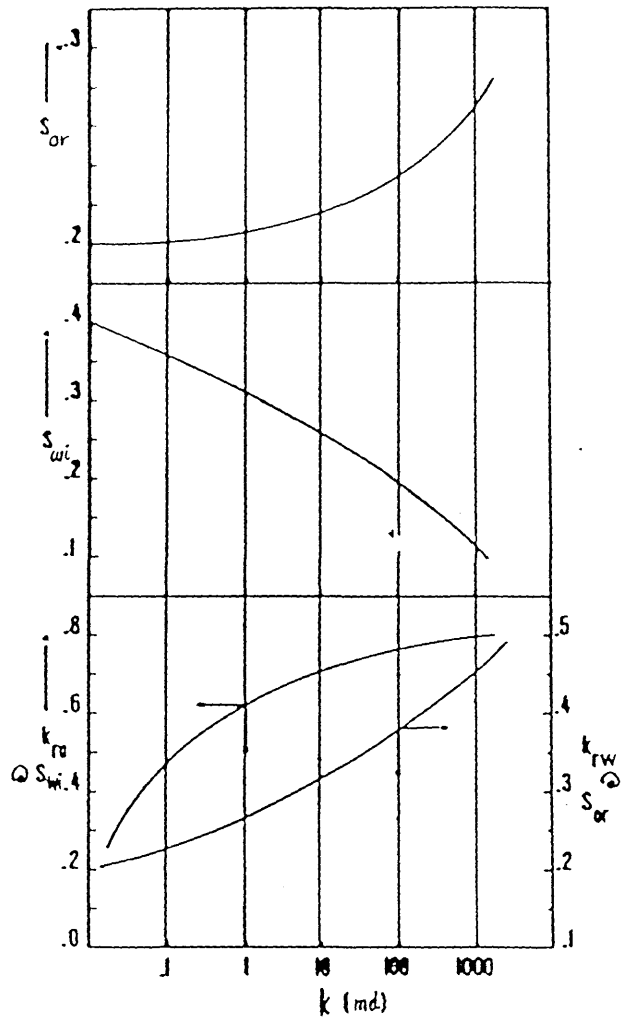


Fig. 6.14 Empirical relative permeability correlation chart.

Oil relative permeability, K_{ro} ,

$$K_{ro} = (1 - \bar{S}_w)^2 * K'_{ro} \quad (6.16)$$

Where,

$$\bar{S}_w = \frac{(S_w - S_{wi})}{(1 - S_{wi} - S_{or})} \quad (6.17)$$

S_w = Water saturation.

The three average permeabilities used for the three zones are 428 md, 328 md, and 370 md for zones 1, 2, and 3 respectively.

Generation of the capillary pressure curve for each zone is tackled by another set of empirical equations as shown in the next section.

6.6.2 COMPUTATION OF THE CAPILLARY PRESSURE

An imbibition capillary pressure curve for each zone can be generated (capillary pressure vs. water saturation) using the following empirical equation (24):

$$P_c = P_{cb} * \left(\frac{1}{(S_{pc})^\lambda} - 1 \right) \quad (6.18)$$

Where,

$$S_{pc} = \frac{S_w - S_{wi}}{S_{wo} - S_{wi}}$$

P_{cb} = A measure of interfacial tension and mean pore size.

λ = A parameter reflecting the breadth of the pore-size distribution.

S_{wo} = The value of wetting phase saturation corresponding to zero capillary pressure.

S_{pc} = Saturation, normalised with respect to S_{wo} and S_{wi} .

For the purpose of this project the following values are used:

$$P_{cb} = 0.27$$

$$\lambda = 6.0$$

$$S_{wo} = 1 - S_{wi}$$

The resulting capillary pressure data are included in the simulation data files in Appendix 6.C.

The characteristics of the three simulation studies are described in the following sections.

6.6.3 THE 3-D SIMULATION STUDY:

The 3-D model is 24 grids long, 12 grids high and 2 grids wide. Two injectors are located at one end (at $x=24$, $y=1$ and 2), and two producers were located at the other (at $x=1$, $y=1$ and 2).

Other relevant data are given below:

Initial oil in place = 30456348 STB

Reservoir pore volume = 44303549 RB

Water injection rate = 19800 RB/Day

Oil (liquid) production rate = 19800 RB/Day

The simulation data-file is prepared to be run by SIMBEST, a simulation software package prepared by SSI (Scientific software-Intercomp, Inc.), on the VAX computer.

6.6.4 THE 2-D SIMULATION STUDIES:

Both of the 2-D models are 24 grids long, 12 grids high, and 1 grid wide. An injector is located at one end ($X=24$), and a producer is located at the other. Other relevant data are given below.

Initial oil in place = 15040805 STB

Reservoir pore volume = 21880401 RB

Water injection rate = 9900 RB/D

Oil (liquid) production rate = 9900 RB/D

6.6.5 SIMULATION RESULTS AND DISCUSSIONS:

6.6.5.1 RESULTS OF THE 3-D STUDY:

The results of the 3-D study are presented in figures 6.15 and 6.16. *Figure 6.15* is a plot of the dimensionless oil production (oil produced/initial oil in place) versus time. Also a plot of water-cut versus time is included in the same figure. *Figure 6.16* is a plot of the produced pore volumes of oil versus the injected pore volumes of water.

In *Figure 6.15* the oil production rate remains constant till the moment of breakthrough at about 1000 days, after then, the oil production rate decreases till the producers are shut-in due to excessive water production (more than 90%) at 2100 days. At this time, 68.15% of the initial oil in place is produced.

The water-cut rises steadily from 0.001 (fraction) at 921 days to reach the maximum of 0.90 at 2100 days.

In *Figure 6.16* the production and injection pore volumes are almost the same till the moment of breakthrough (at 0.50 PV of water) after which injection of huge amounts of water results in very small increase in recovery. The injectors were shut-in after injecting 0.902 pore volumes of water. The produced pore volumes at shut-in time of the producers is 0.58 which is very close to the recoverable pore volumes of oil, 0.60.

6.6.5.2 RESULTS OF THE 2-D STUDY WITH PSEUDO PARAMETERS

The results of the 2-D model with pseudo parameters are presented in *Figure 6.17* and 6.18. In *Figure 6.17* the oil production rate is constant (straight line relationship) up to 960 days when the breakthrough occurs. After then, the oil production rate decreases with time due to excessive water production till the producer is abandoned at 1980 days. At this latter time the recovery is 67.5% which is close to the recoverable percentage of oil (70.6%).

The water-cut rises from 0.0028 at 980 days to reach over 90% at 1980 days.

Figure 6.18 demonstrates the cumulative oil production (in pore volumes) versus injected pore volumes of water. Obvious in the figure is the steady increase of oil production up to 980 days (breakthrough) when the oil production starts

Fig. 6.15 Water-cut & Dimensionless Oil production versus time (3-D model)

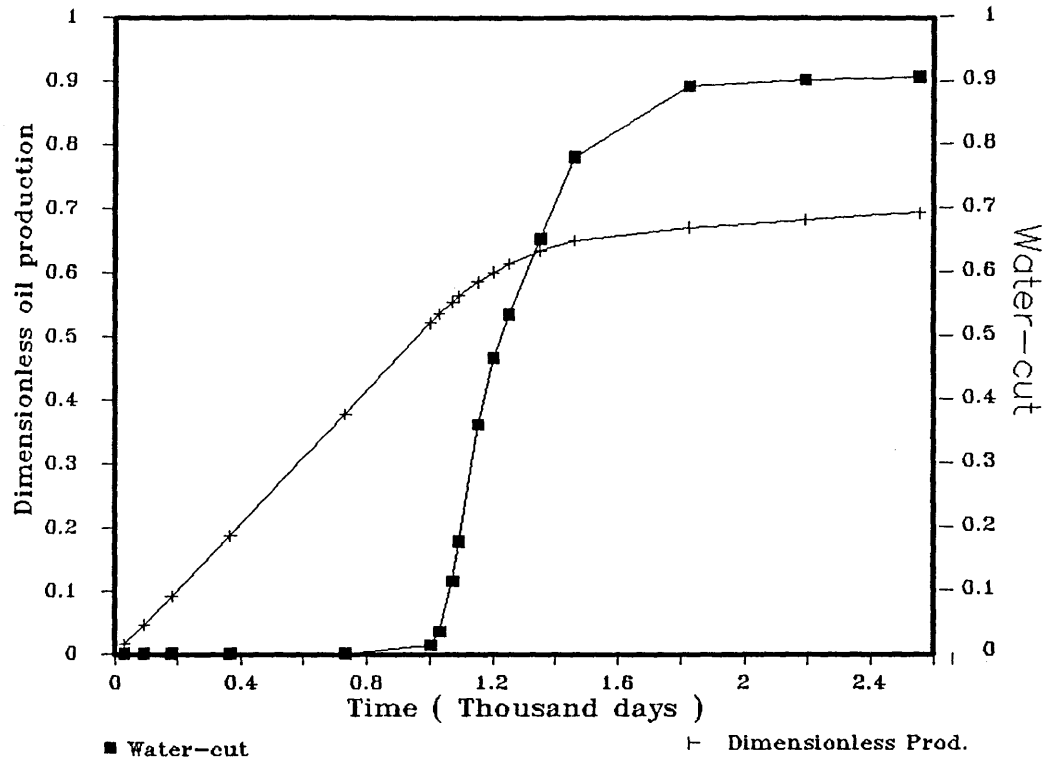


Fig. 6.16 Pore-volumes of Oil produced vs P.V. of water injected (3-D model)

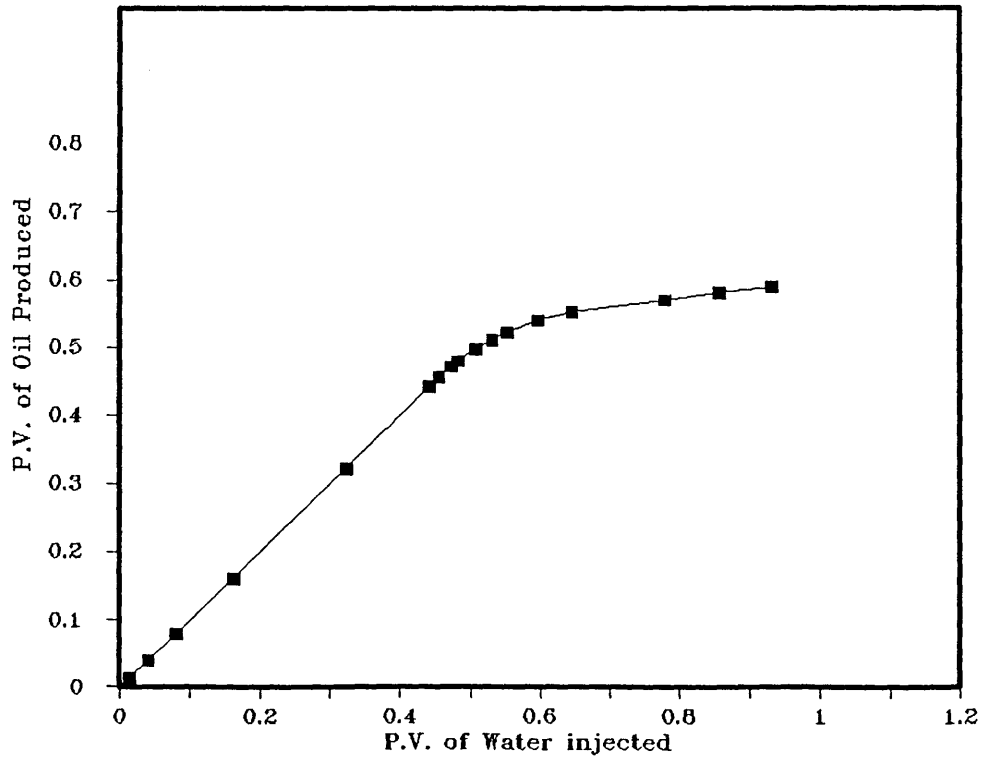


Fig. 6.17 Water-cut and Dimensionless Oil Prod. vs. Time (2-D with Pseudos)

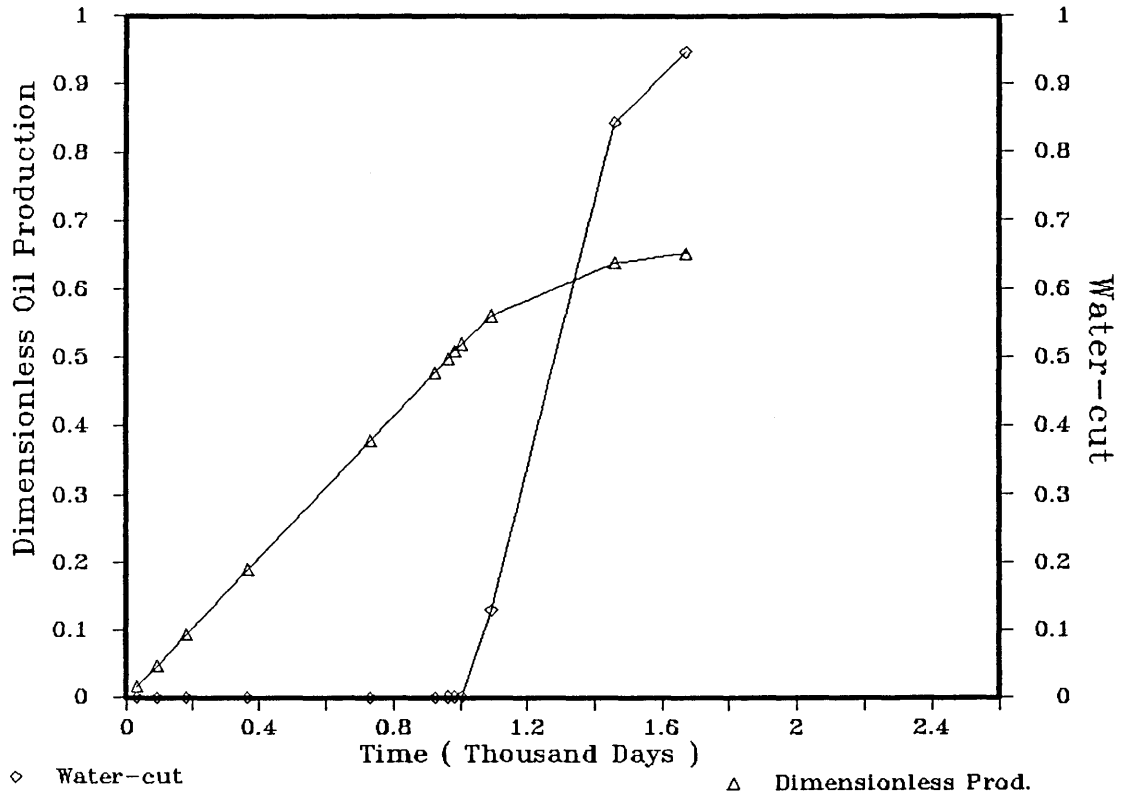
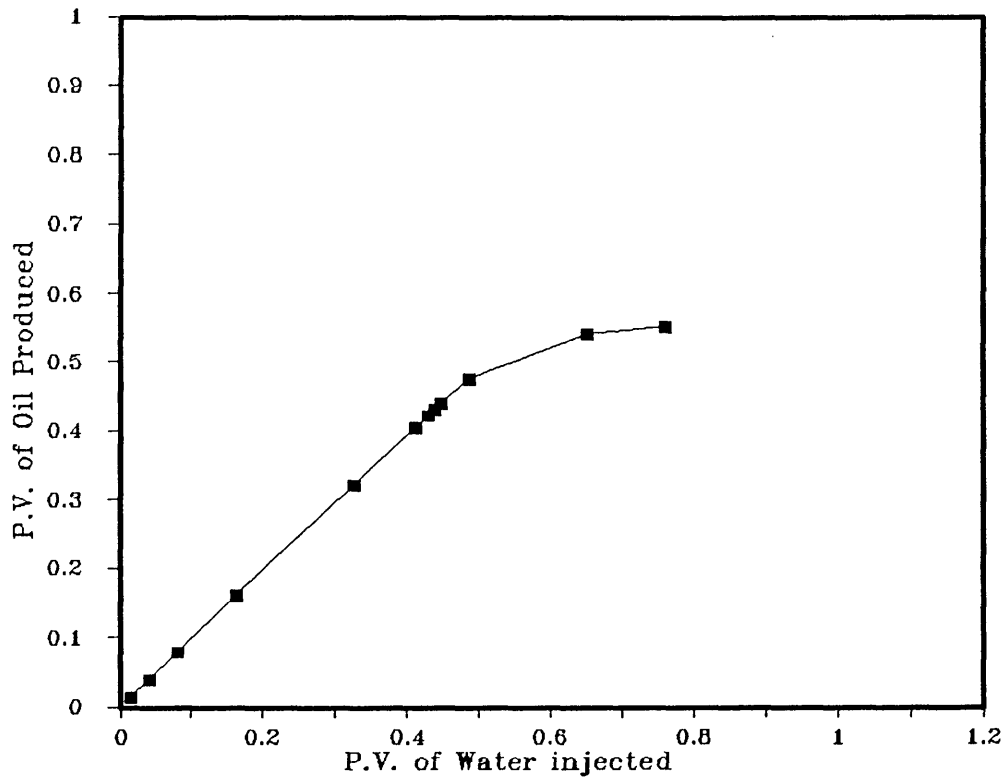


Fig. 6.18 Pore-volumes of Oil produced vs P.V. water inj. (2-D With Pseudos)



decreasing sharply. When the producer was shut-in the injected pore volumes were 0.78 giving 0.57 pore volumes of oil.

6.6.5.3 RESULTS OF THE 2-D STUDY WITHOUT PSEUDO PARAMETERS:

Figures 6.19 and 6.20 present the results of the 2-D model without pseudo parameters.

Figure 6.19 shows the dimensionless oil production and the water-cut versus time. Early breakthrough occurs at 800 days when the oil production decreases sharply with time. The resulting recovery factor was oil 57% when the producer was shut-in at 1620 days (due to exceeding 0.90 water-cut).

Water production starts from 800 days with a water-cut of 0.011 to reach a value of 0.90 at 1620 days.

Oil production versus injected water in pore volumes is plotted in *Figure 6.20*. Obvious in the plot is the sharp decrease of oil production after breakthrough. The producer was shut in 0.66 pore volume of water was injected and the produced pore volumes of oil was 0.46.

6.6.5.4 DISCUSSION OF THE SIMULATION RESULTS:

A combination plot of figures 6.15, 6.17, and 6.19 is presented in *Figure 6.21* for the sake of comparison. Water-cut versus time is presented in a separate combination plot, *Figure 6.22*.

In *Figure 6.21* the performance of all the models is the same up to 800 days when the curve of the 2-D model without pseudo- parameters diverges to give lower oil recoveries. The other models give the same performance up to 980 days when the 2-D model with pseudos slightly diverges towards lower recoveries, but the two curves stay fairly close till the shut-in of the producer in the 2-D model with pseudos at 1980 day. Shortly after, the producers of the 3-D model are also shut-in at 2100 days. The recovery obtained from the 3-D model was 68% while the 2-D model with pseudos gave 67.5%. The 2-D model without pseudos gave only 57% recovery due to improper representation of the reservoir connectivity by the model as grids apparently isolated may be connected through the rear grid-sections. Moreover, improper representation of the connectivities between the grid

Fig. 6.19 Water-cut and Dimensionless Oil Prod. vs. Time (2-D No Pseudos)

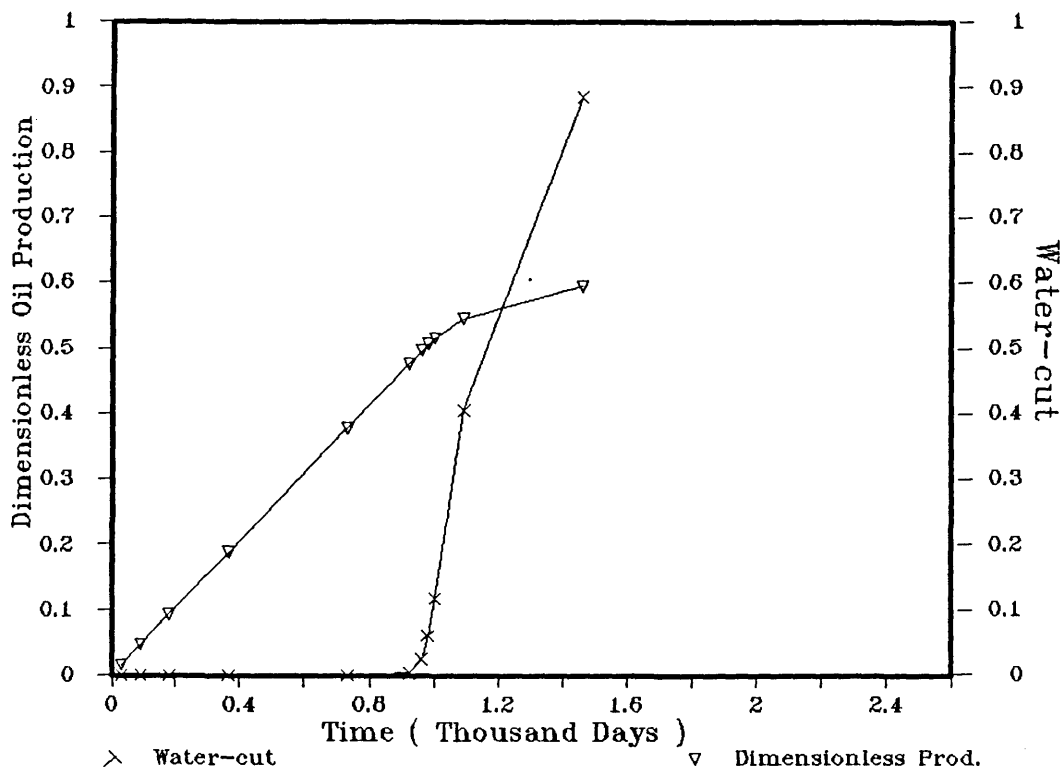


Fig. 6.20 Pore-volumes of Oil produced vs P.V. water inj. (2-D No Pseudos)

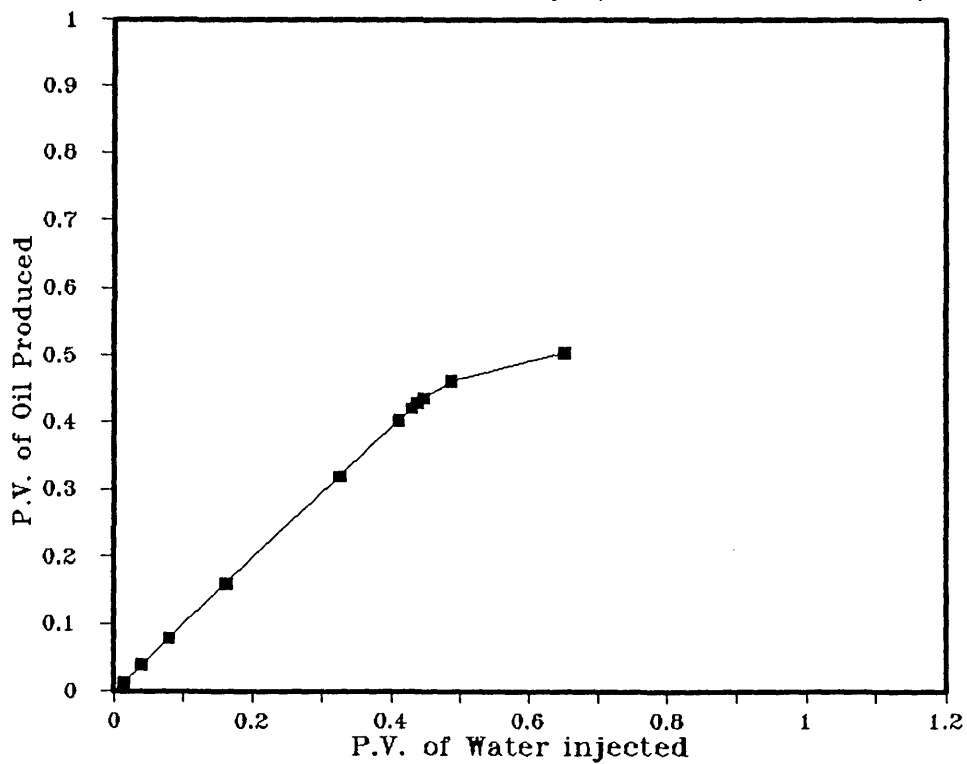


Fig. 6.21 Dimensionless oil prod. vs. Time (All Models)

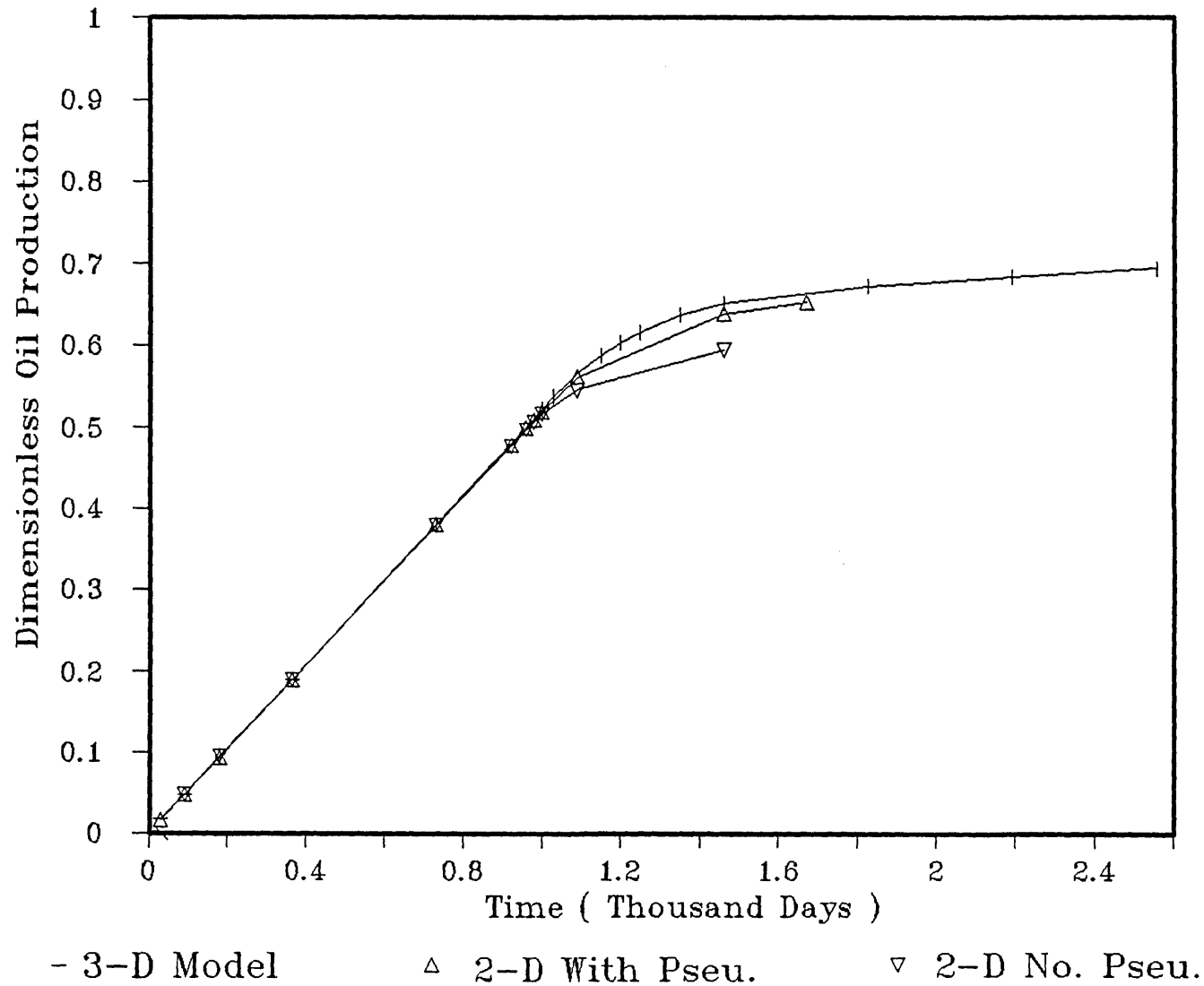
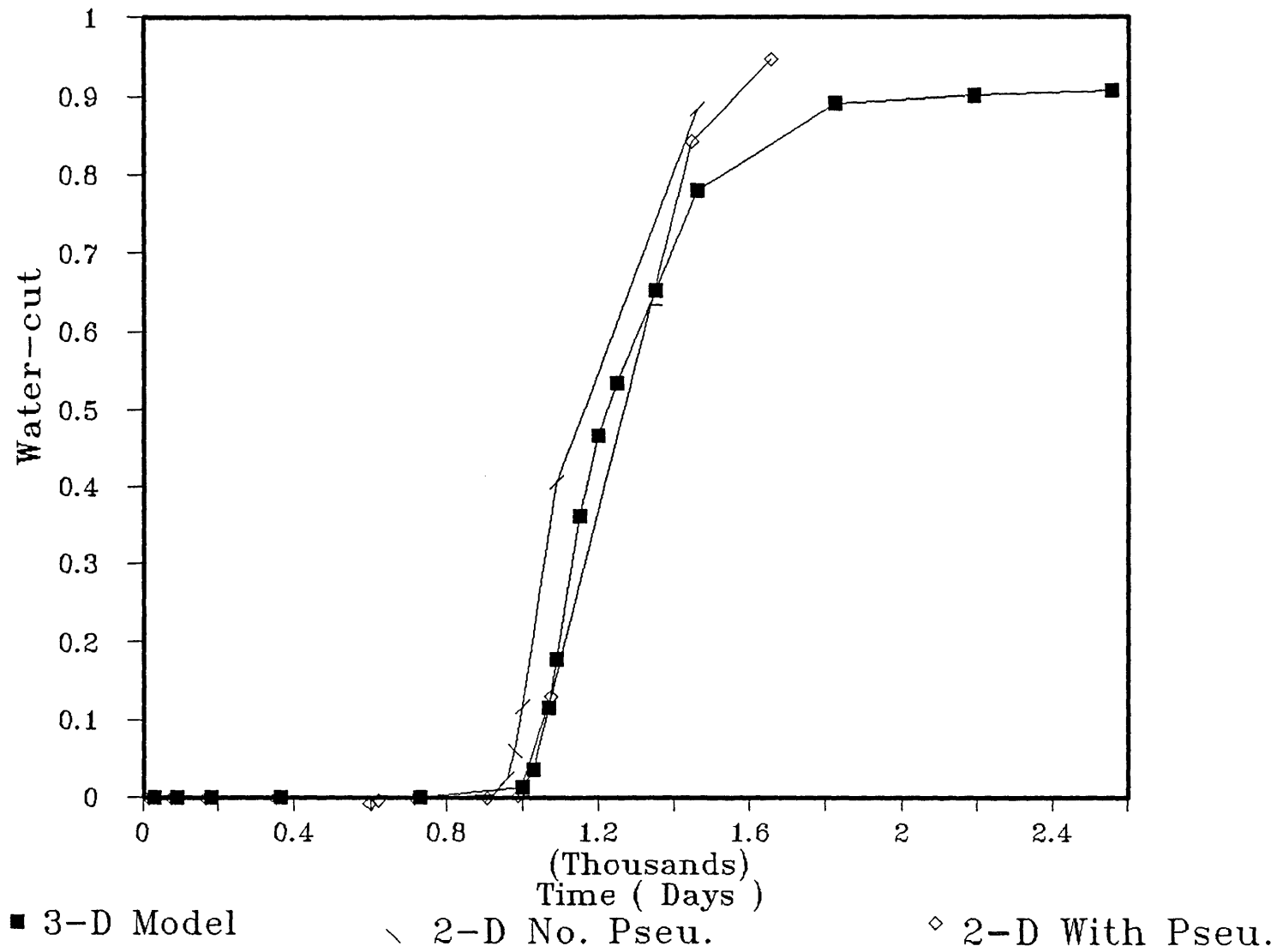


Fig. 6.22 Water-cut vs. Time for all Models



blocks decreases the floodability of the resulting model because many parts of the reservoir sand will be either isolated or appear as dead ends. Early breakthrough is expected due to decrease of floodable reservoir volume and the few number of paths leading from injector to producer. Injecting the same volume of water through a smaller number of paths will result in high speed of water advance and hence, early breakthrough. This can be clearly observed in *Figure 6.22* where model (ii) (without pseudos) gave very early breakthrough at 800 days.

The water-cut curves in *Figure 6.22* have the general features of a sharp increase of water-cut after breakthrough to reach about 0.70 in less than a year time. Above 0.70 water-cut increases relatively slowly revealing the trailing zone phenomenon which is taking place at this later stage of sweeping.

Model (i) (3-D) and model (iii) (2-D with pseudos) give almost identical water-cut curves due to their close breakthrough and abandonment times.

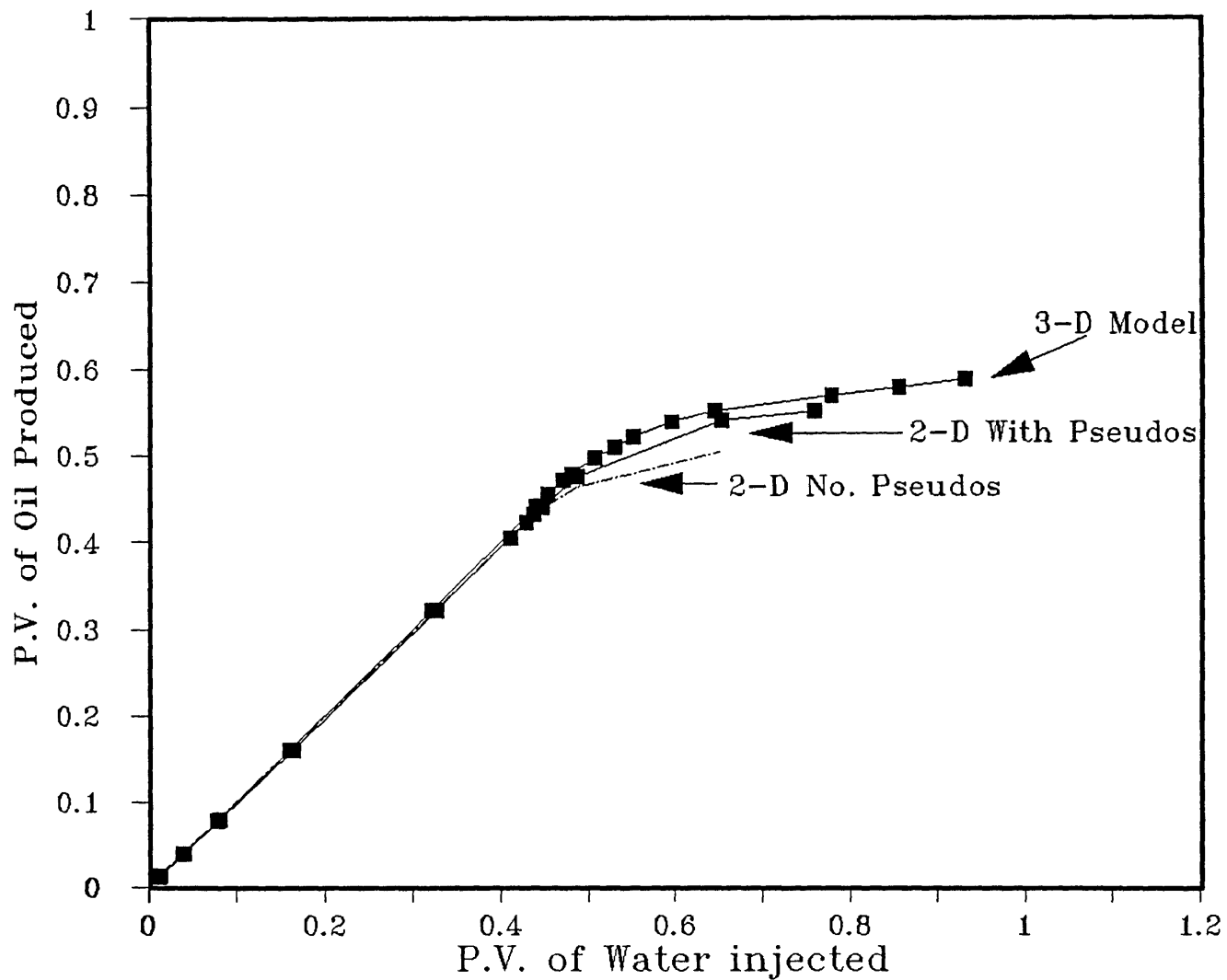
Figure 6.23 is a combination plot of figures 6.16, 6.18, and 6.20. Again, despite the slight difference in breakthrough times between model (i) and (iii) their performance curve stay very close and give almost identical recovery factors at abandonment of the producers, whereas model (ii) (no pseudos) diverges very early from the other models to give low recoveries at abandonment time.

The above comparisons reveal how accurate the 2-D model (with pseudos) represents the reservoir features carefully described by the 3-D model. The remarkable similarity in performance observed in figures 6.21, 6.22, and 6.23 suggests the use of the 2-D model enhanced with pseudo parameters to represent fluvial reservoirs composed of stochastic sands. Using such 2-D models will considerably reduce the computational time and hence, the computational cost. Moreover, the amount of computer memory needed to perform the simulation studies is highly reduced, therefore, the need of super computers or computers with large memory is eliminated.

6.6.5.5 SUMMARY:

A stochastic technique for modelling fluvial reservoirs composed of discontinuous sands is presented. The conditioning process applied in this technique simplifies the reservoir description for simulation and reduces the number of grid blocks needed for accurate reservoir description.

Fig 6.23 Pore-volumes of oil produced vs. P.V. of water injected (all models)



Appropriate definition of grid-block dimensions is key factor for reliable reservoir description in such stochastic domains, and use of the vertical transmissibility modifiers is indispensable for accurate representation of these complex networks.

An automatic reservoir parameter pseudoization procedure is introduced to represent the 3-D connectivities of fluvial reservoirs in 2-D model which results in considerable reduction in computational time and the required size of computer memory.

This parameter pseudoization technique also serves as an intermediate step for averaging the reservoir properties in a one-dimensional model which can be used for waterflood performance prediction by analytical methods. Detailed description of the averaging technique is presented in the next chapter.

CHAPTER 7

NUMERICAL AND ANALYTICAL PREDICTION OF WATERFLOOD PERFORMANCE OF FLUVIAL RESERVOIRS

7.1 INTRODUCTION

In the preceding chapter we have demonstrated the various new techniques applied for modelling and characterising fluvial channelized reservoirs. The network of the reservoir building blocks (sand bodies) was shown to be extremely complex and special techniques (Pseudoization) were used to represent the characteristics of the reservoir in two dimensional models.

Due to the complex architecture of these channelized reservoirs, straightforward application of simple one dimensional analytical methods to predict their waterflood performance is not possible. Averaging the reservoir properties in one-dimensional models is a prerequisite for application of such methods.

In this chapter, averaging of the reservoir permeabilities is performed using a new hybrid averaging technique while other properties are averaged using various conventional techniques (arithmetic, geometric, etc ...).

A single layer as well as a 3-layer anisotropic models were generated as a result of the averaging process. These models were verified by comparison of their waterflood performance with the performance of the 3-D model, and then used by the analytical waterflood prediction methods (13, 31, 34, 81) to predict the performance of the reservoir (ignoring the permeability anisotropy, using the horizontal permeability).

A detailed discussion of the results is given at the end of this chapter. In the next section the techniques used in averaging the reservoir properties are discussed.

7.2 AVERAGING THE RESERVOIR PROPERTIES

Different techniques are used to average the various reservoir parameters due to the particular characteristics of each parameter. Calculation of the averaged value of the reservoir parameters is demonstrated below.

7.2.1 AVERAGING THE HORIZONTAL AND VERTICAL PERMEABILITIES

Averaging of the reservoir permeabilities is performed in two stages. At the first stage the 3-D characteristics of the reservoir are represented in a 2-D model via the pseudoization technique presented in the preceding chapter. The resulting horizontal and vertical permeability maps include pseudo values that are considered in the second averaging stage.

7.2.1.1 AVERAGING THE HORIZONTAL PERMEABILITY

Due to the directional nature of permeability, the conventional averaging techniques such as arithmetic and geometric means may not give accurate results. Moreover, geometric or harmonic averaging is not applicable for domains with zero permeabilities such as reservoirs composed of stochastic sand bodies and shale. Considering the shales to have negligibly small permeabilities the above averaging methods could be used, but the reliability of their results is still questionable. Cardwell and Parsons (16) compared the harmonic and arithmetic averages of permeability of a heterogeneous model, *Figure 7.1*, with the results of an electric analogy experiment. They found that – for various arrangements of permeability – the equivalent permeability of the model lies between the harmonic and arithmetic averages. The harmonic mean always gave the lower value.

Recently, King(56) presented the renormalization averaging technique which is analogous to the electric networks. This technique can handle systems with zero permeabilities similar to Cardwell and Parsons approach (16).

The second stage of averaging the horizontal permeability involves averaging by the arithmetic, harmonic, renormalization, and a combination arithmetic/harmonic method. The renormalization and the combination methods are used to reduce the range of the expected representative value between the harmonic and arithmetic averages. The considered representative value is the arithmetic mean of the values calculated by the renormalization and the combination methods. Numerical simulation is then used to verify the accuracy of the representative value.

Before performing the above calculations the values of the permeability map are weighted according to the respective volume of sand in each grid block. This weighting is done by multiplying the permeability of each grid-block by the NTG

value in that block. This weighting is done automatically during the sand generation process (chapter 6) at the end of the pseudoization stage. The averaging is then performed as follows :

- (i) Read the permeability values taking four at a time from the end of the top two layers.
- (ii) Calculate the average permeability of the four grid blocks and assign it to a coarser grid as shown in *Figure 7.2*.
- (iii) Repeat steps (i)-(ii) moving to the other end of the grid layers. If the number of grids in the layer is odd then the grid before the last one in both grid layers will be used twice, the second time with the last grids to find an average value for the four grids.
- (iv) Repeat steps (i)-(iii) moving vertically – taking two grid layers at a time – towards the bottom of the reservoir. If the number of grid layers is odd, then the grid layer before the last will be used twice, the second time with the grids of the bottom layer.
- (v) Repeat steps (i)-(iv) for the new generated permeability map (coarser grids) till the permeability is reduced to one value.

The averaging calculations in step (ii) are performed using the various averaging techniques as follows :

1 - The arithmetic average K_{ar} :

The averaged permeability is given by,

$$K_{ar} = \frac{(K_1 + K_2 + K_3 + K_4)}{4} \quad (7.1)$$

where,

K_1, K_2, K_3, K_4 = Permeabilities of the four grid blocks, see *Figure 7.1*.

K_{ar} = the averaged permeability of the grid blocks.

The value obtained for our model is 485.54 md.

Fig. 7.1 Averaging a model with 4 permeabilities

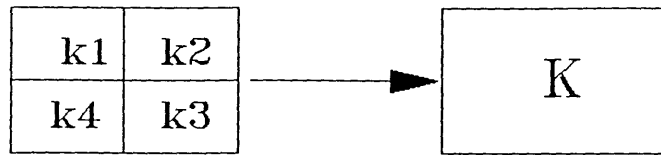
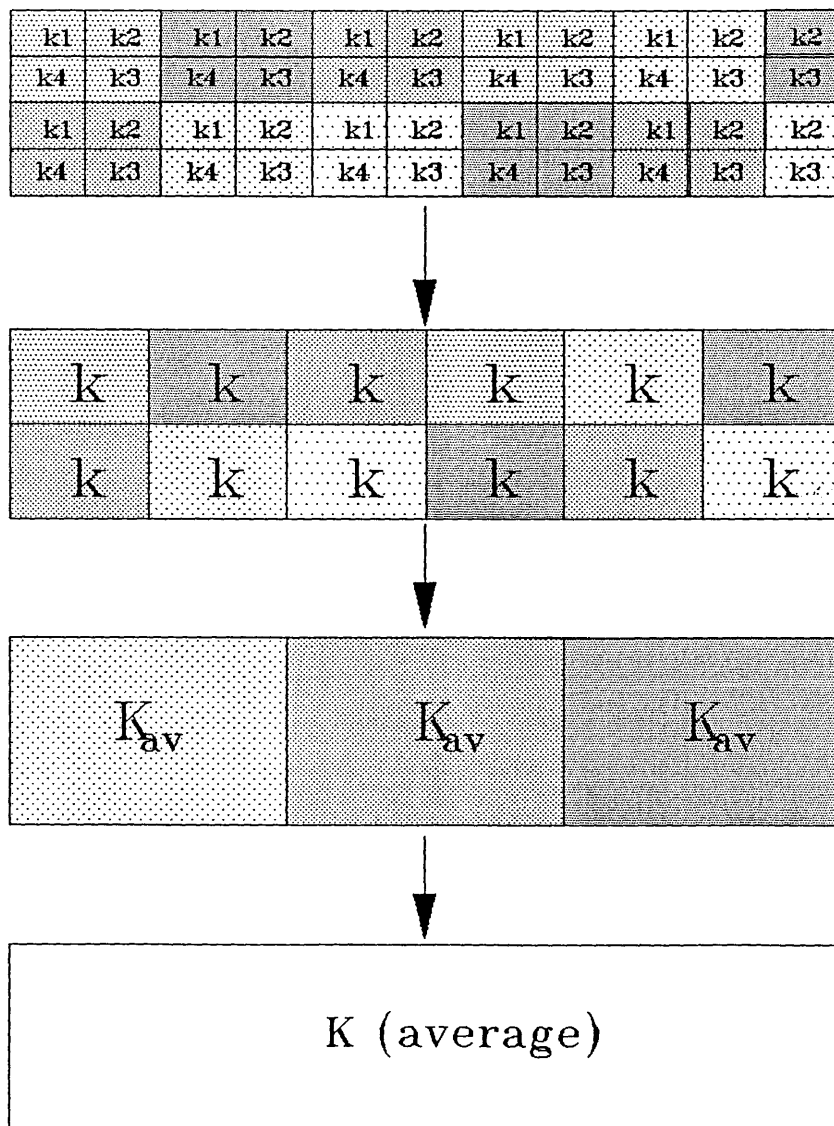


Fig. 7.2 Averaging the horizontal permeability



2 - The harmonic average K_{hr} :

Find the harmonic average of each two grid blocks in series (in the horizontal direction) and then find the arithmetic average of the resulting values. Therefore, the average is given by,

$$K_{hr} = \left(\frac{2}{\frac{1}{K_1} + \frac{1}{K_2}} + \frac{2}{\frac{1}{K_4} + \frac{1}{K_3}} \right) / 2 \quad (7.2)$$

$$K_{hr} = \left(\frac{1}{\frac{1}{K_1} + \frac{1}{K_2}} + \frac{1}{\frac{1}{K_4} + \frac{1}{K_3}} \right)$$

The value obtained for our model is 375.32 md

3 - The renormalization average K_{nr} :

The two dimensional renormalization technique is applied in our case using the following equation:

$$K_{nr} = 4(K_1 + K_3)(K_2 + K_4)[K_2K_4(K_1 + K_3) + K_1K_3(K_2 + K_4)] \\ *[(K_2K_4(K_1 + K_3) + K_1K_3(K_2 + K_4))(K_1 + K_2 + K_3 + K_4) \\ + 3(K_1 + K_2)(K_3 + K_4)(K_1 + K_3)(K_2 + K_4)]^{-1} \quad (7.3)$$

The value obtained for our model is 389.311 md.

4- The combination average K_{co} :

Averaging by the combination method is also performed as a second stage averaging process (after pseudoization and weighting). The calculations using this method are effected as follows :

- (i) Divide the reservoir model into vertical slides, each slide one grid wide and extending from top to bottom of the reservoir.
- (ii) Find the arithmetic average of the grid permeabilities in each slide.
- (iii) Find the harmonic average of the permeabilities calculated in step (ii). The resulting single value, K_{co} , is the representative permeability of the reservoir by this method.

The value obtained for our model is 403.2 md.

The averaged horizontal permeability of the reservoir, K_H , is given by:

$$K_H = \frac{(K_{co} + K_{nr})}{2} \quad (7.4)$$

$$K_H = 396 \text{ md}$$

The resulting average permeabilities from all methods are always in the following sequence:

$$K_{hr} < K_{nr} < K_H < K_{co} < K_{ar}$$

A computer program is coded for calculation of the various averages. This program reads the permeability map from a data file prepared by the sand modelling program, performs the calculations, and prints the resulting averages. This program (OKING), is listed in appendix 7.A at the end of this dissertation.

7.2.1.2 Averaging the vertical permeability

The vertical permeability map needs further treatment after pseudoization. This treatment is needed to compensate for the transmissibility modifiers which were used to define the reservoir connectivity. Therefore, grid blocks with NTG ratios less than 1 are assigned zero vertical permeability as they do not transmit flow in the flow direction. The resulting permeability map is then read by the averaging programme (OKING) to calculate the various averages. In this case, due to the change of flow direction, the vertical permeabilities of the grid blocks are read four by four moving in the vertical direction from bottom to top of the reservoir. Reaching the top of the reservoir, the program starts reading another set permeabilities for two grid columns and so on.

The same averaging methods in the previous section are used and the final averaged value is calculated by equation (7.4).

The average vertical permeabilities obtained for our model are:

$$K_{ar} = 108.774 \text{ md}, K_{hr} = 21.69 \text{ md}$$

$$K_{nr} = 23.69 \text{ md}, K_{co} = 25 \text{ md}$$

Therefore, the vertical permeability for our model is:

$$K_V = 24 \text{ md}$$

7.2.2 AVERAGING THE POROSITY

The equivalent homogeneous (with permeability anisotropy) model of the reservoir has the same dimensions as the original reservoir model. The new net-to-gross (NTG) value will be 1 for all the grids.

Considering the porosity, the averaged value for the homogeneous model must conserve the initial oil in place. Unlike permeability – which is characterized by its directional nature – averaging of porosity is simple and straightforward. The porosity value in each grid block is weighted (according to the respective volume they represent) by multiplying them by the value of NTG in that block. The arithmetic average of the resulting (weighted) porosity map is the averaged porosity of the reservoir. The average porosity for our model is 0.133 (fraction).

7.2.3 GENERATION OF THE AVERAGED RELATIVE PERMEABILITIES

The averaged horizontal permeability, K_H , is being used to generate the average relative permeability curves following the same procedure presented in section (6.6.1).

The average relative permeabilities generated for our model are shown in table 7.3 in chapter 7 of this thesis.

7.3 SIMULATION OF BUILD-UP AND DRAW-DOWN TESTS TO VERIFY THE AVERAGED HORIZONTAL PERMEABILITY

Earlier in this chapter, the representative permeability of the domain was considered the arithmetic mean of the values obtained by the renormalization and the combination methods as shown by equation (7.4). In this section a simulation study is used to verify the validity of the calculation method. The idea is to simulate pressure build-up and draw-down tests in the reservoir and find the reservoir effective horizontal permeability by test analysis. The equations used for test analysis are based on radial flow conditions, therefore, to apply them for calculation of the effective horizontal permeability of our model, a special transformation must be done to the 2-D model (with pseudo parameters) to form a radial model without losing the structure for which we need the averaged permeability. In the next section transformation of the 2-D model is discussed in detail.

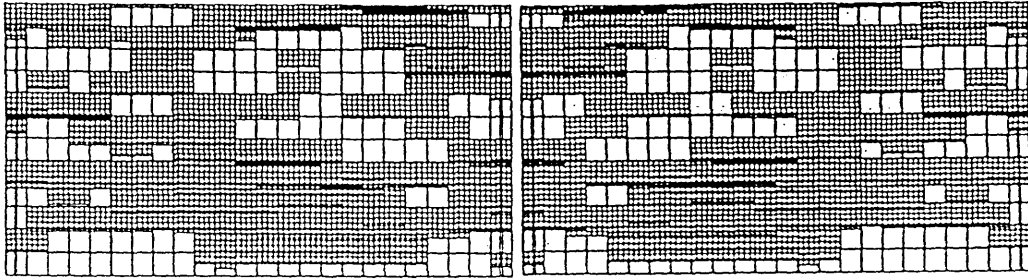


Fig. 7.3 Cross-section of the radial-cylindrical model

7.3.1 CONSTRUCTION OF THE RADIAL MODEL

Consider the 2-D model in *Figure 6.13*. To transform this model into a radial model, the following procedure is followed:

(i) Add one grid column at the left edge of the 2-D model to be used for locating the producer. This grid column will have the same grid thickness and width as the other grids of the model while its length is smaller (360ft instead of 400ft).

(ii) Divide this grid column into six grid columns to maintain gradual increase of the grid lengths from the well outwards as recommended for radial models. The resulting six grid lengths are (8,12,20,40,100,180 foot) from the edge of the model (the well).

* To transform the 2-D model into radial all the grid blocks are extended to form circular rings around the left edge (the well). The resulting shape is a radial cylindrical model. *Figure 7.3* is a cross-section of this model with the producer located at its centre (the left edge of the 2-D model).

Now our model is 30 grids long, 1 grid wide (cylindrical), and 12 grids high.

* Due to the big size of the reservoir, which might not be affected by the test, the model dimensions are scaled down by a factor of 0.1 so as to keep the whole model within the range of the radius of investigation.

Due to the symmetry of the radial model around the well, the draw-down or build-up test permeability is similar to the effective (linear) horizontal permeability of the original 2-D model.

In the test analysis, the total model thickness must be used as the reservoir thickness because the resulting effective permeability will represent an equivalent homogeneous model.

The test procedure simulated in this study is described in the next section.

7.3.2 THE TEST PROCEDURE

* Perforate all the grids containing sand which are all the grids except grid No.7 from the top.

- * Maintain the oil production rate at 6000 STB/Day for 25 hours.
- * Shut-in the well for 25 hours.
- * Record the draw-down and build-up pressure as shown tables 7.1 and 7.2.

7.3.3 ANALYSIS OF THE TEST RESULTS

The general data of the field are given below:

Depth of reservoir top = 10000 ft

Datum (for pressure measurements) = 10012 ft

Reservoir Thickness, $h = 24$ ft

Oil viscosity, $\mu_o = 0.3$ cp

Oil formation volume factor, B_o , (at 5500) = 1.2365 bbl/stb

Initial Reservoir pressure, $P^* = 5500$ psia

Well radius, $R_w = 0.25$ ft

7.3.3.1 Analysis of the Draw-down test (101):

The draw-down pressure readings are shown in table 7.1 (column 3) with the corresponding flow time in minutes. The well was flowed for 25 hours taking pressure readings at very small intervals at the beginning five hours, and every one or two hours towards the end of the flow period when the well is shut-in.

To examine the validity of our data for test analysis, a log-log data plot is required to estimate the end of the storage period. Therefore, column 4 - in table 7.1 - is prepared by subtracting the pressure readings from the initial reservoir pressure (5500 psia). The pressure change is plotted against flow time as shown in *Figure 7.4*. In this plot no unit slope appears and all the points fall after the storage period which is negligible. After about 10 hours the reservoir boundaries are felt by the test. This is demonstrated by the deviation of the pressure - change to give higher values with increasing time (higher pressure drop with time).

Figure 7.5 is a semi-log draw-down curve for the well. This figure shows no storage period while the beginning of the semi- steady state period (when the reservoir boundaries are felt) is about 9 hours. This is indicated by the higher pressure drop and deviation of the points from the straight line. The slope of the straight line drawn through the points of the transient period, M , is 35 psi/cycle and the permeability, K , is given by (68),

$$K = \frac{162.6 Q \mu_o \beta_o}{M * H} \quad (7.5)$$

Where,

Q = Average flow rate, 6000 STB/Day.

M = Slope of the semi-log curve (Psi/log cycle).

H = Reservoir thickness 24 foot.

β_o = Oil formation volume factor, 1.2365 Barrel/STB.

μ_o = Oil viscosity, .3 cp.

Therefore,

$$K = \frac{162.6 * 6000 * 0.3 * 1.2365}{35 * 24}$$

$$K = 430.8 \text{ md}$$

Fig. 7.4 Log-Log plot (Drawdown Test)

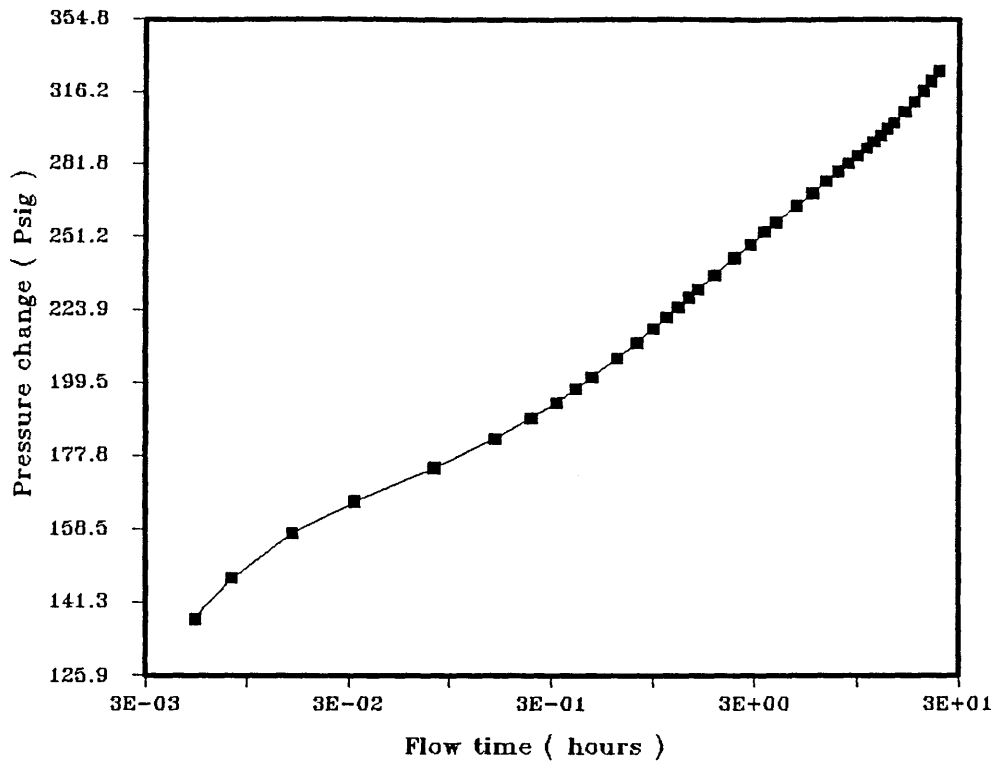


Fig. 7.5 Semi-log Drawdown curve

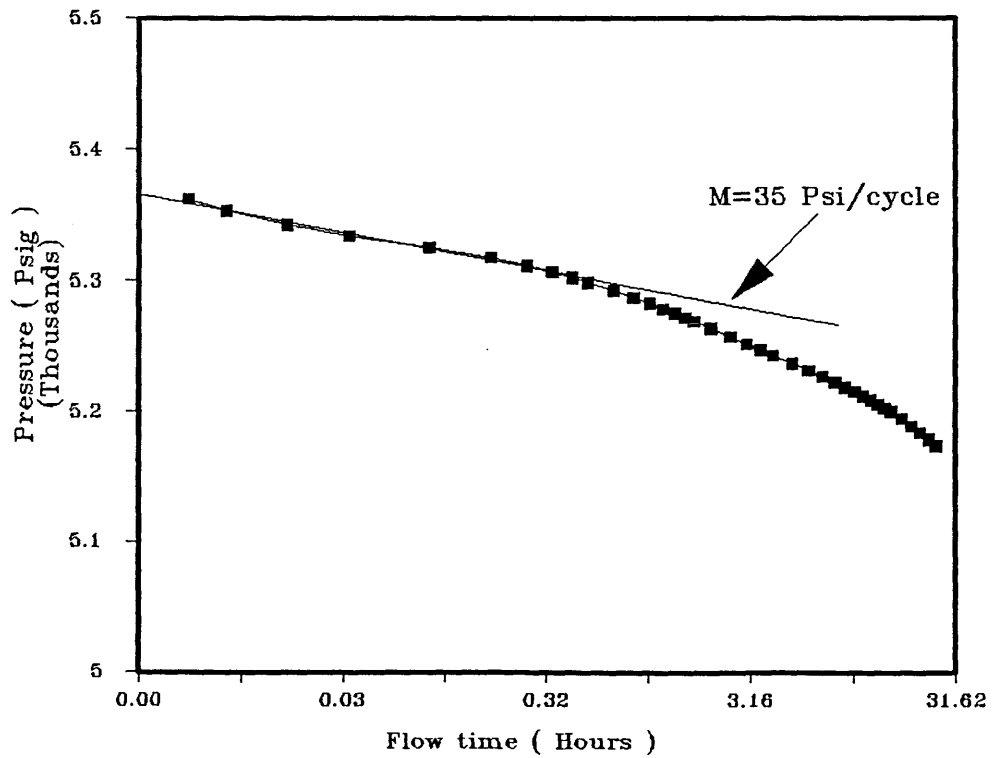


Table 7.1 Analysis of the draw-down test

No.	Time (minutes)	BHFP (psia)	$P_i - P_{wf}$
1	0.33	5362.5	137.5
2	0.5	5353.3	146.7
3	1	5342.5	157.5
4	2	5334.5	165.5
5	5	5325.7	174.3
6	10	5317.5	182.5
7	15	5311.6	188.4
8	20	5307	193.0
9	25	5302.7	197.3
10	30	5299	201
11	40	5292.9	207.1
12	50	5287.7	212.3
13	60	5283.1	216.9
14	70	5279.0	221
15	80	5275.4	224.6
16	90	5272.1	227.9
17	100	5269.0	231.0
18	120	5263.8	236.2
19	150	5257.4	242.6
20	180	5252.0	248.0
21	210	5247.3	252.7
22	240	5243.2	256.8
23	300	5236.6	263.4
24	360	5231.1	268.9
25	420	5226.1	273.9

No.	Time (minutes)	BHFP (psia)	$P_i - P_{wf}$
26	480	5221.9	278.1
27	540	5218.0	282.0
28	600	5214.5	285.5
29	660	5211.2	288.8
30	720	5208.1	291.9
31	780	5205.1	294.9
32	840	5202.2	297.8
33	900	5199.4	300.6
34	1020	5193.9	306.1
35	1140	5188.6	311.4
36	1260	5183.4	316.6
37	1380	5178.3	321.7
38	1500	5173.2	326.8

7.3.3.2 Reservoir limit testing (101) :

The objective of this test is to verify the above calculations by calculating reservoir volume using the draw-down test results and comparing with the actual reservoir pore volume (which is known for our model). The pressure data from table 7.1 are plotted versus flow time on cartesian coordinates as shown in *Figure 7.5 (a)*.

The slope of the data at the late flow period (straight line), M^* , is used in the calculation of the reservoir volume in the equation below (68).

$$HA\phi = \frac{-0.23395Q\beta_o}{M^*C_t}$$

Where,

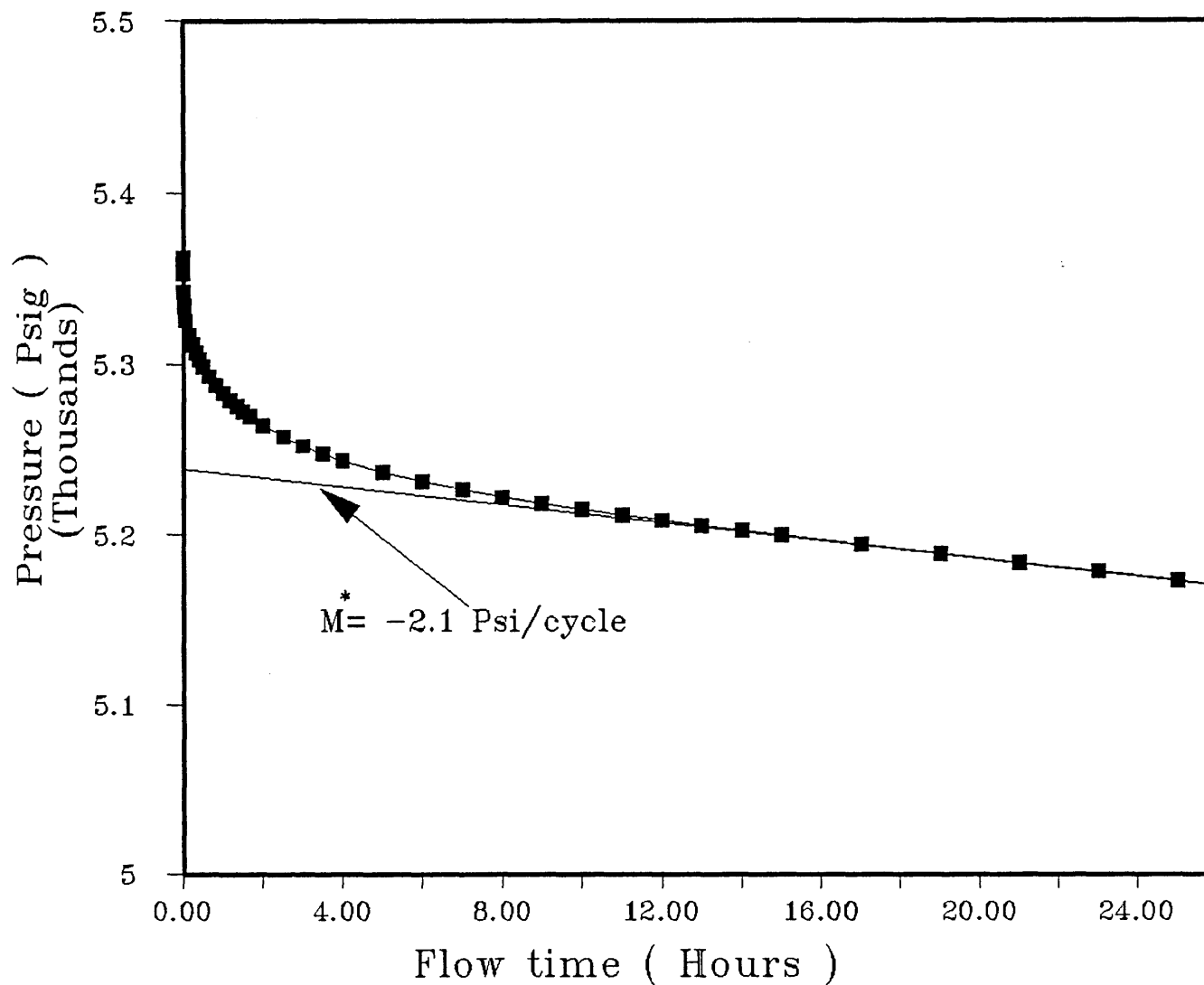
H = Reservoir thickness.

A = Reservoir area.

ϕ = Porosity.

C_t = Total compressibility.

Fig. 7.5 (a) Cartesian plot of the Drawdown data



$$C_t = S_o C_o + S_w C_w + S_g C_g + C_f$$

Where,

S_o, S_w, S_g = Oil, water, and gas saturations.

C_o, C_w, C_g = Oil, water, and gas compressibilities.

Calculations:

$$C_t = 0.85 * .9057 * 10^{-4} + 0.15 * 8 * 10^{-6} + 0.0 + 1 * 10^{-5}$$

$$C_t = 8.8184 * 10^{-5} \text{ Psi}^{-1}$$

$$M^* = 2.1 \text{ Psi/hour (from Figure 7.5 (a))}$$

Then,

$$\begin{aligned} HA\phi &= \frac{-0.23395 * 6000 * 1.2365}{2.1 * 8.8184 * 10^{-5}} \\ &= 9373009 \text{ foot}^3 \\ &= 1669280 \text{ Barrel} \end{aligned}$$

The value obtained for the reservoir pore volume is comparable with the actual volume which is 1725931 barrels. The results of this test verify the accuracy of the above tests to simulate the actual reservoir performance.

7.3.3.3 Analysis of the build-up test (101):

The well was shut-in after flowing for 25 hours. The shut-in pressure readings are recorded in table 7.2 with the corresponding shut-in times. Column 5 of the same table shows the pressure change (shut-in pressure minus final flowing bottom hole pressure) which is plotted against the shut-in time on log-log paper as shown in *Figure 7.6*. All points in the plot fall after the storage period as the portion of the curve with unit slope is absent.

Column 4 of table 7.2 shows the calculated values of the Group $(T_P + \Delta t)/\Delta t$

Where,

T_p = production time (25 hrs)

Δt = shut in time, hours.

P_{ws} = Shut-in pressure.

The final flowing bottom hole pressure (FFBHP), P_{wf} , is 5173.2 psia, the shut-in time is 25 hours, and the well radius is .25 foot.

Horner plot for the pressure build-up data is shown in *Figure 7.7*. Inspection

of the plot reveals that the reservoir is finite (as we know), which is manifested by the flattening of the curve at the end of the shut-in period. Storage effects dominated the whole first hour as shown by divergence from the straight line at the right side of the curve. The straight line (drawn through the points of the infinite-acting period) has slope of 46 psi/cycle and intercept 5493.0 psia with the vertical axis.

Therefore the effective permeability is given by equation 7.5 as follows,

$$K = \frac{162.6 * 6000 * 1.2365 * .3}{24 * 46}$$

$$= 327.8 \text{ md}$$

A representative permeability for the domain can be given by the arithmetic average of the values obtained by the above tests, therefore,

$$K_{eff} = \frac{(430.8 + 327.8)}{2} \text{ md}$$

$$= 379.3 \text{ md}$$

which is very identical to the hybrid effective permeability calculated in section 7.2.1.1, 396 md. This identical similarity verifies the hybrid averaging technique for calculation of the effective permeabilities of reservoir domains composed of stochastic sands.

Fig. 7.6 Log-Log plot (Build-up test)

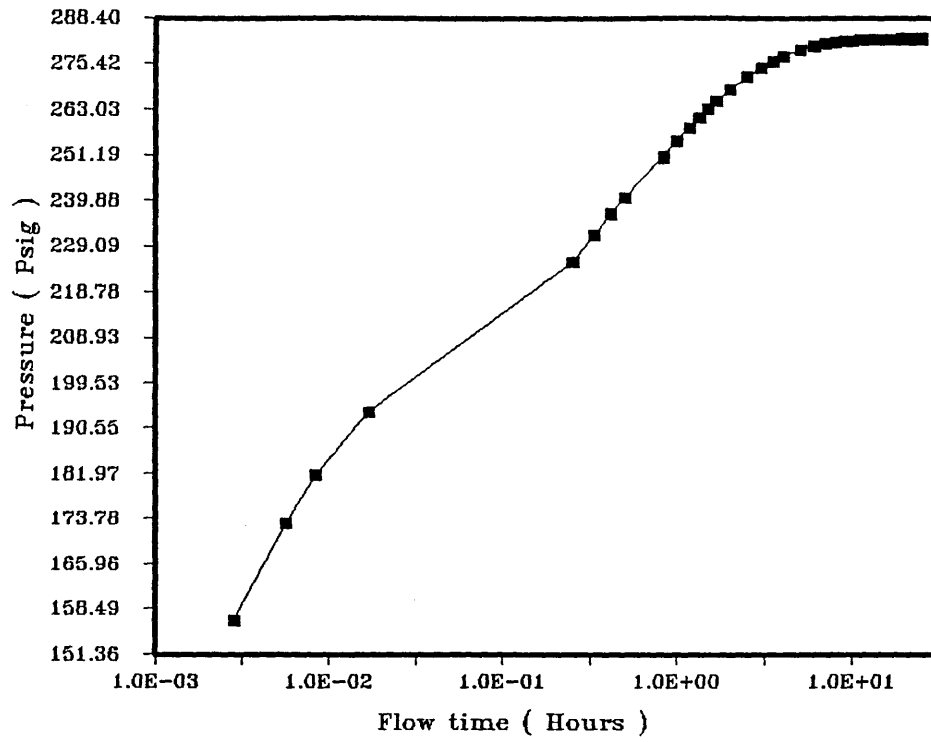


Fig. 7.7 Horner plot (Build-up test)

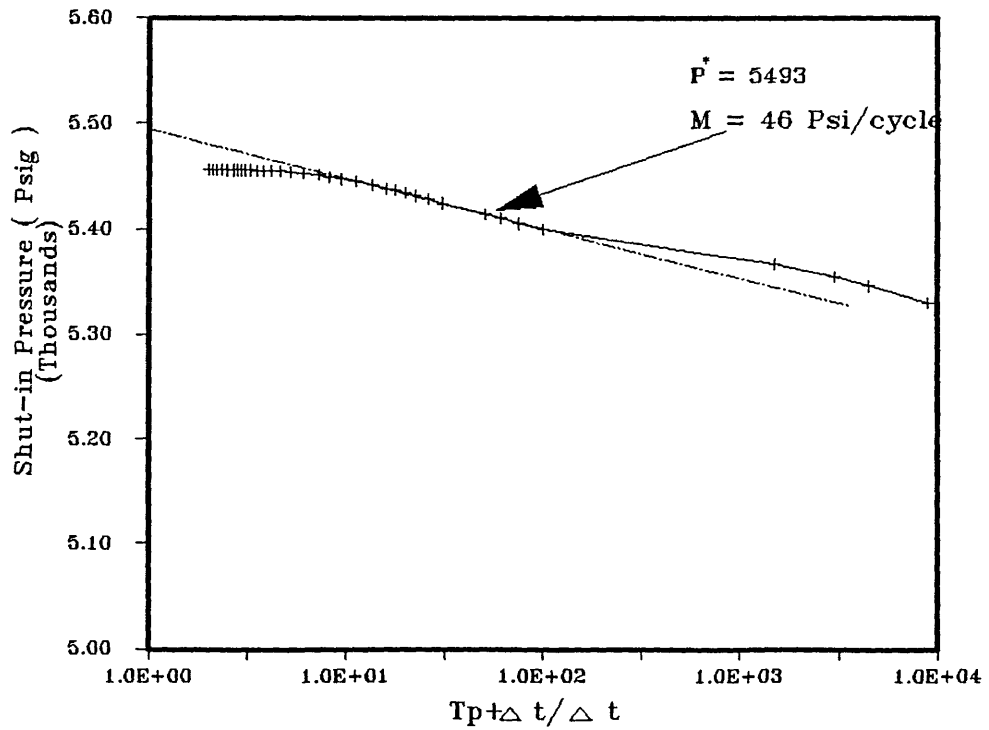


Table 7.2 Analysis of the build-up test

No.	Time(min.)	Pressure (psia)	$\frac{T_p + \Delta t}{\Delta t}$	$P_{ws} - P_{wf}$
1	0.168	5329.7	8928	156.5
2	0.336	5346.1	4465	172.9
3	0.5	5354.9	3001.	181.7
4	1	5366.9	1501	193.7
5	15	5398.6	101.0	225.4
6	20	5404.9	76.0	231.7
7	25	5409.9	61.0	236.7
8	30	5413.8	51.0	240.6
9	50	5423.8	31.0	250.6
10	60	5427.8	26.0	254.6
11	70	5431.2	22.43	258.0
12	80	5433.9	19.75	260.7
13	90	5436.3	17.67	263.1
14	100.0	5438.3	16.0	265.1
15	120.0	5441.4	13.50	268.2
16	150.0	5444.8	11.00	271.6
17	180.0	5447.3	9.33	274.1
18	210.0	5449.1	8.14	275.9
19	240.0	5450.5	7.25	277.3
20	300.0	5452.4	6.0	279.2
21	360.0	5453.6	5.17	280.4
22	420.0	5454.3	4.57	281.1
23	480.0	5454.8	4.13	281.6
24	540.0	5455.1	3.78	281.9
25	600.0	5455.2	3.50	282.0

No.	Time(min.)	Pressure (psia)	$\frac{T_p + \Delta t}{\Delta t}$	$P_{ws} - P_{wf}$
26	660.0	5455.4	3.27	282.2
27	720.0	5455.4	3.08	282.2
28	780.0	5455.5	2.92	282.3
29	840.0	5455.5	2.79	282.3
30	900.0	5455.5	2.67	282.3
31	1020	5455.5	2.47	282.3
32	1140	5455.6	2.32	282.4
33	1260	5455.6	2.19	282.4
34	1380	5455.6	2.09	282.4
35	1500	5455.6	2.00	282.4

7.4 SIMULATION OF THE RESERVOIR PERFORMANCE USING AN ANISOTROPIC MODEL

Using the average properties calculated in the previous section, a representative homogeneous model (with anisotropic permeabilities) can be prepared. This model – which has the same dimensions as the original 2-D model (with pseudos) – should give the same performance as the 2-D model (with pseudos) if the averaging techniques are sufficiently accurate. This model can then be used by the analytical (one dimensional) waterflood performance prediction techniques. In this case the vertical permeability (which is very low) will be ignored, which is always the case in 1-D methods.

To verify how well the homogeneous model represents the 2-D model (with pseudos), a simulation study is done using the homogeneous model with the same scheduling data used for the 2-D model in chapter 6.

A listing of the simulation data file prepared for this homogeneous model is given in Appendix 7(b) and the results of the simulation study are discussed below.

7.4.1 Comparison of simulation results of the homogeneous model with the 2-D & 3-D models

The simulation results of the homogeneous model are plotted with the 2-D and 3-D results in *Figure 7.8*, *Figure 7.9*, and *Figure 7.10*. *Figure 7.8* includes plots of the dimensionless oil production versus time for the three models. In this figure we can see the remarkable similarity between the performance of the three models. Water breakthrough occurs at 1010 days for the homogeneous model while it occurs at 1000 days for both other models. The performance of the homogeneous model stays almost identical with the other two models up to the time when the producer is shut-in due to excessive water production (more than 90% water-cut) at 1700 days. The recovery factor obtained is 69.3% which is close to the factors obtained from the 2-D model, 65.2% and almost identical to the one obtained from the 3-D model, 68.2%. The higher recovery obtained by the homogeneous model as compared with the 2-D model is due to the 100% accessibility of the homogeneous model. The dead ends (that are not floodable) and isolated accumulations of oil in the 2-D model (with pseudos) do not exist in the homogeneous one and there is no means to quantify them in terms of irrecoverable volumes. Due to the higher accessibility of the 3-D model, the dead ends or isolated accumulations phenomena are less severe, therefore, the recovery obtained from the 3-D model is higher than the 2-D model.

Figure 7.9 shows the plots of pore-volumes of oil produced versus pore-volumes of water injected for the three models. At abandonment time of the homogeneous model (1700 days) the injected pore-volumes (P.V.) of water were 0.757 which gave 0.5869 P.V. of oil while 0.758 P.V. of water gave 0.552 P.V. of oil for the 2-D model at 1640 (its abandonment time). For the same time (1700 days) 0.732 P.V. of water injected in the 3-D model gave 0.564 P.V. of oil while the abandonment recovery (2100 days) is 0.58 P.V. The remarkable similarity observed in the above results is further reinforced by comparison of the water-cut curves in *Figure 7.10*. The general shape of the three curves is almost similar. A time lag of about 50 days is observed between similar water-cut values in the homogeneous and 2-D curves, but the time lag decreases to less than 20 days for water-cut values greater than 60%. The curve for the 3-D model stays identical to the 2-D model up to 65% water-cut, where it diverges to give lower water-cut values up to 90%. This log trailing zone is due to production of the less floodable (partial communication with the rest of the reservoir) areas or low permeability zones.

Fig. 7.8 Dimensionless Oil Prod. versus Time (Homogeneous, 2-D pseudos & 3-D)

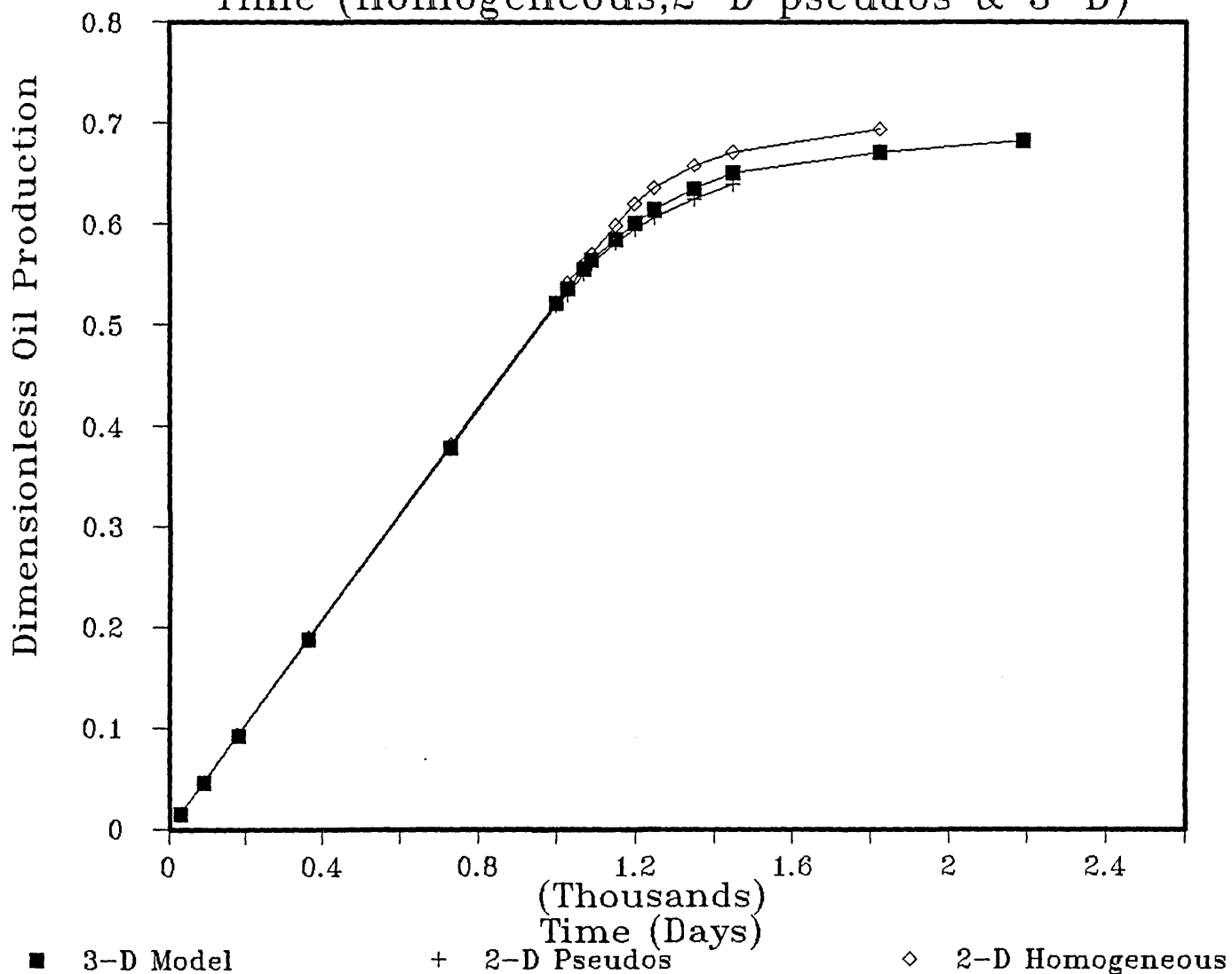


Fig. 7.9 Pore volumes Oil Prod. vs P.V.
Water Inj.(Homo., 2-D Pseu., & 3-D)

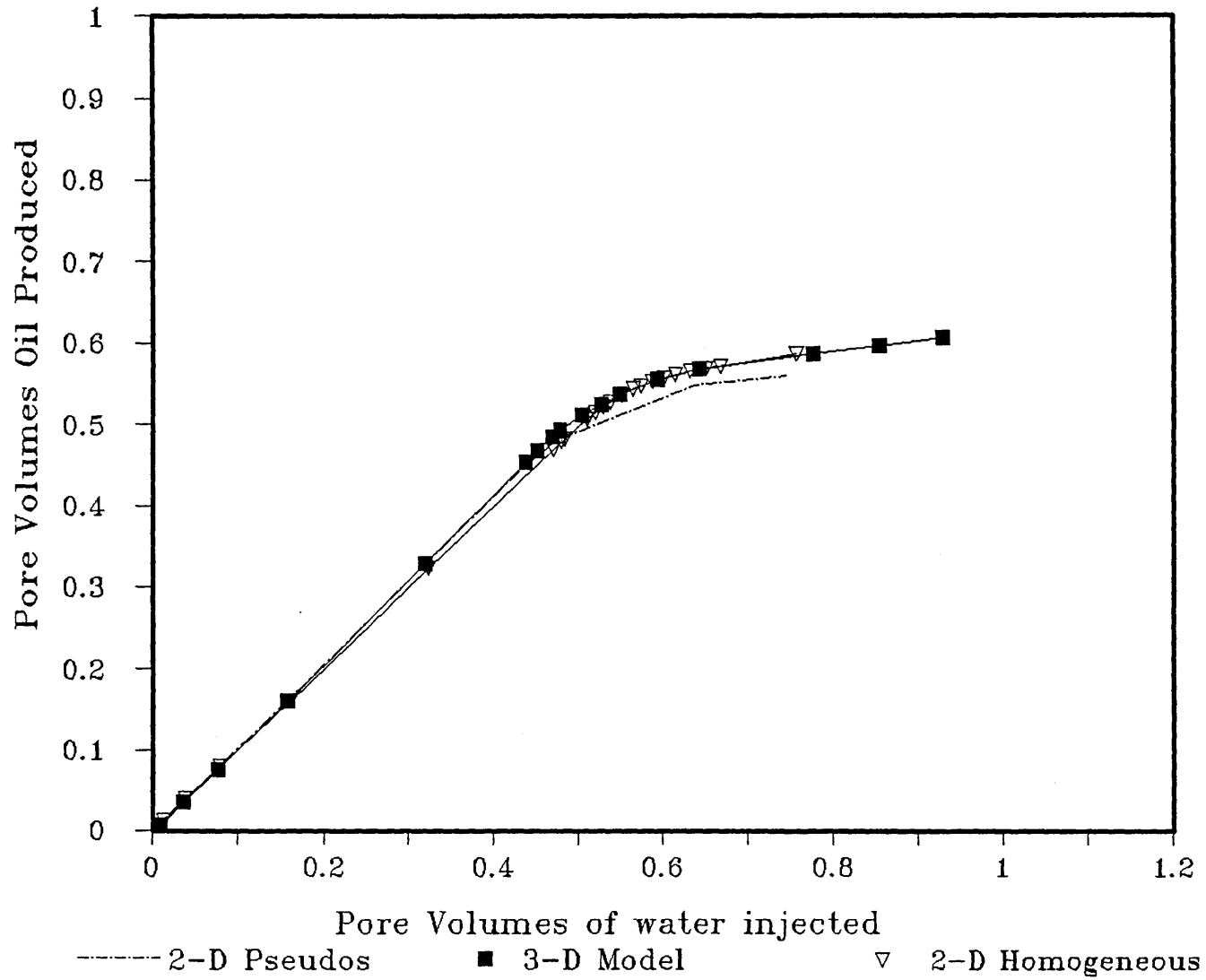
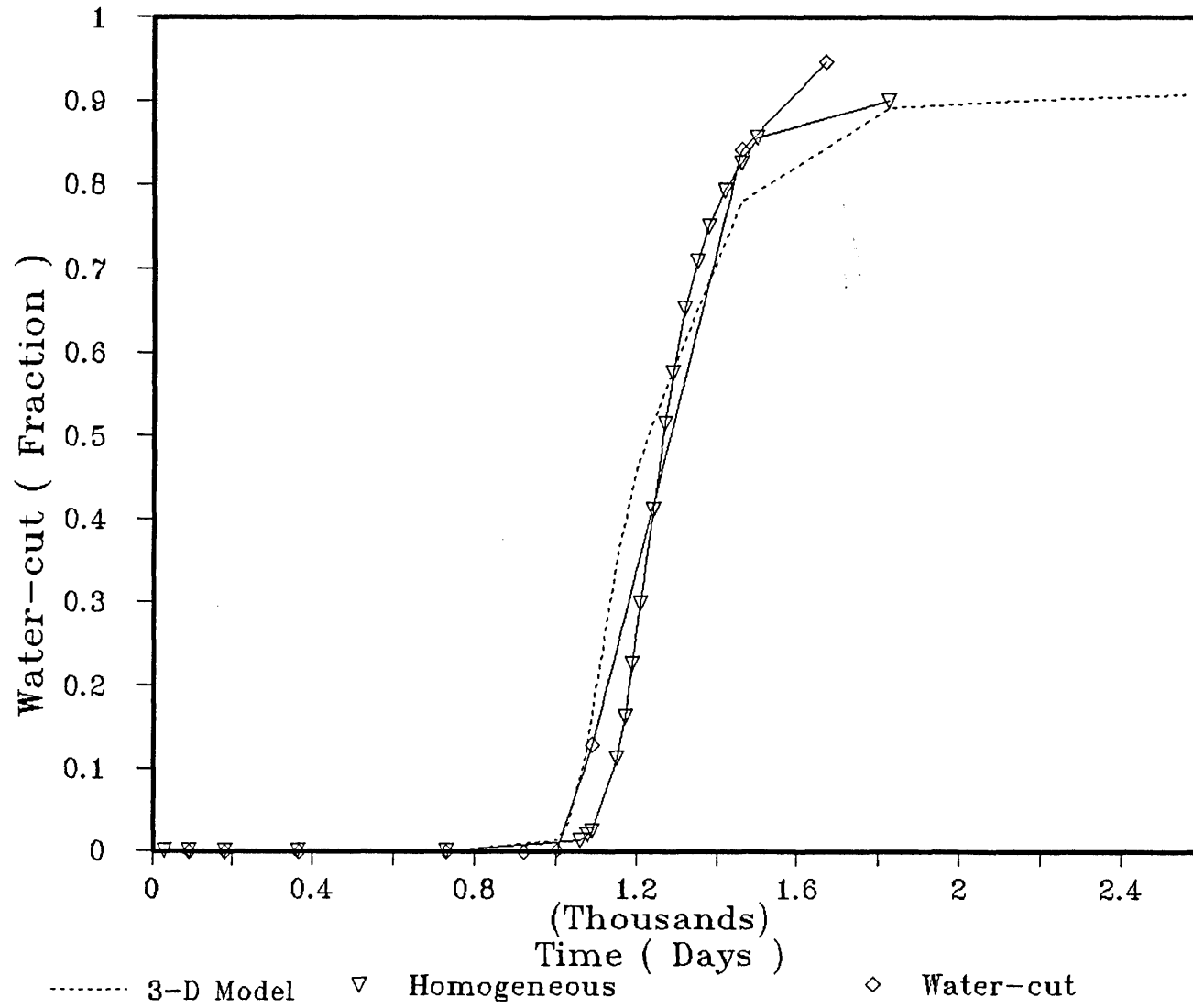


Fig. 7.10 Water-cut vs. Time
(Homo., 2-D Pseu., & 3-D)



In general, there is reasonable agreement between the curves of the 2-D model (with pseudos) and the homogeneous model; and between the homogeneous and 3-D models up to 75% water-cut.

From the above comparisons we can infer the reasonable representation of the 3-D model by the homogeneous model which validates the averaging techniques applied.

Since the vertical permeability of the homogeneous model is very low (24 md) compared with horizontal permeability (396 md), vertical fluid flow (gravity segregation) is negligible and fluid flow in the model is effectively one-dimensional. Therefore, ignoring the vertical permeability (the anisotropy), the model becomes one-dimensional. In this case, straightforward application of analytical waterflood performance prediction methods is quite possible as will be shown later in this chapter.

The water saturation profile along the reservoir (front shape) is closely studied to understand the behaviour of the water front before and after breakthrough. Discussion of the relevant observations is given below.

7.4.2 Observations on water-front profiles for different rates.

To study the characteristics and behaviour of the water-front during the flooding process, the water saturation profile is plotted along the reservoir length (using the simulation results of the homogeneous model) at various times using different injection rates, *Figure 7.11(a)*, *Figure 7.11(b)*. Close inspection of these curves indicates three distinct zones of the water saturation profile. The front section is steeply dipping and the points are approximately in a straight line, the intermediate part, which is concave, and the higher part in which all the points are approximately in one line gently dipping.

It is also noticed that at breakthrough time, when the toe of the water-front reaches the producer, area (A) approximately equals area (B) in *Figure 7.11(b)*. In other words, at breakthrough time, the average water saturation in the reservoir equals the water-front saturation, S_{wf} deduced from the curve of water-cut versus water saturation which is prepared using the fraction flow equation (23).

Using these observations, the actual breakthrough time, TB_a , at which the toe of the water-front reaches the producer can be calculated. Moreover, the water-cut

versus time can be calculated approximately for the early breakthrough times till the water saturation at the producer reaches about two thirds of S_{wf} , thereafter the intermediate (transitional) part of the saturation profile begins.

The following calculations demonstrate how the above observations can be used. Comparisons are made between Buckley-Leverett and the simulation results for various injection rates. The method introduced here will be denoted by (Observation method).

7.4.3 Calculation of the actual breakthrough time.

The water-cut versus water saturation curve *Figure 7.12* is prepared using the fractional flow equation as shown in table 7.3. From this figure (7.12) the water saturation at the shock front is 0.65 (fraction), whereas the average water saturation at the reservoir at breakthrough time – using the shock front convention – is 0.70 (fraction). The breakthrough time (BTT) in days using Buckley-Leverett (BL) is calculated as follows:

$$BTT = \frac{(\bar{S}_w - S_{wi}) * PV}{Q} \quad (7.6)$$

Where,

\bar{S}_w = Average water saturation at BTT.

S_{wi} = Initial water saturation.

Q = Daily injection or production rate in reservoir barrels.

PV = Reservoir pore volume in barrels.

Therefore, for our homogeneous model, for Q = 9900 RB/Day,

$$BTT = \frac{(0.70 - 0.15) * 21880401}{9900}$$

$$BTT = 1215.6 \text{ Days}$$

whereas the breakthrough time using our simulation observations (breakthrough happens when average water saturation = S_{wf}) is given by

$$BTT = \frac{(0.65 - 0.15) * 21880401}{9900}$$

$$BTT = 1105 \text{ Days}$$

The time when the toe of the water-front reaches the producer (BTT) for the simulation study was 1010 days.

Similar calculations were done for a higher injection/production rate, 20000 RB/D, and the following results were obtained:

BTT for BL = 601 Days

Simulation = 495 Days

Observation method = 547 Days

Fig. 7.11(a) Water saturation profiles

Inj. = Prod. = 9900 RB/D

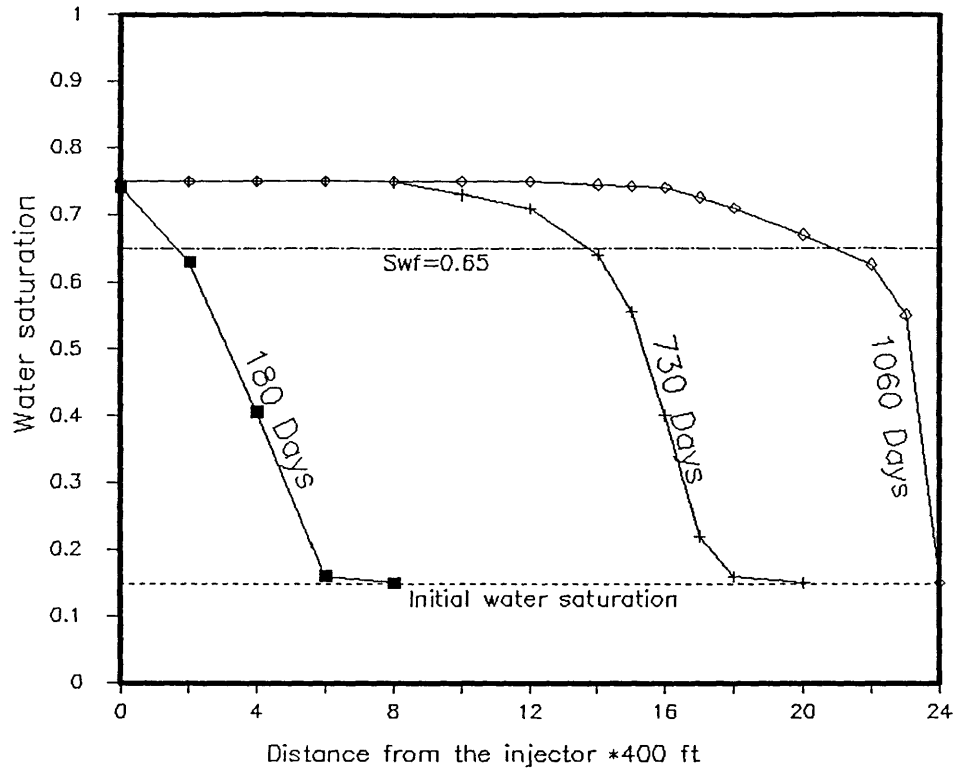
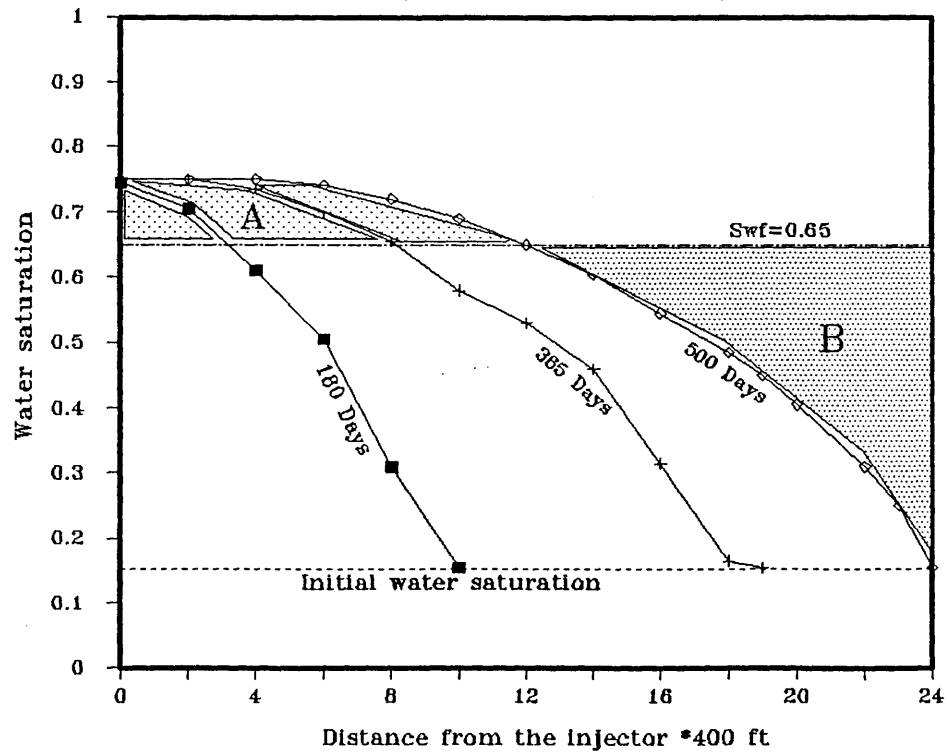


Fig. 7.11(B) Water saturation profiles

Inj. = Prod. = 20000 RB/D



S_w	K_{ro}	K_{rw}	K_{ro}/K_{rw}	f_w
0.15	0.78	0.00	∞	0.0
0.25	0.69	0.0118	58.81	0.0167
0.35	0.444	0.047	10.45	0.0957
0.45	0.250	0.106	2.36	0.2978
0.55	0.111	0.189	0.587	0.630
0.60	0.063	0.239	0.268	0.791
0.63	0.040	0.272	0.147	0.872
0.65	0.028	0.295	0.095	0.9133
0.70	0.007	0.357	0.0196	0.981
0.75	0.000	0.425	0.0000	1.000

Table 7.3 Calculation of the water-cut

Prediction Methods	Injection Rate RB		
	5000	9900	2000
	Breakthrough Times (Days)		
BL	2407	1215	601.7
Simulation	1995	1050	505
Observation	2079	1050	519.7

Table 7.4 Breakthrough times for different rates (Rock type B)

Fig. 7.12 Water-cut vs water saturation
(Homogeneous Model)

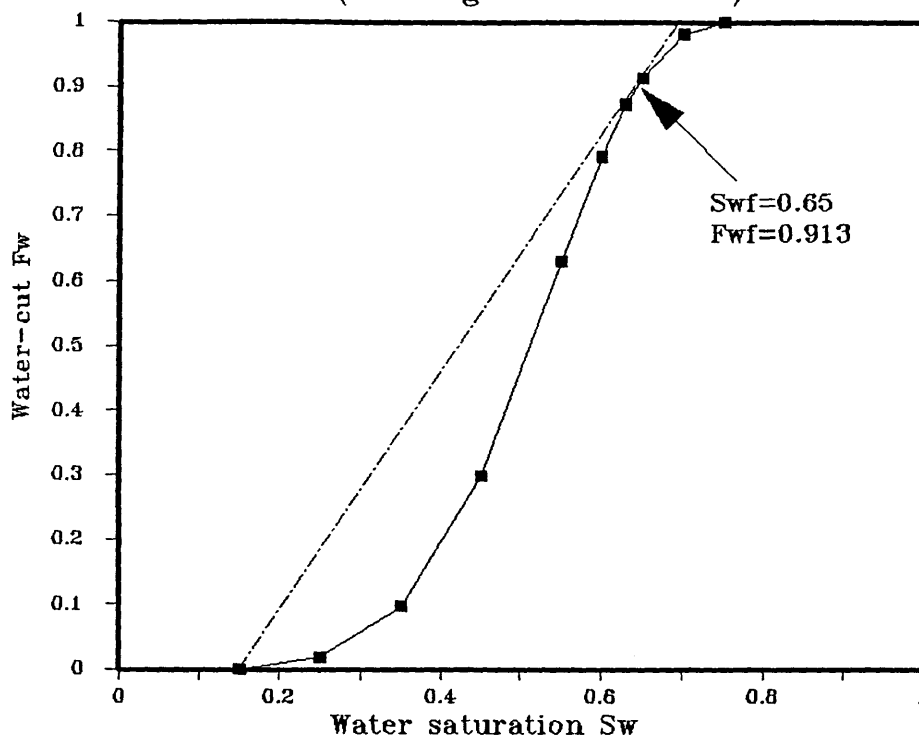


Fig. 7.13 Water-cut vs Time
(Homogeneous Model Rate=9900 RB/D)

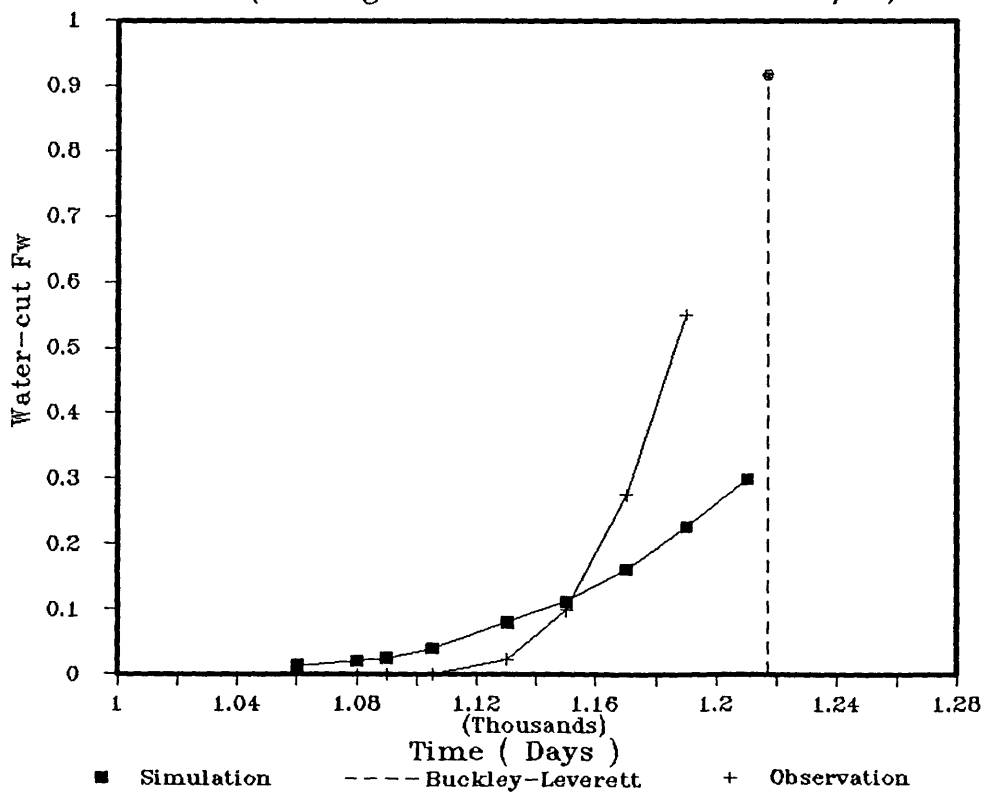


Table 7.4 shows the results of similar calculation for another rock type (type B) with $S_{wf} = .575$ and $\bar{S}_w = 0.65$. As we can see from these calculations, there is reasonable agreement between the simulation results and the observation method, specially at high injection rate when the water-front is very steep and its toe is completely within the straight line zone (in the front part of the water saturation profile) *Figure 7.11(a),(b)*. At low injection rates the slope of the water-front is very small (sharp angle), and its toe diverges from the straight line zone to give earlier BTT. This is due to the considerable time allowed for gravity segregation to take place.

Calculation of the water-cut up to the time when the water saturation at the producer S_{we} , equals $2/3 S_{wf}$ is demonstrated in the next section.

7.4.4 Calculation of the water-cut before the shock-front value

The slope of the first straight line of the front in *Figure 7.11 (a)* can be calculated as follows:

$$\frac{\Delta S_{we}}{\Delta t} = \frac{S_{wf} - S_{wi}}{BTT_b - BTT_o} \quad (7.7)$$

Where,

ΔS_{we} = Increase of water saturation at the producer in Δt time.

BTT_b = BTT calculated by Buckley-Leverett.

BTT_o = BTT calculated by the observation method.

The above equation applies for the case where $S_{we} < 0.6S_{wf}$.

Water saturation at the producer, S_{we} , calculated for the two rates (9900, 20000 RB/D) as shown in tables 7.5 and 7.6 and the corresponding water-cut values are read from *Figure 7.12* using the calculated S_{we} values *Figure 7.13* and *Figure 7.14* show plots of the water-cut versus time for the observation method, the simulation study (homogeneous model), and Buckley-Leverett method, for two injection rates 9900 and 20000 RB/D.

Figure 7.15(a),(b),(c) show plots of water-cut versus time for the other rock type (type B) for which the breakthrough times are shown in table 7.4.

It can be inferred from the above plots that, the time when the toe of the

water-front reaches the producer can reasonably be estimated by the observation method presented here, and the water-cut values for the early breakthrough times can be estimated with a time lag of ± 30 days which is a very short time compared with oilfield production lives.

The above calculations are applicable for stable flow conditions presented by Dietz(23) where the front shape is regular. Great difference in breakthrough times will result if the method is used with unstable flow due to water segregation and bypassing at the bottom of the reservoir.

The simulation results of the homogeneous model – which represents our 3-D reservoir performance – can be used as a base case for the one-dimensional analytical methods which are to be used for predicting the waterflood performance of our stochastic reservoir. In the next section, Buckley-Leverett method will be used for prediction of our reservoir performance.

Time (Days)	Δt	ΔS_{we}	S_{we} $(S_{wi} + \Delta S_{we})$	Water-cut	Remarks
1105	0.0	0.0	0.15	0.0	BT time
1130	25	0.1126	0.2626	0.0225	
1150	45	0.2027	0.3527	0.0975	
1175	70	0.3153	0.4653	0.3450	$S_{we} = 2/3 S_{wf}$
1200	95	0.4279	0.5779	0.7200	

$$\frac{\Delta S_{we}}{\Delta t} = 4.505 * 10^{-3} \text{ 1/Day}$$

Table 7.5 Water-cut calculation for injection rate 9900 RB/Day

Time	Δt	ΔS_{we}	S_{we}	Water-cut	Remarks
547	0.0	0.0	0.15	0.0	BT time
560	13	0.1204	0.2704	0.025	
580	33	0.3056	0.4556	0.315	$S_{we} = 2/3 S_{wf}$
600	53	0.4907	0.6407		

$$\frac{\Delta S_{we}}{\Delta t} = 9.259 * 10^{-3} \text{ 1/Day}$$

Table 7.6 Water-cut calculation for injection rate 2000 RB/Day

Fig. 7.14 Water-cut vs Time
 (Homogeneous Model Rate=20000 RB/D)

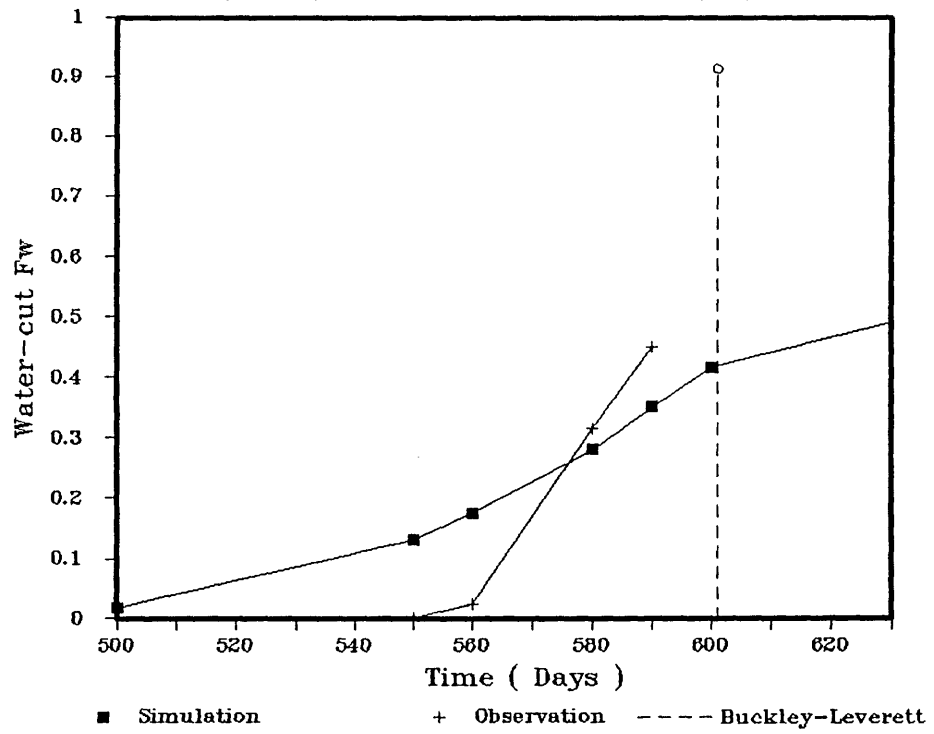


Fig. 7.15(a) Water-cut vs Time
 (Rate=5000 RB/D Rock type B)

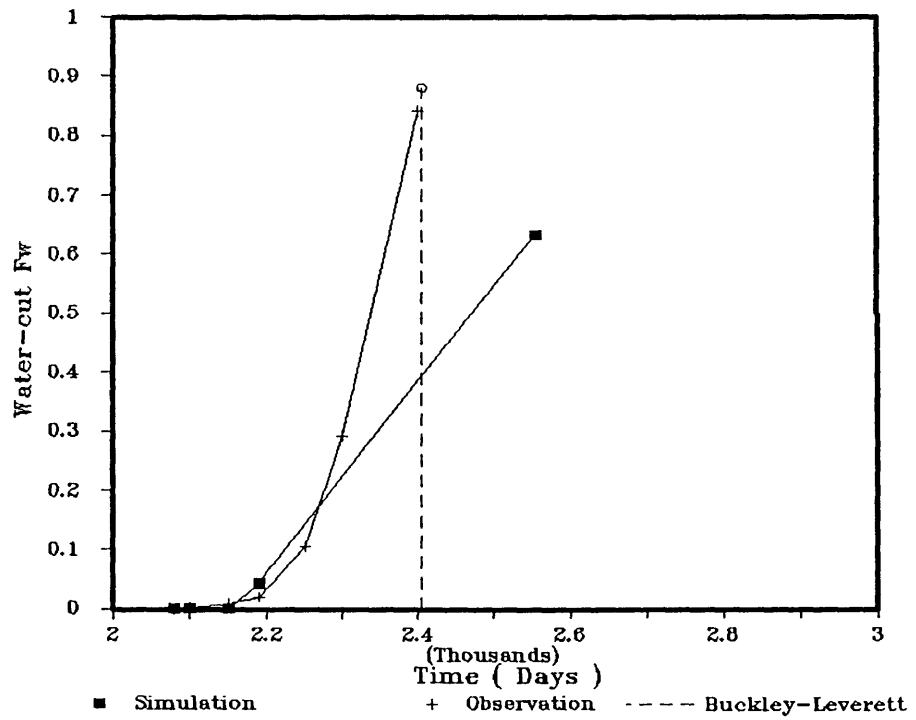


Fig. 7.15(b) Water-cut vs Time
 (Rate=9900 RB/D Rock type B)

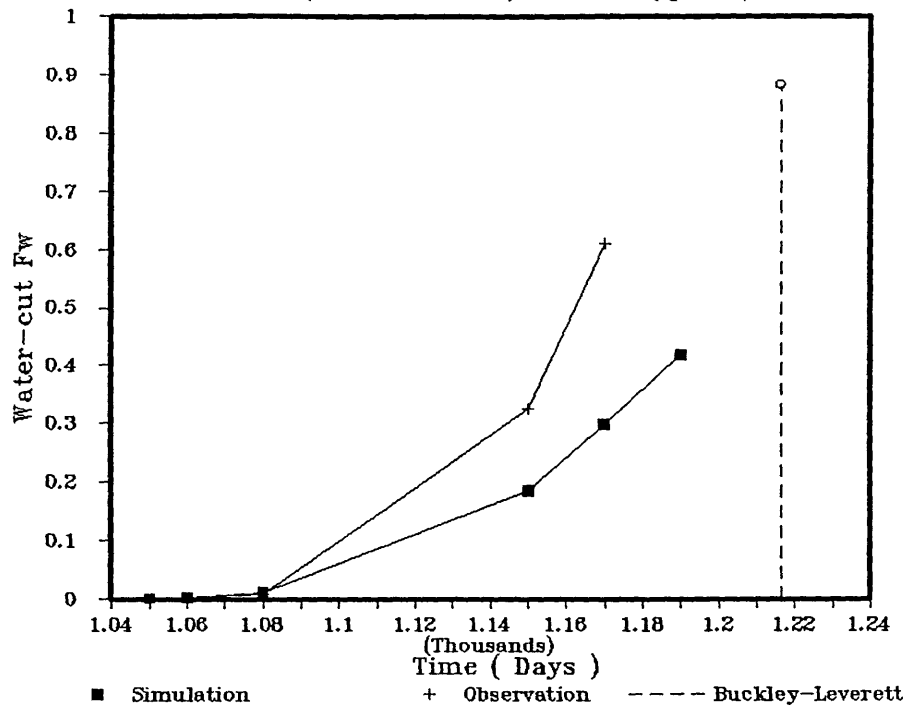
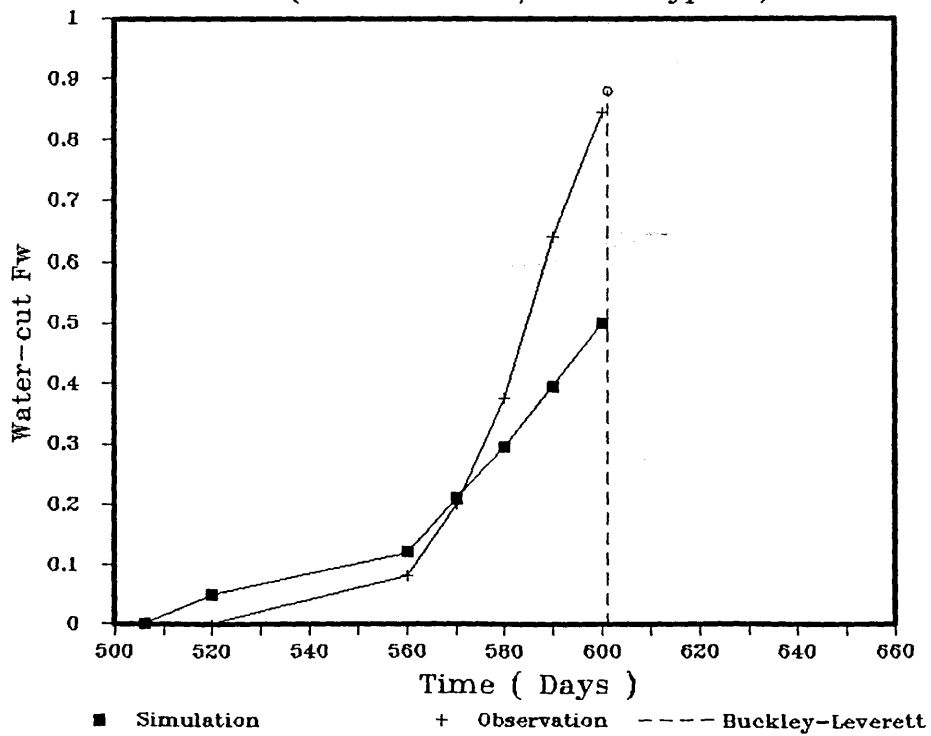


Fig. 7.15(c) Water-cut vs Time
 (Rate=20000 RB/D Rock type B)



7.5 PREDICTION OF THE RESERVOIR PERFORMANCE BY BUCKLEY-LEVERETT

The vertical permeability of the anisotropic model (section 7.4) is ignored as the flow takes place in one direction (as considered by BL). Ignorance of the vertical permeability (i.e. flow in vertical direction) is supported by its low value as compared with the horizontal permeability.

The following data of the homogeneous model are used in the calculations:

Permeability, $k = 396$ md

Porosity, $\phi = 0.1333$ (fraction)

Irreducible oil saturation, $S_{or} = 0.25$ (fraction)

Initial water saturation, $S_{wi} = 0.15$ (fraction)

End point oil permeability, $K'_{ro} = 0.78$ (fraction)

End point water permeability, $K'_{rw} = 0.425$ (fraction)

$B_o = 1.2326$ RB/STB

$B_w = 1.05$ RB/STB

Oil viscosity, $\mu_o = 0.3$ cp

Water viscosity, $\mu_w = 0.3$ cp

Initial oil in place = 15040805 STB

Reservoir pore volume = 21880401 RB

Reservoir dip = 0.0

Reservoir thickness = 240 foot

Reservoir width = 400 foot

Reservoir length = 9600 foot

Injection and production rates = 9900 RB/Day

The relative permeability data are given in column 1-4 of table 7.3.

CALCULATIONS

Using the fractional flow equation (23) the water-cut can be calculated as follows.

$$\begin{aligned} f_w &= \frac{1}{1 + \frac{K_{ro}}{K_{rw}} * \frac{\mu_w}{\mu_o}} \\ &= \frac{1}{1 + \frac{K_{ro}}{K_{rw}} * \frac{0.3}{0.3}} \end{aligned}$$

The calculated water-cut values for different water saturations are shown in

column 5 of table 7.3. *Figure 7.12* shows the water-cut values plotted against water saturation. From *Figure 7.12* we obtain:

$$S_{wf} = 0.65$$

$$\bar{S}_w = 0.70$$

$$f_{wf} = 0.9133$$

where,

f_{wf} is the water-cut at the shock front saturation S_{wf} .

The breakthrough time can be calculated using equation 7.6,

$$BTT = \frac{(0.7 - 0.15) * 21880401}{9900} \text{ Days}$$

$$BTT = 1216 \text{ Days}$$

Table 7.7 demonstrates the calculation of water saturation at the producer, S_{we}^* , and the corresponding pore volumes of water injected, W_{id} . The values of S_{we}^* , in column 6 are the midpoints of each saturation increment and W_{id} values are calculated using the equation below (23).

$$W_{id} = \left(\frac{1}{\delta f_w / \delta S_w} \right) S_{we}^* \quad (7.8)$$

The oil recovery as a function of both W_{id} and time can now be determined using equation (7.9) as listed in table 7.8.

$$N_{pd} = (S_{we} - S_{wi}) + (1 - f_{we})W_{id} \quad (7.9)$$

Where N_{pd} = Pore volumes of oil produced.

The values of f_{we}^* have been obtained from *Figure 7.12* for the corresponding values of S_{we}^* . Column 8 shows the dimensionless oil production (stock tanks of oil produced/ initial oil in place) which is calculated by multiplying N_{pd} values by [pore volume/(B_o *initial oil in place)]

S_{we}	f_{we}	ΔS_{we}	Δf_{we}	$\frac{\Delta f_{we}}{\Delta S_{we}}$	S_{we}^*	W_{id}
0.65	0.9133	0.0	0.0	-	-	-
0.68	0.950	0.03	0.0367	1.2233	0.665	0.8174
0.71	0.980	0.03	0.0300	1.0000	0.695	1.0000
0.75	1.000	0.40	0.0200	0.5000	0.730	2.0000

Table 7.7 Calculation of the saturation at the producer after BT

S_{we}^*	$S_{we}^* - S_{wc}$	f_w^*	$1 - f_w^*$	W_{id} (PV)	N_{pd} (PV)	Time (DAYS)	Dimensionless Production
0.650	0.500	0.913	0.087	-	0.5500	1216	0.649
0.665	0.515	0.935	0.065	0.8174	0.5681	1807	0.670
0.695	0.545	0.965	0.035	1.0000	0.5800	2210	0.6845
0.730	0.580	0.990	0.010	2.0000	0.5820	4420	0.6869

Table 7.8 Oil recovery calculation

7.5.1 COMPARISON BETWEEN BUCKLEY-LEVERETT AND THE SIMULATION RESULTS OF THE HOMOGENEOUS MODEL

Figure 7.16 is a plot of the dimensionless oil production versus time for Buckley-Leverett and corresponding simulation results of the homogeneous model, while *Figure 7.17* shows plot a of pore volumes of oil produced versus pore volumes of water injected for both methods.

Before breakthrough the curves in *Figure 7.16* and *Figure 7.17* follow the same trend and give similar results. Shortly before and after breakthrough time – for BL method – a little off-lap of the curves is observed (Due to shock front conversion). After the breakthrough period the two curve converge to give finally similar recovery.

The remarkable similarity of Buckley-Leverett and the simulation results of the homogeneous model strongly suggest that Buckley-Leverett method can be used to predict the waterflood of fluvial reservoirs composed of stochastic sands. Application of Buckley-Leverett is possible only after averaging the reservoir properties by the procedure presented in section 7.2.

Based on the above observations, fluid flow in reservoirs composed of stochastic sands is effectively one-dimensional (horizontal). If the fluvial reservoir model is composed of zones (layers) with relatively low vertical communication, then the reservoir may be divided into layers and the properties of each layer can be averaged separately. The resulting model will be composed of a number of isolated layers (commingled system). The waterflood performance of these layered models can be investigated by the analytical techniques for layered reservoirs such as Dykstra-Parsons (31), Reznik et al(81), Johnson(49), etc...

In the following section, a 3-layer model for our fluvial reservoir is generated from the data of the 2-D model (with pseudos). The performance of this model is predicted by numerical simulation. The results of this simulation study (which match with the results of 3-D model) are used as a base case in comparison with the performance of the analytical methods.

Fig. 7.16 Dimensionless Oil Production vs. Time (Buckley-Leverett)

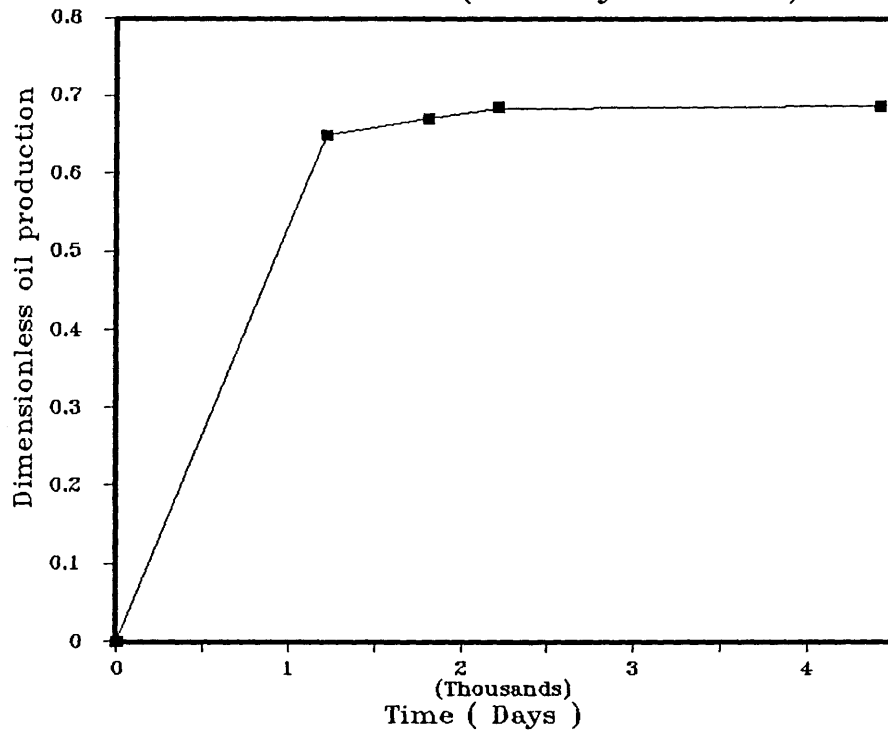
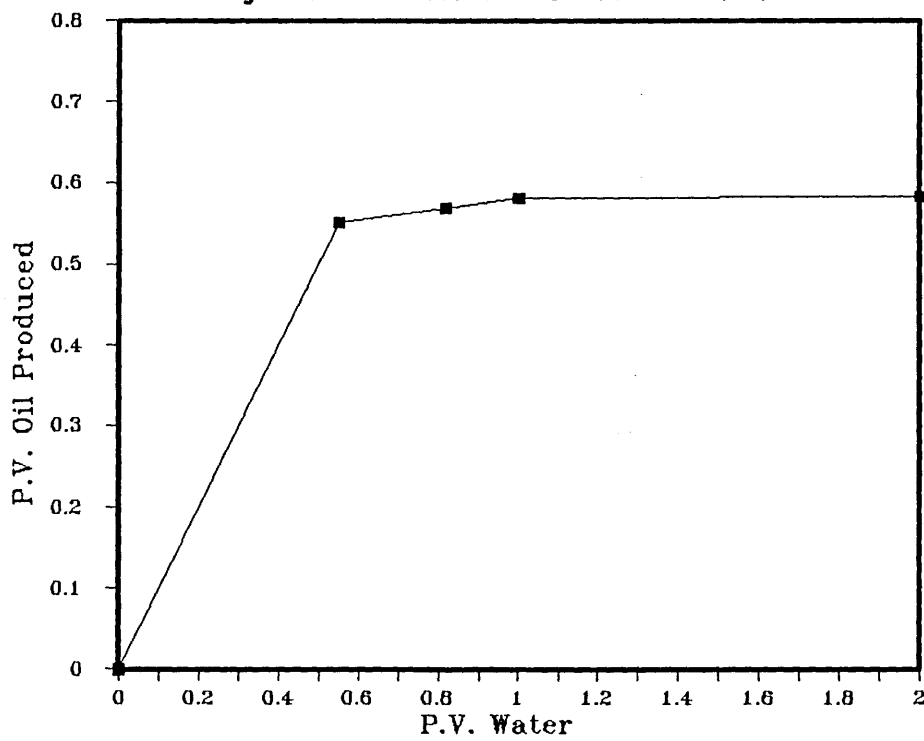


Fig. 7.17 Pore Volumes of water injected vs. P.V. of Oil Produced(BL)



7.6 SIMULATION OF THE FLUVIAL RESERVOIR PERFORMANCE USING A 3-LAYER MODEL.

Using the averaging techniques presented in section 7.2 a 3-layer model is constructed for the reservoir. Table 7.9 demonstrates the characteristics of this model. Other data are similar to the data file of the homogeneous model discussed in section 7.2. Transmissibility modifiers are used to indicate no flow across the layer boundaries.

The simulation results are plotted in *Figure 7.18* and *Figure 7.19* which show plots of the dimensionless oil produced versus time and pore volumes of oil produced versus pore volumes of water injected respectively. *Figure 7.18* also shows the water-cut versus time.

The breakthrough time is 980 days which is the same as the 2-D model (with pseudos) and the maximum recovery (at 90% water-cut) is 0.6754 which is slightly higher than the recovery of the 2-D model due to the accessibility problems discussed in section 7.4.1. The reservoir is abandoned after 1825 days due to excessive water production.

The dotted lines in the above figures represent the performance of the 2-D model (with pseudos).

The similarity between the performances of the two models validate the use of the 3-layer model to represent our fluvial reservoirs.

As mentioned before, the simulation results of this 3-layer model will be used as a base case in comparison with Dykstra-Parsons (31, 49) and Reznik et al (81) methods which are used to predict the reservoir performance in the next section.

Fig. 7.18 Water-cut and dimensionless oil Prod. vs. Time (2-D 3-layer model)

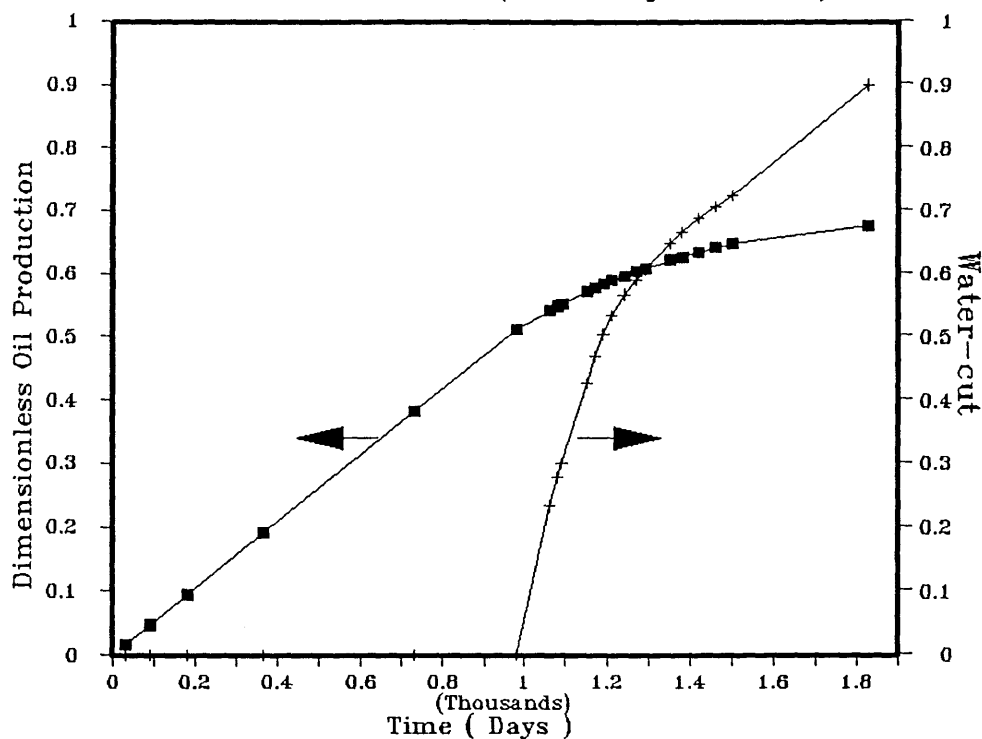
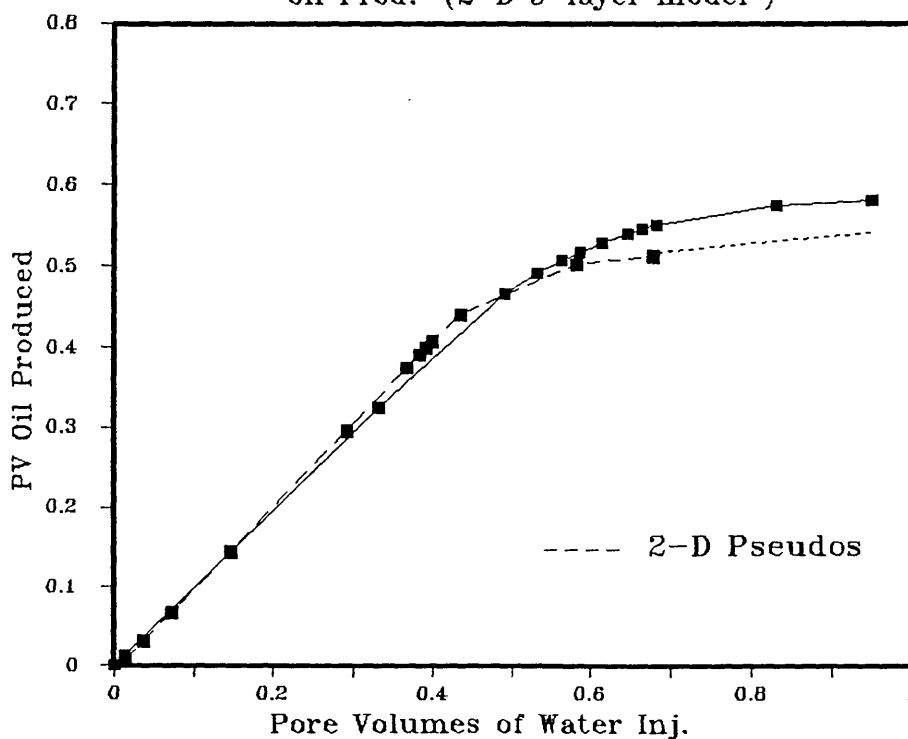


Fig. 7.19 Pore Volumes Water Inj. vs PV oil Prod. (2-D 3-layer model)



Property	Top layer	Middle layer	Bottom layer
Horizontal K, md	502	269	416
Vertical K, md	30	16	24
Porosity	0.1545	0.1121	0.1333
Thickness, ft	80	80	80
Length, ft	9600	9600	9600
Width, ft	400	400	400
S_{wi}	0.14	0.155	0.15
Mobility ratio, M	0.548	0.5355	0.545
K'_{rw}	0.43	0.415	0.425
K'_{ro}	0.785	0.775	0.780
S_{or}	0.26	0.244	0.25

Table 7.9 Characteristics of the 3-Layer model

7.7 WATERFLOOD PREDICTION OF THE LAYERED RESERVOIR BY ANALYTICAL METHODS

Further manipulation of the data of the 3-layer model is needed in order to implement Dykstra-Parsons(31, 49) and Reznik et al (81) methods. Such manipulation to obtain system parameters is demonstrated below.

7.7.1 Calculation of the system porosity:

$$\phi_s = \sum_{i=1}^n \left(\frac{\phi_i H_i}{H_s} \right) \quad (7.10)$$

Where,

ϕ = Porosity of individual layers.

n = Number of layers.

i = 1,2,3,...,n

H = Layer thickness.

H_s = Total thickness of the reservoir.

Using the data of table 7.10 we get ϕ_s ,

$$\begin{aligned}\phi_s &= \frac{0.1545 * 80}{240} + \frac{0.1121 * 80}{240} + \frac{0.133 * 80}{240} \\ &= .1333(\text{fraction})\end{aligned}$$

7.7.2 Calculation of the system mobility ratio, M_s :

$$M_s = \sum_{i=1}^n \left(\frac{H_i M_i}{H_s} \right) \quad (7.11)$$

Where,

M_i = Layer individual mobility ratio.

h_i = Individual layer thickness.

For M_s , we can use the mobility ratio of the homogeneous model which should represent our system. Therefore,

$$\begin{aligned}M_s &= \frac{K'_{rw} * \mu_o}{K'_{ro} * \mu_w} \\ &= \frac{0.425 * 0.3}{0.78 * 0.3} \\ &= 0.545\end{aligned}$$

Initial water saturation, $S_{wi} = 0.15$

7.7.3 Calculation of the Permeability variation:

For our three values of permeability the (percent of samples with greater permeability greater than specific values) is given below.

Permeability md	% Greater than
269	66.6
416	33.3
502	0.00

These values are plotted on Log-probability paper and a line is drawn through

the lining-up points which are only two in our case, see *Figure 7.20*, \bar{K} is read at 50% probability (X axes) and K_σ at 84.4 probability. The coefficient of permeability variation (permeability variation), V , is given by,

$$\begin{aligned}
 V &= \frac{\bar{K} - K_\sigma}{\bar{K}} & (7.12) \\
 &= \frac{340 - 205}{340} \\
 &= 0.397
 \end{aligned}$$

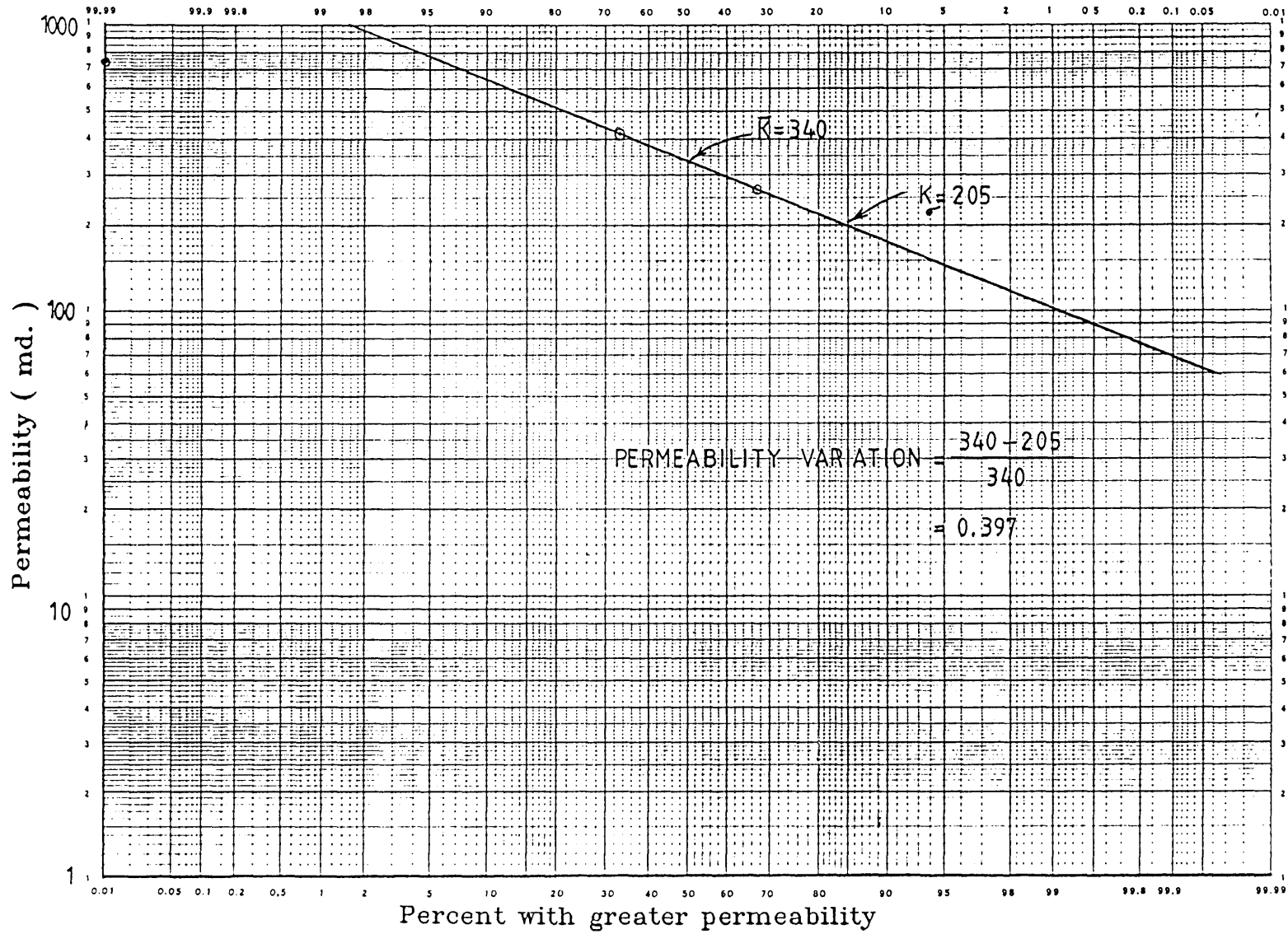
7.7.4 Prediction of the reservoir performance by Dykstra-Parsons Method.

As shown in Chapter 2, the performance of Dykstra-Parson method and its graphical representation (81) is exactly the same. Therefore, in this section, the graphical representation of Dykstra-Parson is used due to its simplicity. *Figure 7.21(a),(b),(c), and (d)* from reference (81) will be used in the calculation as shown in table 7.10. Using the values of permeability variation and mobility ratio enter each figure to find the value of the group $R(1 - S_{wi} * WOR^{-0.2})$. Since the water-oil ratio, WOR, for each graph is known and the initial water saturation is given, then the fractional recovery, R, can be calculated. R must be multiplied by a correction factor which takes into account the fact that the areal sweep efficiency of the pattern is less than one. For the sake of comparison with the 3-layer model we use the same sweep efficiency observed in the results of the 3-layer simulation. 96% of the recoverable oil was swept, therefore, we can use this value as the areal sweep efficiency. The values of column 4 in table 7.10 are multiplied by this factor to create column 5.

Figure used	WOR	$R(1 - S_{wi} * WOR^{-0.2})$	Fractional recovery, R	Corrected R
7.20 (a)	1	0.245	0.327	0.3136
7.20 (b)	5	0.360	0.404	0.387
7.20 (c)	25	0.412	0.447	0.429
7.20 (d)	100	0.455	0.484	0.465

Table 7.10 Recovery calculation by the graphical representation of Dykstra-Parsons (24).

Fig. 7.20 Calculation of the permeability variation



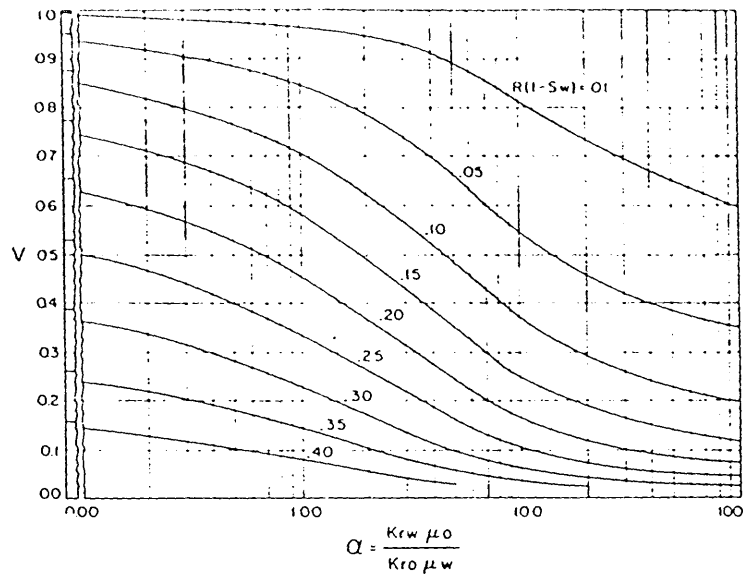


FIG. 7.11a PERMEABILITY VARIATION PLOTTED AGAINST MOBILITY RATIO SHOWING LINES OF CONSTANT $R(1 - S_w)$ FOR A PRODUCING WATER-OIL RATIO OF 1.

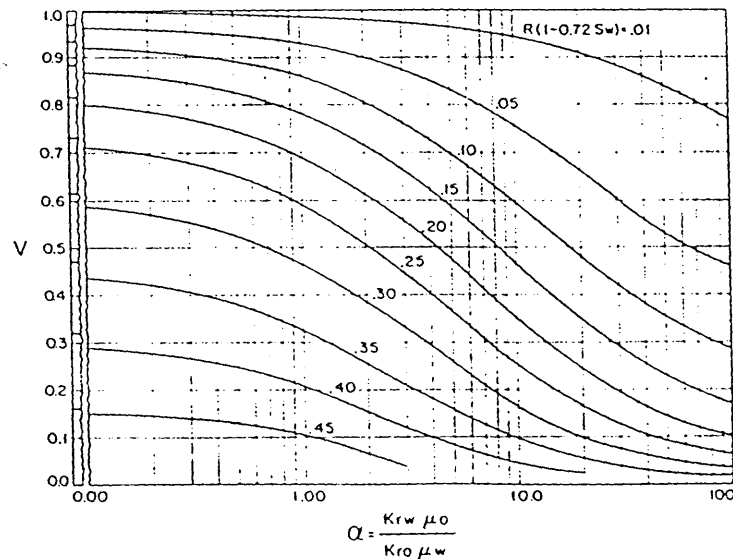


FIG. 7.11b PERMEABILITY VARIATION PLOTTED AGAINST MOBILITY RATIO SHOWING LINES OF CONSTANT $R(1 - 0.72 S_w)$ FOR A PRODUCING WATER-OIL RATIO OF 5.

(After Ref. 81)

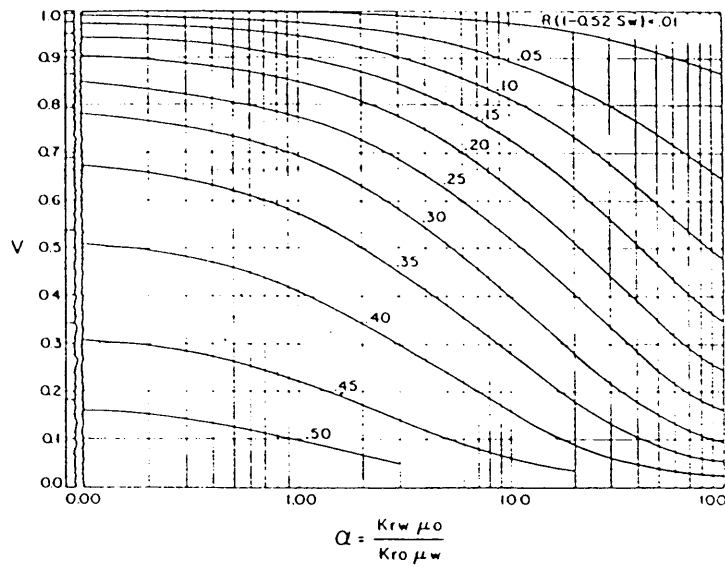


Fig. 7.21C PERMEABILITY VARIATION PLOTTED AGAINST MOBILITY RATIO SHOWING LINES OF CONSTANT $R(1 - 0.52 S_w)$ FOR A PRODUCING WATER-OIL RATIO OF 25.

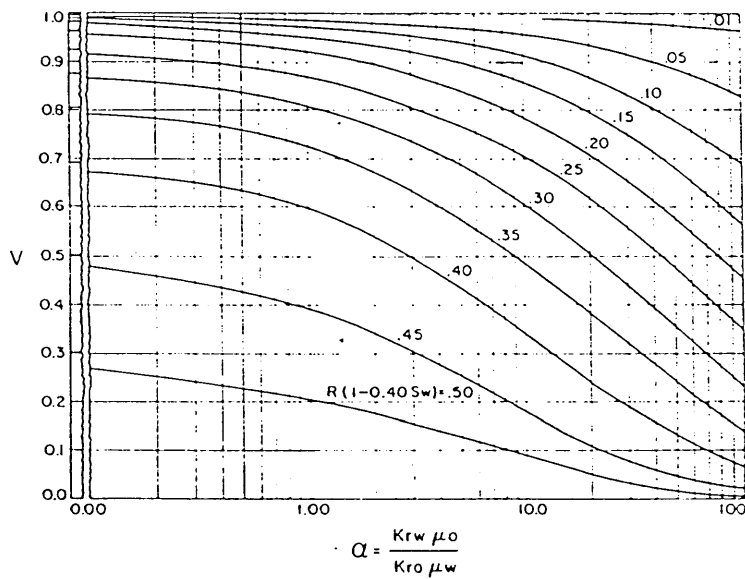


Fig. 7.21D PERMEABILITY VARIATION PLOTTED AGAINST MOBILITY RATIO SHOWING LINES OF CONSTANT $R(1 - 0.40 S_w)$ FOR A PRODUCING WATER-OIL RATIO OF 100.

(After Ref. 81)

* Calculation of breakthrough time for the most permeable layer:

Using Dykstra-Parsons method, only the breakthrough time of the most permeable layer can be predicted. Equation (3) in Reference (31) can be used in the BTT calculations as shown below.

$$\frac{Z_i}{L} = \frac{M - \sqrt{M^2 + \frac{K_i}{K_1}(1 - M^2)}}{M - 1} \quad (7.13)$$

Where,

Z_i = Distance travelled by the water front in bed i.

K_i = permeability of bed i.

K_1 = permeability of the most permeable bed.

L = Length of the reservoir.

Calculate Z_i/L for each layer at BTT of layer 1 as shown below.

Layer	1	2	3
Z_i/L	1	0.606	0.863

BTT of layer 1 = (cumulative oil produced / Daily oil production rate)

Therefore,

$$BTT_1 = \frac{[\sum_{i=1}^n NR_i * (Z_i/L)]}{Q_t} \quad (7.14)$$

Where,

NR_i = Recoverable oil in layer i.

Q_t = Daily oil production rate.

For our case the recoverable oil in each layer is the same, Therefore, the recoverable oil is given by,

$$\begin{aligned} NR_i &= (IOIP/3) * (1 - S_{wi} - S_{or}) \\ &= \frac{21880401}{3} * 0.6 \text{ RB} \\ &= 4376080 \text{ RB} \end{aligned}$$

Where, IOIP =Initial oil in place .

Therefore,

$$BTT_1 = \frac{4376080(1 + 0.606 + 0.863)}{9900} \text{ Days}$$

$$= 1091 \text{ Days}$$

7.7.5 PREDICTION OF THE RESERVOIR PERFORMANCE BY REZNIK METHOD (81)

Calculation of the bed ordering parameter:

For calculation of the bed ordering parameter, the following equation is used:

$$O_i = \frac{\phi_i(\Delta S_w)_i}{M_{wi}} * (1 + M_i) \quad (7.15)$$

Where,

M_{wi} = Water mobility of each layer(K_{rw}/μ_w).

ΔS_w = Saturation gradient at the flood front (recoverable P.V.).

O_i = Ordering parameter of bed i.

K_{rw} = Relative permeability of water.

μ_w = Water viscosity.

Calculation of O_i is shown in table 7.11 using the data in table 7.9.

Bed No. (i)	Bed thickness H_i	Mobility ratio M_i	Permeability K_i	O_i
1	80	0.548	502	0.0972
2	80	0.532	269	0.0997
3	80	0.545	416	0.0982

Table 7.11 Calculation of the bed ordering parameter.

If we arrange the beds in an ascending order according to the ordering parameter, then bed 1 will breakthrough first, followed by bed 3 then bed 2.

Calculation of the front positions according to successive breakthrough times:

Knowing the succession of water breakthrough in the layers, the front positions at successive breakthrough times can be calculated using the equation below:

$$\left(\frac{X_j}{L}\right)_i = \frac{[\sqrt{M_j^2 + \frac{O_i}{O_j}(1 - M_j^2)} - M_j]}{(1 - M_j)} \quad (7.16)$$

Where,

i = Denotes the layer at which breakthrough has just occurred.

j = Denotes the layers still producing oil.

X = Distance travelled by the water-front in layer j.

The fractional front positions at breakthrough times of the different layers are shown in table 7.12.

Bed number	Distance travelled at BT of layer 1	
2	0.9925	At BT of layer 2
3	0.9807	0.988

Table 7.12 The fractional front positions at successive BTT of the layers.

Calculations at BTT of layer 1:

$$\text{Coverage, } C = \frac{\sum_{i=1}^{\alpha-1} NR_i + \sum_{i=\alpha}^n NR_i \frac{X_i}{L}}{\sum_{i=1}^n NR_i} \quad (7.17)$$

Where,

α = Number of beds not watered-out.

Since porosity is considered the same for all the layers (for the sake of comparison with Dykstra-Parsons), then the initial oil in place in all the layers is constant (equal dimensions). The recoverable oil in each layer is then equal to 4376080 RB. The coverage is calculated using the data of table 7.12 in equation 7.17 to give C=0.991.

Calculation of the BTT:

$$BTT = \frac{[NR_1 + \sum_{i=\alpha}^n NR_i \frac{X_i}{L}]}{Q_T} \quad (7.18)$$

$$BTT = 1315 \text{ Days}$$

Calculation of WOR and water-cut:

WOR after BTT of layer 1 is given by,

$$WOR(after BT_1) = \frac{[\sum_{i=1}^{\alpha-1} H_i M_{wi}]}{\sum_{i=\alpha}^n \frac{H_i M_{wi}}{[(1-M_i) \frac{X_i}{L} + M_i]}} \quad (7.19)$$

$$WOR = 0.509(\text{fraction})$$

$$\begin{aligned} \text{Water - cut, } f_w &= \frac{0.509}{0.509 + 1} \\ &= 0.337(\text{fraction}) \end{aligned}$$

Calculation of the incremental oil production, ΔN_{pr} :

The oil produced till the BTT of layer 1 is given by the equation below:

$$\Delta N_{pr} = \sum_{i=\alpha-1}^n NR_i [(\frac{X_i}{L})_{j+1} - (\frac{X_i}{L})_j] \quad (7.20)$$

Where,

j = Denotes the current step.

$j+1$ = Denotes the next step.

Substituting in the above equation we get

$$\Delta N_{pr} = 13043781 \text{ RB}$$

Calculations at BTT of layer 2:

The time lag between BTT of the first and second layer is given by,

$$BTT_2 - BTT_1 = \frac{1}{Q_i} [\sum_{i=1}^{\alpha-1} \frac{NR_i}{1+M_n} \frac{O_n}{O_i} [(1 - M_n)((\frac{X_n}{L})^2 - (\frac{X_n}{L})_{\alpha-1}^2) + 2M_n * ((\frac{X_n}{L}) - (\frac{X_n}{L})_{\alpha-1})] + \sum_{i=\alpha}^n (NR_i [(\frac{X_i}{L}) - (\frac{X_i}{L})_{\alpha-1}])] \quad (7.21)$$

Substituting the values in the above equation gives,

$$BTT_2 - BTT_1 = 11.48 \text{ Days}$$

The coverage is calculated using equation 7.17 to give, $C=0.996$ (fraction).

$$WOR = 2.05$$

$$f_w = 0.672$$

$$\Delta N_{pr} = 64766 \text{ RB}$$

Calculations at BTT of layer 3:

$$C = 1$$

$$BTT_3 - BTT_2 = 19.4 \text{ Days}$$

$$WOR = \infty$$

$$f_w = 1$$

$$\Delta N_{pr} = 52513 \text{ RB}$$

The results obtained from Reznik *et al* method (81) can be summarised as shown in table 7.13.

Time (days)	RB of oil produced	Dimensionless oil production	Water-cut	Remarks
1315	13043781	0.7013	0.337	BT of top layer
1327	13108547	0.7048	0.672	BT of bottom layer
1346	13161060	0.7076	1.0	BT of middle layer

Table 7.13 The Results of Reznik Method

7.7.6 Comparison of the simulation and analytical results.

The breakthrough time obtained from Dykstra-Parsons (DP) method is 1091 days whereas the BTT for Reznik method is 1315 days. There is a great difference in BTTs although latter methods is an extension of the former one. This is due to the expanded bed ordering parameter developed in the latter method. This ordering parameter considers the individual mobility ratios of the layers to specify the sequence in which the layers are watered-out. Beds with lower permeabilities and favourable (smaller) mobility ratios may be watered-out before others with higher permeability and mobility ratios according to the ordering parameter (beds with smaller parameter are watered-out first).

Compared with the simulation results of the 3-layer model the two BTTs of the analytical methods are greater than the simulation value, 980 days, but Reznik method gave a very late BTT due to the almost uniform sweeping of the model. By Reznik method the difference between BTTs of the layers is 11.5 and 19.4 days, therefore the difference between BTT and abandonment of the reservoir is only one month. The corresponding difference from the 3-layer simulation results is more than 945 days (when water-cut is 90%).

The water-cut versus dimensionless oil production curves are plotted in *Figure 7.22* for the simulation and analytical methods. Dykstra-Parsons method gave very pessimistic recovery. At WOR of 100 (water-cut = 0.96) the oil recovery is 0.484 (fraction) assuming 100% areal sweep efficiency whereas Reznik's method gives 0.7076 recovery when water-cut is 1.0 (fraction). The maximum recovery from simulation is 0.6754 (fraction) at water-cut 90% and the curve can be extrapolated to give the recovery of 0.695 (fraction) at 100% water-cut.

The oil recovery at BTT for DP, Reznik, and the simulation method are 0.275, 0.7013, and 0.505 respectively.

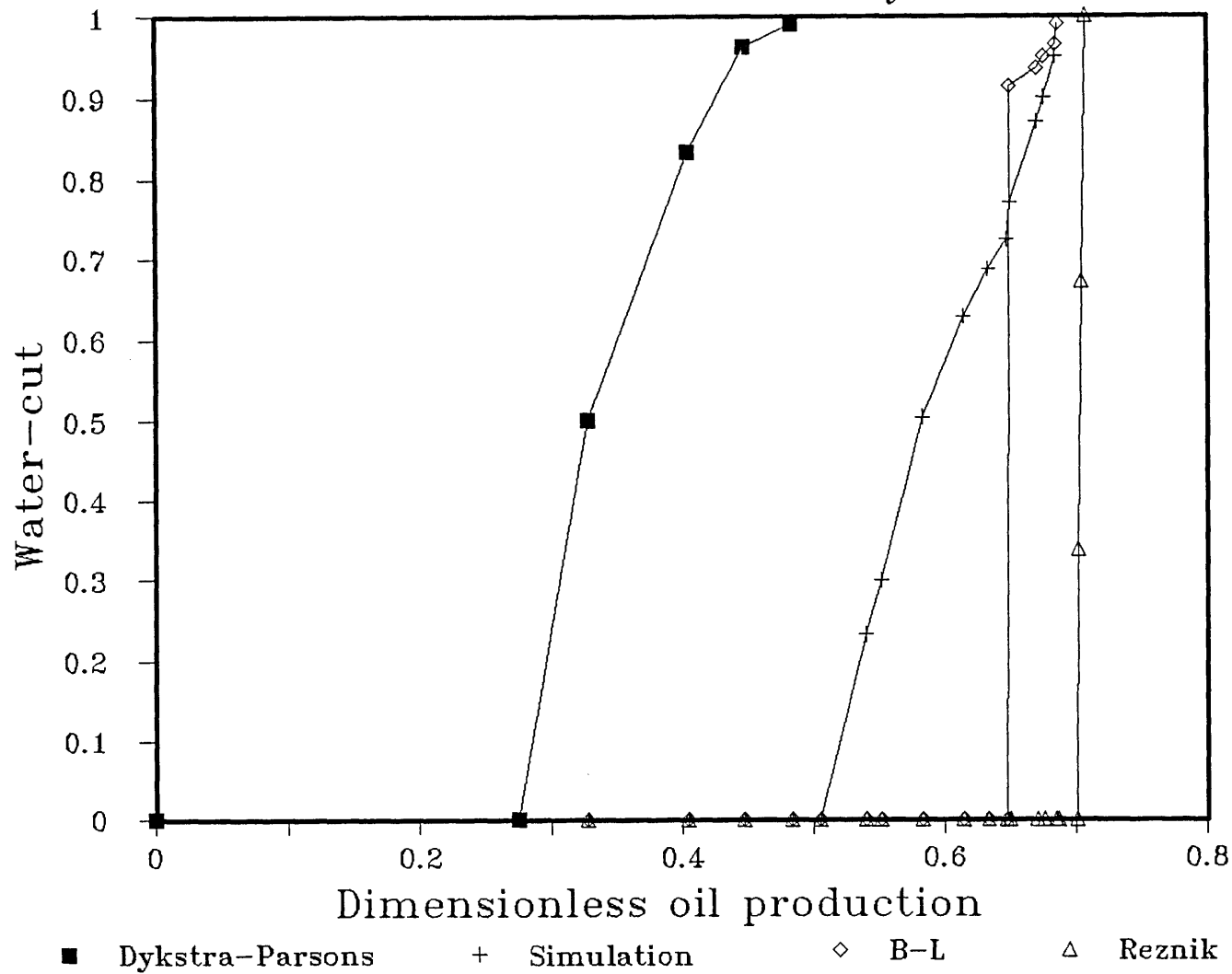
From the above results we can conclude that Reznik method gives reliable maximum recovery values (within 1% difference from simulation) but the recovery at BT given by this method is considerably higher than reality (simulation), whereas DP method gives very low recoveries at BTT and at abandonment when the WOR is higher than 100.

Shown also on *Figure 7.22* are the results of Buckley-Leverett method. The early BT data diverge from the simulation curve due to the shock-front conversion,

but the results after BT converge to the simulation curve to give the same ultimate recovery.

The drawbacks revealed by the above calculations for DP method suggest that this method is not suitable for prediction of waterflood performance of pseudo models for fluvial (stochastic) reservoirs. Reznick method is suitable for estimation of the maximum recovery although it gives high recoveries at BTTs. Buckley Leverett seems to be the best approximation and therefore, it is recommended for such calculations.

Fig. 7.22 Water-cut vs Dimensionless oil Prod. for Simu. & Analy. methods



CHAPTER 8

CONCLUSIONS AND RECOMMENDATIONS

8.1 CONCLUSIONS

This research investigated the various types of heterogeneity that affect the waterflood performance of stratified reservoirs with discontinuous sand bodies. Based on the findings in this study, the following conclusions can be drawn:

- 1 - A comprehensive review is presented including various sand facies found in fluvial depositional environments, their complex geometries, associated vertical and horizontal permeability variation, and the different types of heterogeneity – such as stochastic faults and stochastic shales – which might be dominant in such environments. Also presented is the impact of this heterogeneity on the reservoir performance and oil recovery which suggested considering their various geometrical aspects in the reservoir characterisation schemes.
- 2 - The performances of the popular analytical waterflood prediction methods are critically assessed, their drawbacks and oversimplifications are pointed out, and the effects of the main factors neglected by these methods such as gravity segregation, capillary pressure, and mobility ratio on waterflood performance are examined. The limitations in straightforward application of the conventional analytical waterflood prediction methods for fluvial reservoirs are emphasised. This demonstrates the need for new characterisation and averaging techniques which consider the complex geometries of these sands and their different scales of heterogeneity.
- 3 - Analytical methods for calculation of the effective horizontal and vertical permeabilities of formations containing discontinuous shales are developed. These techniques take into consideration the shale convergence and sand compartmentalisation phenomena. A 3-D numerical technique is used to validate these methods and excellent agreement between the results is obtained.
- 4 - A series of 3-D experiments are used to simulate fluvial sands with converging shales and discontinuous sand units. The permeabilities are measured and compared with numerical and analytical results. The accuracy of the analytical methods – presented in chapter 3 – is confirmed by the good match

obtained with the experimental results. A set of experiments neglecting shale convergence is run to assess the effect of such neglect on the measured permeabilities. The discrepancy observed indicated the importance of consideration of such a phenomenon in the characterisation schemes.

- 5 - The stochastic fault modelling scheme presented in chapter 5 is based on outcrop statistical data for fault throw distribution; and triangular distribution parameters for fault lengths. The application of this method enhanced the degree of realism in predicting the stochastic fault geometry and dimensions. The effect of such faults on the effective horizontal permeability in the presence of stochastic shales is also investigated. A computer code is developed to predict the resulting effective horizontal permeability. The results obtained showed the importance of evaluating the effect of these faults prior to simulating the reservoir's performance.
- 6 - The automatic reservoir descriptor developed in chapter 6 implements a special technique for sand conditioning to facilitate the description of their complex connectivities. This generates 3-D models of the fluvial reservoirs based on statistical data from wells and outcrops, empirical formulae, and a set of assumptions. Proper discretisation of the reservoir sand is achieved, and the number of grid blocks needed to describe the reservoir is reduced minimised, resulting in considerable savings in computational efforts.
- 7 - Two dimensional cross-sectional models are also generated by the reservoir descriptor. To reflect the 3-D characteristics of the reservoir in 2-D models, an automatic parameter pseudoization technique is introduced. This implies assignment of pseudo permeabilities, porosities, and pseudo net-to-gross ratios to grid blocks occupied by non-conductive shales. The comparative simulation studies presented in chapter 6 showed remarkable similarity between the performance of the 2-D model with pseudos and the 3-D model. This suggested the use of these 2-D models to simulate the performance of fluvial reservoirs.
- 8 - To find a homogeneous model which can give the performance of the 3-D model, a hybrid averaging technique is developed. In this technique, the 3-D model is first reduced to a 2-D model with pseudos, then, a combination of the arithmetic, harmonic, and the renormalisation averaging techniques is used to obtain one representative permeability value for the reservoir. This

value is used to generate relative permeability curves based on empirical charts. The arithmetic average of the porosities is used for the homogeneous model. The performance of this model was listed against the performance of the 3-D model showing an excellent agreement, which validated the introduced averaging technique. The simulation performance of the homogeneous model is listed against the performance of Buckley-Leverett (13), Dykstra-Parsons (31), and Reznik (81) methods. The Buckley-Leverett appears to give the closest results to simulation, therefore, it is recommended for fluvial reservoirs after averaging by our techniques.

8.2 RECOMMENDATIONS

- 1 - The degree of sand compartmentalisation with increasing shale frequency should be further studied. Such a study can enhance the accuracy of the methods for calculation of the effective permeabilities by providing reliable statistical data.
- 2 - Application of the stochastic fault generation scheme with the corresponding algorithm for effective permeability calculation, on an actual field with production history can provide more evidence on the validity of the applied techniques.
- 3 - Zero shale permeability was assumed in the methods presented in this work. Consideration of shales with non-zero permeabilities or shales with burrows should be investigated.
- 4 - Accurate techniques that can identify the regional paleocurrent direction of flow should be developed. This is crucial for the reservoir modelling scheme as it indicates the general direction in which the elongate sand bodies are to be extended.
- 5 - Listing of the simulation performance of a 3-D model against the performance of a homogeneous model (averaged by the introduced hybrid technique) of a reservoir with production history can further validate the averaging technique introduced in this study. Application of Buckley-Leverett method on the homogeneous model can provide empirical evidence of the applicability of such a method for fluvial reservoirs after averaging by our new techniques.

REFERENCES

- [1] Abu-elbashar, O.B.: "Modelling and Simulation of Stochastic Sands in Stratified Reservoirs: 2-D Description by Pseudo Parameters," Presented at the Student Paper Competition, Offshore Europe, Aberdeen, 5-8 Sept., 1989.
- [2] Allan, S.: "Gravity Segregation in Two-Phase Displacement Process," Soc. Pet. Eng. J., (Dec. 1971).
- [3] Allen, J.R.L.: "Studies in Fluvial Sedimentation: An Exploratory Quantitative Model for the Architecture of Avulsion-Controlled Alluvial Suites," Sediment. Geol. 21:pp. 129-147, 1978.
- [4] Ameen, M.S.: "Folding of Layered Cover due to Dip-Slip Basement Faulting," PhD Dissertation, Imperial College, London, 1988.
- [5] Beach, A.: "Structural Evolution of the Witch Ground Graben," J. Geol. Soc. L., 141, pp. 621-628.
- [6] Begg, S.H. *et al.* : "Assigning effective values to simulator gridblock parameters for heterogeneous reservoirs," SPE Reservoir Engineering, Nov. 1989.
- [7] Begg, S.H. *et al.*: "A Simple Statistical Method for Calculating the Effective Vertical Permeability of a Reservoir Containing Discontinuous Shales," SPE Paper No. 14271, 1985.
- [8] Begg, S. H. *et al.*: "Modelling the Effects of Shales on Reservoir Performance: Calculation of Effective Vertical Permeability," SPE Paper No. 13529.
- [9] Berruín, N. A.: "A Numerical Simulation Study of the Accuracy of the Recent Engineering Methods for Predicting Waterflood Performance of Stratified Reservoirs," PhD Dissertation Texas A&M Univ., Dec. 1977.
- [10] Berruín, N. and Morse, R.: "Waterflood Performance of Heterogeneous Systems," J. Pet. Tech., July, 1979, pp. 829-836.
- [11] Brand, P.J.: "The Modelling of Faulted Reservoirs with Stochastic Treatment of Faults," MSc. Thesis, Imperial College, London, England, 1986.
- [12] Brydges, W.T., Gulati, S.T., and Baum, G.: "Permeability of Glass Ribbon - Reinforced Composites," Journal of Material Sci., Vol.10, 1975, pp. 2044-2049.

- [13] Buckley, S.E. and Leverett, M.C.: "Mechanism of Fluid Displacement in Sands," Trans. AIME (1942) 146, pp.107-116.
- [14] Cant, D. J. and Walker, R. G.: "Fluvial Process and Facies Sequences in the Sandy Braided South Saskatchewan River, Canada," Sedimentology, Vol. 25, pp. 625-648, 1978.
- [15] Campbell, C.V.: "Reservoir Geometry of Fluvial Sheet Sandstones," The AAPG Bulletin, Vol. 60, No.7, July, 1976.
- [16] Cardwell, W.T. and Parsons, R.L.: "Average Permeabilities of Heterogeneous Oil Sands," T.P. 1853, Petroleum Technology, March 1945.
- [17] Chiles, J.P.: "Geostatistique Des Phenomenes Non-Stationnaires (dans le Plan)," These de docteur-Ingenieur, Centre de Geostatistique, ENSMP, 1977.
- [18] Coats, K. H. *et al.*: "The Use of Vertical Equilibrium in Two- Dimensional Simulation of Three-Dimensional Reservoir Performance," Soc. Pet. Eng. J. March, 1971, pp. 63-71; Trans. AIME, 251.
- [19] Coward, M.P. and Gibbs, A.D.: "Structural Interpretation with Emphasis on Extensional Tectonics," JAPEC Course Notes No.49, JAPEC, London, 1984.
- [20] Craig, F.: "The Reservoir Engineering Aspects of Waterflooding," SPE Monograph series Richardson, TX (1971) 3.
- [21] Craig, F. F. *et al.*: "A Laboratory Study of Gravity Segregation in Frontal Drives," Tran. AIME (1957), Vol. 210, pp. 275-282.
- [22] Crans, W. and Mandl, G.: "On the Theory of Growth Faulting," Pt II (a), Genesis of the 'Unit' J. Pet. Geol. 3, pp. 209-236, 1980.
- [23] Dake, L.P.: "Fundamentals of Reservoir Engineering," Elsevier Scientific Publishing Company, 1978.
- [24] Daltaban, T.S.: Personal consultation.
- [25] Delhomme, A.E. and Giannesini, J.F.: "new Reservoir description Techniques Improve Simulation Results in Hassi- Messaoud Field - Algeria," SPE Paper No. 8435.
- [26] Dietz, D.N.: "A Theoretical Approach to the Problem of Encroaching and By-

Passing Edge Water," Akad. van Wetenschappen, Amsterdam, Proc. Vol.56-B:83, 1953.

[27] Douglas, J. Jr. *et al.*: "Calculation of Linear Waterflood Behaviour Including the Effect of Capillary Pressure," Trans. AIME (1958) 213, pp. 96-102.

[28] Doyen, P. M. *et al.*: "Seismic Description of Lithology - A Monte Carlo Approach," Presented at the Joint IMA/SPE European Conference on the Mathematics of Oil Recovery, Robinson College, Cambridge University, 25-27th July, 1989.

[29] Dupuy, M. and LeFebure Du Prey, E.: "L'anisotropie d'ecoulement en milieu poreux presentant des intercalation horizontale discontinues," Communication No.34, Troisieme Coloque De L'association De Recherch sur les Techniques De Forage et De Production, June 10-14, 1968, PAU, France.

[30] Dykstra, H.: "Discussion of an Analytical Extension of the Dykstra-Parsons Vertical Stratification Discrete Solution to a Continuous, Real-Time Bases," SPE Paper No.13753.

[31] Dykstra, H. and Parsons, R.L.: "The Prediction of Oil Recovery by Waterflood," Secondary Recovery of Oil in the United States, 2nd. Ed., API, New York (1950), 160.

[32] Earlougher, J.R.: "Advances in Well Test Analysis," SPE Monograph Series, Vol.5.

[33] El-Khatib, N.: "The Effect of Crossflow on Waterflooding of Stratified Reservoirs," J. Pet. Tech. April, 1985.

[34] Enick, R. M. *et al.*: "The Statistical and Dimensionless Time Analog to the Generalized Dykstra-Parsons Method," SPE Paper No. 14523.

[35] Farmer, C. L.: "The Mathematical Generation of Reservoir Geology," Presented at the Joint IMA/SPE European Conference on the Mathematics of Oil Recovery, Robinson College, Cambridge University, 25-27th July, 1989.

[36] Fayers, F. J. and Sheldon, J.W.: "The Effect of Capillary Pressure and Gravity on Two-Phase Fluid Flow in a Porous Medium," Trans. AIME (1959) 216, 147-155.

- [37] Focas, A.S. and Yortsos, Y.C.: "On the Exactly Solvable Equation Occurring in Two-Phase Flow in Porous Media," *SIAM J. Appl. Math.* (1982) 42, No. 2, 318.
- [38] Galloway, W. E. and Hobday, D.K.: "Terrigenous Clastic Depositional Systems," *Spring-Verlay, New York* (1983).
- [39] Geehan, G. W. *et al.*: "Geological Prediction of Shale Continuity, Prudhoe Bay Field," in *Reservoir Characterization*, Academic Press, Inc. 1986.
- [40] Gill, W.D.: "Syn depositional Sliding and Slumping in the West Clare Namurian Basin, Ireland," *Geol. Surv. Ireland, S. Paper 4*, 1979.
- [41] Haldorsen, H.H.: "Reservoir Characterisation Procedures for Numerical Simulation," *PhD Dissertation, University of Texas*, (1983).
- [42] Haldorsen, H.H. *et al.*: "Review of the Stochastic Nature of Reservoirs," Presented at the Joint IMA/SPE Seminar entitled, *The Mathematics of Oil Production*, Robinson College, Cambridge, July 6-7, 1987.
- [43] Halderson, H.H., Chang and Begg, S.H.: "Discontinuous Vertical Permeability Barriers: A Challenge to Engineers and Geologists," in *North Sea Oil and Gas Habitat*, Edited by J. Kleppe *et al.*, Published by Graham & Trotman, 1985.
- [44] Halderson, H.H. and Lake, L.W.: "A New Approach to Shale Management in Field-Scale Models," *SPEJ*, Aug. 1984, pp. 447-452.
- [45] Harris, D.G. and Hewitt, C.H.: "Synergism in Reservoir Management - The Geologic Perspective," *J. Pet. Tech.* (July 1977), pp. 761-770.
- [46] Hearn, C.L.: "Simulation of Stratified Waterflooding by Pseudo Relative Permeability Curves," *J. Pet. Tech.* (July 1971).
- [47] Hornbrook, J. and Kelkar, B.G.: "New Method Simplifies Waterflood Predictions," *Oil & Gas Jour.*, May 25, 1987, pp. 65-70.
- [48] Hovanessian, S.A. and Fayers, F.J.: "Linear Waterflood with Gravity and Capillary Effects," *Soc. Pet. Eng. J.*, March 1961, pp. 23-36, *Trans. AIME*, Vol, 222, 1962.
- [49] Johnson, C.E.: "Prediction of Oil Recovery by Water Flood - A Simplified Graphical Treatment of the Dykstra-Parsons Methods," *Trans AIME* , Vol. 207,

1956, pp. 345-346.

[50] Johnson, H.D. and Krol, D.E.: "Geological Modelling of a Heterogeneous Sandstone Reservoir: Lower Jurassic Stratfjord Formation, Brent Field," SPE paper no.13050, Presented at the 51th Annual Technical Conference and Exhibition of the SPE, Houston, Texas, Sept. 16-19, 1984.

[51] Johnson, J.P.: "Prediction of Waterflood Performance by the Graphical Representation of Porosity and Permeability Distribution," JPT, Nov. 1965, pp. 1285-1290.

[52] Johnson, C. R. *et al.*: "Pulse-Testing: A New Method for Describing Reservoir Flow Properties Between Wells," J. Pet. Tech., Dec. 1966.

[53] Journal, A.: "Simulation Conditionnelle - Theorie et Pratique," These de docteur - Ingenieur, Universite de Nancy I, 1974.

[54] Kakimi, T.: "Magnitude - Frequency Relation for Displacement of Minor Faults and its Significance in Crustal Deformation," Bull. Geol. Surv. Japan, 31, pp. 467-487, 1980.

[55] Kamal, M.M.: "The Use of Pressure Transients to Describe Reservoir Heterogeneity," J. Pet. Tech., Aug. 1979.

[56] King, P.R.: "Effective Values in Averaging," Presented at the Mathematics of Oil Production, IMA/SPE Conference, Robinson College, Cambridge, 6-7 July, 1987.

[57] Knight, S.R.: "The Effect of Permeability Variation on Reservoir Waterflood Performance," MSc Thesis, Imperial College, London, 1981.

[58] Knuston, C.F.: "Modelling of Noncontinuous Fort Union and Mesaverde Sandstone Reservoirs, Piceance Basin, Northwestern Colorado," SPEJ, Aug. 1976, pp. 175-188.

[59] Kyte, J.R. and Rapoport, L.A.: "Linear Waterflood Behaviour and End Effects in Water-wet Porous Media," J. Pet. Tech., Oct. 1988, pp. 47-50; Trans AIME, 213.

[60] Lake, L.W.: "The Origin of Anisotropy," JPT., April, 1988.

[61] Lake, L.W. and Carroll, H.B.: "Reservoir Characterization," Academic Press

Inc. (1986).

[62] Lankford, S.M. and Pasquini, D.E.: "How to turn an Oil Field Around," Oil and Gas Jour., Aug., 1986.

[63] Leblanc, R.J. Sr.: "Distribution and Continuity of Sandstone Reservoirs - Part 1," J. Pet. Tech., July 1977, pp. 776-792.

[64] Leverett, M.C.: "Capillary Behaviour in Porous Solids," Trans AIME (1941), 142, pp. 151.

[65] Mandl, G., De Jong, L.N.J. and Maltha, A.: "Shear Zones in Granular Materials: An Experimental Study of their Structure and Mechanical Genesis," Rock Mechanics, 9(1977), pp. 95-144.

[66] Martin, J. H. *et al.*: "Reservoir Modelling of Low-Sinuosity Channel Sands: A Network Approach," SPE Paper No. 18364, presented at the SPE European Petroleum Conference, London, UK, Oct. 16-19, 1988.

[67] Martin, J. H. and Cooper, J.A.: "An Integrated Approach to the Modelling of Permeability Barrier Distribution in a Sedimentologically Complex Reservoir," SPE Paper No. 13051.

[68] Mathews, C. S. and Russel, D. G. : "Pressure Build-up and Flow Test in wells," SPE Monograph series, Vol 1, 1967.

[69] Matherson, G. *et al.*: "Conditional Simulation of the Geometry of Fluvio-Deltaic Reservoirs," SPE Paper No. 16753, Presented at the 62nd. Annual Technical Conference and Exhibition of the SPE, Dallas, TX, Sept. 27-30, 1987.

[70] Mobarek, S.: "Waterflooding Performance using Dykstra-Parsons as Compared with Numerical Model Performance," J. Pet. Tech., Jan. 1975, pp. 113-115.

[71] Montadert, L.: "La Sedimentologie et L'etude Detaillee Des Heterogeneites D'un Reservoir - Application au Gisment D'Hassi-Messaoud," Revenue de L'institut Francais du Petrole (1963).

[72] Muraoka, H. and Kamata, H.: "Displacement Distribution Along Minor Fault Traces," J. Struc. Geol., Vol. 5, No. 5, pp. 483-495, 1983.

[73] Perkins, F.M. Jr.: "An Investigation of the Role of Capillary Pressure in Laboratory Waterfloods," J. Pet. Tech., Nov. 1957, pp. 49-51; Trans. AIME, 210.

- [74] Pierce, A.E.: "Case History: Waterflood Performance Predicted by Pulse Testing," J. Pet. Tech., Aug. 1977.
- [75] Prats, M.: "The Influence of Oriented Array of Thin Impermeable Shale Lenses or of Highly Conductive Natural Fractures on Apparent Permeability Anisotropy," J. Pet. Tech., Oct. 1972, pp. 1219-1221.
- [76] Pryor, W.A.: "Reservoir Inhomogeneities of Some Recent Sand Bodies," SPEJ, June 1972.
- [77] Pryor, W.A. and Fulton, K.: "Geology of Reservoir-Type Sand Bodies in the Holocene Grand Delta and Comparison with Ancient Reservoir Analogs," SPE Paper No. 7054.
- [78] Ravenne, C. et al.: "Heterogeneities and Geometry of Sedimentary Bodies in a Fluvio-Deltaic Reservoir," SPE Paper No. 16752, Presented at the 62nd Annual Technical Conference and Exhibition of the SPE, Dallas, Texas, Sept. 27-30, 1987.
- [79] Ravenne, C. and Beucher, H.: "Recent Developments in Description of Sedimentary Bodies in a Fluvio-Deltaic Reservoir and Their 3-D Conditional Simulations," SPE Paper No. 18310, Presented at the 63rd Annual Technical Conference and Exhibition of the SPE, Houston, Texas, 2-5 Oct. 1988.
- [80] Rettger, R.E.: "Experiments on Soft Rock Deformation," Bulletin of AAPG, Vol. 19, No. 2, Feb. 1935, pp. 271-292.
- [81] Reznik, A.A. et al.: "An Analytical Extension of the Dykstra-Parsons Vertical Stratification Discrete Solution to a Continuous Real-Time Bases," SPE Paper No. 12065.
- [82] Richardson, J.G. et al.: "The Effect of Small Discontinuous Shale on Oil Recovery," J. Pet. Tech., Nov. 1978, pp. 1531-1537.
- [83] Richardson, J. G. *et al.*: "Braided Stream Reservoirs," J. Pet. Tech., Dec., 1987.
- [84] Richardson, J. G. *et al.*: "Permeability Distribution in Reservoirs," J. Pet. Tech., Oct. 1987.
- [85] Richardson, J. G. *et al.*: "Meandering Stream Reservoirs," J. Pet. Tech., Dec., 1987.

- [86] Rider, M.H.: "Growth Faults in the Carboniferous of Western Ireland," Amer. Assoc. Petrol. Geol. Bull., 62, pp. 2191-2213, 1978.
- [87] Selley, R.C.: "Elements of Petroleum Geology," Published by Freeman, New York, 1985.
- [88] Selley, R.C.: "Ancient Sedimentary Environments," Third Edition, Published by Chapman and Hall, London, 1985.
- [89] Shi, L.Q.: "Permeability of Fault Gouges under Confining Pressure and Shear Stress," EOS, Trans. Amer. Geophys. Union, 61, 1120, 1980 (Abstract).
- [90] Sigmund, P.M. and McCaffery, F.G.: "An Improved Unsteady-State Procedure for Determining the Relative Permeability Characteristics of Heterogeneous Porous Media," SPE Paper No. 6720, SPE Jour. Vol.19, pp. 15-28, 1979.
- [91] Smith, D.A.: "Theoretical Consideration of Sealing and Non-Sealing Faults," Bulletin of AAPG, Vol. 50, No. 2, Feb. 1966, pp. 363-374.
- [92] Smith, D.A.: "Sealing and Nonsealing Faults in Louisiana Gulf Coast Salt Basin," Bulletin of AAPG, Vol. 64, No.2, Feb. 1980, pp. 145-172.
- [93] Sneider, R. M. *et al.*: "Deltaic Environment Reservoir Types and Their Characteristics," J. Pet. Tech., Nov. 1978.
- [94] Sneider, R. M. *et al.*: "Predicting Reservoir Rock Geometry and Continuity in Pennsylvanian Reservoirs, Elk City Field, Oklahoma," JPT, July 1977, pp. 851-866.
- [95] Snyder, R.W. and Ramey, H.J.: "Application of Buckley-Leverette Displacement Theory to Noncommunicating Layered Systems," J. Pet. Tech. (Nov. 1967).
- [96] Stiles, W.E.: "Use of Permeability Distribution in Waterflood Calculations," Trans. AIME (1949), 186, pp. 9-13.
- [97] Verrien, J. P. *et al.*: "Application of Production Geology Methods to Reservoir Characteristics Analysis From Outcrops Observations," Seventh World Petroleum Congress, Vol. 2 (1967), pp. 425-446.
- [98] Wadman, D.H.: "Reservoir Description Through Joint Geologic - Engineering Analysis," SPE Paper No. 7531.

- [99] Waggoner, J.R. and Lake, L.W.: "Reservoir Heterogeneities and Their Influence on Ultimate Recovery," in *Reservoir Characterization*, Academic Press Inc. (1986).
- [100] Warren, J.E. and Cosgrove, J.J.: "Prediction of Waterflood Behaviour in a Stratified System," *Soc. Pet. Eng. Jour.*, pp. 149-157, June 1964.
- [101] Warren, J.E. and Price, H.S.: "Flow in Heterogeneous Porous Media," *Trans. AIME* (1961), 222, pp. 153-169.
- [102] Weber, K.K.: "Influence of Common Sedimentary Structures on Fluid Flow in Reservoir Models," *J. Pet. Tech.*, March 1982, pp. 665-672.
- [103] Weber, K.J.: "How Heterogeneity Affects Oil Recovery," in *Reservoir Characterization*, Academic Press, Inc. 1986.
- [104] Weber, K. J. *et al.*: "Permeability Distribution in a Holocene Distributary Channel-Fill near Leerdam," *Geologic en Mijnbouw*, Vol. 51 (1), pp. 53-62 (1972).
- [105] Weber, K.J. *et al.*: "The Role of Faults in Hydrocarbon Migration and Trapping in Nigerian Growth Fault Structure," *OTC 3356*, May 1978.
- [106] Willhite, G.P.: "Waterflooding," *SPE Text Book Series V3*, 1986.
- [107] Willis, S. : "Effective Vertical Permeability in the Presence of Stochastic Shales: Simulation and Estimation," *MSc Thesis*, Imperial College, London, 1986.
- [108] Wu, T. H. *et al.*: "Probabilistic Analysis of Seepage," *Journal of Soil Mechanics and Foundation Mechanics Division*, April 1973, pp. 323-340.
- [109] Yortsos, Y.C. and Focas, A.S.: "An Analytical Solution for Linear Waterflood Including the Effect of Capillary Pressure," *Soc. Pet. Eng. J.*, Feb. 1983.
- [110] Zeito, G.A.: "Interbedding of Shale Breaks and Reservoir Heterogeneities," *J. Pet. Tech.*, Oct. 1965, pp. 1223-1228.

APPENDICES

Due to the big sizes of the computer programs developed in this study, it is preferred to supply them in a floppy disk rather than a hard copy. This will make it easier to use them for relevant calculations and will reduce the thesis to a reasonable size.

APPENDIX 3.A: PROGRAMME VERSIM

It is a programme for generation and distribution of stochastic shales in a grid block; and for calculation of effective horizontal and vertical permeabilities of the grid block considering shale convergence and sand compartmentalisation. This programme also calculates the effect of stochastic faults on the effective horizontal permeability of the grid block, and prepares the matrix coefficients for the solver of the numerical method.

APPENDIX 3.B: PROGRAMME OMASOL

Programme Omasol reads an input file created by Versim and numerically calculates the effective horizontal and vertical permeabilities of a grid block with converging shales.

APPENDIX 4.A: PROGRAMME FAULT

This programme generates and distributes stochastic faults in the reservoir domain. It is a developed version of the computer code presented by Brand (11).

APPENDIX 4.B: PROGRAMME THROW

Generates a series of throws for stochastic faults from one end to another. This programme is a developed version of the computer code presented by Brand (11).

APPENDIX 6.A: PROGRAMME SAND

This programme generates 2-D and 3-D realisation of fluvial reservoirs. It also generates pseudo 2-D models and assigns to the grid blocks all the parameters needed for numerical simulation studies. Data files are produced for plotting cross-sections of the reservoir, for simulating the reservoir performance (data files for SIMBEST simulation package), and for averaging the reservoir properties.

APPENDIX 6.B: PROGRAMME SANDPL

Programme Sandpl reads a data file generated by the programme Sand and produces a cross-section of the reservoir.

APPENDIX 7.A: PROGRAMME OKING

Calculates average horizontal and vertical permeabilities for the reservoir by different averaging methods.